Theoretical Investigations into the Effects of Reaction Environment on

Acid-Catalyzed Dehydration of Biomass-Derived Oxygenates

A DISSERTATION

SUBMITTED TO THE FACULTY OF THE

UNIVERSITY OF MINNESOTA

BY

Chotitath Sanpitakseree

IN PARTIAL FULFILLMENT OF THE REQUIREMENTS

FOR THE DEGREE OF

DOCTOR OF PHILOSOPHY

Advised by Prof. Matthew Neurock

April 2020

Abstract

The growing concerns over greenhouse gas emissions and the limited fossil fuel resources has driven the development of alternative carbon-neutral energy sources. Lignocellulosic biomass is considered an attractive option as they are renewable and are available in abundance at low cost. However, these feedstocks possess relatively low carbon/oxygen ratio and thus making the oxygen removal necessary to increase the energy density. The chemical treatment of biomass in aqueous phase typically involves initial decomposition of sugar polymers into individual sugar monomers followed by a series of acid-catalyzed dehydration steps. The intermediate products that from include 5-hydroxymethylfurfural (HMF), 2-furfuraldehyde (furfural), levulinic acid, and formic acid which can be further upgraded to liquid fuel. These processes are relatively cost-efficient as they can be carried out in aqueous phase at low temperature. Despite its economic potential, very little is known about the effects of solvent on the dehydration kinetics. In this work, we utilized *ab initio* quantum chemical methods to examine the underlying principles that control the reactivity and selectivity of biomass conversion reactions, especially Brønsted acid-catalyzed dehydration of biomass-derived oxygenates in organic solvent/water mixtures.

Recent experimental studies have shown that the rate of acid-catalyzed dehydration of sugars increases by up to two orders of magnitude when the reaction is carried out in polar aprotic solvent/water mixtures such as DMSO/water mixtures and acetonitrile/water mixtures in comparison to water solvent. Furthermore, the addition of metal halides such as chloride anion into the reaction media has been shown to significantly improve the

reactivity and selectivity towards the desired HMF product. In order to develop better understandings of these observations, we used *ab initio* molecular dynamics (AIMD) together with classical molecular dynamics simulations to explore the effects of reaction environment in liquid phase on the dehydration reactions of biomass-derived oxygenates.

Our calculations suggest that the rate of Brønsted acid catalyzed dehydration in polar aprotic solvent/water mixtures is governed by the relative stability between reactants in comparison to transition state in the rate determining step. This difference in the stability is in turn controlled by the different extent of solvation for these reactive species in different solvents which explains the reactivity trend observed experimentally. The molecular dynamics trajectories for organic solvent/water systems reveal that the solvent-solute as well as solvent-solvent interactions result in the reorganization of solvent molecules around the solvated species, leading to the formation of hydrophilic domain on the reactive polyol hydroxyl groups in which the acidic proton and other hydrophilic species reside. The localization of these reactive species in close vicinity facilitates the dehydration reaction, stabilizes the charged transition state, and lowers the activation free energy of dehydration. The investigation is also extended to different reaction paths leading to the formation of humins side products to elucidate the effects of solvent on the selectivity of dehydration reactions toward HMF.

In the second part of this thesis, we focus on the use of heterogeneous catalyst for dehydration reactions. The use of heterogeneous catalyst is favored over homogeneous catalyst due to the ease of catalyst recovery. However, the *ab initio* computational investigation of liquid-phase reactions in microporous catalyst is challenging as the result

can be sensitive to the number of solvent molecules and reactive species available in the zeolite pore. In this work, we thus focused on developing an atomistic model to predict the adsorption properties of water molecules in industrially common Faujasite and Mordenite zeolites. The model features a new 'cluster swap' Monte Carlo move that allows simultaneous simulation of cation siting and aluminum distribution within the zeolite framework. The simulation results were found to satisfactorily reproduce the cationic siting in Faujasite as well as aluminum occupancy of the framework T-sites in Mordenite over a broad range of Si/Al ratios. The obtained parameters can be further improved to include the adsorption affinity for each solvent and solvated species.

Table of Contents

List of Tables

List of Figures

Chapter 1 – Introduction

Lignocellulosic biomass is considered an economical, carbon-neutral source that can fulfill the growing demand for carbon-based chemicals. The conversion of biomass to energy-dense platform chemicals can be an effective strategy that provides molecular building blocks to produce valuable products such as liquid fuels. However, the lignocellulosic biomass feedstocks contain significant oxygen content which is undesirable as a carbon source for fuels and upgraded chemicals.[1–16] Thus, the conversion of biomass to platform chemicals requires the selective removal of oxygen in order to improve the energy density. In this work, our aim is to understand the underlying principles that govern the kinetics of catalytic processes in the conversion of biomass to platform chemicals.

The oxygen removal of biomass can be achieved via different processes including gasification, pyrolysis, and aqueous-phase processing.[5] The aqueous phase route utilizes liquid phase reactions at low temperatures as opposed to the more energy intensive gasification and pyrolysis route and thus has the lowest production costs. The conversion of biomass in aqueous phase utilizes acid-catalyzed hydrolysis to depolymerize the carbohydrate polymers into glucose and xylose monomers which undergo multiple acid-catalyzed dehydration steps to yield desirable chemical intermediates such as 5-hydroxymethylfurfural[17] (HMF) and furan-2-carboxaldehyde[18] (furfural). Experiments have reported that the Brønsted acid-catalyzed dehydration of these sugars in polar aprotic solvent–water mixtures can improve the reactivity of dehydration by up to two order of magnitudes.[19–24] As such, the reaction has been extensively investigated in different solvent systems including water,[25–33] dimethyl sulfoxide (DMSO),[34–37] tetrahydrofuran (THF),[19,38–40] dioxane,[41,42] acetone,[43–45] γ-valerolactone (GVL),[20–22,46–52] and ionic

liquids.[38,53–55] Despite their importance, the effects of organic solvent on these reactions are not well understood.

A large number of computational investigations have been done to elucidate the effect of solvents on the biomass conversion reactions. Computational studies for biomass conversion in liquid phase have been performed utilizing atomistic simulation approach that simplifies complex molecular interactions into a few simple equations derived from Newton's laws of motion.[56–58] The lower computational cost for this approach allows for the simulation of large chemical systems. However, the method does not permit the simulation of rare events such as chemical reactions and therefore cannot quantitatively explain the change in experimental reaction kinetics.

The alternative *ab initio* approach, on the other hand, is used to calculate the activation energy of chemical reactions is directly related to the reaction rate. Nevertheless, the high computational cost for *ab initio* calculations limits the simulation to small molecular systems of up to a few hundred atoms. Early *ab initio* studies[37,59–68] for biomass conversion in liquid phase employed implicit solvation model that substitutes solvent molecules and their interactions for a continuum electric field in order to lower the requirement for computational resource. The implicit solvation model has been used to identify possible dehydration paths for sugars in pure solvents. However, the solvent represented by electric field is unable to simultaneously reproduce the interactions between solute and multiple solvent species and thus is inadequate for simulation in solvent mixtures. The use of an explicit solvation model which keeps solvent molecules present

have been performed[69–75] successfully but only in pure solvent systems while the experiments, which show enhanced dehydration rates, are carried out in solvent mixtures.

In order to elucidate the nature of solvent effects on dehydration reaction kinetics, we carried out both atomistic and first-principles quantum chemical calculations to examine the solvent rearrangement as well as solvent interactions between solvent molecules, reactive species, and non-reactive solute on the initial state and transitions state of the rate determining step. **Chapter 2** explores the effect of polar aprotic solvent–water mixtures on the dehydration of *tert*-butanol, 1,2-propanediol, and fructose catalyzed by a variety of strong homogeneous Brønsted acids. The computational investigations were carried out in different polar aprotic solvent–water mixtures including dimethyl sulfoxide (DMSO), dioxane, tetrahydrofuran (THF), acetonitrile, and γ -valerolactone (GVL). *Ab initio* molecular dynamics (AIMD) simulation and free energy sampling techniques were used to characterize the solvent rearrangement, measure the extent of solvation for each reactive species, and calculate the activation free energy of dehydration with explicit solvent molecules. The results were used to establish structure-reactivity relationship and explain the experimental dehydration rates which shows complex trends with respect to the composition of organic solvents.[76]

Chapter 3 studies the effect of the anion on the dehydration kinetics of fructose conversion to HMF. Experiments[77–81] have shown that both the rate and selectivity of HMF production in polar aprotic solvent–water mixtures can be improved with the addition of metal halide salts. *Ab initio* calculations were used to explore various conjugate anions of strong Brønsted acid catalyst including chloride (Cl^-), bisulfate (HSO_4^-), and triflate (TfO^-

) anions. The molecular dynamics trajectories were used to elucidate the change in solvation environment of proton, fructose, and the anions. The free energy of activations where then computed to measure the relative changes in the stability of reactants due to the changes in the solvation environment. We showed that the reaction rate enhancement from anion additives can be described in terms of solvent rearrangement and its effects on molecular interactions between reactive species

Chapter 4 discusses the solvent effects on the reaction network of glucose and fructose dehydration. Dumesic et al.[82] recently developed a catalytic process for the production of HMF from naturally abundant glucose with excellent selectivity and reactivity. The process utilizes Sn-BEA zeolite catalyst for isomerization of glucose to fructose, followed by acid-catalyzed dehydration of fructose to HMF in acetone–water mixtures using HCl. We examined the effect of solvent mixtures on various reaction paths including the direct dehydration of glucose to HMF, the isomerization of glucose to fructose in zeolite catalyst, and the dehydration of fructose to HMF. The calculated overall activation energies for the relevant elementary steps reveal the most favorable reaction path. In addition, the investigation was extended to other dehydration paths leading to undesired humins side products in order to explain the high selectivity toward HMF in acetone–water mixtures.

In order to provide insight into the solvent effects in microporous acid catalyst, it is crucial to determine the number of solvent molecules and reactants available in the zeolite pore. The adsorption affinity of acidic zeolite is highly dependent on the location of extraframework cationic binding sites and the aluminum distribution within the zeolite

framework. **Chapter 5** presents an atomistic model that can simultaneously replicate experimental cation siting and aluminum distribution in Faujasite and Mordenite zeolite. We developed a Monte Carlo 'cluster swap' move that relocates framework T-atom along with four adjacent bridging oxygen atoms to allow the migration of aluminum atoms within the framework. The obtained force-field parameters are useful for the development of solvent adsorption model.

Chapter 6 outlines the fundamental principles of reaction environment effects using results from a collection of computational studies. The structure-reactivity relationship[83,84] is established for dehydration of 2-butanol in gas phase catalyzed by Brønsted acid. This concept is extended to similar reactions carried out in acidic zeolite,[85] where the zeolite pore can interact with the transition state structure and alters the reactivity of dehydration. The effects of reaction environment in gas phase are compared with the solvent effects for homogeneous reactions previously described in Chapters 2 and 3. The discussion further explores the influence of the solvent in heterogeneous reactions, specifically the alkoxy and hydroxy paths of 2-butanone hydrogenation over a metal catalyst.[86] The interaction between liquid water molecules and the reactive species in both paths can significantly affect the reactivities and ultimately control the dominating reaction path. Finally, we demonstrate that the presence of liquid water in the electrocatalytic dissociation of water molecule over metal alloy[87] may enable a new reaction path not observed in gas phase. These established concepts can aid in the effective design of selective catalytic systems for the chemical upgrading of biomass-derived feedstocks.

Chapter 2 – Solvent-Enabled Control of Reactivity for Liquid Phase Reactions of Biomass-Derived Compounds

Adapted from Mellmer, M. A. *et al.* Solvent-enabled control of reactivity for liquid-phase reactions of biomass-derived compounds. *Nat. Catal.* **1**, 199–207 (2018). Reproduced using non-exclusive right as an author https://www.nature.com/nature-research/reprints-and-permissions/permissions-requests.

Theoretical calculations were performed by CS under the supervision of MN.

2.1 Introduction

Catalytic upgrading of biomass to renewable chemicals and fuels requires the selective removal of oxygen by dehydration of highly functionalized biomass components.[9,88,89] This requirement of achieving high selectivity is critical for catalytic processes in the chemical and pharmaceutical industries, for example, processes that take place through consecutive reaction steps, where an intermediate species is the desired product. The challenge for such catalytic processes is to identify catalysts and/or reaction conditions that allow for the selective production of the desired intermediate but minimize the subsequent conversion of the intermediate to other products.

We report herein results for Brønsted acid-catalyzed conversions of a carbohydrate (fructose), two alcohols (*tert*-butanol and 1,2-propanediol) and a furan (hydroxymethylfurfural, HMF) in liquid-phase organic solvents mixed with water. We show that the rates of dehydration of reactants containing multiple hydroxyl groups are promoted in organic solvent mixtures with water, and the promotional effects for these

reactions can be understood in terms of solvation effects for the acidic proton, reactants and transition states for these catalytic reactions. Moreover, we show that the extent of promotion by the solvent increases as the number of vicinal hydroxyl or oxygen-containing groups in the reactant increases (that is, as the reactant becomes more hydrophilic). This behavior makes it possible to achieve high yields for the partial dehydration of highly functionalized biomass-derived reactants, such as carbohydrates. We utilize these solvent effects to achieve high yields for the production of HMF from fructose by promoting the conversion of fructose to HMF, while limiting the subsequent conversion of HMF to levulinic acid.

2.2 Results and Discussions

2.2.1 Experimental reaction kinetics studies

The effects of various polar aprotic solvents mixed with water on the rates of Brønsted acid-catalyzed dehydration reactions in the liquid-phase are shown in Figure 2.1. The Brønsted acid-catalyzed dehydration of fructose to HMF is an important reaction for catalytic biomass upgrading strategies, because HMF is a desirable platform chemical with applications for transportation fuels and polymeric materials.[1,53,90–94] We have also studied the dehydration of reactants containing fewer hydroxyl groups (that is, *tert*-butanol and 1,2-propanediol) to probe how the effects of the solvent depend on the hydrophilicity of the reactant. Previous mechanistic studies of fructose dehydration to HMF have shown that the rate-determining step involves the first water elimination step,[95,96] allowing for direct comparison of the reaction kinetics between fructose dehydration and the dehydrations of butanol and 1,2-propanediol with a single water elimination step. These reaction kinetics experiments for dehydration of fructose, *tert*-butanol and 1,2-propanediol were performed

using triflic acid as the catalyst, a strong Brønsted acid (reaction conditions and experimental results can be found in Supplementary Tables 2.1–2.5 and Supplementary Figures 2.1–2.4).
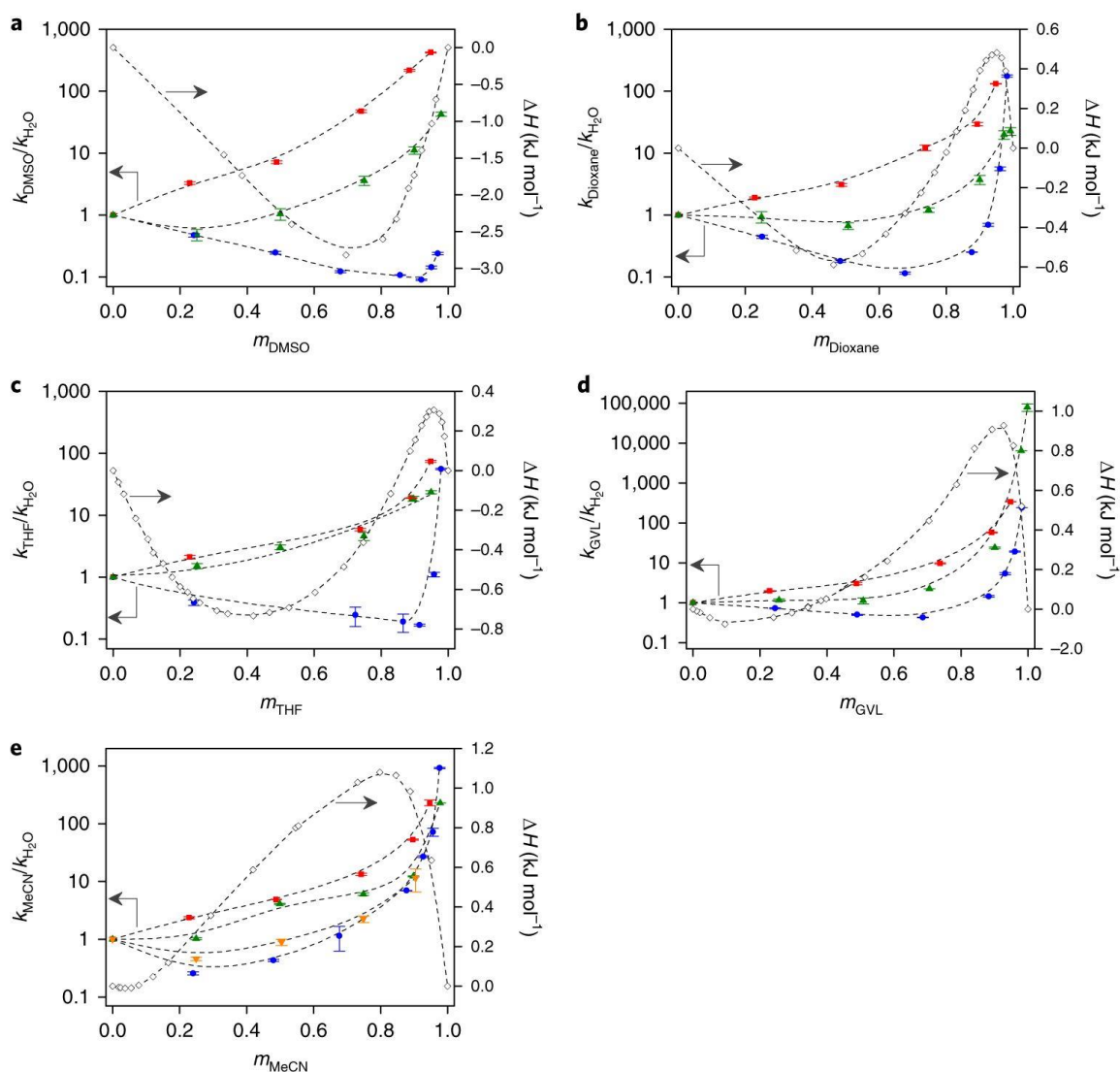
Figure 2.1 Solvation effects on the kinetics of Brønsted acid-catalyzed dehydration reactions. a–e, Ratios of the acidic proton-catalyzed rate constants (k_{H_+}) for organic solvent mixtures with water relative to the value in water (left axis) for dehydration of *tert*-butanol (blue circles), *sec*-butanol (orange triangles), 1,2-propanediol (green triangles) and fructose (red squares), and enthalpies of mixing (ΔH, hollow diamonds) for organic solvent mixtures with water (right axis), plotted against the mass fraction (m) of DMSO (**a**), dioxane (**b**), THF (**c**), GVL (**d**) and MeCN (**e**) in organic solvent mixtures with water. Black dashed lines are visual guides. Reaction conditions and references for the enthalpies of mixing for organic solvent mixtures with water can be found in the Supplementary Information and Methods. Rate constants were derived from equation (2.1). Error bars represent 95% confidence intervals.

9

The rate (r) of an acid-catalyzed conversion of a reactant, R, in solution by the acidic proton, H^+, and the undissociated acid, HB, is written as:

$$r = k_{H^+}[R][H^+] + k_{HB}[R][HB] \tag{2.1}$$

where k_{H^+} and k_{HB} are the rate constants for the specific-acid-catalyzed and general-acid-catalyzed reactions, respectively. We measured an inverse kinetic isotope effect for each reactant using D_2O as solvent ($r_{D_2O}/r_{H_2O} > 1.6$), indicating that the acid-catalyzed dehydrations of fructose, *tert*-butanol and 1,2-propanediol are catalyzed primarily by the acidic proton (that is, proton transfer is not rate-determining), and therefore, general-acid catalysis (k_{HB}) can be neglected.[97,98]

The equilibrium constant for dissociation of a Brønsted acid (that is, pK_a value) is dependent on the nature of the solvent.[99] Our reaction kinetics experiments for fructose conversion show that the rate is independent of the addition of the conjugate base of the acid catalyst (for example, potassium triflate), indicating that triflic acid is completely dissociated in each of these solvents (Supplementary Figure 2.1). Accordingly, we report in Figure 2.1 the values of k_{H^+} for dehydration of fructose, *tert*-butanol and 1,2-propanediol in organic solvents consisting of dimethyl sulfoxide (DMSO), 1,4-dioxane, tetrahydrofuran (THF), γ-valerolactone (GVL) and acetonitrile (MeCN) mixed with water. These results are reported as the value of the rate constant measured in the organic solvent mixture relative to the acidic-proton rate constant in water, plotted against the mass fraction of organic solvent in the organic solvent mixture with water.

The rate constant for the dehydration of *tert*-butanol shows complex behavior with respect to increasing the content of the organic solvent component with water. In DMSO mixtures with water (Figure 2.1a), the reactivity decreases by an order of magnitude with increasing DMSO fraction until reaching higher DMSO concentrations, where the rate begins to increase. The value of the rate constant is always lower in DMSO–water mixtures than the value in water. The use of dioxane and THF as solvents (Figures 2.1b and 2.1c, respectively) leads to similar decreases in reactivity with increasing mass fraction of organic solvent; however, at high dioxane and THF mass fractions, the reactivity for *tert*-butanol dehydration increases by 100-fold relative to the reactivity in water. Solvents consisting of GVL or MeCN mixed with water (Figures 2.1d and 2.1e, respectively) lead to slight decreases (for example, 2- to 4-fold) in reactivity at moderate fractions of these organic compounds, and lead to increases by 250-fold and 1,000-fold at high mass fractions of GVL and MeCN, respectively, relative to using water as the solvent.

The enthalpies of mixing of the aforementioned organic solvents with water provide a qualitative explanation of the reactivity trends for *tert*-butanol, as shown in Figure 2.1. Organic solvents with exothermic enthalpies of mixing with water, such as DMSO, lead to decreased reactivity of *tert*-butanol relative to water, whereas organic solvents with primarily endothermic enthalpies of mixing with water, such as GVL and MeCN, lead to increases in *tert*-butanol reaction rates compared with using water as solvent. Dioxane and THF have exothermic and subsequent endothermic enthalpy of mixing trends with increasing organic fraction, and accordingly, *tert*-butanol reactivity shows an initial decrease and a subsequent increase with increasing organic fraction. Excess enthalpies of mixing are indicative of the solvation potential of organic solvent mixtures,[100] suggesting

11

that the solvation of the kinetically relevant steps of *tert*-butanol dehydration in organic solvents is important in influencing the reaction kinetics.

The reactivity profiles in Figure 2.1 show that the rate of fructose dehydration in each organic solvent mixture with water is always higher compared with the reactivity using water as solvent. In addition, the reactivity trends for dehydration of 1,2-propanediol (Figure 2.1) correlate more closely to the trends displayed by fructose dehydration compared with those for *tert*-butanol. Furthermore, we measured the reactivity trend for dehydration of *sec*-butanol in MeCN mixtures with water using triflic acid as a catalyst (Figure 2.1e), and this trend correlates strongly with that for *tert*-butanol dehydration. Accordingly, the reactivity trends observed in this study for dehydration of *tert*-butanol, *sec*-butanol, 1,2-propanediol and fructose suggest that the extent of solvation effects on the reactivity is dependent on the hydrophilicity of the reactant for these dehydration reactions in organic solvent mixtures with water.

2.2.2 Molecular dynamics simulations

The rate for the proton-catalyzed conversion of a reactant in solution is controlled by the stability of the activated complex in the rate-determining step relative to the stabilities of the solvated proton and reactant.[101,102] Classical force-field-based molecular dynamics and *ab initio* density functional theory (DFT) molecular dynamics simulations were used to obtain equilibrium configurations for the reactant, acid and solvent mixtures, to establish elementary pathways, and to predict activation and reaction free energies for the acid-catalyzed dehydration of *tert*-butanol and 1,2-propanediol in different solvent systems. Simulation details are reported in the Supplementary Information and Methods.

The mechanisms for the acid-catalyzed dehydrations of *tert*-butanol and 1,2-propanediol (equations (2.2)–(2.7)) proceed by the quasi-equilibrated protonation of the tertiary and secondary hydroxyl groups of *tert*-butanol and 1,2-propanediol, respectively. The water molecule that results is then eliminated from the protonated alcohol to form a tertiary carbenium ion from *tert*-butanol and a secondary carbenium ion from 1,2-propanediol, which deprotonate to yield isobutene and propanal, respectively. The free energies for proton transfer from the solvent to the alcohol, alcohol protonation, water removal, carbenium ion formation and nucleophilic deprotonation were calculated to determine the activation barriers for *tert*-butanol dehydration in water, 90 wt% DMSO, 100 wt% DMSO, 70 wt% GVL and 100 wt% GVL–water mixtures (see Figure 2.2). The activation barriers for 1,2-propanediol dehydration were calculated in water and 90 wt% GVL–water mixtures. The initial solvent structures around the alcohol for all of the systems studied here and used in the DFT simulations were determined from classical molecular dynamics simulations. The 90 wt% co-solvent systems were examined to understand the qualitative differences that appear in the experimental rates for these systems. Furthermore, additional force-field simulations were carried out for 20 wt% mixtures to provide information about solvent clustering that occurs in solvent mixtures at lower concentrations of the co-solvent. The overall reaction energies and barriers determined from *ab initio* molecular dynamics simulations are reported in Figure 2.2.
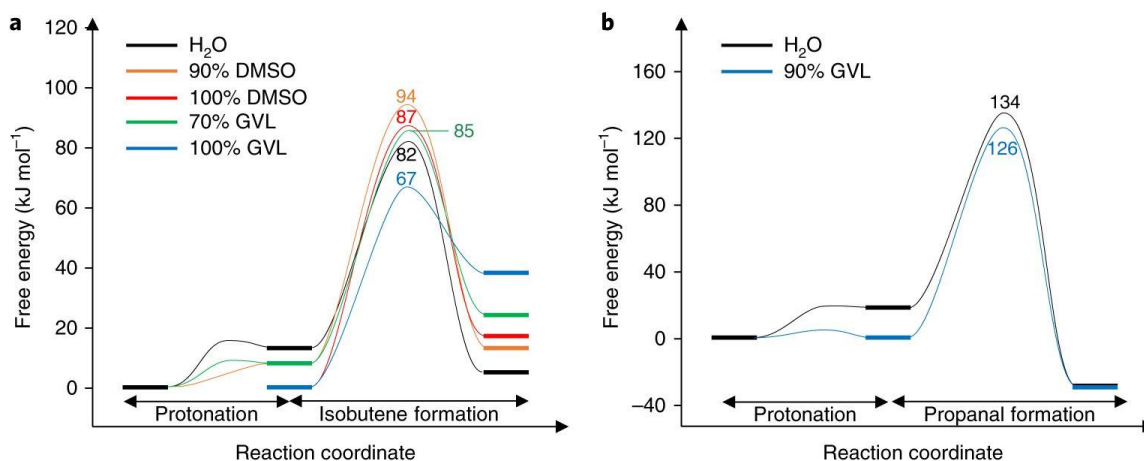
Figure 2.2 DFT simulation results of the Brønsted acid-catalyzed dehydration of *tert*-butanol and 1,2-propanediol. a, Free energy diagram for *tert*-butanol dehydration in water (black profile), 90 wt% DMSO (orange profile), 100 wt% DMSO (red profile), 70 wt% GVL (green profile) and 100 wt% GVL (blue profile) catalyzed by a Brønsted acid. **b**, Free energy diagram for 1,2-propanediol dehydration in water (black profile) and 90 wt% GVL (blue profile) catalyzed by a Brønsted acid. The free energies are relative to the lowest energy state. Detailed simulation methods and results can be found in the Methods and Supplementary Information.

Ab initio molecular dynamics simulations with umbrella sampling were used to calculate the change in free energy along the reaction coordinates (Supplementary Figures 2.5 and 2.6) for the different elementary steps and determine the free energy profiles for the dehydrations of *tert*-butanol and 1,2-propanediol in DMSO–water and GVL–water mixtures reported in Supplementary Figures 2.7–2.13. In pure water, triflic acid readily dissociates to form a hydrated proton and the corresponding triflate anion (Supplementary Figure 2.14a). The activation free energy and the overall free energy of reaction to protonate *tert*-butanol from an aqueous-phase proton were calculated to be 15 and 13 kJ mol^{-1}, respectively (Supplementary Figure 2.15). The activation free energy for the subsequent carbenium ion formation and dehydration energy was found to be 69 kJ mol^{-1}, thus resulting in an apparent activation free energy barrier of 82 kJ mol^{-1} for dehydration. The subsequent deprotonation of the carbenium ion intermediate that forms occurs very

14

rapidly and is just $1\,\mathrm{kJ\,mol^{-1}}$ higher in energy. As such we simplify the subsequent free energy profiles by combining the carbenium ion formation and deprotonation into a single step and reporting only the highest-energy transition state (Figure 2.2a and Supplementary Figure 2.7). The free energies of protonation and dehydration of 1,2-propanediol in pure water were calculated to be 18 and $116\,\mathrm{kJ\,mol^{-1}}$, respectively. The overall barrier of $134\,\mathrm{kJ\,mol^{-1}}$ for the dehydration of 1,2-propanediol at the secondary position (Figure 2.2b and Supplementary Figure 2.12) is $52\,\mathrm{kJ\,mol^{-1}}$ higher than the barrier for dehydration of *tert*-butanol, because the secondary carbenium ion that forms in 1,2-propanediol is less stable than the tertiary carbenium ion for *tert*-butanol. This result is consistent with the lower experimentally measured reactivity in water for 1,2-propanediol dehydration compared with *tert*-butanol dehydration. The transition state that forms on the elimination of water (Supplementary Figure 2.12) is characteristically different from that involved in the elimination of water from *tert*-butanol in that the OH that sits at the C_α stabilizes the 1,2-hydride shift, which is consistent with previous reports for acid-catalyzed dehydration of polyols.[103]

Results from classical and *ab initio* molecular dynamics simulations show that addition of DMSO to water at up to $90\,\mathrm{wt\%}$ DMSO results in the formation of complex DMSO–water clusters, consistent with previous experimental and simulation studies of DMSO–water mixtures.[104–107] DMSO is polarized in water to form a $(CH_3)_2S^+$–O^--like species that strongly interacts with and alters the water hydration structure, thus resulting in DMSO–water structures that are more basic than water or DMSO alone. These structures stabilize the formation of $(H_3O)^+$ and $(H_5O_2)^+$ clusters via hydrogen bonding to between one and four local DMSO molecules that strongly bind these protonated water clusters and

inhibit proton release (Supplementary Figure 2.14b). The apparent activation free energy

for *tert*-butanol dehydration increases from $82\,\text{kJ}\,\text{mol}^{-1}$ in pure water to $94\,\text{kJ}\,\text{mol}^{-1}$ in

DMSO mixtures with water ($\leq 90\,\text{wt}\%$; Figure 2.2a and Supplementary Figure 2.8),

because there is now a 6–$24\,\text{kJ}\,\text{mol}^{-1}$ energy penalty (~$6\,\text{kJ}\,\text{mol}^{-1}$ for each DMSO

molecule) to release the proton from the DMSO-stabilized H_3O^+ or $H_2O_5^+$ clusters and to

transfer it to the hydrophilic water domain near the OH group of the alcohol. This increased

binding of the proton is in accordance with the increased basicity of DMSO and DMSO–

water mixtures compared with pure water.[105,108,109] This increase in free energy is

consistent with the experimentally observed decrease in reactivity for the DMSO–water

system.

At high DMSO concentrations (approaching 100% DMSO), the apparent activation

free energy for dehydration of *tert*-butanol decreases from 94 to $87\,\text{kJ}\,\text{mol}^{-1}$. At these high

concentrations of DMSO, triflic acid remains fully dissociated.[110] The proton that forms,

however, is no longer confined to DMSO–water clusters as there is little water present in

the bulk. The proton instead binds more weakly to two DMSO molecules in solution. While

the proton is more weakly bound to DMSO than to DMSO–water clusters, it is still more

strongly bound than the proton bound to water clusters in pure water, as DMSO is more

basic than water. The proton can transfer from the bulk DMSO solvent to the *tert*-butanol

to form the protonated alcohol that is stabilized by its interaction with two bulk DMSO

molecules, analogous to the stabilization of the protonated DMSO–water clusters in the

DMSO–water mixtures. As such, the energy costs required to release the proton from the

more basic DMSO reactant state are counterbalanced, in part, by the ability of DMSO to

stabilize the protonated hydroxyl intermediate that forms in the transition state at high

DMSO concentrations. The resulting apparent activation free energy of 87 kJ mol^{-1} (Figure 2.2a and Supplementary Figure 2.9) is in agreement with experimental observations that the rate of *tert*-butanol dehydration at DMSO concentration >90 wt% is faster than the rate at lower DMSO concentrations, yet still slower than the rate in pure water.

The dehydration behavior of *tert*-butanol in GVL–water mixtures at concentrations ≤70 wt% GVL is similar to the DMSO solvent system. The solvent mixture bonds to the proton in small water clusters that are stabilized by their interactions with GVL (Supplementary Figure 2.15d). This behavior results in a 3 kJ mol^{-1} energy cost to transfer the proton from these stable GVL–water clusters to the hydrophilic domain near the hydroxyl of *tert*-butanol. This energy cost, taken together with the intrinsic barrier for the dehydration of *tert*-butanol (82 kJ mol^{-1}), results in an apparent barrier for dehydration of 85 kJ mol^{-1} (Figure 2.2a and Supplementary Figure 2.10). This higher barrier is consistent with the lower experimental dehydration rates for *tert*-butanol in GVL–water mixtures than in pure water.

The dehydration reactivity trends for 1,2-propanediol in GVL–water mixtures with <90 wt% GVL are different to those for *tert*-butanol dehydration reactivity in that the rates always increase with increasing GVL concentrations. Classical molecular dynamics simulations of 1,2-propanediol in GVL–water mixtures show that the OH substituents on the diol lead to more extensive water clusters near the vicinal hydroxyl groups than the OH group on *tert*-butanol. This bonding results in the formation of a local hydrophilic domain at the reaction site, as shown in the representative structure in Supplementary Figure 2.16c and in the radial distribution functions in Supplementary Figures 2.17 and 2.18. The

distribution of water near the OH group of *tert*-butanol, in contrast, is less extensive than the distribution of water near the hydroxyl for 1,2-propanediol. The large local water domains near the hydroxyl groups of 1,2-propanediol allow the protons to favorably reside in hydrophilic domains that surround the active OH sites. Thus, there is no energy cost to transfer the proton from the reactant state to the transition state, because the proton already resides in these larger hydrophilic domains near the two hydroxyl groups on 1,2-propanediol. As a result, the activation barrier decreases by 8 kJ mol^{-1} to 126 kJ mol^{-1} from that in pure water. The higher barrier for the dehydration of 1,2-propanediol versus that of *tert*-butanol is the result of the difference in a secondary versus tertiary carbenium ion formation. The radial distribution functions in Supplementary Figure 2.19 for the C atoms of *tert*-butanol show that the alcohol resides primarily in hydrophobic domains in DMSO and GVL, while the lack of organic solvent molecules around the methyl and methylene groups of 1,2-propanediol indicates the enhanced hydrophilicity of this species.

At high GVL concentrations (approaching 100 wt% GVL), the apparent activation free energy for dehydration of *tert*-butanol was calculated to be 67 kJ mol^{-1} (Figure 2.2a and Supplementary Figure 2.11), which is 15 kJ mol^{-1} lower than the activation free energy in water. The lower barrier results from a destabilization of the reactant state, as the water clusters in the solvent mixture that bond to the protons are eliminated. This behavior is similar to the destabilization of the proton in the 100% DMSO solvent system. The interaction of the proton with the C=O bond in GVL, however, is even weaker than its interaction with S=O of DMSO, because the C=O bond does not polarize like the S=O bond, that is, the C=O group does not interact or intermix with water as strongly as the more basic S=O group. This result is consistent with the more negative pK_a value for

protonated GVL (approximated here as protonated ester; $pK_a = -7$) compared with protonated DMSO ($pK_a = -2$), and it is consistent with the endothermic enthalpy of mixing of GVL with water. This liberation of the proton in the solvent mixture removes the free energy required to transfer the proton from bulk solution to the reactive OH group on the alcohol. The overall barrier for dehydration then solely comprises the energy cost for water elimination–carbenium ion formation (67 kJ mol^{-1}), as shown in Figure 2.2a (Supplementary Table 2.6). We note here that the GVL–water mixtures stabilize the reactant proton at low GVL weight fractions but destabilize this proton at high weight fractions. This behavior is consistent with other polar aprotic solvent mixtures, such as dioxane and acetonitrile mixture with water.[111–113] The changes in the basicity of the local solvent environment presented here appear to correlate with the reactivity and endothermic enthalpy of mixing for the different solvents, as presented in Supplementary Table 2.7 and the Supplementary Discussion.

For 1,2-propanediol dehydration at high GVL concentrations (≥90 wt% GVL), the proton is present in the hydrophilic domains that surround the hydroxyl groups of 1,2-propanediol, and thus, the reaction proceeds without the need for proton transfer across hydrophobic domains. The free energies of the protonation and dehydration steps were calculated to be 0 and 126 kJ mol^{-1}, respectively, thus resulting in an apparent activation free energy for 1,2-propanediol dehydration of 126 kJ mol^{-1} (Figure 2.2b and Supplementary Figure 2.13). This value is lower by 8 kJ mol^{-1} than the value of 134 kJ mol^{-1} in water. The transition state stabilization at ≥90 wt% GVL concentration is more significant than the stabilization for ≥90 wt% DMSO. The GVL encapsulated water domains better stabilize the carbenium ion transition state than the intermixed DMSO and

water molecules, which do not encapsulate the carbenium ion transition state. This behavior is consistent with experimental results that show greater than two orders of magnitude increases in rates at $\geq$90 wt% GVL than those at $\geq$90 wt% DMSO. The calculated apparent activation barriers for *tert*-butanol and 1,2-propanediol dehydration in different solvent and co-solvent systems derived here from *ab initio* molecular dynamics simulations show good agreement with those determined from experiments, as shown in Figure 2.3.
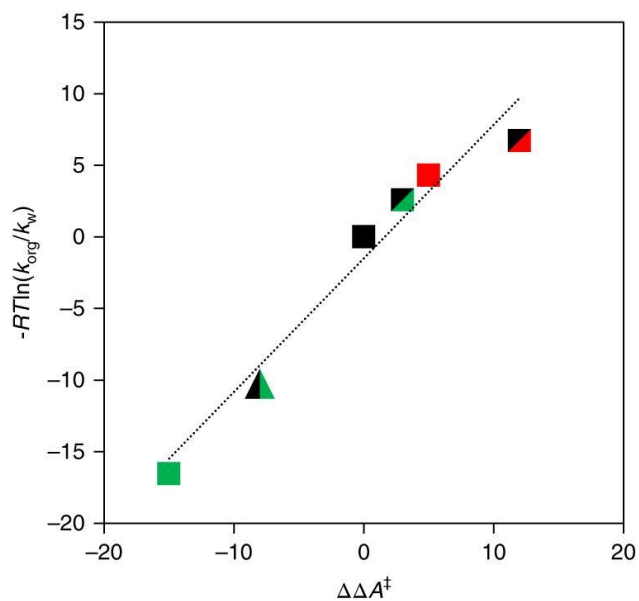
Figure 2.3 Linear relationship between experimentally measured and DFT-calculated apparent activation free energies. The natural log of the ratio of the experimentally measured rate constants in polar aprotic solvent mixtures with water (k_{org}) relative to rate constant in water (k_w) correlates linearly with the difference in DFT-calculated apparent activation free energies ($\Delta\Delta A^{\ddagger}$) for the Brønsted acid-catalyzed dehydration of *tert*-butanol to isobutene in 100 wt% GVL (green rectangle), 100 wt% water (black rectangle), 70 wt% GVL (green and black rectangle), 100 wt% DMSO (red rectangle) and 90 wt% DMSO (red and black rectangle). The same plot for 1,2-propanediol dehydration to propanal is shown for the reaction in 90 wt% GVL (green and black triangle) and in 100 wt% water (black triangle, overlapping with black rectangle at the origin). The black dotted line with the equation $y = 0.9333x - 1.4895$ and the r^2 value of 0.9552 represents the linear fit. The parameters R and T are the gas constant and temperature, respectively.

2.2.3 Solvent-enabled control of reactivity for liquid-phase reactions

The aforementioned computational results provide insight into solvent effects for fructose dehydration. These results show that the stabilities of the reactant, the acid catalyst and the transition state need to be considered together, as suggested previously.[48] The hydroxyl groups adjacent to the sites of dehydration in fructose will promote the formation of water clusters and hydrophilic domains at the dehydration site of the fructose reactant in the organic solvent mixtures with water, thereby allowing the acidic protons to interact directly with the hydroxyl groups within the same hydrophilic domains. Increasing the composition of the organic solvent will result in the encapsulation of the hydrophilic environment at the active hydroxyl on the alcohol, which will result in a stronger binding to the carbenium ion that forms, and enhanced stabilization of the transition state for the fructose dehydration as speculated in previous studies.[57,114]

Figure 2.4 shows the rates of fructose dehydration to HMF and the rates of HMF conversion to levulinic acid using triflic acid and HCl in water and in GVL (containing 10 wt% water). With water as the solvent, the turnover frequency (TOF) values for fructose conversion to HMF using triflic acid and HCl are approximately 30% lower than the TOF values for HMF conversion to levulinic acid. Accordingly, low HMF yields of approximately 40% are achieved from fructose using triflic acid and HCl as catalysts in water as solvent. In contrast, use of GVL with 10 wt% water as solvent and triflic acid as catalyst leads to an increase in the rate of fructose dehydration by approximately 150-fold relative to water, whereas the HMF conversion rate increases by only 10-fold. Thus, increased HMF yields of 60% are achieved using GVL as solvent for this consecutive reaction scheme. Using HCl as catalyst in the 90 wt% GVL solvent mixture leads to

fructose dehydration TOF values that are 450-fold higher than TOF values using water as solvent, whereas the HMF conversion rate increases by only 10-fold. Therefore, greater than 80% HMF yields are achieved in 90 wt% GVL using HCl as catalyst.
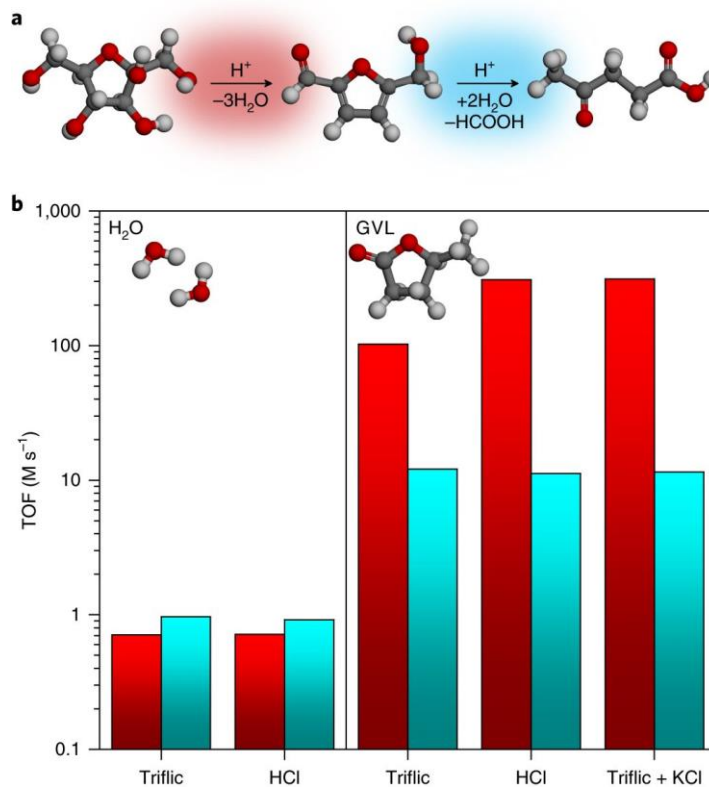
Figure 2.4 Reaction kinetics of the consecutive acid-catalyzed conversion of fructose to HMF to levulinic acid. a, Consecutive reaction network for conversion of fructose to levulinic acid, passing through HMF. **b**, Reaction kinetics results for conversion of fructose and HMF in water and 90 wt% GVL with 10 wt% water. TOF values are plotted for fructose conversion (red bars) and HMF conversion (cyan bars). Reaction conditions: fructose or HMF concentration, 0.05 M; acid concentration, 0.5 M for water, 0.005 M for 90% GVL; salt concentration, 0.005 M for 90% GVL; solvent, 5 ml; temperature, 373 K for TOF values, 393 K for yield values; stir rate, 700 r.p.m.; reaction times, 0–240 min. TOF values were derived from equation (2.1).

The higher reactivity for fructose dehydration using HCl compared with using triflic acid as catalyst in 90 wt% GVL can also be achieved by addition of an equimolar amount of KCl to triflic acid. These results indicate that the higher reactivity observed in the presence of the chloride ion is caused by involvement of this anion in the solvation of

the transition state, which is in agreement with previous results showing that halide anions stabilize critical intermediates in carbohydrate dehydration reactions.[78–80] This behavior is consistent with our theoretical results for the dehydration of *tert*-butanol in the presence of HCl reported in Supplementary Figure 2.20, which show that Cl– stabilizes the carbenium ion that forms in the water elimination transition state, thus lowering the apparent barrier by 16 kJ mol−1 for reactions in GVL mixtures with water.

2.3 Conclusions

We have elucidated the use of organic solvents and inorganic additives to alter the relative stabilities of initial states and transition states for dehydration reactions, and we have utilized these effects to optimize production of a targeted compound (HMF) in a consecutive reaction sequence (fructose dehydration to HMF coupled with HMF conversion to levulinic acid). This approach should be relevant for parallel and more complex reaction schemes, ultimately facilitating the development of new catalytic processes.[46] Advances in this direction can be accelerated by quantifying solvation effects in terms of initial and transition state contributions using experimental and computational methodologies, thereby elucidating the fundamental bases for predicting solvent effects and rational solvent design for liquid-phase catalytic processes.[115,116]

2.4 Methods

2.4.1 Reaction kinetics experiments

Chemicals were obtained from Sigma-Aldrich, including reactants and products (fructose, *tert*-butanol, *sec*-butanol, 1,2-propanediol, HMF and levulinic acid), inorganic salts (KCl and K-triflate), solvents (DMSO, dioxane, THF, GVL, MeCN and D_2O) and acid catalysts (triflic acid and HCl).

Reaction kinetics experiments for *tert*-butanol and *sec*-butanol conversion in DMSO, dioxane, GVL, H_2O, D_2O and mixtures thereof were carried out in an open batch reactor consisting of a 250 ml round-bottom three-neck flask (Ace Glass). The top neck of the flask was equipped with a Graham-condenser (Ace Glass; 300 mm) cooled to 275 K with 50/50 (v/v) ethylene glycol mixed with water (PolyScience) as coolant provided by a recirculating chiller (PolyScience). One side neck of the round-bottom flask included a glass sparger (Ace Glass; 25–50 μm porosity) flowing 25 cm^3 (standard temperature and pressure) min^{-1} helium (Airgas) through the reaction mixture, and the other side neck of the round-bottom flask served as a sampling port through a rubber septum (Sigma-Aldrich). The round-bottom flask was heated in a temperature-controlled oil bath on top of a magnetic stirrer (Fisher Scientific). In a typical experiment, 100 ml of 0.25 M *tert*-butanol and 0.01 M triflic acid in an organic solvent mixed with water (for example, 90 wt% GVL with 10 wt% water) was poured into a pre-heated round-bottom flask reactor at 363 K and stirred at 700 r.p.m. with a magnetic stir bar. After 15 min of solution preheating, 300 μl samples were collected at 40 min intervals through the sampling port with a stainless-steel needle and glass syringe.

Reaction kinetics measurements were carried out in closed thick-walled glass batch reactors (10 ml) for fructose and 1,2-propanediol dehydration in DMSO, dioxane, THF, GVL, MeCN, H_2O, D_2O and mixtures thereof. This approach was also used to study HMF hydration in H_2O and 90 wt% GVL, and to study *tert*-butanol and *sec*-butanol dehydration in solutions of THF and MeCN mixed with water. Reaction kinetics data for fructose dehydration in pure organic solvents without water could not be obtained due to low fructose solubility. In a typical experiment, 5 ml solutions of 0.1 M reactant (for example, fructose) and 0.01 M acid (for example, HCl) in an organic solvent mixed with water (for example, 25 wt% MeCN with 75 wt% water) were added into closed batch reactors. The reactors were placed in an oil bath and stirred at 700 r.p.m. with magnetic stir bar at 373 K for fructose and HMF conversion; 363 K for *tert*-butanol and *sec*-butanol dehydration; 393 K for 1,2-propanediol dehydration in mixtures containing THF and MeCN; and 433 K for 1,2-propanediol dehydration in mixtures of GVL, DMSO and dioxane. The reactors were removed at specific reaction times and the reactions were stopped by cooling the reactors in an ice bath at 273 K.

After each reaction, the content of the reactor was filtered using a 0.2 μm membrane (VWR International; polytetrafluoroethylene). Sample analyses were performed using a gas chromatograph equipped with a flame ionization detector (Shimadzu GC-2010) and a high-performance liquid chromatograph (Waters Alliance 2695) instrument equipped with a differential refractometer (Waters 410) and a photodiode array detector (Waters 996). Concentrations of propanal and acetone were obtained using a flame ionization detector and a Zebron ZB-BAC-2 gas chromatography column (Phenomenex). Concentrations of fructose (refractive index detector, RID), 1,2-propanediol (RID), HMF (ultraviolet

detector; 320 nm) and levulinic acid (RID) in liquid solution were monitored using an ion-exclusion column (Bio-Rad; Aminex HPX-87H; 7.8×300 mm, 5 μm). A mobile phase of 5 mM sulfuric acid aqueous solution at a flow rate of 0.6 ml min^{-1} was used. Concentrations of *tert*-butanol and *sec*-butanol (RID) in liquid solution were monitored using a reversed-phase column (Agilent Technologies; Zorbax SB-C18; 4.6×300 mm; 5 μm). A mobile phase of 5 mM sulfuric acid aqueous solution at a flow rate of 1.0 ml min^{-1} was used.

From the aforementioned reaction kinetics data, reaction kinetics profiles for the formation of dehydration products were constructed. Specific reaction conditions for all reactions are presented in Supplementary Tables 2.1–2.3. Each reaction time represents an individual experiment, which were combined to produce reaction kinetics profiles. Notably, for each reactant, *tert*-butanol, *sec*-butanol, 1,2-propanediol, fructose and HMF, specific conditions regarding temperature and acid concentration were selected to minimize side reactions. A comparison of the reactant consumption and dehydration product formation results for 1,2-propanediol dehydration and fructose dehydration are presented in Supplementary Figure 2.2 and 2.3, respectively. Rate constants (k_{H+}; equation (2.1)) and TOF values were derived from the reaction kinetics profiles for reactant consumption using nonlinear least squares regression in MATLAB (nlinfit function; Levenberg–Marquardt nonlinear least squares algorithm). Confidence intervals were calculated at the 95% confidence level (nlparci function). The kinetics profiles for dehydration products formation were obtained by multiplying the aforementioned reactant consumption rate constants by the product selectivity data in Supplementary Tables 2.4 and 2.5 (that is, the propanal selectivity plus the acetone selectivity for 1,2-propanediol, and the HMF selectivity for fructose). The dehydration of *tert*-butanol using reactive

distillation has been shown to be highly selective to isobutene based on previous studies.[117] Importantly, based on the reaction rate values (TOF values from 10^{-8} to $10^{-1}\,\mathrm{s^{-1}}$ for all reactions), we do not anticipate any mass transport limitations for these homogeneous Brønsted acid-catalyzed dehydration reactions.

For 1,2-propanediol dehydration, the selectivity results for propanal and acetone (Supplementary Table 2.4) are relatively low due to the formation of cyclic acetal and ketal compounds such as 2-ethyl-4-methyl-1,3-dioxolane, 2-methoxy-1,3-dioxolane, 4-methyl-1,3-dioxolane and 1,3-dioxolane.[118,119] These by-products are formed through reactions between 1,2-propanediol and propanal/ketone. Furthermore, small quantities of 3-hydroxyl-2-methyl-pentanal, 3-hydroxyl-2-methyl-pentanal, 2-ethyl-2-butenal, heptanal and 2-(1-methylethoxy)-1-propanol were detected due to homogeneous-phase side reactions. The reaction order for the 1,2-propanediol dehydration was experimentally determined to be approximately first order, as shown in Supplementary Figure 2.4. Fructose dehydration has been shown to be first order with respect to both reactant and proton concentration[11], and levulinic acid and formic acid products were also detected in these reactions. Moreover, excess enthalpies of mixing for organic solvents systems in water are plotted in Figure 2.1 (right axes) at 298 K for the following organic solvents: DMSO,[120] 1,4-dioxane,[121] THF,[122] GVL,[123] and MeCN.[124]

2.4.2 Reaction mechanisms

Equations considered for the acid-catalyzed dehydration of *tert*-butanol:
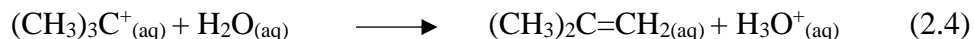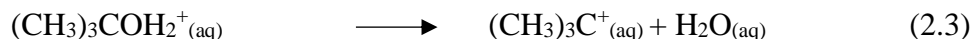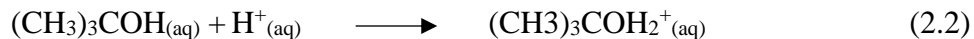
$$(CH_3)_3COH_{(aq)} + H^+_{(aq)} \longrightarrow (CH3)_3COH_2^+_{(aq)} \qquad (2.2)$$

$$(CH_3)_3COH_2^+_{(aq)} \longrightarrow (CH_3)_3C^+_{(aq)} + H_2O_{(aq)} \qquad (2.3)$$

$$(CH_3)_3C^+_{(aq)} + H_2O_{(aq)} \longrightarrow (CH_3)_2C{=}CH_{2(aq)} + H_3O^+_{(aq)} \qquad (2.4)$$

Equations considered for the acid-catalyzed dehydration of 1,2-propanediol:

$$CH_2(OH)CH(OH)CH_{3\,(aq)} + H^+_{(aq)} \longrightarrow CH_2OHCH(OH_2^+)CH_{3(aq)} \qquad (2.5)$$

$$CH_2OHCH(OH_2^+)CH_{3\,(aq)} \xrightarrow{\text{H-shift}} CH_2OHCHCH_3^+_{(aq)} + H_2O_{(aq)} \qquad (2.6)$$

$$CH_2OHCHCH_3^+_{(aq)} + H_2O_{(aq)} \longrightarrow CHOCH_2CH_{3\,(aq)} + H_3O^+_{(aq)} \qquad (2.7)$$
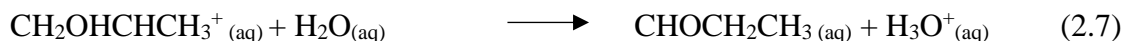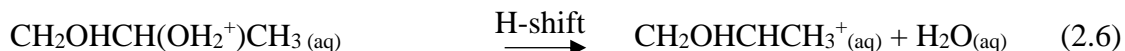
2.4.3 Simulation details

The molecular configurations for *tert*-butanol and 1,2-propanediol in each of the different co-solvent systems were initially generated using classical molecular dynamics simulation implemented in GROMACS using a constant number of particles, constant volume and constant temperature (NVT) as well as and constant number of particles, constant pressure and constant temperature (NPT) ensembles.[125] The subsequent calculations for the electronic structure and reactivity of these systems were carried out using *ab initio* molecular dynamics simulations implemented in the CP2K program.[126]

The condensed-phase systems of *tert*-butanol and 1,2-propanediol were created by placing alcohol and solvent molecules in a $15 \times 15 \times 15$ Å^3 box. The water system consists of 100 H$_2$O, one alcohol molecule and one hydronium ion. The 90 wt% DMSO–water system consists of 21 DMSO, 10 H$_2$O, one *tert*-butanol molecule and one hydronium ion.

The 100 wt% DMSO system consists of 25 DMSO, one *tert*-butanol molecule and a protonated DMSO species. The 70 wt% GVL–water system consists of 12 GVL, 28 H_2O, one *tert*-butanol molecule and one hydronium ion. The 100 wt% GVL system consists of 18 GVL, one *tert*-butanol molecule and a protonated GVL species. The 90 wt% GVL system consists of 15 GVL, 9 H_2O, one 1,2-propanediol and one hydronium ion.

The molecular systems were equilibrated for 1 ns in an NVT ensemble followed by 10 ns of equilibration in NPT ensemble at 1 atm. The temperatures were kept at 363 K and 393 K for systems of *tert*-butanol and 1,2-propanediol, respectively. Leap-frog stochastic dynamics integrator[127] was used to control the dynamics and temperature of the systems with 0.5 fs time step and 2 ps temperature coupling time constant. The pressure of the system was regulated using Parrinello–Rahman barostat[128,129] with a 2 ps coupling time constant. The molecular interactions of *tert*-butanol and 1,2-propanediol were described using all-atom version of optimized potentials for liquid simulations (OPLS–AA)[130] and OPLS–AA scaling electrostatic interaction (OPLS–AA–SEI) force fields,[131] respectively. The OPLS–AA force field was also used for DMSO and GVL. Water molecules were represented with an extended simple point charge (SPC/E) water model.[132] The bond distance and angle in water molecules were constrained using the SETTLE algorithm.[133] The intermolecular interactions were truncated at 7 Å spherical cut-off. Long-range electrostatic was included using a particle mesh Ewald scheme. The average lattice size and final atomic coordinates were used to establish the initial configuration for the *ab initio* molecular dynamics simulations (AIMD) in CP2K software.

All systems obtained from the classical simulation were further equilibrated for 10 ps using AIMD. The Perdew–Burke–Ernzerhof functional was used to calculate electron exchange and correlation energies in the periodic simulation boxes.[134] Kohn–Sham orbitals were expanded using a short-ranged version of Gaussian-type double-ζ basis set optimized for molecular systems.[135] The electronic density was described using a norm-conserving Goedecker–Teter–Hutter pseudopotentials[136] with a plane wave cut-off of 320 Ry. DFT–D3(BJ) dispersion corrections[137] were used to account for the mid- and long-range van der Waals interactions. The neutralizing background charge was implicitly assumed by CP2K. Molecular dynamic simulations utilized a canonical sampling through velocity rescaling (CSVR) thermostat[138] to control temperature of the system in NVT ensemble at 363 K and 433 K for *tert*-butanol and 1,2-propanediol systems, respectively. A time step of 0.5 fs was used, and the mass of deuterium was assigned to all hydrogen atoms to attenuate the high frequency vibration modes.

2.4.4 Free energy calculations

Ab initio molecular dynamics carried out using the umbrella sampling technique were used to improve configurational sampling during the calculation of activation free energy. The umbrella sampling simulations were performed at the same conditions as the unbiased AIMD runs. At least 18 evenly distributed umbrella windows were used to ensure proper overlapping of sampled populations, with additional windows added around the transition state. For each umbrella sampling window, the simulation was equilibrated for 10 ps followed by 20 ps of data collection. Weighted histogram analysis method (WHAM) was used to obtain the shape of the free energy surface.[139] As an exception for *tert*-butanol dehydration in 100 wt% DMSO and GVL, each window in the water removal step

(equations (2.3) and (2.4)) was equilibrated for 2 ps followed by 3 ps of data collection because we observe significant solvent reconfiguration around the transition state when the simulation is prolonged beyond 5 ps. Such behavior would not be observed in an experimental setting as the short lifetime of an activated species does not allow solvent reconfiguration. This phenomenon is not observed in other cases where the shape of free energy surface quickly stabilizes at around 3 ps and the activation free energy remains consistent throughout the end of 30 ps duration. The results for free energy sampling are presented in Supplementary Figure 2.21 and 2.22.

Umbrella sampling was performed on each elementary step of the reaction. The dehydration of *tert*-butanol was separated into protonation step (equation (2.2)) and water elimination step (equations (2.3) and (2.4)). The dehydration of 1,2-propanediol was separated into protonation step (equation (2.5)) and water elimination step (equations (2.6) and (2.7)). The reaction coordinates used in these simulations were defined in term of coordination number as follows:

$$CN_{ij} = \frac{1-(q_{ij}/1.5)^9}{1-(q_{ij}/1.5)^{14}} \qquad (2.8)$$

where CN $_{ij}$ is the coordination number of atom *i* with respect to atom *j*, and d_{ij} is the distance between atom *i* and *j* in angstrom units. The reaction coordinate used in the protonation step for both *tert*-butanol and 1,2-propanediol was a sum of coordination number of hydroxyl oxygen with respect to hydroxyl hydrogen and a closest water hydrogen (Supplementary Figure 2.23a). This reaction coordinate ranges from 1.0 to 2.0

with a spring constant for bias harmonic potential of 1 Hartree. The bias potential takes the form:

$$V = K * (CV - CV_{target})^2 \tag{2.9}$$

where K is the spring constant, CV is the instantaneous reaction coordinate and CV_{target} is the center of bias harmonic potential.

The reaction coordinate for the water removal step in *tert*-butanol dehydration was defined as a sum of coordination numbers of the quaternary carbon with respect to all oxygens in the system, and primary carbon with respect to the connecting hydrogens (equation (2.10) and Supplementary Figure 2.23b). This reaction coordinate ranges from 7.5 to 9.5 with a spring constant for bias potential of 0.5 Hartree.

$$\text{Reaction coordinate} = \sum_{j=1}^{n} CN_{C4-Oj} + \sum_{i=1}^{3}\sum_{j=1}^{3} CN_{Ci-Hij} \tag{2.10}$$

The propanal formation step in 1,2-propanediol dehydration involves a 1,2-hydride shift process. The reaction coordinate in this case is defined as follows

$$\text{Reaction coordiate} = (d_{C1-H} - d_{C2-H})/4 - \sum_{j=1}^{n} CN_{C2-Oj} \tag{2.11}$$

where d_{C1-H} is the distance between C1 and the hydrogen used in hydride shift, and d_{C2-H} is the distance between C2 and the same hydrogen (Supplementary Figure 2.23b). A scaling factor of 4 was applied to normalize the magnitude of the first term in equation (2.11). This

reaction coordinate ranges from −1.4 to 0.4 with a spring constant for bias potential of 0.7 Hartree.

To test the accuracy and reliability of the reaction coordinate shown in Supplementary Figure 2.23a, the reaction coordinate was expanded beyond the protonation of the alcohol (CN_2, H_2^+–O_{water} formation) and the O–H scission of the alcohol (CN_1, O_1–H_1) to include the O–H scission (CN_4) involved in the transfer of the hydrogen from the oxygen atom (O_{water}) in a water molecule in solution to alcohol O_1 as well as the O–H bond formation step (CN_3) to transfer the proton on the alcohol (H_1) to a solution phase oxygen atom (O_{water}). The reaction coordinate for the protonation step that follows the descriptions above is shown in Supplementary Figure 2.23c.

The reaction coordinate is now defined as:

$$\text{Reaction coordiate} = \left(CN_1 - CN_3 \right) + \left(CN_2 - CN_4 \right) \tag{2.12}$$

where CN_1, CN_2, CN_3 and CN_4 are the coordination numbers of: O_1–H_1 (bond scission), O_1–H_2 (bond formation), H_1–O_i (bond formation) and H_2–O_i (bond scission).

$$CN_3 = \sum_{i=2}^{n} CN_{H1-Oi} \tag{2.13}$$

$$CN_4 = \sum_{i=2}^{n} CN_{H2-Oi} \tag{2.14}$$

The comparison between results obtained using reaction coordinates displayed in Supplementary Figure 2.23a and 2.23c are presented in Supplementary Figure 2.24. The activation barriers and the overall reaction energies change by less than $3\,\text{kJ}\,\text{mol}^{-1}$ in

moving from the local yet concise reaction coordinate shown in Supplementary Figure 2.23a to the more expanded reaction coordinate in Supplementary Figure 2.23c.

2.4.5 Radial distribution functions

The condensed-phase systems of *tert*-butanol and 1,2-propanediol were generated from force-field molecular dynamics simulations using the same procedure described previously. The alcohol and solvent molecules were placed in a $30 \times 30 \times 30$ Å^3 box. The concentrated DMSO systems consist of 205 DMSO, 101 H_2O and 4 alcohol molecules and a triflic acid ion pair. The concentrated GVL systems consist of 205 GVL, 101 H_2O and 4 alcohol molecules and a triflic acid ion pair. The dilute DMSO systems consist of 43 DMSO, 750 H_2O and 4 alcohol molecules and a triflic acid ion pair. The dilute GVL systems consist of 32 GVL, 711 H_2O and 4 alcohol molecules and a triflic acid ion pair. The co-solvent concentrations are approximately 90%, 92%, 20% and 20% by weight, respectively. The force-field parameters for the triflic acid ion pair were taken from Reference [140].

2.5 Supplementary Information

Supplementary Table 2.1 Reactions performed for the Brønsted acid-catalyzed *tert*-butanol dehydration results presented in Figure 2.1. Reaction conditions: *tert*-butanol concentration (0.25 M); temperature (363 K); stir rate (700 rpm).

Solvent / Mass Fraction of Organic Solvent		Temperature (K)	Triflic Acid Concentration ([M])	Reaction Times (min)
Water		433	0.4	0, 120, 360, 600, 900, 1470
GVL	0.25	433	0.6	0, 30, 60, 90, 120, 150
	0.5	433	0.2	0, 30, 60, 90, 120, 180, 240
	0.7	433	0.2	0, 30, 60, 90, 120
	0.9	433	0.02	0, 60, 90, 120
	0.98	433	0.0003	0, 10, 15, 20, 25, 40
	1	433	0.0001	0, 4, 5, 7, 8, 25
DMSO	0.25	433	0.75	0, 20, 40, 60, 80
	0.5	433	0.45	0, 40, 60, 90, 120
	0.75	433	0.3	0, 15, 30, 45, 60
	0.9	433	0.1	0, 15, 30, 45, 75
	0.95	433	0.025	0, 15, 30, 45, 60
	0.98	433	0.025	0, 15, 30, 45, 75
THF	0.25	393	2.5	0, 60, 120, 180, 240
	0.5	393	2.0	0, 30, 60, 90, 120
	0.75	393	0.8	0, 30, 60, 90, 120
	0.9	393	0.4	0, 10, 20, 30, 40, 60
	0.95	393	0.2	0, 15, 30, 45, 60
MeCN	0.25	393	2.5	0, 60, 120, 180, 240
	0.5	393	2.0	0, 30, 60, 90, 120
	0.75	393	0.7	0, 30, 60, 90, 120
	0.9	393	0.3	0, 30, 60, 90, 120
	0.98	393	0.025	0, 20, 40, 60, 90
Dioxane	0.25	433	0.7	0, 30, 60, 90, 120
	0.5	433	1.0	0, 15, 30, 45, 60, 90
	0.75	433	0.75	0, 15, 30, 45, 60, 90
	0.9	433	0.2	0, 20, 40, 60, 80
	0.98	433	0.02	0, 10, 15, 20, 25, 45, 60
	0.99	433	0.05	0, 10, 15, 20, 25, 30

Supplementary Table 2.2 Reactions performed for the Brønsted acid-catalyzed 1,2-propanediol dehydration results presented in Figure 2.1. Reaction conditions: 1,2-propanediol concentration (0.01 M); solvent (5 mL); stir rate (700 rpm).

Solvent / Mass Fraction of Organic Solvent		Temperature (K)	Triflic Acid Concentration ([M])	Reaction Times (min)
Water		433	0.4	0, 120, 360, 600, 900, 1470
GVL	0.25	433	0.6	0, 30, 60, 90, 120, 150
	0.5	433	0.2	0, 30, 60, 90, 120, 180, 240
	0.7	433	0.2	0, 30, 60, 90, 120
	0.9	433	0.02	0, 60, 90, 120
	0.98	433	0.0003	0, 10, 15, 20, 25, 40
	1	433	0.0001	0, 4, 5, 7, 8, 25
DMSO	0.25	433	0.75	0, 20, 40, 60, 80
	0.5	433	0.45	0, 40, 60, 90, 120
	0.75	433	0.3	0, 15, 30, 45, 60
	0.9	433	0.1	0, 15, 30, 45, 75
	0.95	433	0.025	0, 15, 30, 45, 60
	0.98	433	0.025	0, 15, 30, 45, 75
THF	0.25	393	2.5	0, 60, 120, 180, 240
	0.5	393	2.0	0, 30, 60, 90, 120
	0.75	393	0.8	0, 30, 60, 90, 120
	0.9	393	0.4	0, 10, 20, 30, 40, 60
	0.95	393	0.2	0, 15, 30, 45, 60
MeCN	0.25	393	2.5	0, 60, 120, 180, 240
	0.5	393	2.0	0, 30, 60, 90, 120
	0.75	393	0.7	0, 30, 60, 90, 120
	0.9	393	0.3	0, 30, 60, 90, 120
	0.98	393	0.025	0, 20, 40, 60, 90
Dioxane	0.25	433	0.7	0, 30, 60, 90, 120
	0.5	433	1.0	0, 15, 30, 45, 60, 90
	0.75	433	0.75	0, 15, 30, 45, 60, 90
	0.9	433	0.2	0, 20, 40, 60, 80
	0.98	433	0.02	0, 10, 15, 20, 25, 45, 60
	0.99	433	0.05	0, 10, 15, 20, 25, 30

Supplementary Table 2.3 Reactions performed for the Brønsted acid-catalyzed fructose dehydration results presented in Figure 2.1. Reaction conditions: temperature (373 K); solvent (5 mL); stir rate (700 rpm).

Solvent / Mass Fraction of Organic Solvent		Triflic Acid Concentration ([M])	Reactant Concentration ([M])	Reaction Times (min)
Water		0.5	0.05	0, 30, 60, 90
GVL	0.25	0.5	0.05	0, 30, 60, 90, 120
	0.5	0.1	0.05	0, 30, 60, 90, 120
	0.75	0.025	0.05	0, 30, 60, 90, 120
	0.9	0.005	0.05	0, 10, 12, 30, 40
	0.95	0.001	0.01	0, 15, 30, 45, 60
DMSO	0.25	0.5	0.05	0, 30, 60, 90, 120
	0.5	0.1	0.05	0, 30, 60, 90, 120
	0.75	0.025	0.05	0, 30, 60, 90, 120
	0.9	0.001	0.1	0, 30, 60, 90, 120
	0.95	0.001	0.01	0, 15, 30, 45, 60
THF	0.25	0.01	0.05	0, 30, 60, 90, 120
	0.75	0.05	0.05	0, 30, 60, 90, 120
	0.9	0.01	0.05	0, 15, 30, 45, 60
	0.95	0.025	0.01	0, 15, 30, 45, 60
MeCN	0.25	0.5	0.05	0, 15, 30, 45, 60
	0.5	0.1	0.05	0, 15, 30, 45, 60
	0.75	0.1	0.05	0, 15, 30, 45, 60
	0.9	0.01	0.01	0, 15, 30, 45, 60
	0.95	0.0025	0.01	0, 15, 30, 45, 60
Dioxane	0.25	0.5	0.05	0, 30, 60, 90, 120
	0.5	0.1	0.05	0, 30, 60, 90, 120
	0.75	0.05	0.05	0, 30, 60, 90, 120
	0.9	0.01	0.05	0, 15, 30, 45, 60
	0.95	0.0025	0.01	0, 15, 30, 45, 60

Supplementary Table 2.4 Product selectivity results of the Brønsted acid-catalyzed dehydration of 1,2-propanediol in different polar solvents. Reaction conditions given in Supplementary Table 2.2.

Solvent / Mass Fraction of Organic Solvent		1,2-Propanediol Conversion (%)	Propanal Selectivity (%)	Acetone Selectivity (%)
Water		19	62	9
GVL	0.25	28	74	22
	0.50	15	60	29
	0.70	22	78	19
	0.90	24	81	17
	0.98	24	56	19
	1.00	27	66	6
DMSO	0.25	23	0	41
	0.50	33	0	50
	0.75	38	0	48
	0.90	37	0	59
	0.98	30	0	87
THF	0.25	19	21	11
	0.50	22	17	7
	0.75	22	9	5
	0.90	29	3	4
	0.95	32	5	1
MeCN	0.25	15	27	1
	0.50	23	15	22
	0.75	16	14	8
	0.90	17	14	3
	0.98	14	17	9
Dioxane	0.25	27	44	49
	0.50	13	84	9
	0.75	13	90	4
	0.90	23	68	12
	0.98	14	36	12
	0.99	27	21	6

Supplementary Table 2.5 Product selectivity results of the Brønsted acid-catalyzed fructose dehydration in different polar solvents. Reaction conditions given in Supplementary Table 2.3.

Solvent / Mass Fraction of Organic Solvent		Fructose Conversion (%)	HMF Selectivity (%)
Water		49	53
GVL	0.25	49	67
	0.50	29	62
	0.75	33	45
	0.90	23	27
	0.95	30	39
DMSO	0.25	59	77
	0.50	42	92
	0.75	57	91
	0.90	20	81
	0.95	15	97
THF	0.25	50	70
	0.75	32	52
	0.90	16	37
	0.95	18	35
MeCN	0.25	42	80
	0.50	20	76
	0.75	53	83
	0.90	37	60
	0.95	23	21
Dioxane	0.25	46	68
	0.50	28	66
	0.75	42	65
	0.90	24	39
	0.95	24	45

Supplementary Table 2.6 *Ab initio* MD simulation results for the Brønsted acid-catalyzed dehydration of *tert*-butanol and 1,2-propanediol in different polar solvents. DFT-calculated free energies changes for the different elementary steps outlined in Figure 2.2 are compared for *tert*-butanol and 1,2-propanediol dehydration in water, carried out at low DMSO–water concentrations (≤ 90 wt%; orange profile), high DMSO–water concentrations > 90 wt% (100 wt%; red profile), low GVL–water mixtures (≤ 70 wt%; green profile), and high GVL–water mixtures > 70 wt% (100 wt%; blue profile) catalyzed by a Brønsted acid. The elementary steps involve protonation of the alcohol; and water elimination with carbenium ion formation. The final deprotonation of the carbenium ion to form the olefin is lower in energy (quasi-equilibrated) for each of these systems and as such inconsequential to the apparent activation energy.

Reactant	Solvent System	Protonation (kJ mol^{-1})	Water Elimination[‡] (kJ mol^{-1})	Total $\Delta F^{\ddagger}$ (kJ mol^{-1})
tert-butanol	H_2O	13	69	82
	90 wt% DMSO	8	86	94
	100 wt% DMSO	n/a	87	87
	70 wt% GVL	8	77	85
	100 wt% GVL	n/a	67	67
1,2-propanediol	H_2O	18	116	134
	90 wt% GVL	0	126	126

Supplementary Table 2.7 Comparison of the pK_a values for different polar solvents (in their protonated form), their range of enthalpy of mixing over the co-solvent composition ratios of 0 to 1, the composition ratio where the minimum in $k_{solvent}/k_{H_2O}$ lies and the actual value of $k_{solvent}/k_{H_2O}$ at the minimum.

Reactivity	pKa[a]	Enthalpy of Mixing[b]	[Solvent]/[H2O] at minimum $k_{solvent}/k_{H_2O}$	Minimum $k_{solvent}/k_{H_2O}$
MeCN	-10.1	0 to +1.2	0.5	0.2
GVL	-7.0 (protonated ester)	0 to +1.0	0.7	0.65
Dioxane	-3.0 (protonated ether)	-0.6 to 0 and O to 0.4	0.7	0.2
THF	-2.05	mainly negative	0.9	0.13
H2O	-1.74			

(a) Organic Chemistry, 3nd Edition by David R. Klein

(b) W. E. Waghorne, Thermodynamics of solvation in mixed solvents. *Chem. Soc. Rev.* **22**, 285- 292 (1993).

Supplementary Discussion: Relationship between the pK_a of the conjugate acid and enthalpy of mixing and reactivity for co-solvent systems.

The results in Supplementary Table 7 compare the pK_a values for different protonated solvents in water (i.e., Solvent–H$^+$ → Solvent$_{aq}$ + H$^+_{aq}$) and their enthalpies of mixing and reactivity over the composition ranges of co-solvent from 0 to 1.

The pK_a values of the protonated co-solvents are controlled by the binding energy of the proton to the co-solvent as well as the mixing between the co-solvent and water. More basic solvents, such as DMSO strongly bind to the protons in solution. Its conjugate acid (DMSO–H$^+$) is somewhat weak with pK_a value of −1.8. It is slightly more acidic than water.

DMSO is readily polarized and in the presence of solution takes on the form of $(CH_3)_2S^+$–O where the negatively charged oxygen strongly bind to the positively charged hydrogen of water resulting in a high degree of intermolecular hydrogen bonding and interactions between the DMSO and water. The polarized S$^+$–O$^-$ also strongly binds to free protons or small H$_3$O$^+$ or H$_2$O$_5^+$ clusters. This ultimately acts to lock up the proton which significantly increases the activation barrier and likely leads to the lower rates seen experimentally. The rates in the cosolvent system continue to decrease in rate as you increase the fraction of protons that are tied up in these less reactive states. At very high concentrations of the co-solvent, the co-solvent begins to stabilize the protonated transition states in a similar manner thus decreasing the barriers slightly. This is consistent with the minimum in the experimental relative rates in the co-solvent ($k_{solvent}/k_{H2O}$) occurring at ~95% DMSO.

THF and dioxane co-solvents are less basic (with pK_a values for their conjugate acid that range from -2 to -3). As such they do not polarize as much and do not interact as strongly with the protons in solution or those on the water as the more basic DMSO does. This ultimately leads weaker interactions between the water and the co-solvent and more moderate heats of mixing that can change from endothermic at low concentrations to exothermic at higher concentrations of co-solvents. The weaker basicity of the THF and DMSO may also help to explain the shift to lower values of co-solvent concentrations (from [DMSO]/[H_2O]=0.9 to [THF or Dioxane]/[H_2O]=0.7) for the minimum in the relative dehydration rates.

The GVL and MeCN co-solvents do not interact with the protons in solution or with the positively charged hydrogens on the water or the alcohol. Their conjugate acid forms are highly acidic with pK_a values that range from -7 for GVL and -10 for MeCN. The weak interactions between the positively charged hydrogens of water (or alcohol) and the $-CO_2$ and the $-C\equiv N$ groups of the ester and the nitrile, respectively is consistent with the endothermic heats of mixing between these co-solvents and water. The weak interactions with hydrogen indicate that the protons are not tied up in the solution phase when the concentration of protons is increased. This is consistent with the earlier onset of the minimum (at [GVL]/[H_2O] ~ 0.5) in the relative reactivity of GVL in water with increasing GVL composition.
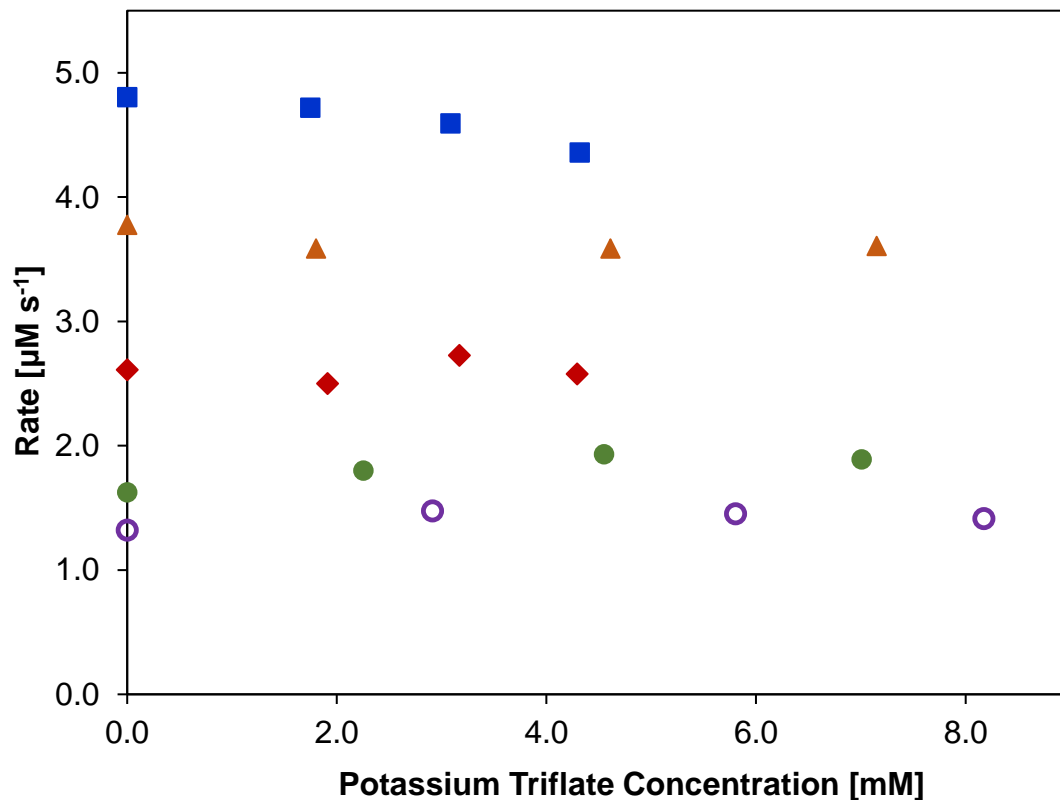
Supplementary Figure 2.1 Reaction rates with varying potassium triflate salt concentrations. Solvent systems: (◆) 90 wt% DMSO, (▲) 90 wt% dioxane, (●) 88 wt% THF, (■) 90 wt% GVL, and (○) 82 wt% MeCN with constant triflic acid catalyst concentrations. Reaction conditions: fructose concentration (0.05 M); triflic acid concentration (0.001 M for 90% DMSO; 0.01 M for 90% dioxane, 88% THF, and 82% MeCN; 0.005 M for 90% GVL); solvent (5 mL); temperature (373 K); stir rate (700 rpm); reaction times (0–60 min).
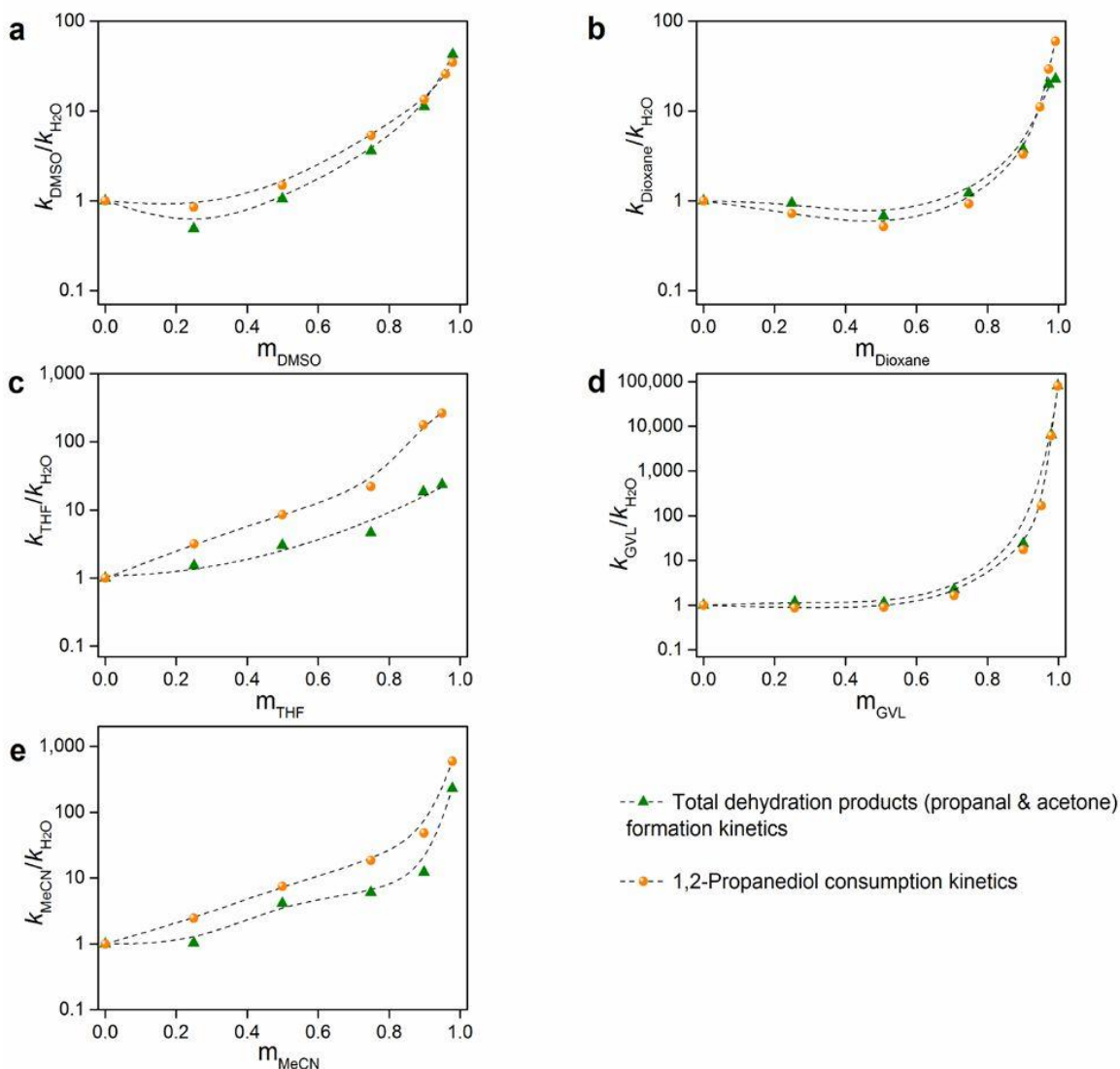
Supplementary Figure 2.2 Solvation effects on the kinetics of Brønsted acid-catalyzed 1,2-propanediol dehydration reaction. a–e, Left axis; Ratios of the acidic proton-catalyzed rate constants (k_{H^+}) for organic solvent mixtures with water relative to the value in water for total dehydration products (i.e., propanal and acetone) formation (green triangles) and 1,2-propanediol consumption (yellow circles) plotted against the mass fraction of DMSO, dioxane, THF, GVL, and MeCN in organic solvent mixtures with water, respectively. Black dashed lines are visual guides. Reaction conditions: 1,2-propandiol concentration (0.01 M); acid concentration (0.001M – 2.5 M); solvent (5 mL); temperature (393 K for THF and MeCN; 433 K for DMSO, Dioxane, and GVL); stir rate (700 rpm); reaction times (0–1470 min). Rate constants were derived from equation (2.1).
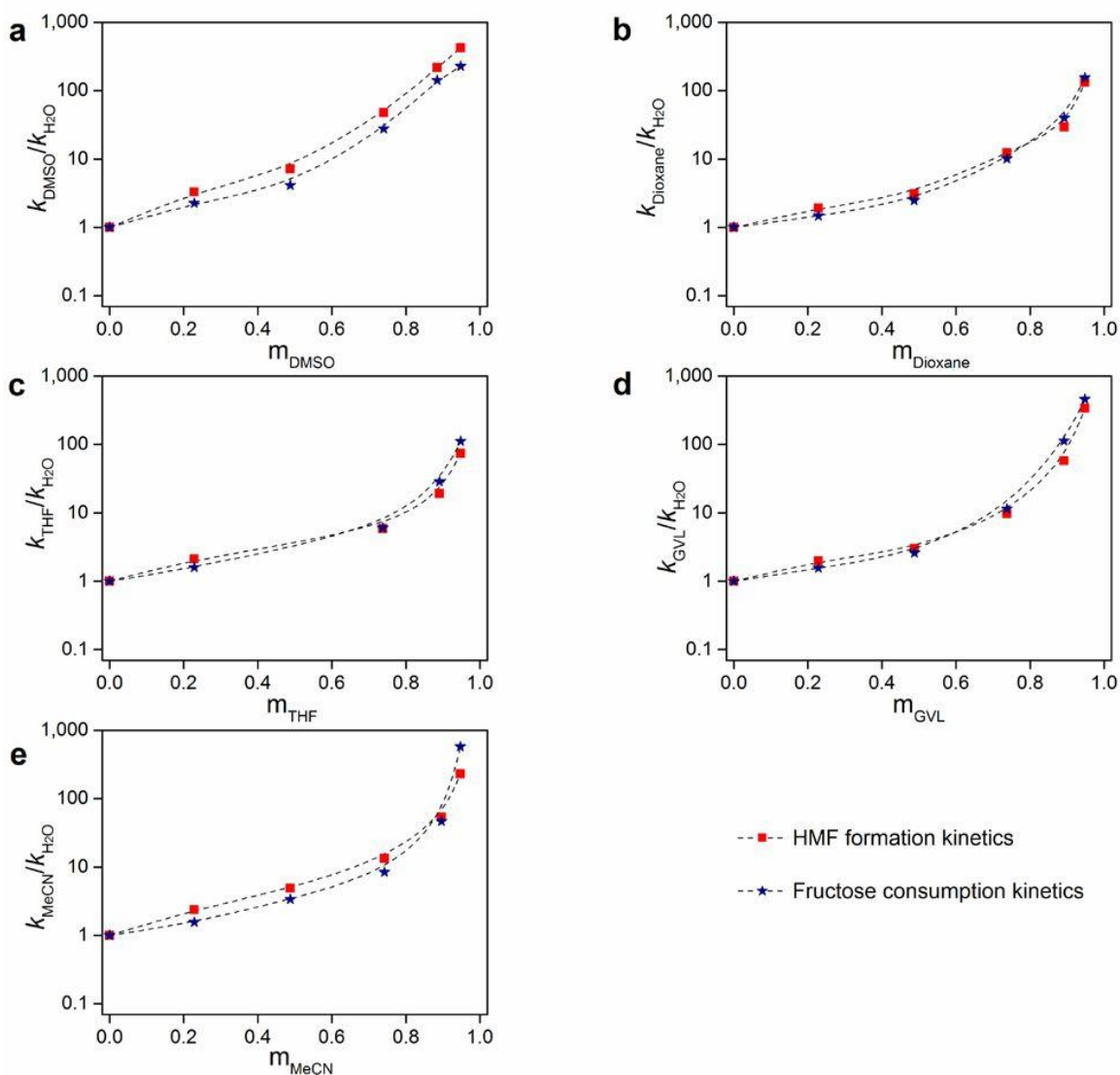
Supplementary Figure 2.3 Solvation effects on the kinetics of Brønsted acid-catalyzed fructose dehydration reaction. a–e, Left axis; Ratios of the acidic proton-catalyzed rate constants (k_{H^+}) for organic solvent mixtures with water relative to the value in water for HMF formation (red squares) and fructose consumption (blue stars) plotted against the mass fraction of DMSO, dioxane, THF, GVL, and MeCN in organic solvent mixtures with water, respectively. Black dashed lines are visual guides. Reaction conditions: fructose concentration (0.05 M); acid concentration (0.0001 M – 0.5 M); solvent (5 mL); temperature (373 K); stir rate (700 rpm); reaction times (0–120 min). Rate constants were derived from equation (2.1).
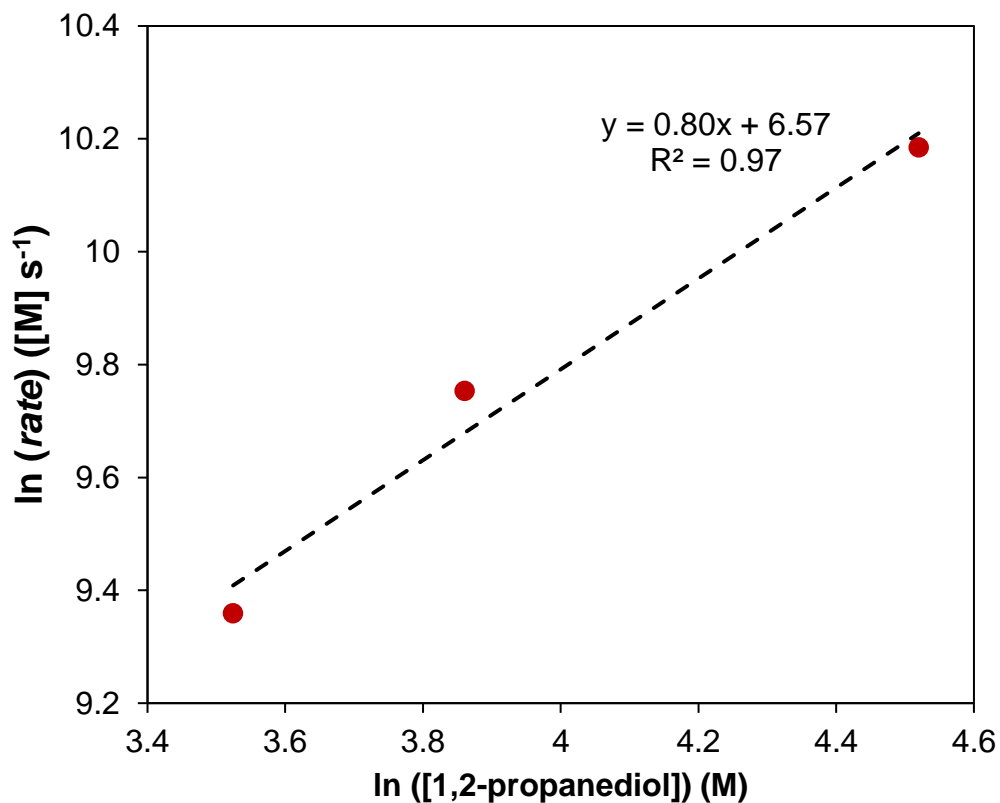
Supplementary Figure 2.4 Reaction order of Brønsted acid-catalyzed 1,2-propanediol dehydration with respect to reactant concentration. Left axis; natural logarithm of the rate of the formation of total dehydration products (i.e., propanal and acetone) plotted against natural logarithm of the reactant (i.e., 1,2-propanediol) concentration. Reaction conditions: solvent (5 mL, 90% GVL); acid concentration (0.02 M); temperature (433 K); stir rate (700 rpm); reaction times (0–120 min).
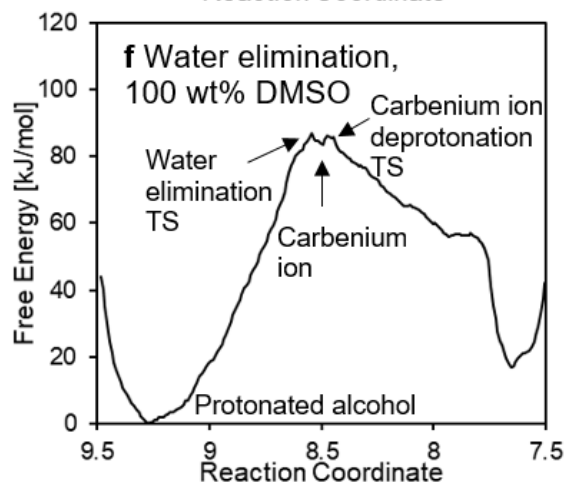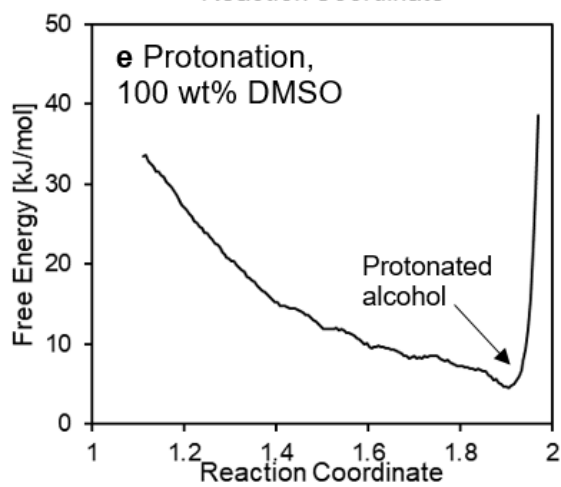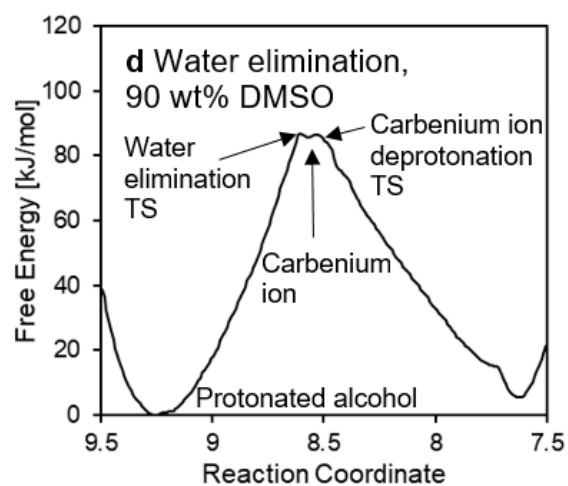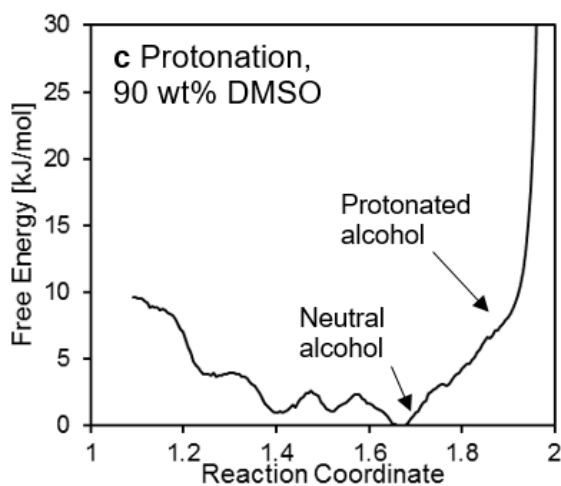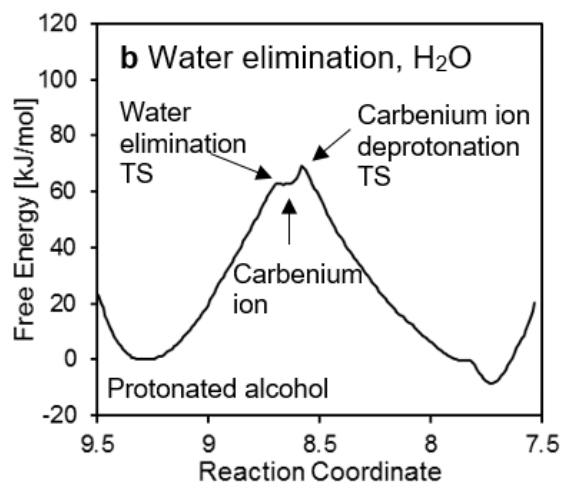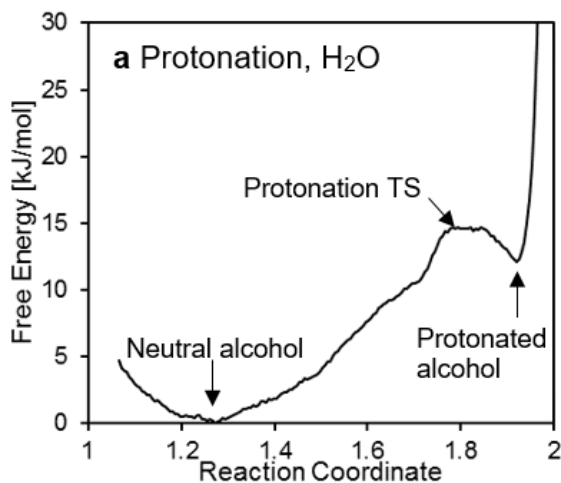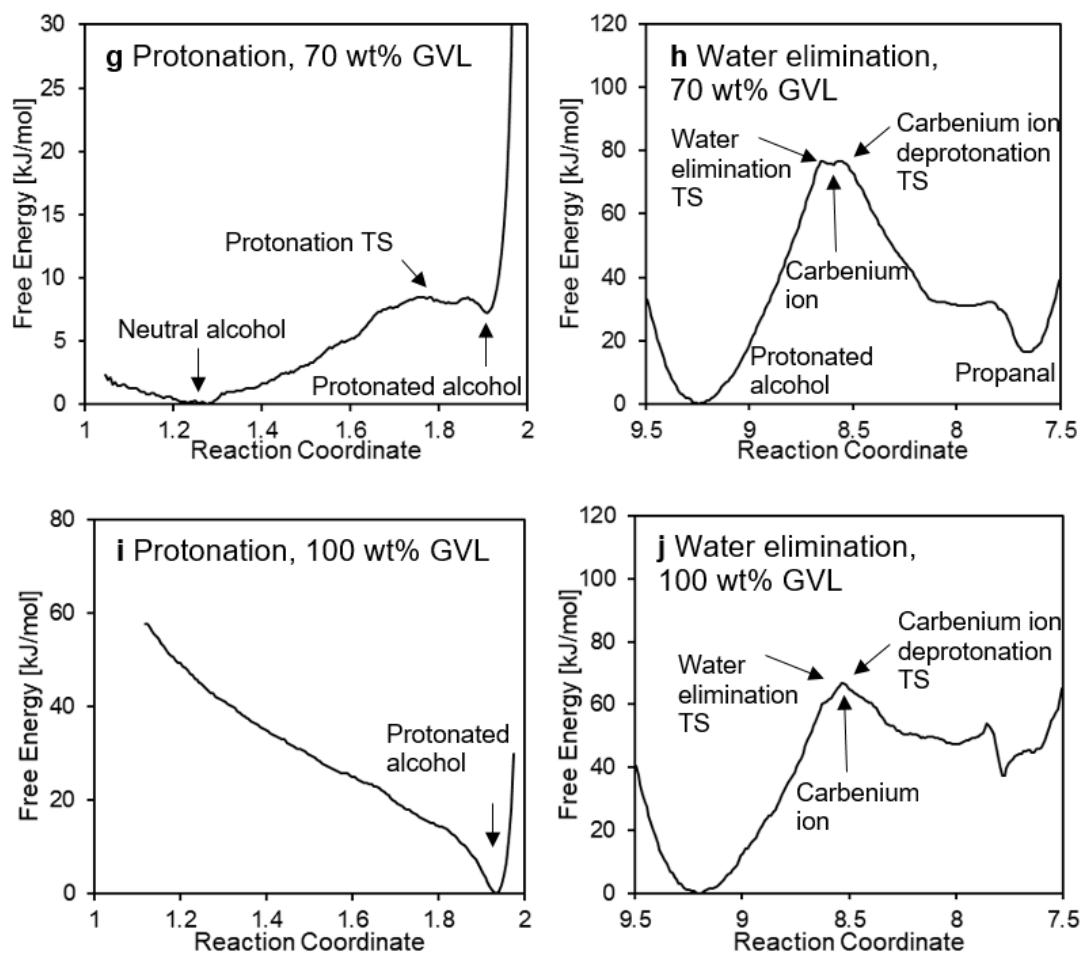
Supplementary Figure 2.5 Free energy reaction coordinate diagrams for the elementary steps in the dehydration of *tert*-butanol in different solvent mixtures. **a**, protonation of *tert*-butanol; in 100 wt% H_2O; **b**, water elimination in 100 wt% H_2O; **c**, protonation of *tert*-butanol in 90 wt% DMSO; **d**, water elimination in 90 wt% DMSO; **e**, protonation of *tert*-butanol in 100 wt% DMSO; **f**, water elimination in 100 wt% DMSO; **g**, protonation of *ter*t-butanol in 70 wt% GVL; **h**, water elimination in 70 wt% GVL; **i**, protonation of *tert*-butanol in 100 wt% GVL; **j**, water elimination in 100 wt% GVL. Both the protonation and water elimination reactions progress from the left-hand side of the plot to the right-hand side.
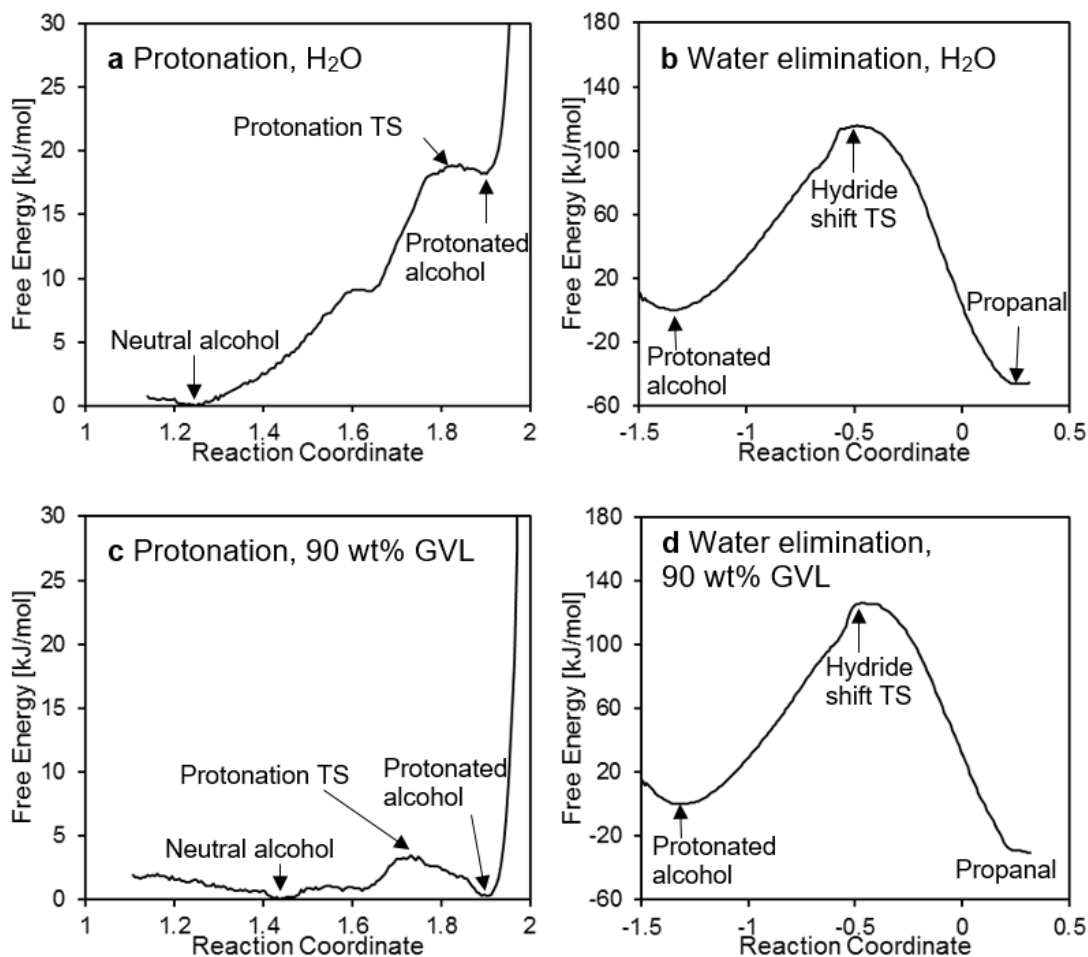
Supplementary Figure 2.6 Free energy profile plots for the elementary steps in the dehydration of 1,2-propanediol. a, protonation 1,2-propanediol in 100 wt% H_2O; **b,** water elimination in 100 wt% H_2O; **c,** protonation 1,2-propanediol in 90 wt% GVL; **d,** water elimination in 90 wt% GVL.
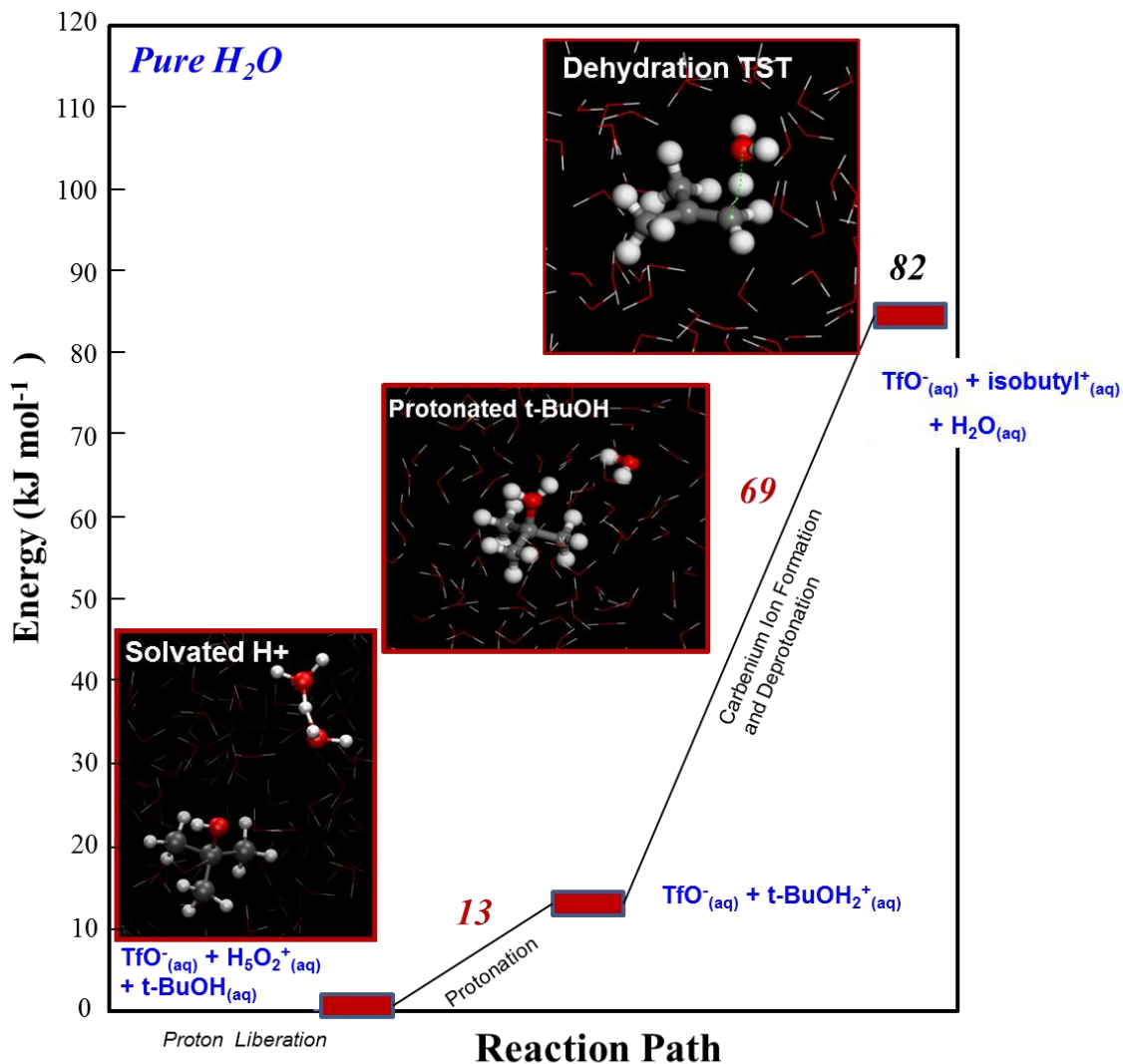
Supplementary Figure 2.7 *Ab initio* **MD calculated potential energy profile for the dehydration of *tert*-butanol in pure water.** Triflic acid readily dissociates in water to form solvated H^+ and TfO^-. The reaction steps then involve the liberation of the proton from solution and its transfer to the hydrophilic domain near *tert*-butanol, protonation of *tert*-butanol, elimination of water to form the isobutyl cation, and the nucleophilic deprotonation of the carbenium ion by water to form isobutene and H^+.
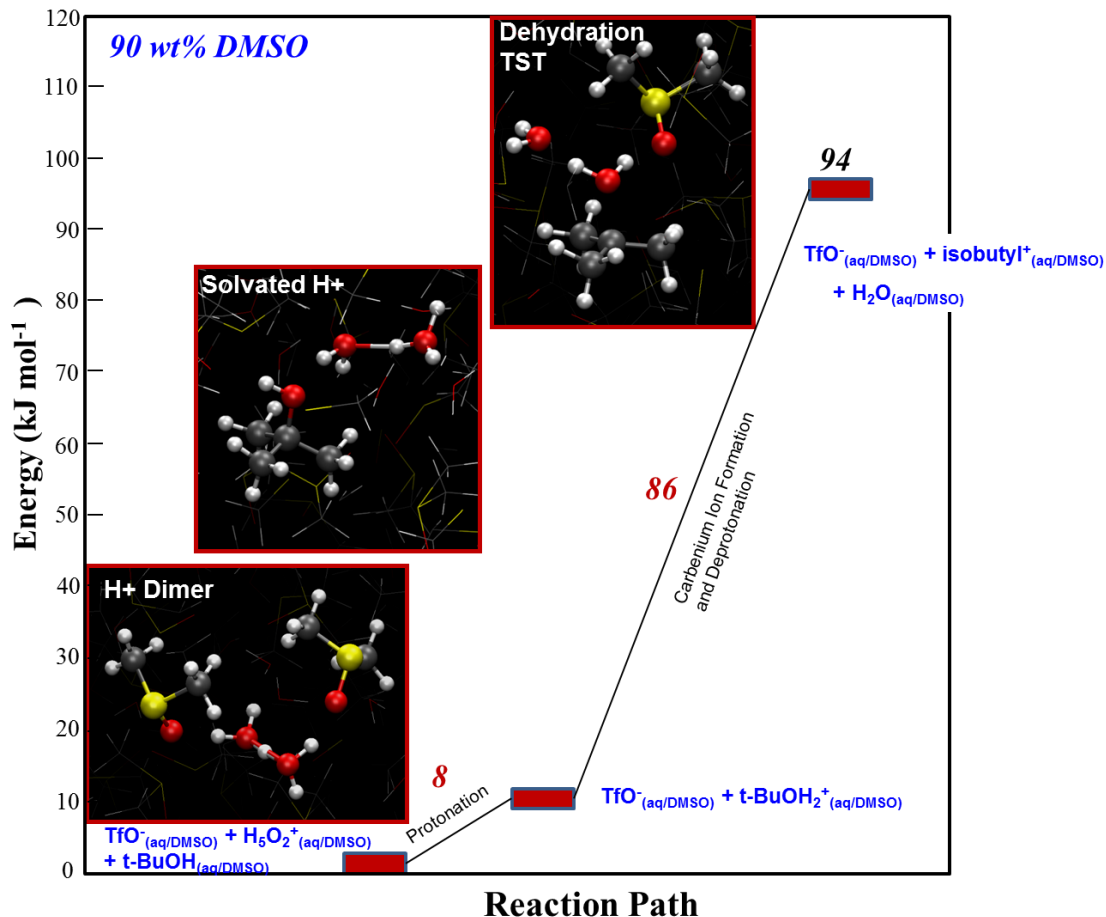
Supplementary Figure 2.8 *Ab initio* **MD calculated potential energy profile for the dehydration of *tert*-butanol in 90 wt% DMSO mixtures**. Triflic acid readily dissociates in DMSO–water mixtures to form solvated H^+ and TfO^-. The reaction steps considered then involve the liberation of the proton from solution and its transfer to the hydrophilic domain near *tert*-butanol, protonation of *tert*-butanol, elimination of water to form the isobutyl cation, and the nucleophilic deprotonation of the carbenium ion by water to form isobutene and H^+. The final nucleophilic deprotonation of the carbenium ion was calculated to be lower in energy and is not shown here.
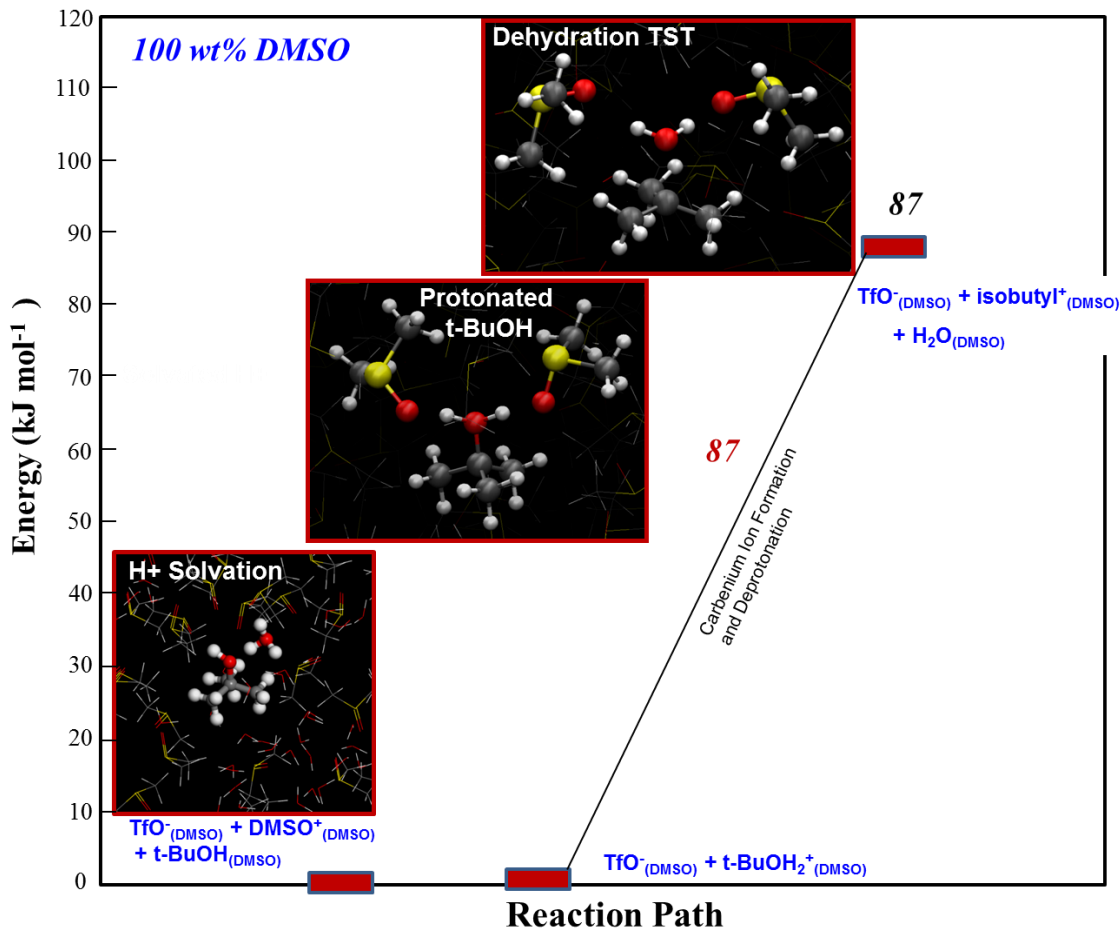
Supplementary Figure 2.9 *Ab initio* **MD calculated potential energy profile for the dehydration of *tert*-butanol in 100 wt% DMSO.** Triflic acid dissociates in DMSO to form DMSO–solvated H^+ and TfO^-. The reaction steps thus involve the liberation of the proton from solution and its transfer to the hydrophilic domain near *tert*-butanol, protonation of *tert*-butanol, elimination of water to form the isobutyl cation, and the nucleophilic deprotonation of the carbenium ion by DMSO to form isobutene and H^+. The final nucleophilic deprotonation of the carbenium ion was calculated to be lower in energy and is not shown here.
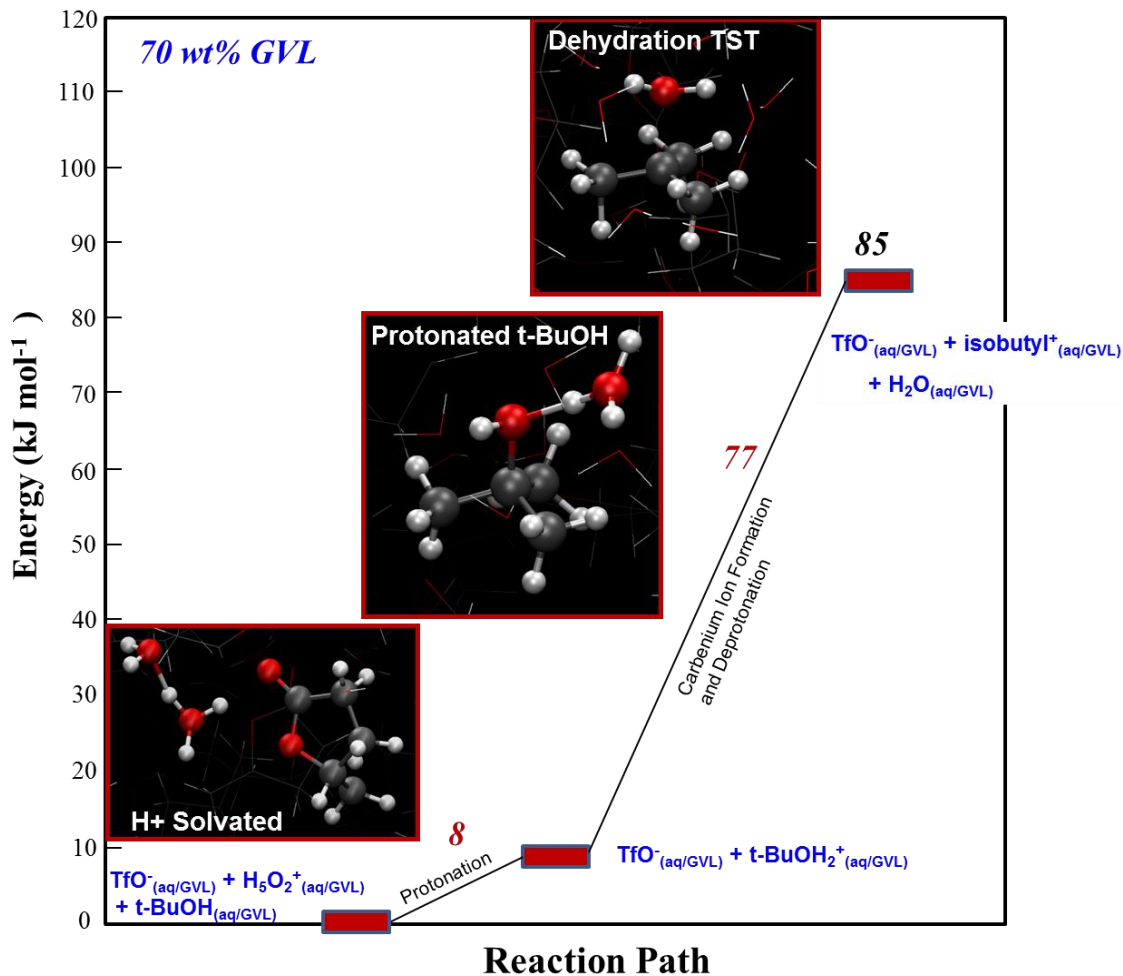
Supplementary Figure 2.10 *Ab initio* **MD calculated potential energy profile for the dehydration of *tert*-butanol in 70 wt% GVL mixtures**. Triflic acid readily dissociates in the water/GVL mixtures to form solvated H^+ and TfO^-. The reaction steps thus involve the liberation of the proton from solution and its transfer to the hydrophilic domain near *tert*-butanol, protonation of *tert*-butanol, elimination of water to form the isobutyl cation, and the nucleophilic deprotonation of the carbenium ion by water to form isobutene and H^+. The final nucleophilic deprotonation of the carbenium ion was calculated to be lower in energy and is not shown here.
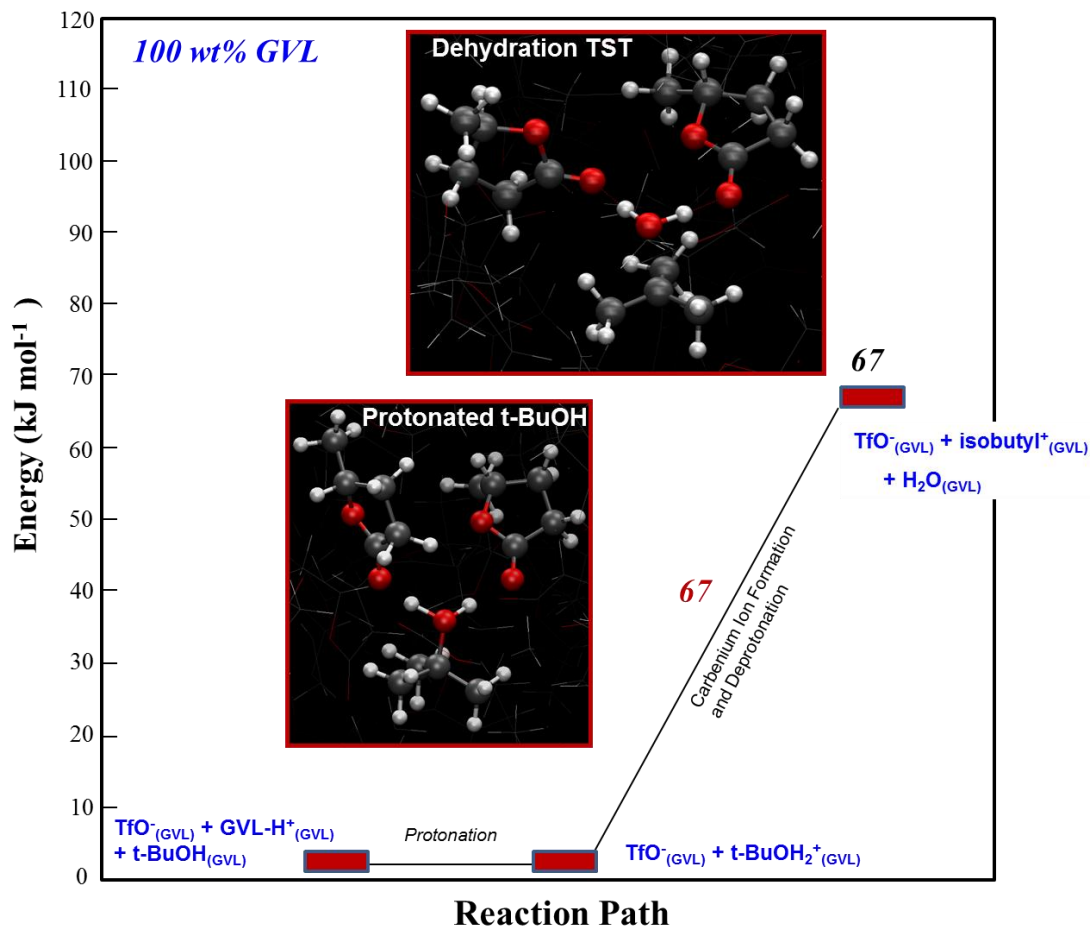
Supplementary Figure 2.11 *Ab initio* **MD calculated potential energy profile for the dehydration of *tert*-butanol in 100 wt% GVL.** Triflic acid readily dissociates in GVL to form solvated H$^+$ and TfO$^-$. The reaction steps thus involve the liberation of the proton from solution and its transfer to the hydrophilic domain near *tert*-butanol, protonation of *tert*-butanol, elimination of water to form the isobutyl cation, and the nucleophilic deprotonation of the carbenium ion by GVL to form isobutene and H$^+$. The final nucleophilic deprotonation of the carbenium ion was calculated to be lower in energy and is not shown here.
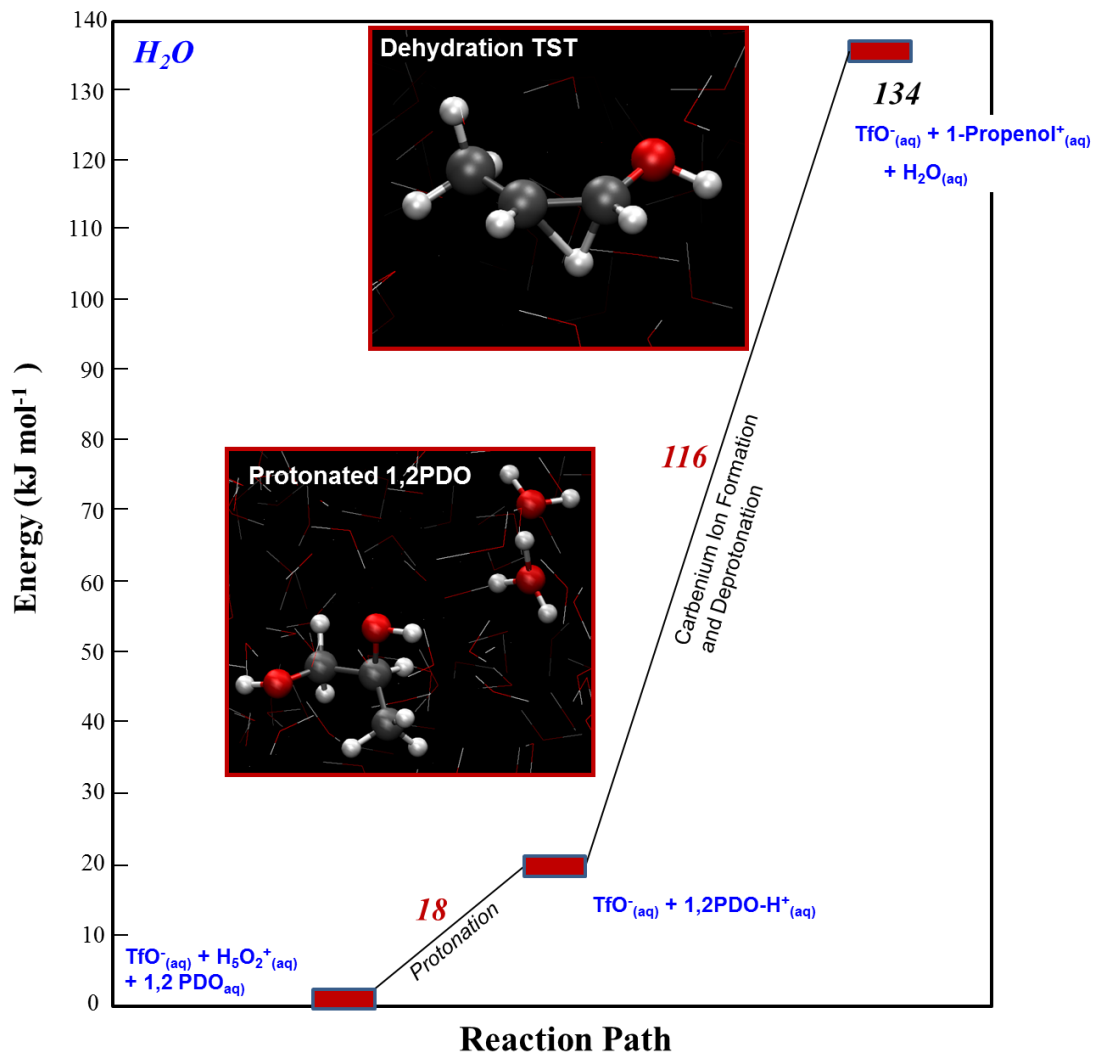
Supplementary Figure 2.12 *Ab initio* **MD calculated potential energy profile for the dehydration of 1,2-propanediol in 100 wt% water**. Triflic acid readily dissociates to form solvated H^+ and TfO^-. The reaction steps thus involve the liberation of the proton from solution and its transfer to the hydrophilic domain near 1,2-propanediol, protonation of 1,2-propanediol, elimination of water to form 1,2-PDO-H^+ cation, and the nucleophilic deprotonation of the carbenium ion by water to form (which undergoes an enol tautomerization to form propanal) and H^+. The final nucleophilic deprotonation of the carbenium ion was calculated to be lower in energy and is not shown here.
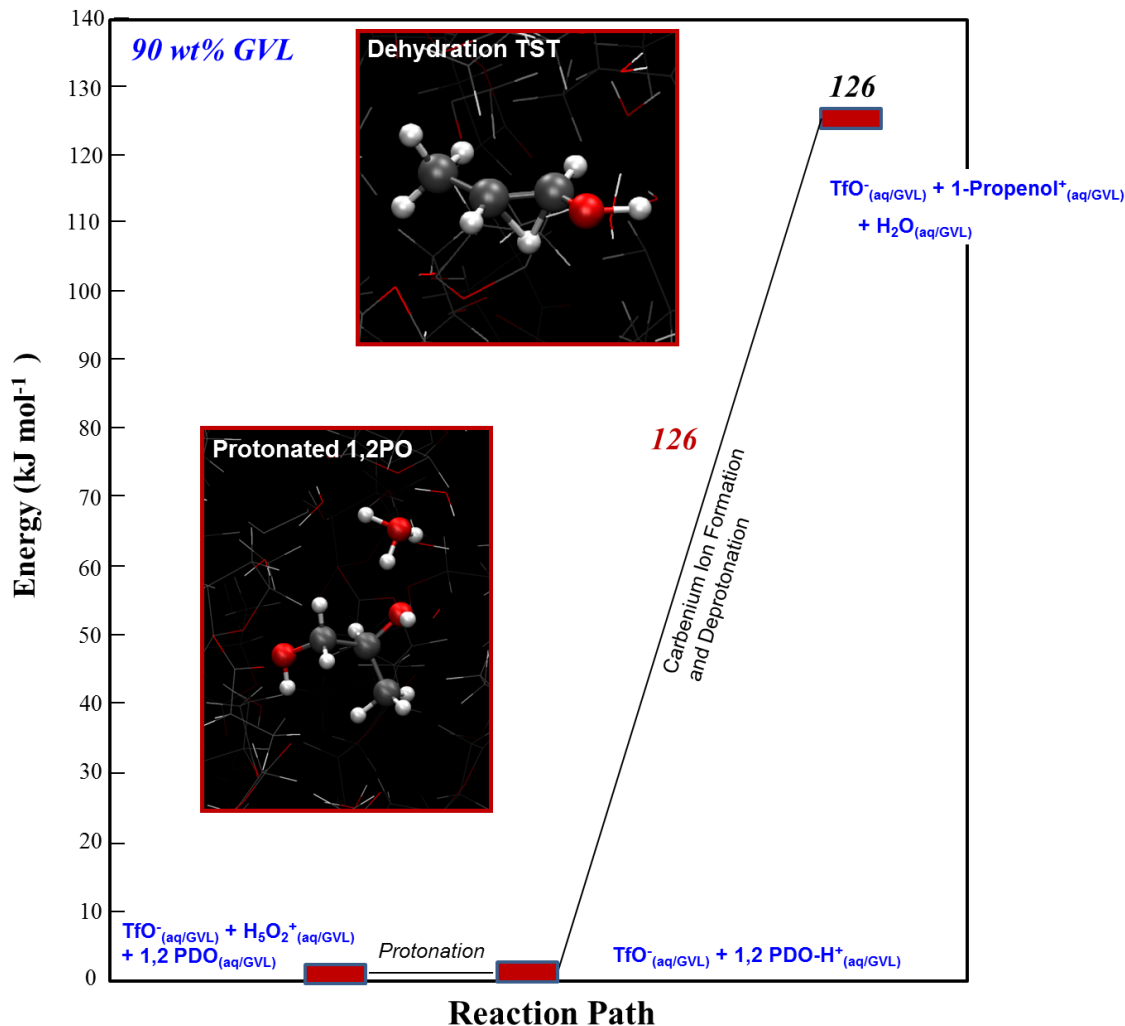
Supplementary Figure 2.13 *Ab initio* **MD calculated potential energy profile for the dehydration of 1,2-propanediol in 90 wt% GVL–water mixtures**. Triflic acid readily dissociates to form solvated H$^+$ and TfO$^-$. The reaction steps thus involve the liberation of the proton from solution and its transfer to the hydrophilic domain near 1,2-propanediol, protonation of 1,2-propanediol, elimination of water to form 1,2-PDO–H$^+$ cation, and the nucleophilic deprotonation of the carbenium ion by solution to form 1-propenol (which undergoes an enol tautomerization to form propanal) and H$^+$. The final nucleophilic deprotonation of the carbenium ion was calculated to be lower in energy and is not shown here.
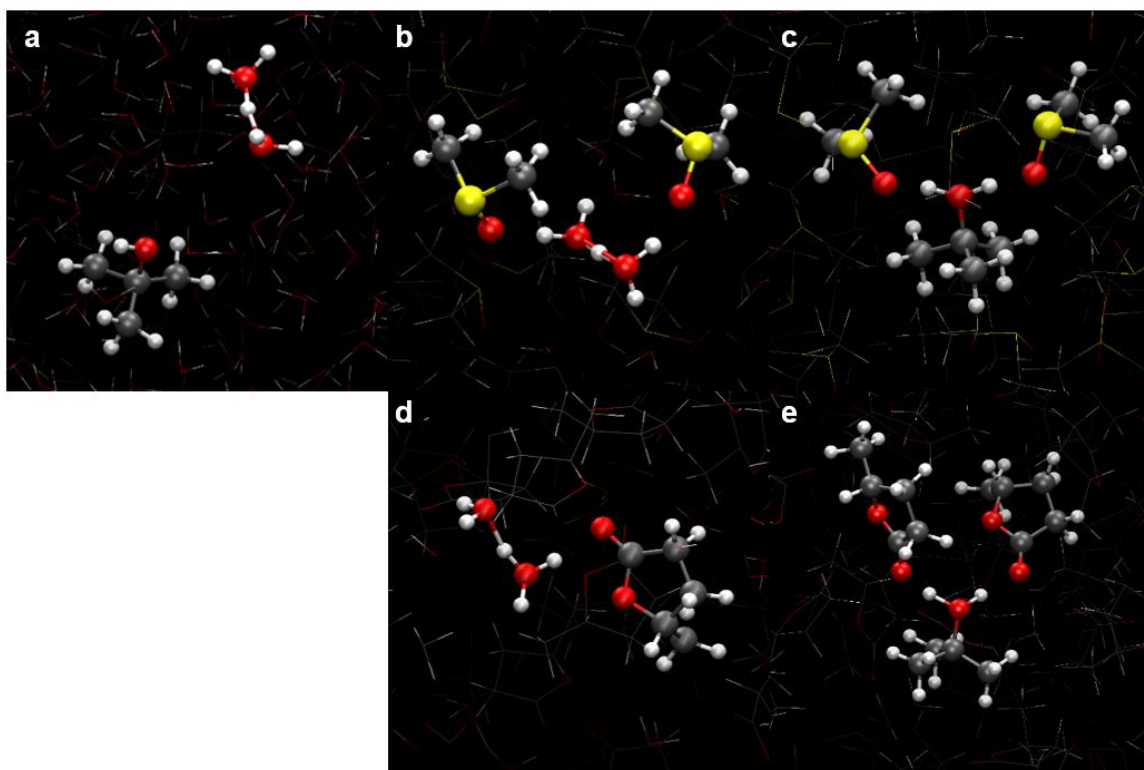
Supplementary Figure 2.14 Proton solvation in solvent mixtures. DFT-calculated structures for a proton in: (**a**) bulk water, (**b**) 90 wt% DMSO, (**c**) 100 wt% DMSO, (**d**) 70 wt% GVL, and (**e**) 100 wt% GVL. The binding strength of the proton increases from bulk water < GVL Clusters < DMSO–H_2O clusters thus following the basicity of local solvent mixture.
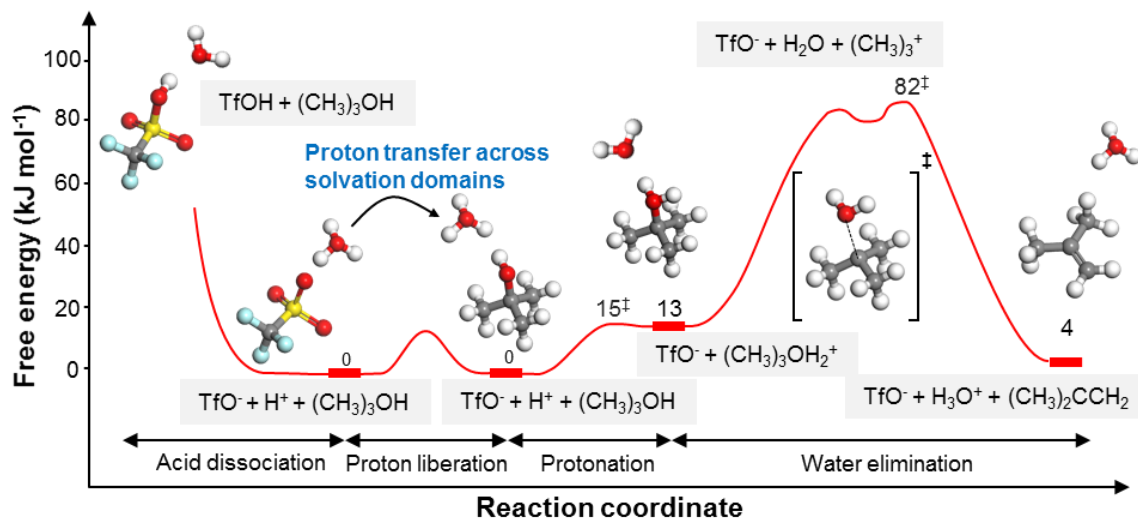
Supplementary Figure 2.15 *Ab initio* **MD simulation results of the Brønsted acid-catalyzed dehydration of *tert*-butanol in water**. Free energy path for *tert*-butanol dehydration in water which involves the dissociation of triflic acid, proton liberation and transfer from solution to the hydrophilic domain near the alcohol, protonation of the alcohol and water elimination.
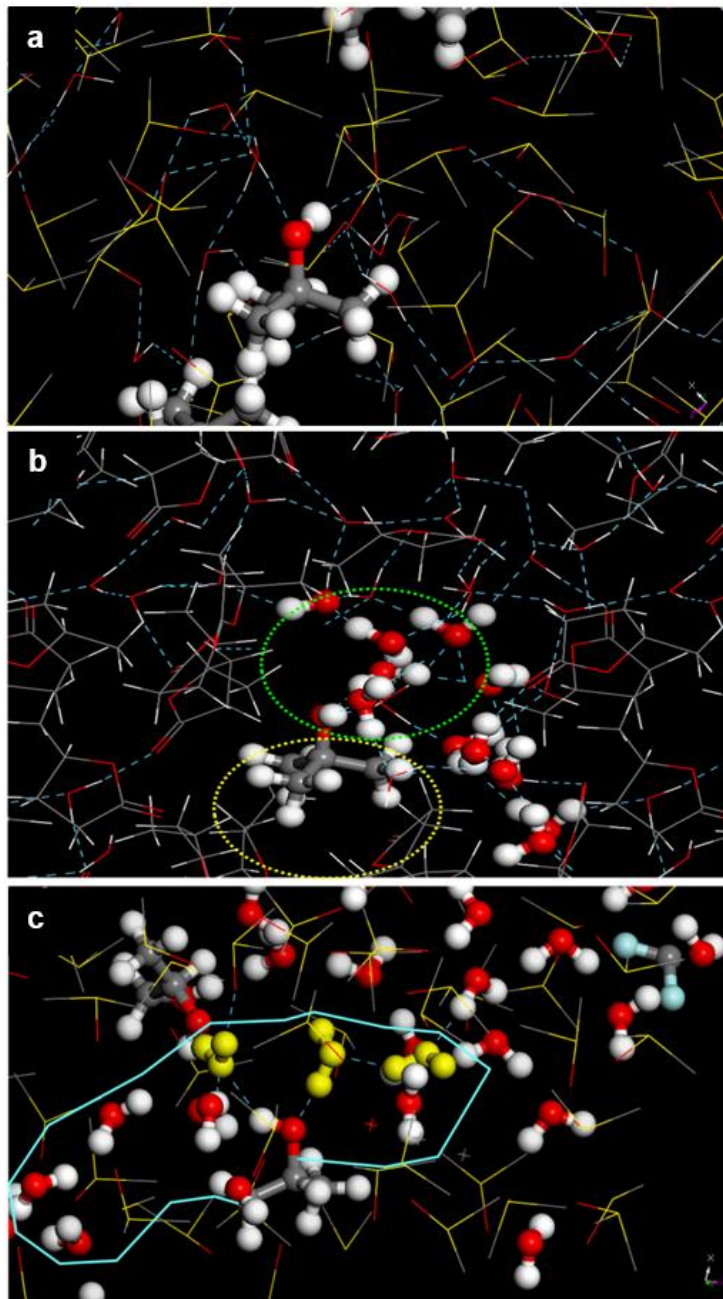
Supplementary Figure 2.16 Snapshots from molecular dynamics simulations. a, *tert*-butanol in ~90 wt% DMSO–water mixtures showing the intermixing of DMSO and water with the formation of strong $(CH_3)_2S=O$---H-OH interactions, which is consistent with their exothermic heats of mixing. **b,** *tert*-butanol in ~90 wt% GVL–water mixtures showing the formation of hydrophilic domains near the OH of the alcohol and larger hydrophobic domains that surround and encapsulate the hydrophilic domains. **c,** 1,2-propanediol in ~90 wt% GVL–water mixtures showing a significantly increased water cluster of hydrophilic domain size near the OH groups on the alcohol.
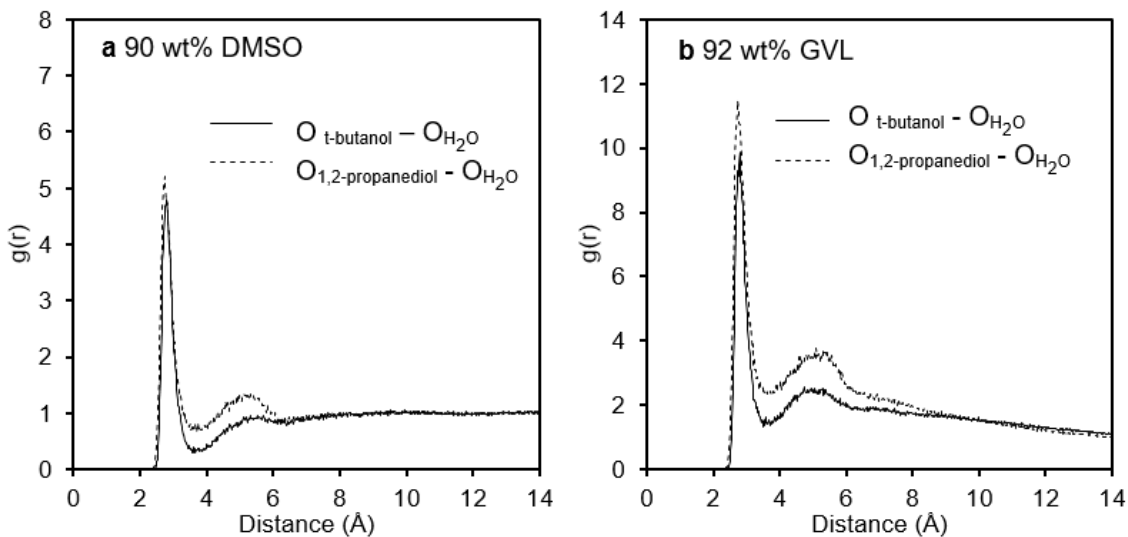
Supplementary Figure 2.17 Radial distribution functions (RDF) of the water oxygen atom around the *tert*-butanol and 1,2-propanediol oxygen atoms in: (a) 90 wt% DMSO mixture and in (b) 92 wt% GVL mixture. The solid lines are the RDFs of water oxygen–*tert*-butanol oxygen, and the dashed lines are the RDFs of water oxygen–1,2-propanediol oxygen connecting to the C2 carbon. The RDF of 1,2-propanediol in DMSO shows a small, broad peak at 4–6 Å, indicating a formation of water cluster around the C_2 hydroxyl group. In contrast, the RDF of *tert*-butanol in DMSO indicates the lack of water around the hydroxyl group. A water cluster around the hydroxyl group is observed in the case of 1,2-propanediol in GVL, while the extent of water clustering around *tert*-butanol is lower.
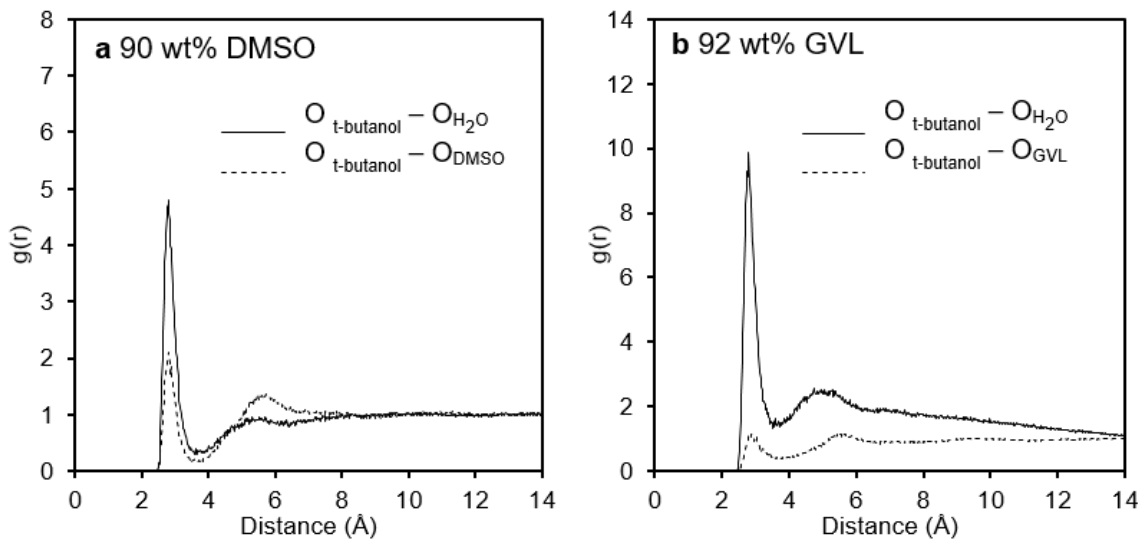
Supplementary Figure 2.18 Radial distribution functions (RDF) for the distance between the O of the hydroxyl group on *tert*-butanol and the O atom of water and the O atom of the organic solvent for: (a) 90 wt% DMSO and (b) 92% GVL mixtures. In 90 wt% DMSO, the integration of the RDF out to the first minima at ~4 Å results in 1.57 water and 0.73 DMSO molecules that interact with the OH group of *tert*-butanol. In 92 wt% GVL, the integration of the O–O RDF out to the first minima at ~4 Å indicates that there are 1.33 water molecules and 0.48 GVL molecules. The total percentage of water in the DMSO mixture through the 1st minimum is 68% whereas the total percentage of water in the GVL mixture is 73%.
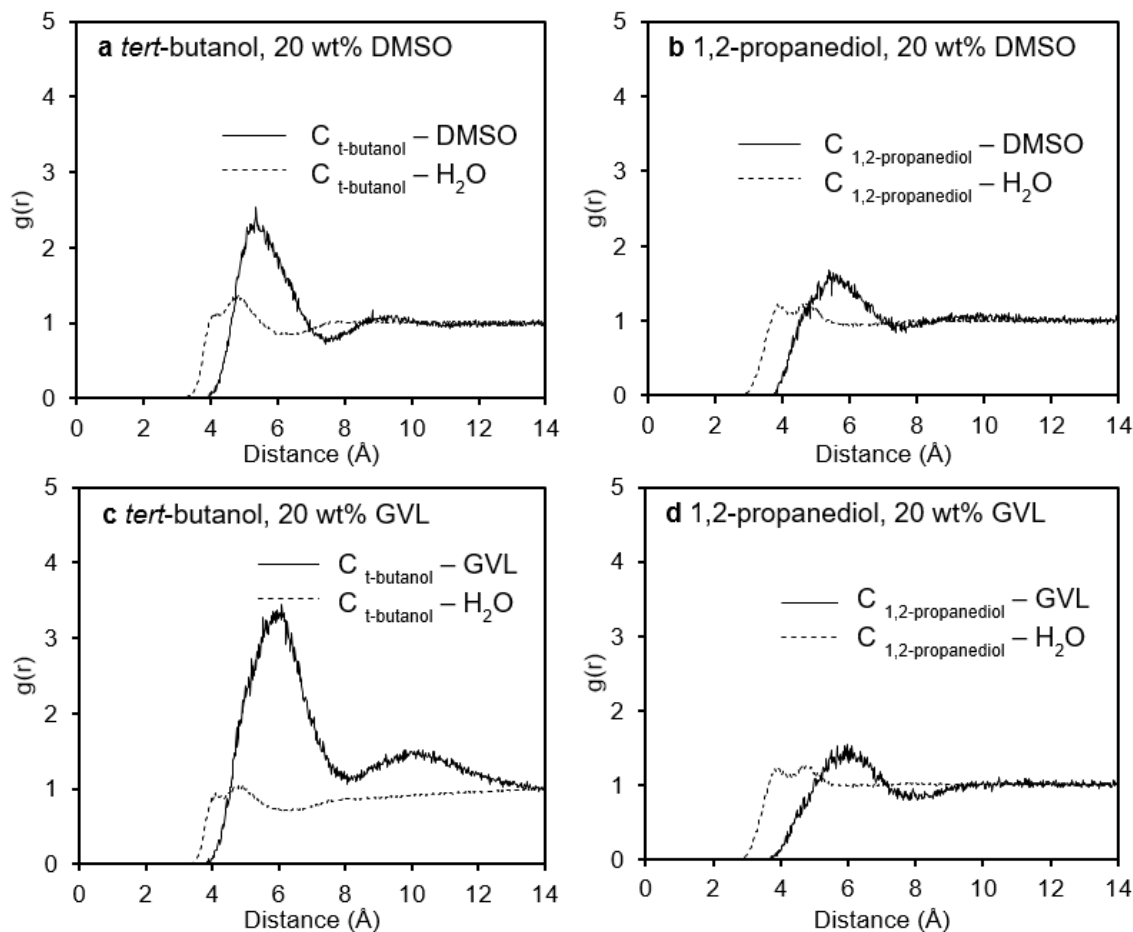
Supplementary Figure 2.19 Radial distribution functions (RDF) of solvent molecules around: (**a**) *tert*-butanol in 20 wt% DMSO, (**b**) 1,2-propanediol in 20 wt% DMSO, (**c**) *tert*-butanol in 20 wt% GVL, and (**d**) 1,2-propanediol in 20 wt% GVL. In the 20% DMSO mixtures, the solid lines are the RDFs for (a) DMSO center of mass –*tert*-butanol carbons of the three methyl groups and (b) DMSO center of mass –1,2-propanediol carbons. The dashed lines are the RDFs for (a) water center of mass –*tert*-butanol carbons of the three methyl groups and (b) water center of mass –1,2-propanediol carbons. The methyl and methylene carbons for 1,2-propanediol were similar to one another, and the RDFs of different carbon atoms were averaged into a single RDF. In GVL mixtures, the solid lines are the RDFs for (a) GVL center of mass –*tert*-butanol carbons in methyl groups and (b) GVL center of mass –1,2-propanediol carbons. The dashed lines are the RDFs for (a) water center of mass –*tert*-butanol carbons in methyl groups and (b) water center of mass –1,2-propanediol carbons. For *tert*-butanol, the large, broad peaks of organic solvent molecules at 5-8 Å in panels (a) and (c) indicate the significant aggregation of DMSO and GVL molecules around the methyl groups of the alcohol, indicating that the alcohol resides primarily in hydrophobic domains. The lack of organic solvent molecules around the methyl and methylene groups of 1,2-propanediol indicates the enhanced hydrophilicity of alcohol, which can be attributed to the presence of multiple hydroxyl groups. The free energy penalty for transferring the hydrophilic proton to the hydrophobic domains results in the decrease in reactivity observed for *tert*-butanol dehydration.
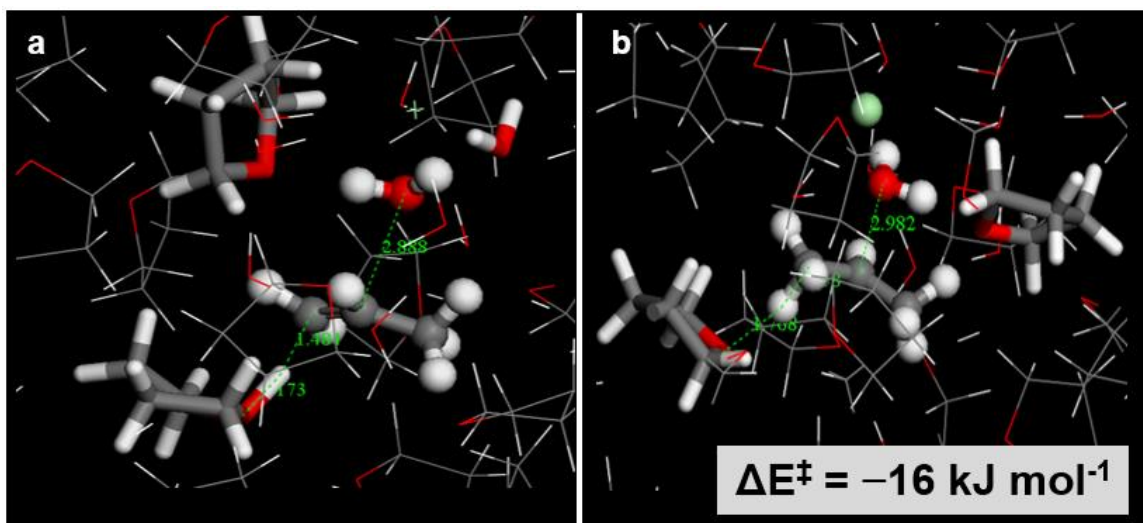
Supplementary Figure 2.20 The role of Cl⁻ in stabilizing the water elimination transition state in GVL. DFT-calculated stabilization free energy for the influence of Cl⁻ on stabilizing the carbenium ion transition state for the elimination of water from the protonated *tert*-butanol in the polar aprotic GVL solution.

a Protonation, H$_2$O

b Water elimination, H$_2$O

c Protonation, 90 wt% DMSO

d Water elimination, 90 wt% DMSO

e Protonation, 100 wt% DMSO

f Water elimination, 100 wt% DMSO
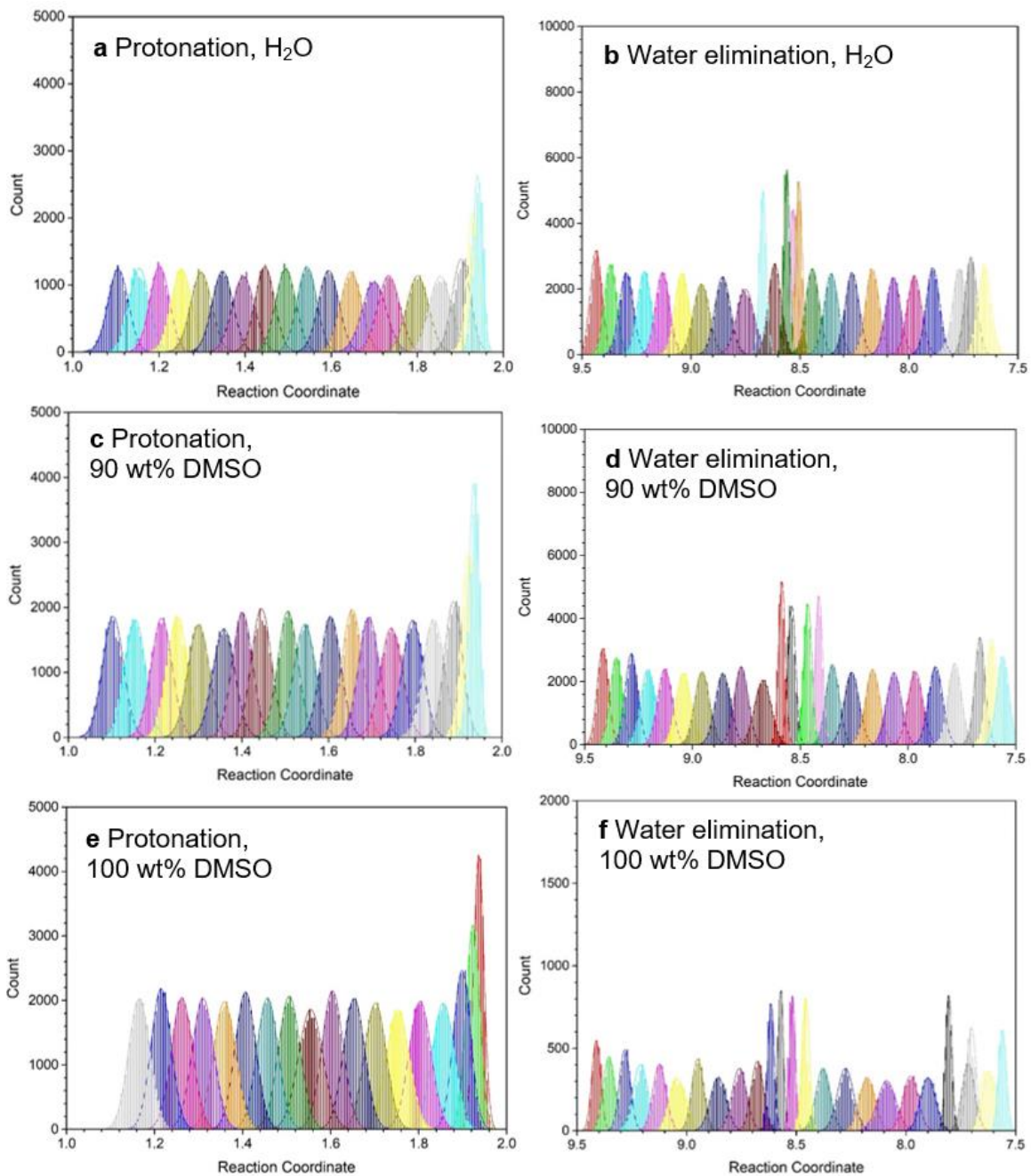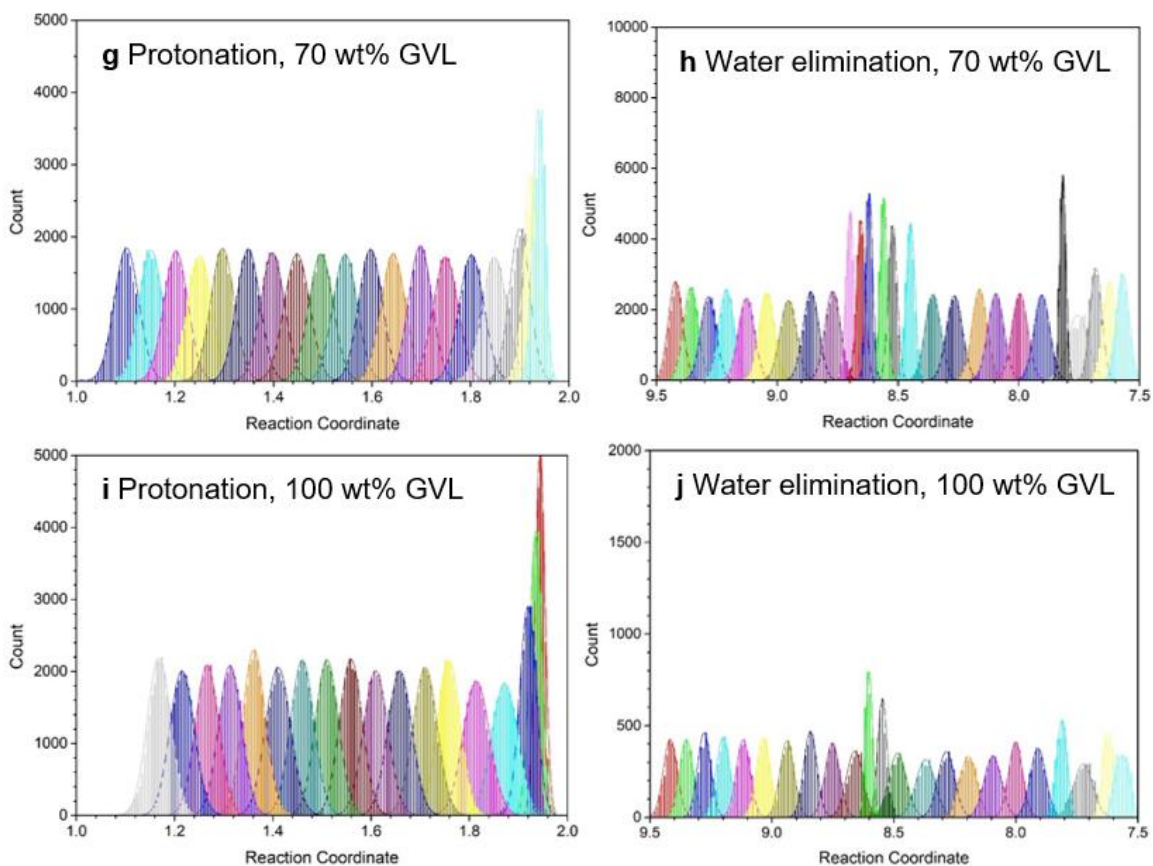
Supplementary Figure 2.21 Histograms of umbrella sampling for the elementary steps in the dehydration of *tert*-butanol. a, protonation *tert*-butanol in 100 wt% H₂O; **b**, water elimination in 100 wt% H₂O; **c,** protonation *tert*-butanol in 90 wt% DMSO; **e,** water elimination in 90 wt% DMSO; **e,** protonation *tert*-butanol in 100 wt% DMSO; **f,** water elimination in 100 wt% DMSO; **g,** protonation *tert*-butanol in 70 wt% GVL; **h,** water elimination in 70 wt% GVL; **i,** protonation *tert*-butanol in 100 wt% GVL; **j,** water elimination in 100 wt% GVL.
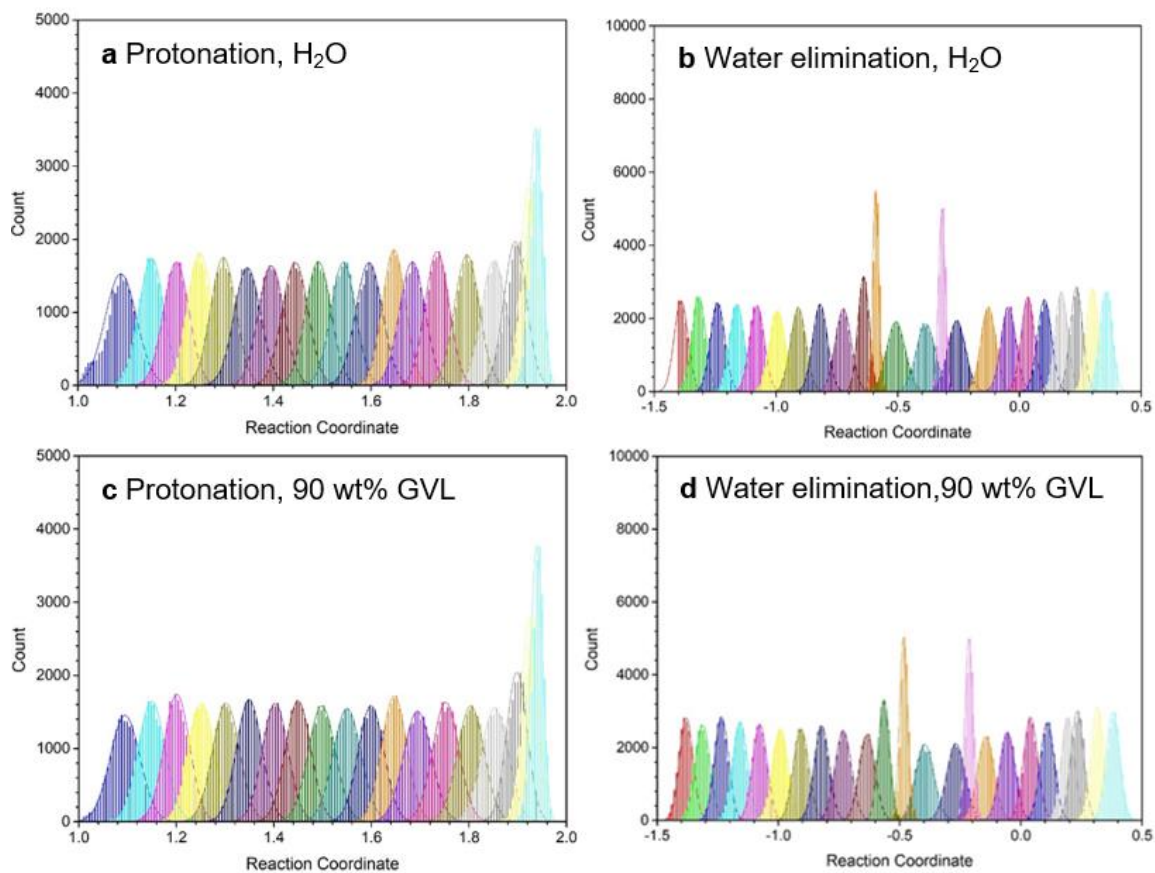
Supplementary Figure 2.22 Histograms of umbrella sampling for the elementary steps in the dehydration of 1,2-propanediol. **a**, protonation of 1,2-propanediol in H_2O; **b**, water elimination in H_2O; **c**, protonation of 1,2-propanediol in 90 wt% GVL; **d**, water elimination in 90 wt% GVL

a
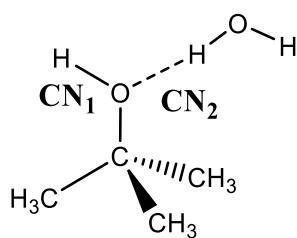
t-butanol
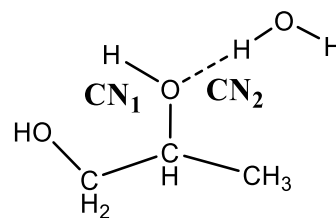
1,2-propanediol

b
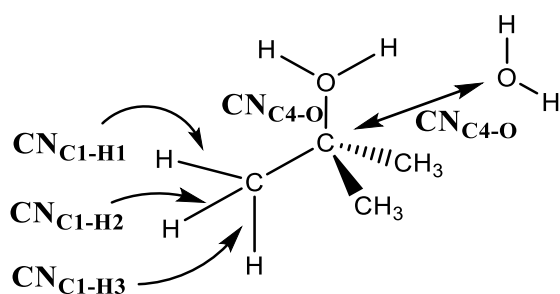
t-butanol
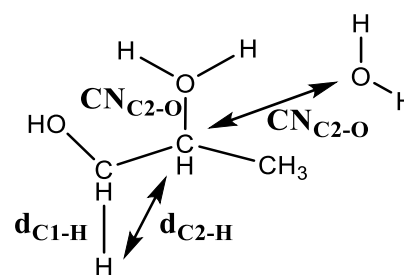
1,2-propanediol

c
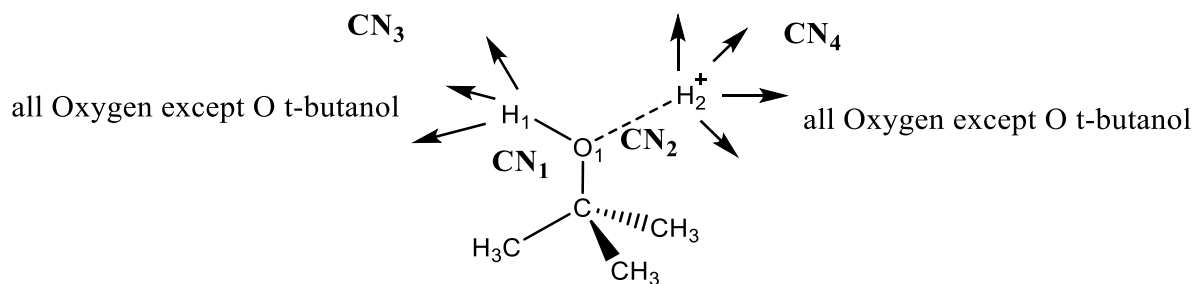
t-butanol

Supplementary Figure 2.23 Reaction coordinates used for *tert*-butanol and 1,2-propanediol dehydration. a, The protonation steps; **b**, the water removal steps; **c**, the expanded protonation coordinate for *tert*-butanol.
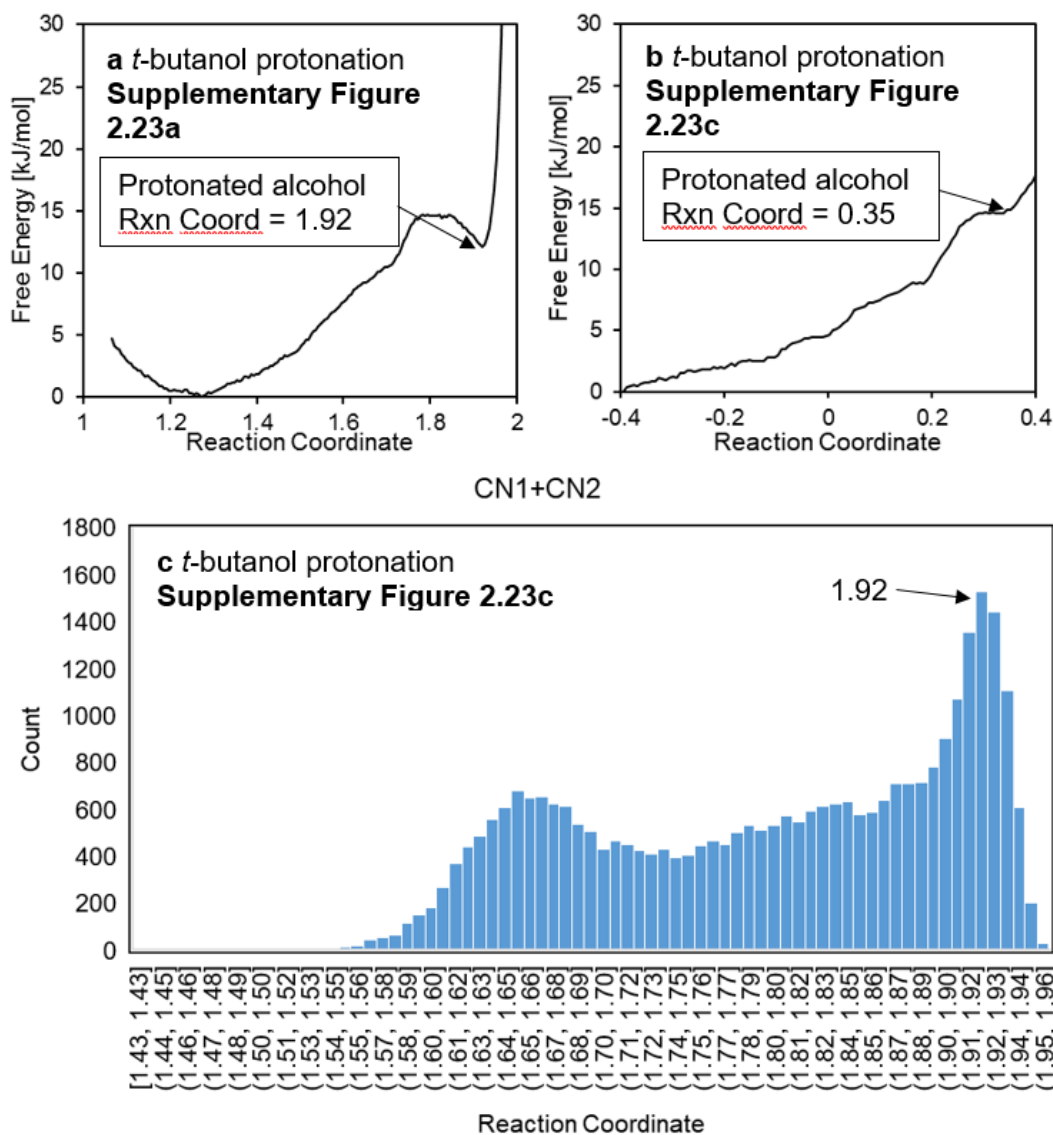
Supplementary Figure 2.23 Free energy profile for the protonation of *tert*-butanol obtained using Supplementary Figure 2.23a and Supplementary Figure 2.23c reaction coordinates. **a**, The free energy profile from Supplementary Figure 2.23a involves an activation free energy of 15 kJ mol^{-1} and free energy of reaction of 12 kJ mol^{-1} the protonated structure is observed at reaction coordinate 1.92. **b**, The free energy profile from Supplementary Figure 2.23c involves an activation free energy of 15 kJ mol^{-1} and free energy of reaction of 14 kJ mol^{-1}. The protonated structure is observed at reaction coordinate ~ 0.35. **c**, A histogram of CN1 + CN2 from Supplementary Figure 2.23c at reaction coordinate ~ 0.35 shows a peak at 1.92, the exact reaction coordinates of the protonated alcohol observed in Supplementary Figure 2.23a.

Chapter 3 – Effects of Chloride Ions in Acid-Catalyzed Biomass Dehydration Reactions in Polar Aprotic Solvents

Reprinted from Mellmer, M. A. *et al.* Effects of chloride ions in acid-catalyzed biomass dehydration reactions in polar aprotic solvents. *Nat. Commun.* **10**, 1132 (2019). Reproduced under the terms of the Creative Commons Attribution 4.0 International License https://creativecommons.org/licenses/by/4.0/.

Theoretical calculations were performed by CS under the supervision of MN.

3.1 Introduction

Acid catalysis is ubiquitous in biomass-conversion processes to produce chemicals and fuels. It has been shown recently that the use of organic solvents for such biomass-upgrading reactions leads to increased catalytic activity and selectivity compared with reactions in aqueous media.[19,21,56,57,141–148,34,149–153,46–52] Accordingly, we explored the processing strategies using γ-valerolactone (GVL) solvent mixtures with water to produce concentrated streams of C_5 and C_6 sugars[46] as well as valuable platform chemicals[51] and high-value products[142] from biomass using dilute concentrations of mineral acids. In subsequent studies on acid-catalyzed dehydration of xylose to furfural, we reported a 30-fold increase in reactivity and a 25% increase in selectivity (furfural yield increased from 50% to 75%) using GVL as a solvent compared with the reaction carried out in water.[48] Similar solvent enhancement effects have been reported using other polar aprotic solvents, such as tetrahydrofuran (THF),[19,143] dimethyl sulfoxide,[34,56,57,144] 1,4-dioxane,[145] and sulfolane.[146] Despite the potential advantages of using polar aprotic solvents for biomass-

upgrading reactions, fundamental understanding of these solvation effects in acid-catalyzed processes using non-aqueous solvents is limited at present.

Herein, we show that the addition of catalytic concentrations (e.g., < 5 mM) of inorganic salts, specifically chloride salts, in polar aprotic solvents, such as GVL, can further enhance the reactivity and yield for acid-catalyzed reactions related to biomass conversion. The dehydration of fructose to 5-hydroxymethylfurfural (HMF) is a Brønsted acid-catalyzed reaction, which is recognized as a promising biomass utilization platform. In addition, this extensively characterized reaction serves as a model system to study the mechanisms behind observed solvent effects. Based on fundamental reaction kinetics studies and *ab initio* molecular dynamics studies, we show that chloride ions participate in stabilizing protonated transition states for these acid-catalyzed reactions, leading to improvements in reaction rates and selectivities.

3.2 Experimental Results

Table 3.1 compares fructose conversion reaction rate constant values and HMF yield values for various strong homogeneous Brønsted acids (e.g., H_2SO_4, triflic acid, and HCl) in water and several polar aprotic solvents (containing 10 wt% water) at 373 K (rate constant values) and 393 K (yield values). Similar fructose conversion rate constant values were obtained in water (i.e., ~0.15 M^{-1} ks^{-1}) regardless of the acid used, and HMF yields in water of 40% were achieved with both H_2SO_4 and HCl. Rate constant values increased by over an order of magnitude and HMF yields increased by 15% when GVL was used as the solvent with H_2SO_4 and triflic acid compared with using water as the solvent. Similar

improvements in reactivity and HMF yields were also observed using dioxane and THF as solvents.

Table 3.1 Fructose conversion experimental results using homogeneous acid catalysts[a]

Solvent	Acid Catalyst	Rate Constant $(M^{-1} ks^{-1})$[b]	HMF Yield (%)[c]
H_2O	H_2SO_4	0.14 ± 0.01	38 ± 1
H_2O	Triflic acid	0.15 ± 0.03	35 ± 2
H_2O	HCl	0.14 ± 0.01	40 ± 1
90% GVL/10% H_2O	H_2SO_4	20 ± 1	57 ± 1
90% GVL/10% H_2O	Triflic acid	21 ± 4	56 ± 2
90% GVL/10% H_2O	HCl	62 ± 4	78 ± 1
90% THF/10% H_2O	H_2SO_4	5.8 ± 1	70 ± 1
90% THF/10% H_2O	Triflic acid	5.6 ± 1	72 ± 5
90% THF/10% H_2O	HCl	28 ± 5	76 ± 1
90% Dioxane/10% H_2O	H_2SO_4	10 ± 2	64 ± 1
90% Dioxane/10% H_2O	Triflic acid	7.7 ± 1	57 ± 2
90% Dioxane/10% H_2O	HCl	95 ± 6	73 ± 1

[a] Reaction conditions: fructose (50 mM); acid (0.5 M for H_2O; 5 mM for polar aprotic solvents); solvent (5 mL); stirring (700 rpm). [b] Rate constant values at 373 K; $r = k$ [R] [HB]. [c] HMF yield values at 393 K at approximately 90% conversion.

We observe a substantial difference in the fructose conversion rate constant values as well as HMF yield when HCl is used as the acid catalyst in these polar aprotic solvent systems compared with other strong acids. For example, in GVL with HCl, a rate constant value of $62 \, M^{-1} \, ks^{-1}$ and HMF yield of 80% were achieved, a threefold increase in rate constant value, and a 25% increase in HMF yield compared with using H_2SO_4 and triflic acid in GVL. Similar improvements using HCl compared with H_2SO_4 and triflic acid were observed in THF and dioxane solvents, with a 5-fold and 10-fold increase in rate,

respectively. This increased reaction performance using HCl compared with other strong Brønsted acid catalysts is not observed using water as the solvent under these conditions.

As shown in Table 3.2, the improved performance of the fructose dehydration reaction can also be achieved with the addition of equimolar concentrations (i.e., 5 mM) of chloride-containing salts (e.g., KCl) with H_2SO_4 and triflic acid in GVL solvent, suggesting that ions are involved in the fructose dehydration catalytic process in polar aprotic solvents. The use of KCl for fructose dehydration without a Brønsted acid catalyst in GVL led to a low fructose conversion rate and shows that the chloride anion alone does not catalyze fructose dehydration.

Table 3.2 Fructose conversion experimental results in 90% GVL using homogeneous acid/salt systems.[a]

Acid Catalyst	Salt	Rate Constant (M^{-1} ks^{-1})[b]
–[c]	KCl	3.2 ± 1
H_2SO_4	KCl	53 ± 9
Triflic acid	KCl	64 ± 5[e]
HCl	KCl	78 ± 8[f]
H_2SO_4	NaCl	55 ± 20
Triflic acid	NaCl	53 ± 6
Triflic acid	LiCl	69 ± 10
Triflic acid	$CaCl_2$[d]	71 ± 10
HBr	–	28 ± 3
Triflic acid	KBr	22 ± 3
Triflic acid	NaBr	25 ± 2
Triflic acid	LiBr	29 ± 1
HI	–	2.7 ± 1
Triflic acid	KI	4.0 ± 1
Triflic acid	KF	1.9 ± 1

[a] Reaction conditions: fructose (50 mM); acid (5 mM); salt (5 mM); solvent (90% GVL/10% H_2O; 5 mL); stirring (700 rpm). [b] Rate constant values at 373 K; $r = k$ [R] [HB]. [c] No acid catalyst; $r = k$ [R] [Salt]. [d] Salt concentration (2.5 mM). [e] 78% HMF yield at 393 K at approximately 90% conversion. [f] 81% HMF yield at 393 K at approximately 90% conversion.

We also explored the effects of adding various cations (Na^+, Li^+, and Ca^{2+}) and anions (Br^-, I^-, and F^-) using H_2SO_4 and/or triflic acid as catalysts in GVL (Table 3.2). The addition of the cations Na^+, Li^+, and Ca^{2+}, and the anion Br^- with H_2SO_4 and/or triflic acid did not lead to significant differences in fructose conversion reaction rates. The addition of the anions I^- and F^- (with K^+) led to lower reaction rates for fructose conversion reactions with triflic acid.

The iodide ion is strongly electronegative and may potentially promote a substitution reaction mechanism over an elimination mechanism, as no detectable production of HMF was observed using HI as a catalyst in GVL. Furthermore, iodide anions are strong reducing agents and have the potential to oxidize to diatomic iodine and water, deactivating the acid catalyst. The fluoride ion is more basic and has a strong affinity for the proton in solution relative to the other halogen ions used in this study (i.e., HF is a weaker acid; pK_a value in water of 3.2), and thus, F^- likely competes with fructose for the acidic proton, leading to decreased fructose dehydration rates.

Importantly, we found that the increased reactivity and yield with the addition of chloride ions in GVL is also observed for other acid-catalyzed sugar dehydration reactions, and this behavior thus appears to be of general significance (Supplementary Table 3.1). For example, the acid-catalyzed dehydration of xylose to furfural displays a similar increase in reactivity in GVL with HCl compared with H_2SO_4 (e.g., fourfold rate increase). Furthermore, the furfural yield from xylose increased from 60% using H_2SO_4 as a catalyst to 75% using HCl as a catalyst in GVL. Similarly, a twofold increase in glucose conversion reactivity and 25% HMF yield increase were achieved in GVL with HCl compared with H_2SO_4 as a catalyst, which has also been shown previously by Li et al.[154]

3.3 Discussion

3.3.1 Experimental discussion

Promotional effects in reactivity and selectivity have been reported in the literature for biomass conversion reactions using metal halides, such as NaCl, in aqueous media.[78–81] For example, Marcotullio et al. reported a 20% increase in furfural yield from xylose

(i.e., from 60% to 80% furfural yield) and three- to fourfold increases in xylose dehydration reaction rates using 1 M NaCl in aqueous solution.[78,79] Similarly, Enslow et al. explored the role of various metal halides for xylose dehydration to furfural using salt cations (i.e., Li^+, Na^+, and K^+) and anions (i.e., Cl^-, Br^-, and I^-) at 5 M metal halide aqueous solutions, suggesting that metal halide cations disrupt the solvation of xylose by water, and metal halide anions act to stabilize critical xylose dehydration intermediates, leading to increased reactivity and selectivity.[80] In the present study, we observe promotional effects of inorganic salts in polar aprotic solvents at ~250- to 1000-fold lower concentrations compared with these chloride effects in water (e.g., 5 mM).

Mascal et al.[155,156] have previously reported a method to produce chloromethylfurfural from carbohydrates (e.g., glucose) using HCl as a catalyst in a biphasic reaction system with concentrated HCl and dichloroethane, where Cl^- is directly involved in the reaction. Thus, we performed variable-temperature ^{13}C NMR experiments for fructose conversion with ^{13}C-enriched fructose, using both HCl and H_2SO_4 (0.05 M) in 90 wt% dioxane-d_8–water at 340 K. Under these conditions, we did not detect any differences in the ^{13}C NMR spectra between HCl and H_2SO_4-catalyzed reactions in dioxane-d_8, suggesting that the observed reaction rate and product yield increases in the presence of chloride ions are not caused by changes in the reaction mechanism involving chlorinated species.

GVL has previously been shown to reversibly hydrate to 4-hydroxyvaleric acid (4-HVA) under acidic liquid-phase conditions.[157] Quantitative solution-phase ^1H NMR was performed to display the effects of chloride ions on the 4-HVA equilibrium concentration

in 90 wt% GVL–water mixtures with fructose and H_2SO_4 at various temperatures (Supplementary Figure 3.2a). Equilibrium concentrations of 4-HVA are marginally lower in the presence of KCl at typical reaction conditions (e.g., 1.2 vs. 1.4 mol% at 373 K). In addition, Supplementary Figure 3.2b displays the concentration of 4-HVA as a function of reaction time during fructose dehydration in 90 wt% GVL–water mixtures using H_2SO_4 with or without the presence of KCl. From the initial reaction start time to 10 min under reaction conditions (the period during which the reactor achieves the desired temperature of 373 K), the amount of 4-HVA in solution decreases slightly, and it then remains constant throughout the remainder of the experiment, indicating that GVL and 4-HVA are in equilibrium for both cases under typical reaction times and conditions. Moreover, reaction kinetics experiments were performed for fructose dehydration in 90% GVL–water containing H_2SO_4, KCl, and valeric acid (a molecular surrogate for 4-HVA at representative equilibrium concentrations of 1 mol% 4-HVA), as shown in Supplementary Figure 3.3. Negligible differences in fructose dehydration reaction kinetics were observed with the presence of valeric acid in the reactor. Thus, based on this analysis, we conclude that the increased reaction performance for fructose dehydration with chloride anions in GVL does not involve 4-HVA species.

The equilibrium of an acid, HB, in the liquid phase into an acidic proton, H^+, and its conjugate base, B^-, is written as

$$HB \rightleftarrows H^+ + B^- \tag{3.1}$$

Acid catalysis of a reactant, R, in solution by H^+ and an undissociated acid, HB, is often described by a reaction kinetics rate expression in the following form:

$$r = k_{H^+}[R][H^+] + k_{HB}[R][HB] \tag{3.2}$$

where k_{H^+} and k_{HB} are the rate constants for the specific-acid catalyzed and general-acid catalyzed reactions, respectively. We have measured an inverse kinetic isotope effect (KIE) using D_2O as a solvent, and also using GVL mixtures with D_2O as a solvent, as shown in Supplementary Table 3.2. These measurements of the KIE led to rate constant value ratios (k_D/k_H) of 1.7−2.7. The measured KIE suggests that acid-catalyzed dehydration of fructose is catalyzed primarily by the acidic proton, H^+ (i.e., acid dissociation is not rate-determining), and therefore, general-acid catalysis (k_{HB}) can be neglected.[97,98] Thus, the improved performance for the fructose dehydration reaction with the addition of chloride ions is not due to general-acid catalysis by undissociated HCl.

The equilibrium constant for dissociation of a Brønsted acid (equation (3.1)) (i.e., a pK_a value) is dependent on the nature of the solvent.[99] Previously, we carried out reaction kinetics experiments for fructose conversion with triflic acid in GVL, THF, and dioxane with the addition of the conjugate base of the acid catalyst (i.e., potassium triflate).[76] These reaction kinetics experiments for fructose conversion show that the rate is independent of the addition of the conjugate base of the acid catalyst, indicating that these strong acids are largely dissociated in each of these solvents. Thus, the measured rate allows calculation of the value of the specific acid rate constant (i.e., k_{H^+}).

We measured the apparent activation energies and pre-exponential factors for the specific acid-catalyzed fructose conversion in water using HCl and 90 wt% GVL–water mixtures with triflic acid and HCl. As shown in Supplementary Figure 3.1, the apparent activation energy values for water with HCl and for GVL with triflic acid are similar (e.g., ~110 kJ mol^{-1}); however, the pre-exponential value is higher by an order of magnitude in the GVL solvent relative to water. The use of GVL as a solvent with HCl increases the apparent activation energy by 25 kJ mol^{-1} and increases the pre-exponential value by four orders of magnitude compared with using triflic acid in GVL.

Values of the enthalpy change for dissolution of fructose in water and 90% GVL–water with combinations of triflic acid and potassium salts were measured at 298 K (Supplementary Table 3.3) by solution calorimetry. These values show that a mixed solvent consisting of 90% GVL–water had a destabilizing effect on fructose relative to pure water ($+ 5.2$ kJ mol^{-1}). The presence of 5 mM triflic acid in 90% GVL–water did not influence the stability of fructose relative to 90% GVL–water without an acid. Similarly, the presence of 5 mM KBr in 90% GVL–water did not have a significant effect on the enthalpy change for dissolution of fructose relative to 90% GVL–water without salt. In contrast, the addition of 5 mM KCl to 90% GVL–water increased fructose stability by 2.3 kJ mol^{-1} relative to 90% GVL–water without salt, which is in agreement with previous results showing the ability of chloride anions to stabilize carbohydrates in the gas phase.[158,159] However, the combined presence of 5 mM triflic acid and 5 mM KCl in 90% GVL–water negates the small stabilizing effect of 5 mM KCl on fructose in 90% GVL–water, resulting in no net stabilization. Thus, the calorimetric data suggest that the influence of the Cl$^-$ is unlikely driven by enthalpic destabilization of reactants, but rather the

promoting effect of Cl^- is either through stabilization of the transition state or by entropic contributions to the activation free energy.

Figure 3.1a displays the results for the effects of varying the chloride ion concentration on the fructose conversion rate constant value using triflic acid as a catalyst in 90% GVL–water. The reaction rate constant shows an increasing, concave down reactivity trend with increasing chloride ion concentration, meaning there is a diminishing promotional effect using chloride ions. Furthermore, we explored the effect of varying the GVL solvent concentration on the enhancement in the rate caused by changing from H_2SO_4 to HCl (equimolar amounts) as the acid catalyst, plotted as the ratio of fructose conversion rate constant values for HCl and H_2SO_4 versus the mass fraction of GVL in solvents consisting of GVL mixed with water (Figure 3.1b). The effect of chloride ions on the fructose conversion reaction rate relative to H_2SO_4 has an increasing trend with increasing concentrations of GVL in the solvent system.
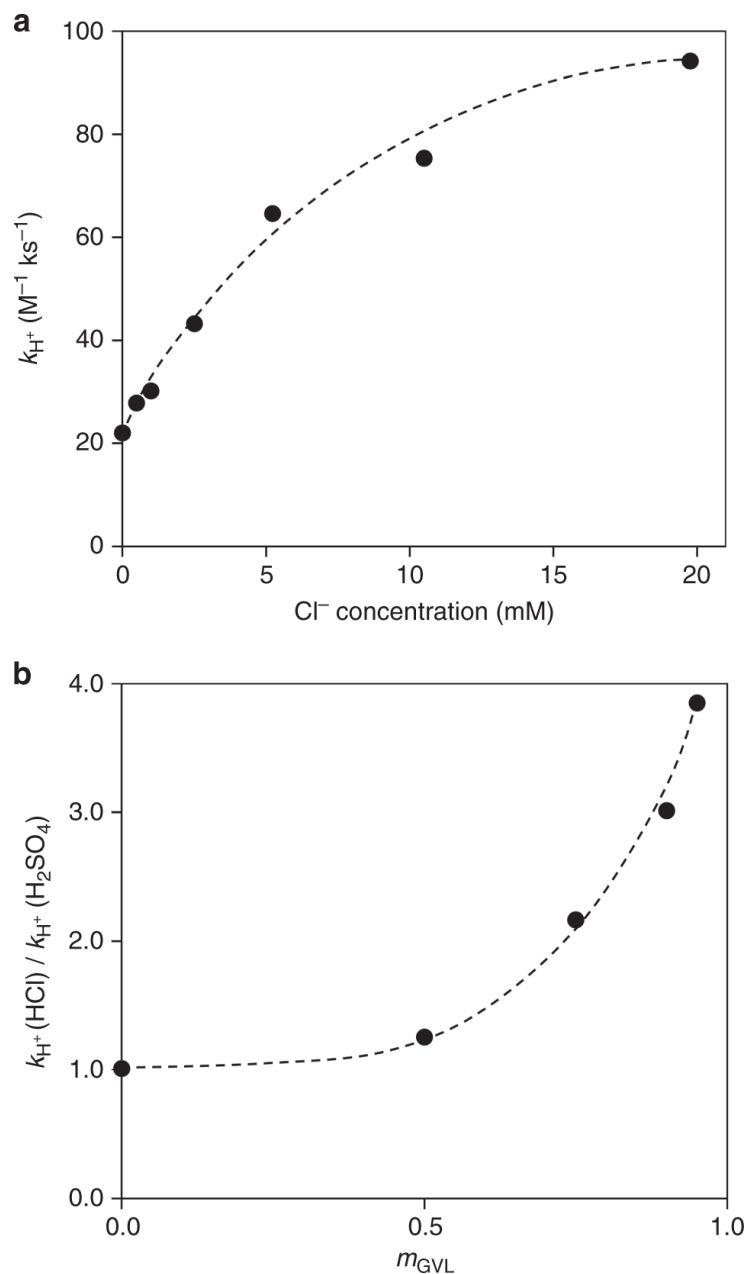
Figure 3.1 Fructose conversion rate constant versus Cl⁻ and GVL concentrations. a, Fructose conversion rate constant values in 90% GVL–water with varying Cl⁻ concentration using triflic acid (5 mM acid). **b,** ratio of fructose conversion rate constant values for fructose conversion into HMF for HCl and H_2SO_4 (equimolar catalyst concentrations) with varying GVL solvent concentration (mass fraction with water). Black dashed lines represent visual guides. Reaction conditions: fructose (50 mM); acid (Figure 3.1a: 5 mM; Figure 3.1b: 5 mM–0.5 M), 373 K; solvent (5 mL); stirring (700 rpm). Reaction rate constant values: $r = k_{H+} [R] [H^+]$

Based on the aforementioned reaction kinetics results, we suggest that the rate-determining transition state, $R^{\ddagger}$, interacts with a Cl^- ion:

$$Cl^- + R^{\ddagger} \overset{K_{Cl}}{\longleftrightarrow} RCl^{\ddagger} \tag{3.3}$$

where K_{Cl} is the equilibrium constant for the formation of a chloride transition state, $RCl^{\ddagger}$. The fraction of the transition state that is interacting with Cl^- is equal to $[RCl^{\ddagger}]/[R^{\ddagger}]_{total}$, given by

$$\frac{[RCl^{\ddagger}]}{[R^{\ddagger}]_{total}} = \frac{K_{Cl}[Cl^-]}{1 + K_{Cl}[Cl^-]} \tag{3.4}$$

where $[R^{\ddagger}]_{total}$ is the total concentration of the transition state. The rate that proceeds through transition state $R^{\ddagger}$ is defined as r_o, and the rate through the chloride transition state $RCl^{\ddagger}$ is equal to some faster value, r_{Cl}. The total rate is now

$$rate = r_o + r_{Cl}\left(\frac{K_{Cl}[Cl^-]}{1 + K_{Cl}[Cl^-]}\right) \tag{3.5}$$

Based on the results in Figure 3.1b, the value of K_{Cl} increases as we add GVL to the solvent, in the same way that the value of the proton rate constant increases, i.e., the presence of GVL enhances the free energy for interaction of Cl^- with the transition state.

We can define an enhancement factor, $r_{enhance}$, such that

$$r_{enhance} = \frac{r_{Cl}}{r_o} \tag{3.6}$$

The rate becomes

$$rate = r_{\mathrm{o}}\left[1 + r_{\mathrm{enhance}}\left(\frac{K_{\mathrm{Cl}}[\mathrm{Cl}^-]}{1 + K_{\mathrm{Cl}}[\mathrm{Cl}^-]}\right)\right] \qquad (3.7)$$

To probe the behavior predicted by equation (3.7), we collected reaction kinetics data for fructose conversion using H_2SO_4 and varying amounts of KCl for a variety of solvent mixtures consisting of GVL and water (i.e., 5% GVL, 25% GVL, 50% GVL, 75% GVL, and 90% GVL). Figure 3.2 displays rate constant values plotted against the chloride ion concentration for each solvent mixture. Equation (3.7) was used to model these reaction kinetics data in various GVL–water solvent systems, using r_{enhance} and K_{Cl} as parameters. This analysis shows that the value of r_{enhance} is a constant (equal to ~5) for all GVL concentrations, and the values of r_{o} and K_{Cl} depend on the solvent concentration. Figure 3.3 shows a plot of the value of the chloride ion-free fructose conversion rate constant values (i.e., $k_{\mathrm{H+}}$) versus the modeled equilibrium constants for the formation of the chloride transition state (i.e., K_{Cl}) for each GVLs–water solvent system. This plot shows that the enhancements of both the rate of acid-catalyzed conversion of fructose as well as the K_{Cl} have a linear dependence with increasing concentrations of GVL solvent.
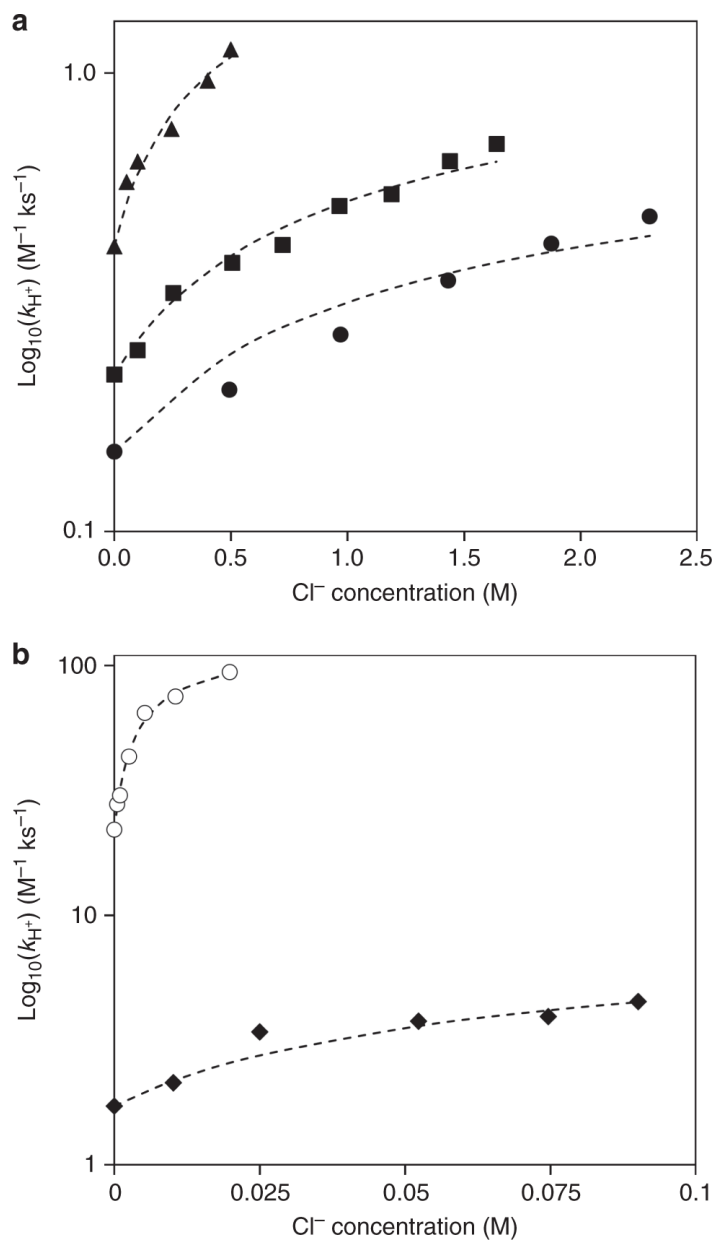
Figure 3.2 Fructose conversion rate constant versus Cl⁻ concentration in GVL–water mixtures. a, Overall, 5% GVL (black circles), 25% GVL (squares), and 50% GVL (triangles). **b,** In all, 75% GVL (diamonds) and 90% GVL (hollow circles). Black dashed lines represent the model fits using equation (3.7). Reaction conditions: fructose (50 mM); acid (H_2SO_4; 5 mM–0.5 M); salt (KCl; 5 mM–2.5 M), 373 K; solvent (5 mL); stirring (700 rpm). Reaction rate constant values: $r = k_{H+}$ [R] [H⁺]
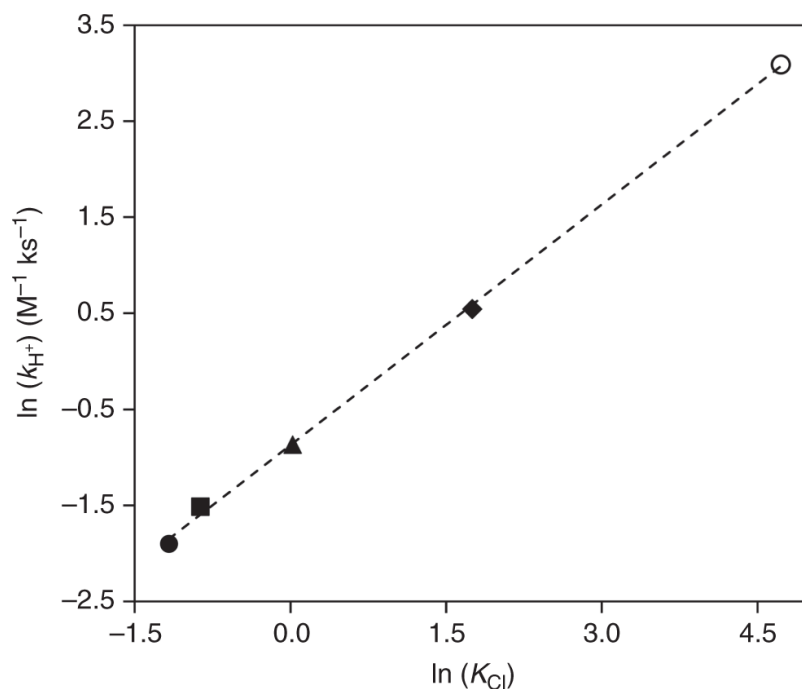
Figure 3.3 Fructose conversion rate constant versus K_{Cl} for Cl^- transition state formation. Data points represent the following GVL concentrations: 5% GVL (black circle), 25% GVL (square), 50% GVL (triangle), 75% GVL (diamond), and 90% GVL (hollow circle). The black dashed lines represent a linear trend line: $y = 0.84 \times -0.87$, $R^2 = 0.99$. Reaction rate constant values: $r = k_{H+}$ [R] [H$^+$]. K_{Cl} represents the equilibrium constant. Equilibrium constant values (i.e., K_{Cl}): model fits using equation (3.7) with data from Figure 3.2. Reaction conditions: fructose (50 mM); acid (H$_2$SO$_4$; 5 mM–0.5 M); salt (KCl; 5 mM–2.5 M), 373 K; solvent (5 mL); stirring (700 rpm)

3.2.2 Computational discussion

Previously, we suggested that increased reactivity in polar aprotic solvents, such as GVL, for acid-catalyzed reactions is due to destabilization of the acidic proton, where the protonated transition state is destabilized by a fraction of this amount in these polar aprotic solvents relative to water.[48] More recently, we quantified these solvation effects in terms of initial and transition state contributions[76,160] and developed a multi-descriptor correlation model that predicts rate constants as a function of solvent composition[58] for acid-catalyzed reactions. Based on the experimental results of the present study, we now probe whether the observed increases in acid-catalyzed dehydration rates with chloride salts in polar

aprotic solvents are due to the stabilization of the protonated transition state by chloride ions.

Ab initio density functional theory molecular dynamic simulations were used to explore the effects of GVL solvent, as well as the influence of the chloride ion and other anions on the different elementary steps for the acid-catalyzed dehydration of fructose. We calculated intrinsic activation energies and reaction energies as well as the overall activation free energy for fructose dehydration in presence of chloride, triflate, and bisulfate anions that result from the dissociation of hydrochloric acid, triflic acid, and sulfuric acid, respectively. For comparison purposes we also carried out simulations with and without the corresponding anions. The simulations of fructose dehydration with and without a chloride anion were performed in pure water, 75 wt% GVL–water mixtures, and 90 wt% GVL–water mixtures, while the simulations with triflate and bisulfate anions were performed in 90 wt% GVL–water mixtures.

The Brønsted-acid catalyzed conversion of fructose to HMF involves multiple dehydration steps. The initial dehydration of the hydroxyl group at the anomeric C2 carbon is considered to be the rate-determining step.[76,95,96] This step proceeds via the initial protonation and elimination of water from the C2 hydroxyl of fructose (Supplementary Figure 3.4a; Structures A–C). The resulting oxocarbenium intermediate, which is stabilized by the lone pair of electrons on the ring oxygen, is subsequently deprotonated by the basic oxygen of a water molecule in solution, resulting in the formation of the enol (Supplementary Figure 3.4a; Structures D–F). The initial proton transfer from solution to fructose, proton addition and the elimination of water at the C2 position of fructose, and

the deprotonation of the corresponding oxocarbenium ion are illustrated in the structures shown in Supplementary Figure 3.5.

For fructose dehydration in pure water without anion, the activation free energy and the reaction free energy for the initial protonation of the C2 hydroxyl of fructose and the simultaneous formation of the oxocarbenium ion (Supplementary Figure 3.6a–b) were calculated to be 65 kJ mol^{-1} and 57 kJ mol^{-1}, respectively. The activation free energy of the subsequent proton abstraction step from the oxocarbenium ion to form the enol intermediate (Supplementary Figure 3.6b–c) was found to be 35 kJ mol^{-1}. The overall apparent activation free energy is 92 kJ mol^{-1} for the first dehydration step. The subsequent transformation of the olefin intermediate into HMF is likely fast and therefore not considered.[95,96] We combined the free energy of reaction for the carbenium ion formation step with the activation free energy of proton abstraction step. The resulting value is reported as an overall apparent activation free energy of the reaction, summarized in Table 3.3.

Table 3.3 AIMD-calculated reaction free energies for fructose dehydration

Solvent System	Catalyst/ Anion	Oxocarbenium Ion Formation[a] $(kJ\ mol^{-1})$	Proton Abstraction[‡b] $(kJ\ mol^{-1})$	Total Free Energy of Activation[‡c] $(kJ\ mol^{-1})$
H_2O	H^+	57	35	92
H_2O	H^+/Cl^-	58	35	93
75% GVL	H^+	49	35	84
75% GVL	H^+/Cl^-	44	30	74
90% GVL	H^+	43	33	76
90% GVL	H^+/Cl^-	38[d]	29	67
90% GVL	H^+/TfO^-	43[e]	33[e]	76
90% GVL	H^+/HSO_4^-	45	33	78

[a] The values for oxocarbenium ion formation are the reaction free energies for the simultaneous protonation of the C2 hydroxyl of fructose and the elimination of water that forms. [b] The proton abstraction values refer to the activation free energies for water to deprotonate the oxocarbenium ion that forms. [c] The apparent activation barrier listed as the total activation free energy is the sum of the free energy of reaction to form the oxocarbenium ion and the activation free energy to deprotonate it. [d] The free energy of oxocarbenium ion formation in 90 wt% GVL–water mixtures with HCl required a correction calculated from the 75 wt% GVL–water system to ensure the complete dissociation of the H^+ and Cl^- in the initial reactant state as discussed in the Supplementary Information. [e] The triflate anion migrated away from fructose and local water molecules during the free energy sampling and partitioned between the water and GVL domains away from the active site. The numbers reported in this column were therefore taken from the 90 wt% GVL–water system without an anion.

In the 75 wt% GVL–water system without anion, the reaction free energy of the oxocarbenium ion formation of fructose and the activation free energy of subsequent proton abstraction were calculated to be $49\ kJ\ mol^{-1}$ and $35\ kJ\ mol^{-1}$, respectively. The total apparent activation free energy of $84\ kJ\ mol^{-1}$ is $8\ kJ\ mol^{-1}$ lower than the reaction in water without an anion. This computational result agrees with the higher experimentally measured fructose conversion reaction rates in GVL–water systems. This enhancement in reactivity in GVL is in part the result of the destabilization of reactant proton, since GVL

molecules disrupts the hydrogen bond network and lead to the formation of hydrophilic domains near the fructose that are surrounded by hydrophobic GVL domains.[76] The encapsulated hydrophilic domains localize the protons near the fructose, thus facilitates the proton transfer from bulk solvent to fructose. The results in 90 wt% GVL–water system (Supplementary Figure 3.9a–c) are consistent with the experimental fructose dehydration reactivity trend. In this case, the overall activation free energy of fructose dehydration was calculated to be 76 kJ mol^{-1}, which was 8 kJ mol^{-1} and 16 kJ mol^{-1} lower than the activation energies in 75 wt% GVL–water systems and pure water systems, respectively.

The force-field molecular dynamics simulations were performed prior to the *ab initio* molecular dynamics simulations to examine the solvation structure of the chloride anion in the water system. The results show extensive solvation of the anion in the hydrogen bond network between water molecules (Supplementary Figure 3.8). The solvation structure inhibits any significant interactions between the chloride anion and the reactive site on fructose (Supplementary Figure 3.6d–f). The reaction free energy of oxocarbenium ion formation of fructose in water with a chloride anion was calculated to be 58 kJ mol-1, which is similar to the 57 kJ mol^{-1} with no chloride anion. The activation free energy for the subsequent proton abstraction step from the oxocarbenium ion to form the enol intermediate (Figure 3.4c) was calculated to be 35 kJ mol^{-1}. Thus, the apparent barrier which involves the free energy to form the oxocarbenium ion and the intrinsic activation free energy to subsequently deprotonate the ion is calculated to be 93 kJ mol^{-1}. This behavior is consistent with the experimental results, which shows that chloride ions and other anions have little effect on the rates or the yields for fructose dehydration reactions carried out in water at low ion concentrations. At higher concentrations of salt,

such as those reported in previous studies,[78–81] chloride ions reside near the alcohol, promoting the acid-catalyzed dehydration.
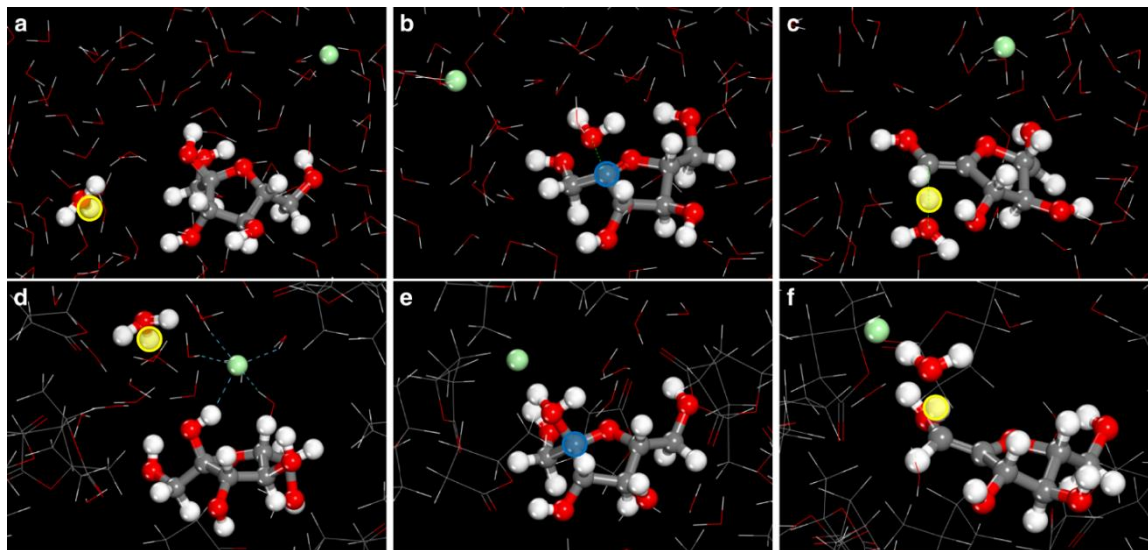
Figure 3.4 Fructose dehydration reaction structures. Structures along the reaction path for fructose dehydration carried out in water and HCl mixtures (**a**–**c**) and in 90% GVL and HCl mixtures (**d**–**f**). The structure in the first (**a**, **d**), second (**b**, **e**), and third (**c**, **f**) columns refers to fructose along with H^+ and Cl^- in their reactant state in solution, the resulting oxocarbenium ion from the initial protonation of the C2 hydroxyl group and the elimination of water, and the transition state for the deprotonation of the oxocarbenium ion to form the enol product, respectively. Red, gray, green, and white spheres refer to the oxygen, carbon, chlorine, and hydrogen atoms, respectively. The yellow and blue highlighted circles refer to the reactive proton and oxocarbenium ion centers, respectively (additional structures along the path are presented in Supplementary Figure 3.6 and Supplementary Figure 3.9)

The effect of the chloride anion on the reaction energetics could be studied if the anion is arranged near the fructose hydroxyl group at the beginning of the *ab initio* simulations (Supplementary Figure 3.6g–i and Supplementary Figure 3.7b). Relatively short *ab initio* molecular dynamics simulations (20 ps in total) allow the chloride anion to stay near fructose, whereas a longer simulation time will eventually result in the migration of chloride anion into bulk water. At short simulation times, the reaction free energy of carbenium ion formation was calculated to be 50 kJ mol^{-1}, which is 7 kJ mol^{-1} lower than the system without anion. This result suggests the direct interaction between anion and the

90

reactive species plays a major role in the experimentally observed reaction rate enhancement in presence of anions. The chloride anion, initially located at the fructose hydroxyl group, becomes fully solvated in bulk water solvent at the end of carbenium formation step (Supplementary Figure 3.6e). Therefore, the chloride anion does not participate in the subsequent proton abstraction step. This behavior is supported by the calculated 35 kJ mol^{-1} activation free energy of the proton abstraction in the system which has chloride ion initially located on the fructose in the reactant state. The overall apparent activation energy of this artificial system then becomes 85 kJ mol^{-1}.

The simulation results show that increasing GVL concentration localizes the Cl$^-$ anion within the hydrophilic domain near fructose (Supplementary Figure 3.10 and Supplementary Figure 3.11). For 75 wt% and 90 wt% GVL solvent mixtures with water, the chloride ion preferentially resides in the local hydrophilic water domain near the C2 hydroxyl of fructose. The calculated reaction free energy of carbenium ion formation and the activation free energy of subsequent proton abstraction in 75% GVL–water system were 44 kJ mol^{-1} and 30 kJ mol^{-1}, respectively. The resulting overall activation free energy of 74 kJ mol^{-1} is 10 kJ mol^{-1} lower than the 75% GVL–water system without chloride anion. The transition state complex formed during the proton abstraction step in 75% GVL–water featured a chloride ion near the reactive complex (Supplementary Figure 3.10c), contrary to the transition state in the water system (Supplementary Figure 3.6h). This chloride interaction is made possible by the diminishing available phase space, which is largely taken up by GVL molecules. This behavior allows the negatively charged chloride anion to be located near the transition state structure and contributes to the stabilization of the positively charged transition state (Figure 3.4f).

The simulations in 90 wt% GVL–water (Supplementary Figure 3.9d–f) resulted in 55 kJ mol^{-1} and 29 kJ mol^{-1} for the free energy of carbenium ion formation and the activation free energy of proton abstraction, respectively. The overall activation free energy of 84 kJ mol^{-1} for fructose dehydration contradicts the experimental results that the addition of chloride anion positively affects the overall fructose conversion rate. Detailed inspection revealed that the hydrochloric acid did not fully dissociate in the simulations (Supplementary Figure 3.12a). The use of a small box size in the simulations led to a high acid concentration (~ 0.5 M) with few water molecules present, while a much lower acid concentration (e.g., 5 mM) was used in the fructose dehydration experiments. Therefore, the higher overall activation free energy is a result of computational artifact that requires a correction. The correction for the results in 90 wt% GVL–water was taken from the results in 75 wt% GVL–water system, where the chloride anion lowers the reaction free energy of carbenium ion formation from 49 kJ mol^{-1} to 44 kJ mol^{-1}. The correction factor of 5 kJ mol^{-1} is then subtracted from the 43 kJ mol^{-1} reaction free energy of carbenium ion formation in 90% GVL–water without an anion. This correction leads to values of 38 kJ mol^{-1} and 29 kJ mol^{-1} for the free energy of carbenium ion formation and the activation free energy of proton abstraction, respectively. The overall activation free energy of fructose conversion in 90% GVL–water becomes 67 kJ mol^{-1}, which is 9 kJ mol^{-1} lower than the reaction in 90% GVL–water without anion. This result is in agreement with the experimentally observed higher fructose conversion rates with the addition of chloride anion in 90% GVL–water and indicates the enhanced dehydration reactivity is due to the anion-stabilized positively charged transition state structure (Figure 3.5).
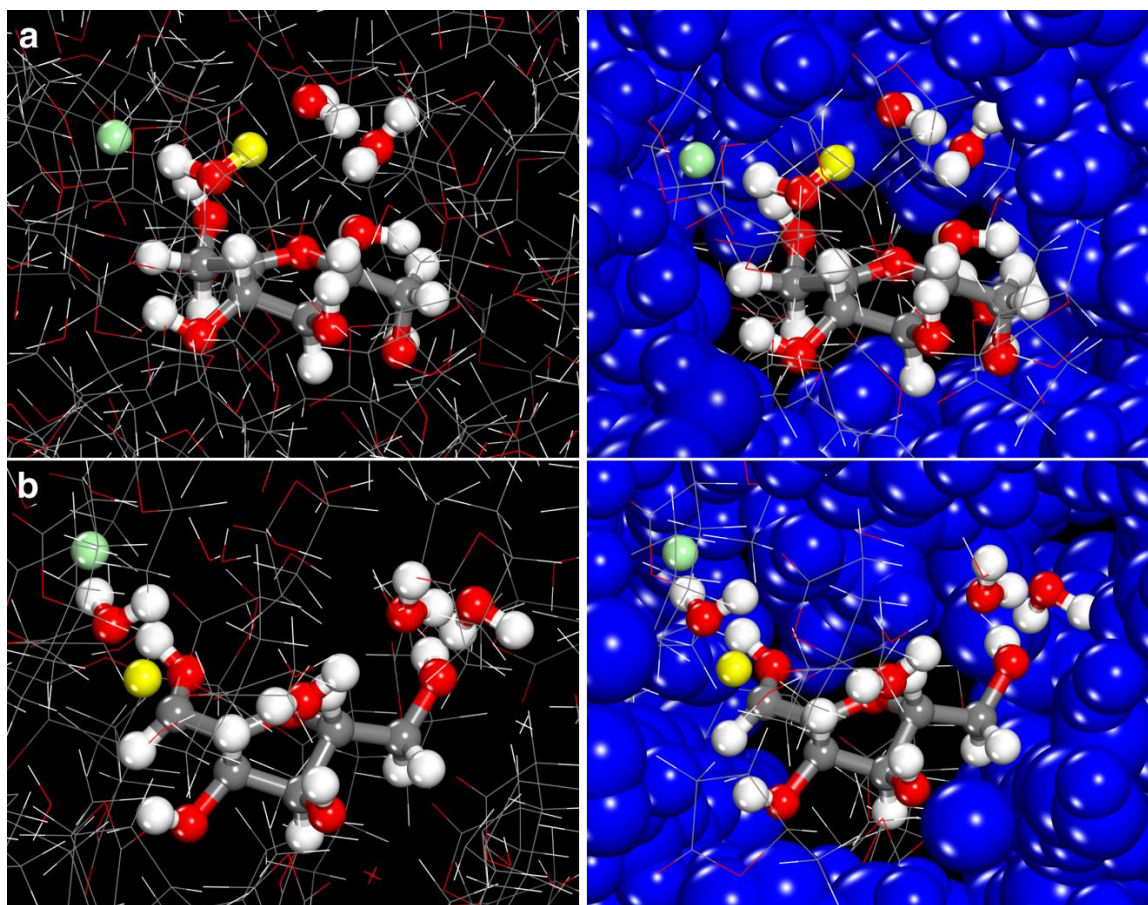
Figure 3.5 Structures representing solvation by Cl⁻ of transition states in 90% GVL. a, The protonation of the C2 hydroxyl and the elimination of water to form the oxocarbenium ion. **b,** the deprotonation of the oxocarbenium ion to form the enol. The Cl⁻ (green sphere) in both transition state structures directly interacts with the active protons (yellow sphere) and resides in the hydrophilic shell that surrounds fructose. The active hydrophilic cavity which is shown via the ball-and-stick structures is encapsulated by the hydrophobic shell comprising GVL. The structures on the left-hand side show the hydrophobic outer shell via simple stick figures, whereas those on the right-hand side depict the atoms in the hydrophobic shell as CPK structures to better highlight the inner hydrophilic cavity and the outer hydrophobic shell. The high concentration of GVL localizes the H^+ and Cl^- ions at the active site, enabling Cl^- to promote the reaction. The structures of transition states for fructose dehydration carried out in 90 wt% GVL–water mixtures.

Simulations carried out in the 90 wt% GVL–water system using triflic acid and sulfuric acid (Supplementary Figure 3.9) for fructose dehydration gave apparent activation energies of $76\,\text{kJ}\,\text{mol}^{-1}$ and $78\,\text{kJ}\,\text{mol}^{-1}$, respectively, showing minimal change from the barrier of $74\,\text{kJ}\,\text{mol}^{-1}$ in the absence of the Cl^- anion in 90% GVL–water. Both triflic acid

($pK_a = -15$)[161] and sulfuric acid ($pK_a = -10$; Supplementary Table 3.4)[162,163] are more acidic than HCl ($pK_a = -6$; Supplementary Table 3.4).[161] Relative to the Cl^- anion, the triflate ($CF_3SO_3^-$) and bisulfate (HSO_4^-) anions delocalize the negative charge over their corresponding structures and are therefore more stable (i.e., weaker conjugate bases), leading to weaker interactions with the charged oxocarbenium-ion intermediate and the transition state for deprotonation of fructose dehydration. In simulations with triflic acid in 90% GVL–water, the $CF_3SO_3^-$ anion migrates away from fructose and resides instead at the interface of the water–GVL domains, where the CF_3 group interacts with the hydrophobic GVL domain and the SO_3^- group resides in the hydrophilic water domain (Supplementary Figure 3.13). This behavior inhibits the interaction of the $CF_3SO_3^-$ anion with the oxocarbenium-ion intermediate or the charged transition state, and therefore offers little stabilization. The changes in the calculated activation free energies found in changing the acid or the solvents used in carrying out the dehydration agree with those trends determined by the changes in the experimental rate constants, as is shown in Supplementary Figure 3.14. While chloride ions increase the rate of conversion of fructose into HMF, they also increase the overall reaction selectivity and yield of HMF as they do not promote the subsequent C–C bond activation that controls the conversion of HMF into levulinic acid.[76] Full simulation details can be found in the Supplementary Methods, Supplementary Discussion, and Supplementary Figures 3.4–3.20.

The effects of chloride ions in polar aprotic solvents for fructose dehydration to HMF can also be achieved using heterogeneous Brønsted acids as catalysts (Supplementary Table 3.5). Rate constant values for fructose conversion in the presence of chloride ions were measured by adding benzyltriethylammonium chloride (BTEAC) to propylsulfonic

acid-functionalized silica (PSA/SiO$_2$) and Amberlyst 70 catalysts in 90% GVL–water. The benzyltriethylammonium cation was used to provide sufficient steric hindrance to prevent cation exchange with the acidic protons of the solid catalysts. The addition of chloride ions led to only slight improvements in fructose conversion rate constant values for these heterogeneous catalysts. However, increased HMF yields (80%) from fructose were obtained with the addition of BTEAC for both PSA/SiO$_2$ and Amberlyst 70, an increase of ~10% HMF yield compared with the chloride ion-free GVL.

3.4 Conclusions

We have studied the effects of salts in polar aprotic solvents, such as GVL, on acid-catalyzed biomass dehydration reactions. Significant increases in reactivity (e.g., 10-fold) and product selectivities (> 80% yields) were observed for the acid-catalyzed dehydration of fructose to HMF with the addition of catalytic concentrations (e.g., 5 mM) of chloride salts in polar aprotic solvents. Based on reaction kinetics results and *ab initio* molecular dynamics simulations for a variety of strong homogenous acid catalysts and salts in polar aprotic solvent mixtures with water, we show that chloride ions aid in the stabilization of protonated transition states for these acid-catalyzed reactions.

3.5 Methods

3.5.1 Reaction kinetics experiments

Chemicals were obtained from Sigma-Aldrich, including reactants (fructose, glucose, and xylose) and products (HMF, furfural, and levulinic acid), inorganic salts (KCl, NaCl, LiCl, CaCl$_2$, KBr, NaBr, LiBr, KI, KF, K-triflate), solvents (dioxane, THF, GVL, D$_2$O, and 1,4-dioxane-d$_8$), and acid catalysts (H$_2$SO$_4$, triflic acid, HCl, HBr, HI) were used

as acquired. Purified water was used and obtained through an in-house Milli-Q water purification system. Amberlyst 70 (The Dow Chemical Company; acid site density = 2.55 mmol g^{-1}) was washed, dried, and crushed before use. Si-propylsulfonic acid was obtained from SiliCycle (SiliaBond Propylsulfonic Acid SCX-2; acid site density = 0.63 mmol g^{-1}) and was used as acquired.

Reaction kinetics measurements were carried out in closed thick-walled glass batch reactors (10 mL) for fructose, xylose, and glucose dehydration in dioxane, THF, GVL, H$_2$O, D$_2$O, 1,4-dioxane-d$_8$ and mixtures thereof. Reaction kinetics data for fructose dehydration in pure organic solvents without water could not be obtained due to low fructose solubility. In a typical experiment, 5 mL solutions of 50 mM reactant (e.g., fructose), 5 mM acid (e.g., HCl), and 5 mM salt (e.g., KCl) in an organic solvent mixed with water (e.g., 25 wt% GVL with 75 wt% H$_2$O) were added into closed batch reactors. The reactors were placed in an oil bath and stirred at 700 rpm with magnetic stir bars at reaction temperature. The reactors were removed at specific reaction times, and the reactions were stopped by cooling the reactors in an ice bath at 273 K.

After each reaction, the content of the reactor was filtered using a 0.2 μm membrane (VWR International; PTFE). Sample analyses were performed using a high-performance liquid chromatograph (Waters Alliance 2695) instrument equipped with a differential refractometer (Waters 410) and a photodiode array detector (Waters 996). Concentrations of fructose (RID), HMF (UV; 320 nm), levulinic acid (RID) in liquid solution were monitored using an ion-exclusion column (Bio-Rad; Aminex HPX-87H; 7.8 × 300 mm, 5

μm). A mobile phase of 5 mM sulfuric acid aqueous solution at a flow rate of 0.6 mL min$^-$^{1} was used.

Reaction kinetics profiles for the reactant conversion were constructed from the aforementioned reaction kinetics data. As an example, a table showing a subset of reactions performed including experimental conditions for the Brønsted acid-catalyzed fructose dehydration is presented in Supplementary Table 3.6. Each reaction time represents an individual experiment, and these values were combined to produce reaction kinetics profiles. Values of rate constants (k_{H+}; equation (3.2)), reaction energetics values (A and E_a), and equilibrium constants (K_{Cl}) were derived from the reaction kinetics profiles for reactant consumption using nonlinear least squares regression in MATLAB (nlinfit function; Levenberg-Marquardt nonlinear least squares algorithm). Confidence intervals were calculated at the 95% confidence level (nlparci function). Fructose dehydration has been shown in previous studies to be first order with respect to both reactant and proton concentration,[95] and small quantities of levulinic acid and formic acid products were also detected in these reactions.

3.5.2 NMR spectroscopy

For detection and analysis of chloride-containing species, ^{13}C NMR experiments were performed using a Bruker spectrometer equipped with a 14.1 T superconducting magnet and acquired and processed using TOPSPIN. The samples were prepared in a glovebox and kept on ice until analysis. NMR tubes with sealed screw caps purchased from Wilmad Glass were used for all spectra. ^1H spectra were acquired using a recycle delay of 3.0 s with 30° ^1H excitation pulse lengths. ^{13}C spectra were acquired by using a recycle

delay of 5.0 s with 30° ^{13}C excitation pulse lengths using a carrier frequency offset of 100 ppm.

Quantitative solution-phase ^{1}H NMR experiments of GVL and 4-HVA (Supplementary Figure 3.2) were performed on a Bruker AV 500-MHz spectrometer equipped with an N$_2$-cooled cryogenic probe. To avoid any confounding effects on the equilibrium conversion of GVL into 4-HVA, samples did not contain deuterated solvents or internal standards. Spectra were collected with the deuterium lock channel off, and shimming was performed manually on the residual water resonance at ~3.5 ppm. Quantitative ^{1}H spectra were collected using a standard 45° pulse sequence with a pulse delay of 10 s, an acquisition time of 2 s, and eight scans per spectrum. The relative values of the peak integrals at ~0.5 and ~0.7ppm, corresponding to 4-HVA and GVL, respectively, were used to assess the mole fraction of 4-HVA in solution as a function of temperature and reaction time. Samples generated under reaction conditions were stored at 277 K overnight. For the variable-temperature experiments, samples were allowed to equilibrate for 30 min after the sample and probe reached the desired temperature.

3.5.3 Solution calorimetry

Solution calorimetry experiments were performed on a semi-adiabatic solution calorimeter (TAMIII Precision Solution Calorimeter, TA Instruments) with the bath temperature controlled to ± 0.0001 K. A glass ampoule was loaded with fructose through a small opening in the ampoule. The opening was closed with a rubber stopper and sealed with wax. The ampoule was immersed in a 25 mL vessel containing solvent and inserted into the calorimeter. The contents of the vessel were stirred at 600 rpm to ensure proper

dissolution of fructose and proper heat transfer. Dissolution of the fructose was initiated by breaking the top and bottom of the ampoule on a spike within the vessel, exposing the contents of the ampoule to the solvent. The change in temperature was measured with SolCal v1.2 software. Internal calibrations were performed before and after the dissolution process by charging 3 J of heat into the vessel and measuring the change in temperature. The heat of the dissolution process was determined using the two calibrations. To account for the heat associated with solvent–ampoule interactions, the heat associated with breaking an empty ampoule in the solvent was subtracted from the observed heat. The adjusted heat was then normalized by the number of moles of fructose.

3.5.4 Computational simulations

For computational simulations, the liquid-phase systems with fructose were initially prepared by placing fructose, solvent molecules, one proton, and one anion in a 15 $\times$ 15 $\times$ 15 Å^3 periodic box using Packmol tool.[164] The molecular configurations for fructose dehydration in different solvent systems were equilibrated using classical molecular dynamics as implemented in GROMACS software package.[125] The subsequent equilibration and *ab initio* density functional theory (DFT)-based molecular dynamics simulations of these systems were carried out using CP2K program.[126]

The water system consisted of 100 H_2O molecules, one hydronium ion, and one fructose molecule. The water system with free chloride also included one chloride anion in solution. In the system where the chloride anion was artificially placed near fructose, the chloride ion was bound to the C2 hydroxyl group of fructose, resulting in a single fructose–Cl$^-$ entity. An unconstrained molecular dynamics simulation was carried out to establish

the radial distribution function and determine the distance between the anion and hydrogen on the fructose hydroxyl group (2.1 Å). The 75 wt% GVL–water system consisted of 13 GVL molecules, 23 H_2O molecules, one hydronium ion, and one fructose molecule. The 75 wt% GVL–water system with chloride anion consisted of 13 GVL molecules, 23 H_2O molecules, one hydronium ion, and one fructose–Cl^- structure. The 90 wt% GVL–water system consisted of 15 GVL molecules, 10 H_2O molecules, one hydronium ion, and one fructose molecule. The 90 wt% GVL–water system with a chloride anion, bisulfate anion, or triflate anion each consisted of 15 GVL molecules, 10 H_2O molecules, one hydronium ion, and one fructose–anion structure. The distances from the bisulfate sulfur atom and triflate sulfur atom to the hydrogen atom on the C2 fructose hydroxyl group were set to 3.0 Å and 2.9 Å, respectively.

The prepared periodic molecular systems were equilibrated in GROMACS for 1 ns using constant number of particles, constant volume, and constant temperature (NVT) ensembles followed by 10 ns of equilibration using constant number of particles, constant pressure, and constant temperature (NPT) ensembles. The temperature was kept near 373 K using the Leap-frog stochastic dynamics integrator[127] with a 2 ps temperature coupling time constant. The pressure of the system was controlled by the Parrinello–Rahman barostat[128,129] with a 2 ps coupling time constant. The molecular interactions of fructose and GVL molecules were adapted from the all-atom version of Optimized Potentials for Liquid Simulations[130,131] (OPLS–AA) force field. Force fields for the hydronium ion,[165] chloride anion,[166] bisulfate anion,[167] and triflate anion[140] were adopted from the literature. The interactions of water molecules were taken from an Extended Simple Point Charge (SPC/E) water model.[132] The SETTLE algorithm[133] was used to constrain the bond angle

and bond distance in water molecules. The cut-off value for intermolecular interactions was set at 7 Å. The Particle Mesh Ewald (PME) scheme was used to account for the long-range electrostatic interactions.

The final atomic coordinates and the average lattice sizes were taken as the initial configurations for the periodic *ab initio* molecular dynamics simulations (AIMD). All systems were further equilibrated for 5 ps using AIMD without any constraints. The exchange and correlation energies were calculated within the generalized gradient approximation using Perdew–Burke–Ernzerhof (PBE) functional.[134] Goedecker–Teter–Hutter pseudopotentials[136] were used to represent the electronic density with a plane wave cut-off of 280 Ry. A short-ranged version of Gaussian-type double-ζ basis set[135] was used to expand the Kohn-Sham orbitals. DFT–D3(BJ) dispersion corrections[137] were applied to correct for the medium and long range van der Waals interactions. The neutralizing background charge was assumed by CP2K. The temperature of the systems was kept at 373 K using canonical sampling through a velocity rescaling (CSVR) thermostat.[138] A time step of 0.5 fs was used, and all the hydrogen mass was replaced with deuterium to attenuate the fast vibration associated with light hydrogen atoms.

Ab initio molecular dynamics were performed using an umbrella sampling technique to calculate the reaction free energy and activation free energy. The umbrella samplings were carried out under the same conditions as the unbiased AIMD runs. A minimum of 16 sampling windows evenly distributed over the reaction coordinate were used to ensure a reasonable overlapping of sampled configurations between adjacent windows. For each sampling window, the condensed systems were further equilibrated for

5 picoseconds followed by 15 picoseconds of data collection. The shapes of free energy profiles were obtained using Weight Histogram Analysis Method[139] (WHAM). All the free energy profiles are presented in Figures 3.15–3.17.

The free energy calculations of fructose dehydration were performed on the carbenium ion formation step (Supplementary Figure 3.4a; Structures A–C) and proton abstraction step (Supplementary Figure 3.4a; Structures D–F). The reaction coordinates used were defined based on coordination numbers:

$$CN_{ij} = \frac{1 - (d_{ij}/c)^9}{1 - (d_{ij}/c)^{14}} \tag{3.8}$$

where CN_{ij} is the coordination number of atom i with respect to atom j, d_{ij} is the distance between atom i and j in angstroms, and c is the parameter that controls the shape of equation (3.8). The c parameter was set to 1.3 for coordination numbers involving the C–H as well as O–H bonds and 1.6 for the longer C–O bond.

The reaction coordinate for the carbenium ion formation step (Supplementary Figure 3.4b) was defined as:

$$\text{reaction coordinate} = CN_{O-2H} - CN_{C-\text{all O}} \tag{3.9}$$

where CN_{O-2H} is a sum of the coordination numbers of fructose hydroxyl oxygen with respect to hydroxyl hydrogen and a closest water hydrogen. The $CN_{C-\text{allO}}$ is a sum of the coordination numbers of fructose C2 carbon with respect to all oxygen atoms and other anions in the solvent, including the oxygens on the triflate and bisulfate anions and the

chloride anion. This reaction coordinate describes a simultaneous protonation of the C2–OH group along with C–O bond cleavage. The sampling on this coordinate ranged from −0.1 to 1.8 with a spring constant for bias harmonic potential of 0.3 Hartree. The bias potential, V, takes the harmonic form of:

$$V = K * (CV - CV_{t\arg et})^2 \qquad (3.10)$$

where K is the harmonic spring constant, CV is the instantaneous reaction coordinate described in equation (3.9), and CV_{target} is the center of bias harmonic potential.

The reaction coordinate for the proton abstraction step (Supplementary Figure 3.4c) is defined as follows:

$$\text{reaction coordinate} = CN_{H-O} - CN_{C-H} \qquad (3.11)$$

where CN_{C-H} is the coordination number of C1 fructose carbon to the cleaving proton, and CN_{H-O} is the coordination number of the cleaving proton with respect to an oxygen atom of a water molecule. The water molecule associated with the CN_{H-O} term is selected using the following function:

$$d_{H-O} = \frac{\sum\limits_{i \in O_{all}} d_{H-i} \exp(200 * CN_{H-i})}{\sum\limits_{i \in O_{all}} \exp(200 * CN_{H-i})} \qquad (3.12)$$

where d_{H-O} is the distance from the cleaving proton to the oxygen of the closest water molecule.

The O_{all} is a set of all solvent oxygen and chloride atoms including the oxygens on triflate and bisulfate anions as well as the Cl of the chloride anion. The parameter c used in CN calculations was set to 1.8 for the equation (3.12). Each term in the numerator of equation (3.12) is relatively small except the term for the closest water molecule. When the denominator is applied, the term with the largest d_{H-i} remains relevant while the other terms with smaller d_{H-i} become negligible. equation (3.12) results in the distance between the cleaving proton to the closest oxygen atom of a water molecule, including oxygens on anions and the chloride anion. This distance, $d_{H-O\ water}$, is used in the calculation of $CN_{H-O\ water}$ in equation (3.11). Overall, the second reaction coordinate describes a proton transfer from the fructose oxocarbenium ion to the closest water molecule that acts as a base, thus, involving both O–H bond breaking and O–H bond formation. The sampling along this coordinate ranged from −0.85 to 0.95 with a spring constant for bias harmonic potential of 0.45 Hartree. The reaction coordinates for the proton abstraction (equations (3.11)–(3.12)) were also used in conjunction with a potential wall on the reaction coordinates for carbenium ion formation (second term of equation (3.9)) to deter the carbenium ion from turning back to initial state. The position of the potential wall was determined from the fluctuation of the reaction coordinate equation (3.9) in the window corresponding to the carbenium ion, where the wall was set at the maximum reaction coordinate observed in the simulation.

3.6 Supplementary Information

Calculation of acidities

The dissociation of Brønsted acid in aqueous solution can be described using Born-Haber cycle as follows:

$$H\text{-}B_{(g)} \xrightarrow{\Delta G_{(g)}} H^+_{(g)} + B^-_{(g)}$$

with vertical processes $\Delta G_{(sol,\ H\text{-}B)}$, $\Delta G_{(sol,\ H^+)}$, $\Delta G_{(sol,\ B^-)}$

$$H\text{-}B_{(aq)} \xrightarrow{\Delta G_{(aq)}} H^+_{(aq)} + B^-_{(aq)}$$
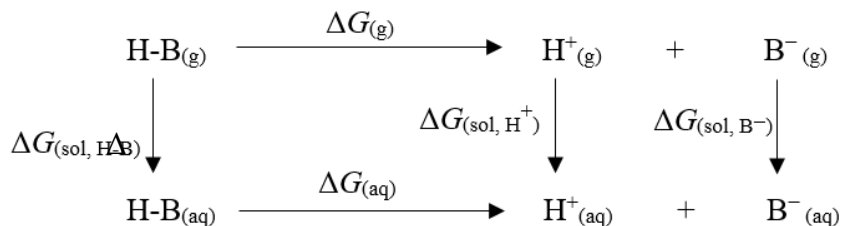
where B is the conjugate base of the H–B acid and $\Delta G_{(g)}$ and $\Delta G_{(aq)}$ are acid dissociation free energies in gas and aqueous phase, respectively. The $\Delta G_{(sol)}$ terms represent the solvation free energies. The comparison of acidity was carried out using pK_a values calculated by:

$$pK_a = -\frac{\Delta G_{(aq)}}{RT \ln(10)} \tag{3.13}$$

where $\Delta G_{(aq)}$ is the free energy for dissociation of the acid in the aqueous phase.

The value of $\Delta G_{(aq)}$ for each acid was calculated from the following equation:

$$\Delta G_{(aq)} = -\Delta G_{(sol,\ H-B)} + \Delta G_{(g)} + \Delta G_{(sol,\ H^+)} + \Delta G_{(sol,\ B^-)} - 7.93 \text{ [kJ mol}^{-1}] \tag{3.14}$$

where $\Delta G_{(sol,\ H\text{-}B)}$ is determined from DFT simulations as the difference in the free energy of the acid in the solution compared to the free energy of the acid in the gas phase, whereas the values for $\Delta G_{(g)}$, $\Delta G_{(sol,\ H^+)}$, and $\Delta G_{(sol,\ B^-)}$ were taken from the literature values[26-28], as shown in Supplementary Table 3.4. The final term, 7.93 kJ mol^{-1}, is associated with the

change in standard concentration from 1 atm in gas phase to 1 mol L^{-1} in aqueous phase. DFT calculations were carried out using Gaussian 09 software using M06–2X[29] DFT hybrid functional and 6–311+g(d,p) basis set. The solvation free energies were obtained using SMD[30] implicit solvation model.

The relationship between the proton activity coefficient and the reactivity can be established by writing the rate in terms of the activities which are equal to the activity coefficients multiplied by the concentrations of the reactants.

$$r = k_{H^+} \gamma_{H^+} \gamma_R [H^+][R] \tag{3.15}$$

where r is an experimentally measured rate, kH+ is a rate constant for specific-acid catalyzed and γH+ and γR are the activity coefficient of proton and fructose, respectively. Transition state theory can then be used to express the rate constants in term of activation free energy:

$$r = \kappa \frac{k_B T}{h} e^{\frac{-\Delta G^{\ddagger}}{RT}} \gamma_{H^+} \gamma_R [H^+][R] \tag{3.16}$$

where κ is a transmission coefficient, k_B is Boltzmann constant, T is temperature, and h is Planck constant. We can see that the activity coefficients γ_{H+} and γ_R can be combined with the activation free energy term:

$$r = \kappa \frac{k_B T}{h} e^{\frac{\ln(\gamma_{H^+})RT + \ln(\gamma_R)RT - \Delta G^{\ddagger}}{RT}} [H^+][R] \tag{3.17}$$

to express rate in terms of an apparent free energy barrier:

106

$$r = \kappa \frac{k_B T}{h} e^{\frac{\Delta G_{calculated}^{\ddagger}}{RT}} [H^+][R] \tag{3.18}$$

As such, the experimental as well as the calculated activation free energies reported in the manuscript due include these changes in proton activity. The simulations model the proton and transition state interactions with the explicit solvent molecules in the local environment and as such directly calculate the explicit changes in proton activities.

Supplementary Table 3.1 Sugar conversion reaction rate constant values and yield values in 90% GVL/10% H_2O using homogeneous acid catalysts.[a]

Sugar	Acid	Rate Constant $(M^{-1} ks^{-1})$[b]	HMF or Furfural Yield (%)[c]
Glucose	H_2SO_4	23	20
Glucose	HCl	41	45
Xylose	H_2SO_4	25	60
Xylose	HCl	95	74

[a] Reaction conditions: sugar (25 mM for glucose; 50 mM for xylose); acid (10 mM); solvent (90% GVL/10% H_2O; 5 mL); 433 K; stirring (700 rpm). [b] $r = k$ [R] [HB]. [c] HMF (for glucose dehydration) and furfural (for xylose dehydration) yield values at approximately 90% conversion.

Supplementary Table 3.2 Solvent kinetic isotope effect for fructose dehydration to HMF.[a]

Solvents	Acid / Salt	k_D/k_H[b]
D_2O/H_2O	H_2SO_4	1.9
D_2O/H_2O	HCl	2.4
10%D_2O/10%H_2O in 90% GVL	H_2SO_4	1.7
10%D_2O/10%H_2O in 90% GVL	HCl	2.7
10%D_2O/10%H_2O in 90% GVL	H_2SO_4 / KCl	2.4

[a] Reaction conditions: fructose (50 mM); acid (0.5 M for H_2O/D_2O; 5 mM for GVL with H_2O/D_2O); salt (5 mM); 373 K; solvent (5 mL); stirring (700 rpm). [b] $r = k_H$ [R] [HB] using H_2O; $r = k_D$ [R] [HB] using D_2O.

Supplementary Table 3.3 Enthalpy changes for dissolution of fructose in solvent mixtures containing combinations of potassium salts and triflic acid.[a]

Solvent	Acid	Salt	ΔH_{sol} (kJ mol^{-1})	95% C.I. (kJ mol^{-1})
H_2O	–	–	8.9	[8.5, 9.3]
90% GVL/10% H_2O	–	–	14.1	[13.5, 14.7]
90% GVL/10% H_2O	–	KCl	11.8	[11.2, 12.4]
90% GVL/10% H_2O	–	KBr	14.2	[12.8, 15.6]
90% GVL/10% H_2O	Triflic	–	14.8	[13.9, 15.5]
90% GVL/10% H_2O	Triflic	KCl	14.4	[13.6, 15.2]

[a] Solution calorimetry conditions: fructose (2 mM); acid (5 mM); salt (5 mM); solvent (25 mL); temperature (298 K).

Supplementary Table 3.4 DFT-calculated pK_a values for HCl and H$_2$SO$_4$. All free energies are reported in kJ mol^{-1}.

Acid	$\Delta G_{(g)}$ (kJ mol^{-1})	$\Delta G_{(sol, H^+)} + \Delta G_{(sol, B^-)}$ (kJ mol^{-1})	$\Delta G_{(sol, H-B)}$ (kJ mol^{-1})	$\Delta G_{(aq)}$ (kJ mol^{-1})	Calculated pK_a	Literature pK_a
HCl	1373 [26]	−1408 [28]	−8.4	−34.6	−6.1	−6.1 [31,32]
H$_2$SO$_4$	1265 [27]	−1394 [28]	−69.7	−67.3	−11.8	−10 [a,33,34]

[a] There are two rather different pK_a values for H$_2$SO$_4$ in water reported in the literature: (1) the value of −10 reported in References [33,34], which is in good agreement with our calculated value of −11.8 and (2) the value of −2 reported in Reference 35, which is not referenced to any publication.

Supplementary Table 3.5 Fructose conversion reaction rate constant values and HMF yields for fructose dehydration to HMF in 90% GVL using heterogeneous acid/salt systems.[a]

Acid Catalyst	Solvent/Salt	Rate Constant (M^{-1} ks^{-1})[b]	HMF Yield (%)[c]
H$_2$SO$_4$	90% GVL/BTEAC	53	79
PSA/SiO$_2$	90% GVL	23	72
PSA/SiO$_2$	90% GVL/BTEAC	35	80
Amberlyst 70	90% GVL	31	70
Amberlyst 70	90% GVL/BTEAC	36	80

[a] Reaction conditions: fructose (50 mM); acid (5 mM); solid acid (25 μmol of acid sites); salt (5 mM); solvent (5 mL); stirring (700 rpm). [b] Rate constant values at 373 K; $r = k_{H+}$ [R] [H$^+$]. [c] HMF yield values at 393 K at approximately 90% conversion.

Supplementary Table 3.6 Example subset of reactions performed with experimental conditions for the Brønsted acid-catalyzed fructose dehydration to HMF in H_2O and polar aprotic solvent systems.

Solvent / Mass Fraction of Organic Solvent		Acid / Concentration ([M])		Salt / Concentration ([M])		Reaction Times (min)
Water		HCl	0.5	−	−	0, 15, 30, 45, 60
		H_2SO_4	0.5	−	−	0, 15, 30, 45, 60
		H_2SO_4	0.5	KCl	1	0, 15, 30, 45, 60
		H_2SO_4	0.5	KCl	2	0, 15, 30, 45, 60
		H_2SO_4	0.5	KCl	3	0, 15, 30, 45, 60
GVL	0.05	H_2SO_4	0.5	−	−	0, 15, 30, 45, 60
	0.25	H_2SO_4	0.5	−	−	0, 15, 30, 45, 60
	0.25	H_2SO_4	0.5	KCl	0.5	0, 15, 30, 45, 60
	0.50	H_2SO_4	0.1	−	−	0, 15, 30, 45, 60
	0.50	H_2SO_4	0.1	KCl	0.25	0, 15, 30, 45, 60
	0.75	H_2SO_4	0.025	−	−	0, 15, 30, 45, 60
	0.90	HCl	0.005	−	−	0, 15, 30, 45, 60
	0.90	Triflic	0.001	−	−	0, 30, 60, 90, 120
	0.90	Triflic	0.005	KBr	0.005	0, 10, 20, 30, 40
	0.90	Triflic	0.005	NaBr	0.005	0, 10, 20, 30, 40
	0.90	Triflic	0.005	LiBr	0.005	0, 10, 20, 30, 40
	0.90	Triflic	0.005	KCl	0.001	0, 10, 20, 30, 40
	0.90	Triflic	0.005	KCl	0.01	0, 10, 20, 30, 40
	0.90	Triflic	0.005	NaCl	0.005	0, 10, 20, 30, 40
	0.90	Triflic	0.005	LiCl	0.005	0, 10, 20, 30, 40
	0.90	−	−	KCl	0.005	0, 10, 20, 30, 40
THF	0.90	H_2SO_4	0.005	−	−	0, 15, 30, 45, 60
	0.90	Triflic	0.005	−	−	0, 15, 30, 45, 60
	0.90	HCl	0.005	−	−	0, 15, 30, 45, 60
Dioxane	0.90	H_2SO_4	0.005	−	−	0, 15, 30, 45, 60
	0.90	Triflic	0.005	−	−	0, 15, 30, 45, 60
	0.90	HCl	0.005	−	−	0, 15, 30, 45, 60

[a] Reaction conditions: fructose (50 mM); solvent (5 mL); temperature (373 K); stirring (700 rpm).

a
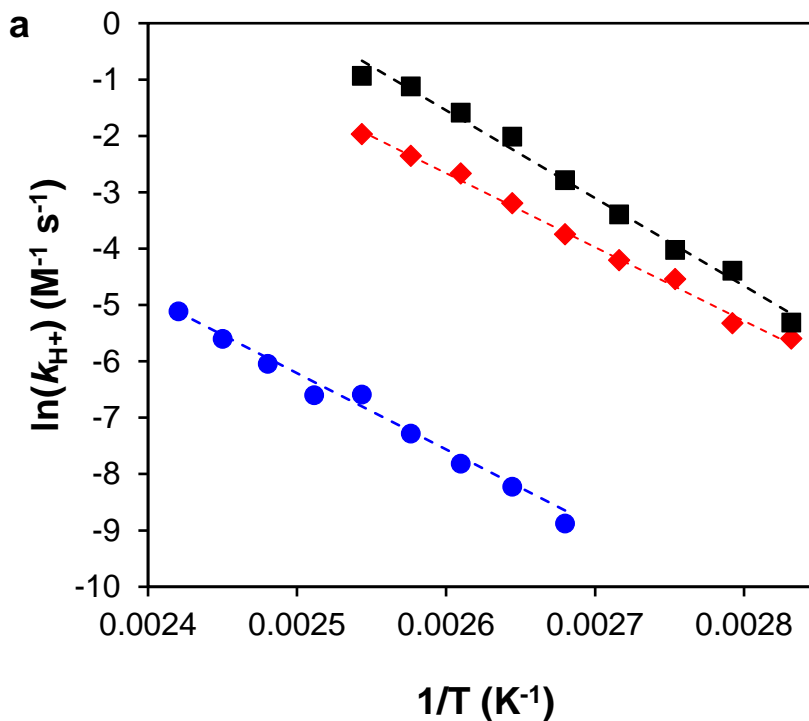
b

Solvent[a]	Catalyst	$A^{[c,d]}$ $(M^{-1} s^{-1})$	95% C.I. $(M^{-1} s^{-1})$	$E_a^{[c,d]}$ $(kJ\ mol^{-1})$	95% C.I. $(kJ\ mol^{-1})$
H_2O	HCl	1.04E12	[2.8E11, 3.9E12]	113	[108, 117]
90% GVL[b]	Triflic	4.38E13	[1.1E13, 1.8E14]	109	[105, 113]
90% GVL[b]	HCl	5.15E17	[5.5E16, 4.8E18]	135	[128, 142]

[a] Reaction conditions: fructose (50 mM); acid (0.025 – 0.5 M for water; 1 – 10 mM for 90% GVL/10% H_2O); solvent (5 mL); stirring (700 rpm). [b] 90 wt% GVL–water mixtures. [c] $r = Ae^{-(Ea/RT)}$ [R] [H$^+$]. [d] Temperature ranges: 373 – 413 K for H_2O; 353 – 393 K for 90% GVL/10% H_2O.

Supplementary Figure 3.1 Fructose dehydration reaction energetics. a, Arrhenius plot of the apparent reaction rate constant values at various temperatures for fructose dehydration to HMF in H2O with HCl (blue circles); 90% GVL with triflic acid (red diamonds); and 90% GVL with HCl (black squares). **b**, Table of apparent activation energy values derived from data in Supplementary Figure 3.1, a (reaction conditions listed in table footer).
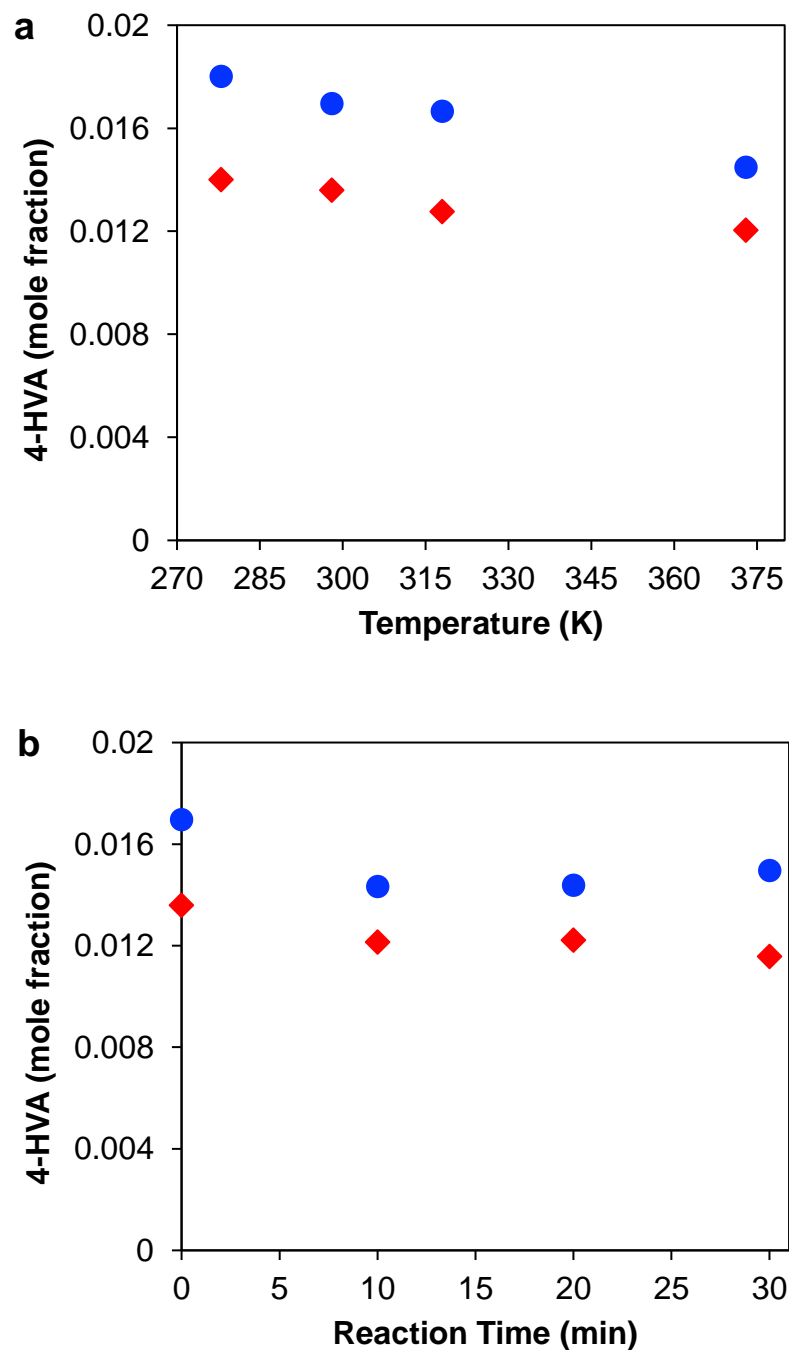
Supplementary Figure 3.2. NMR results with 4-HVA. Mole fraction of 4-HVA as function of (a) temperature and (b) reaction time during the fructose dehydration reaction in 90% GVL with H_2SO_4 (blue circles) and with H_2SO_4 and KCl (red diamonds). Reaction conditions: fructose (50 mM); acid (H_2SO_4; 5 mM); salt (KCl; 5 mM); 373 K for (b); solvent (5 mL); stirring (700 rpm).
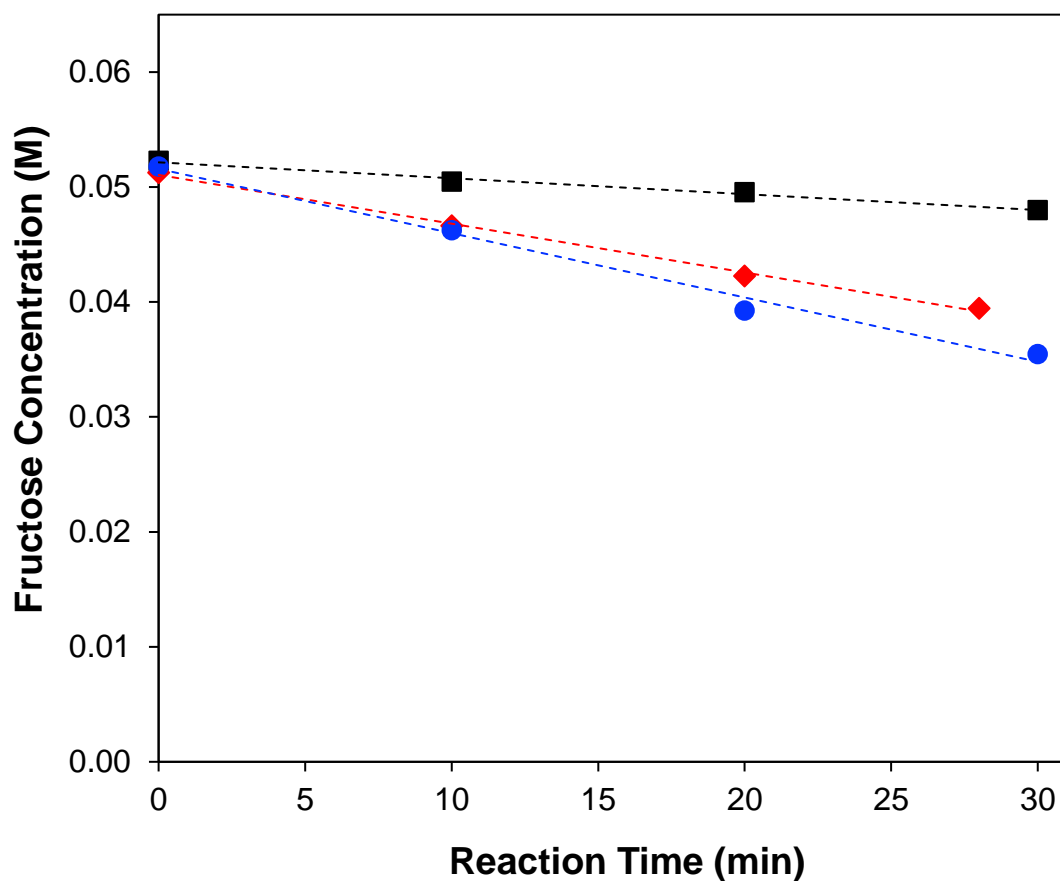
Supplementary Figure 3.3 Reaction kinetics data for fructose dehydration in 90% GVL with H_2SO_4 (black squares); H_2SO_4 and KCl (red diamonds); and H_2SO_4, KCl, and valeric acid (blue circles). Reaction conditions: fructose (50 mM); acid (H_2SO_4; 5 mM); salt (KCl; 5 mM); valeric acid (90 mM); 373 K; solvent (5 mL); stirring (700 rpm).
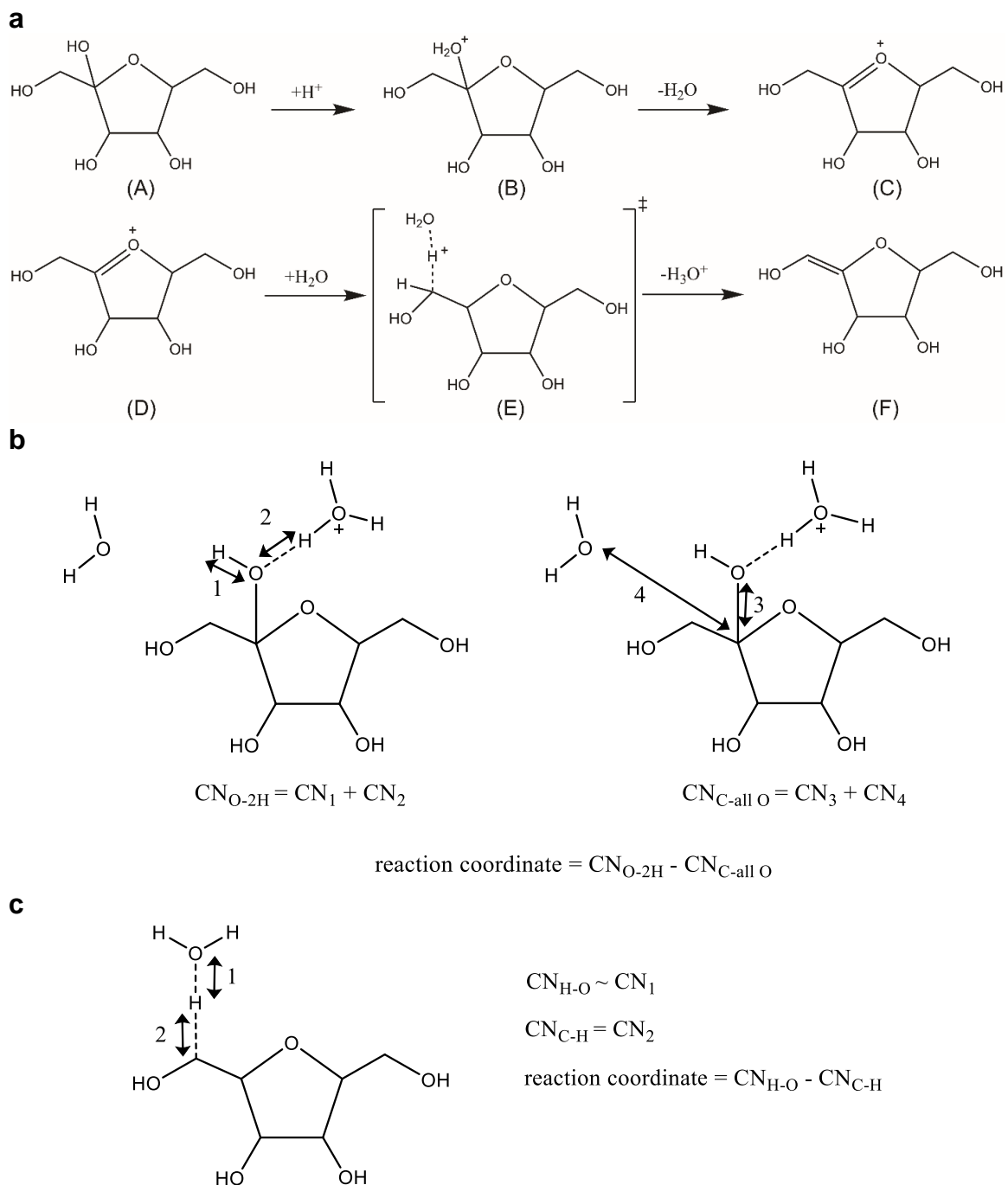
Supplementary Figure 3.4 Reaction schemes for the Brønsted-acid catalyzed conversion of fructose to HMF. **a**, Proposed mechanism for fructose dehydration; **b**, Reaction coordinate for the oxocarbenium ion formation step; **c**, Reaction coordinate for the proton abstraction step.
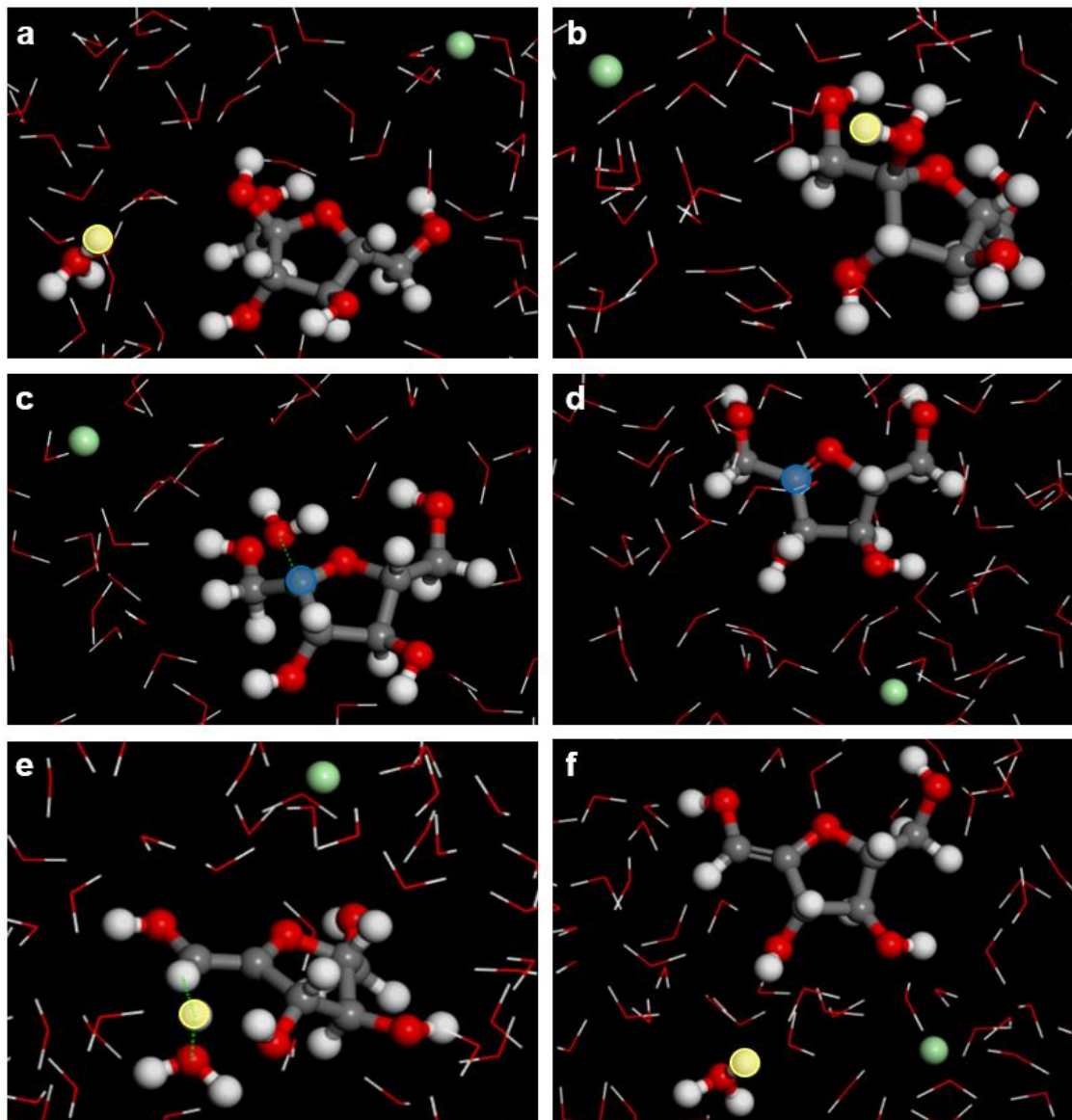
Supplementary Figure 3.5 The progression of fructose dehydration in water with HCl catalyst. a, The initial state involves fully dissociated HCl as hydronium and chloride ions together with a single fructose molecule in water (proton is highlighted in yellow). **b**, The protonated fructose structure without stabilization from chloride ion. **c**, The transition state for the oxocarbenium ion formation step where the scission of C–O bond is shown via the dotted line. **d**, The carbenium ion intermediate that results from fructose shows the formation of a double bond between ring oxygen and C2 carbon (center of the oxocarbenium ion shown in blue), suggesting a stabilization via the lone pair of electrons on the ring oxygen. **e**, The transition state for the deprotonation of the oxocarbenium ion without stabilization from chloride ion. **f**, The resulting olefin product. Figures in panels (**e**) and (**f**) were taken from the systems with bounded chloride anion in the initial state (Supplementary Figure 3.6g–i). The red, grey, green, and white spheres refer to the oxygen, carbon, chlorine, and hydrogen atoms, respectively. The yellow and blue highlighted circles refer to the reactive proton and oxocarbenium ions centers, respectively.

115
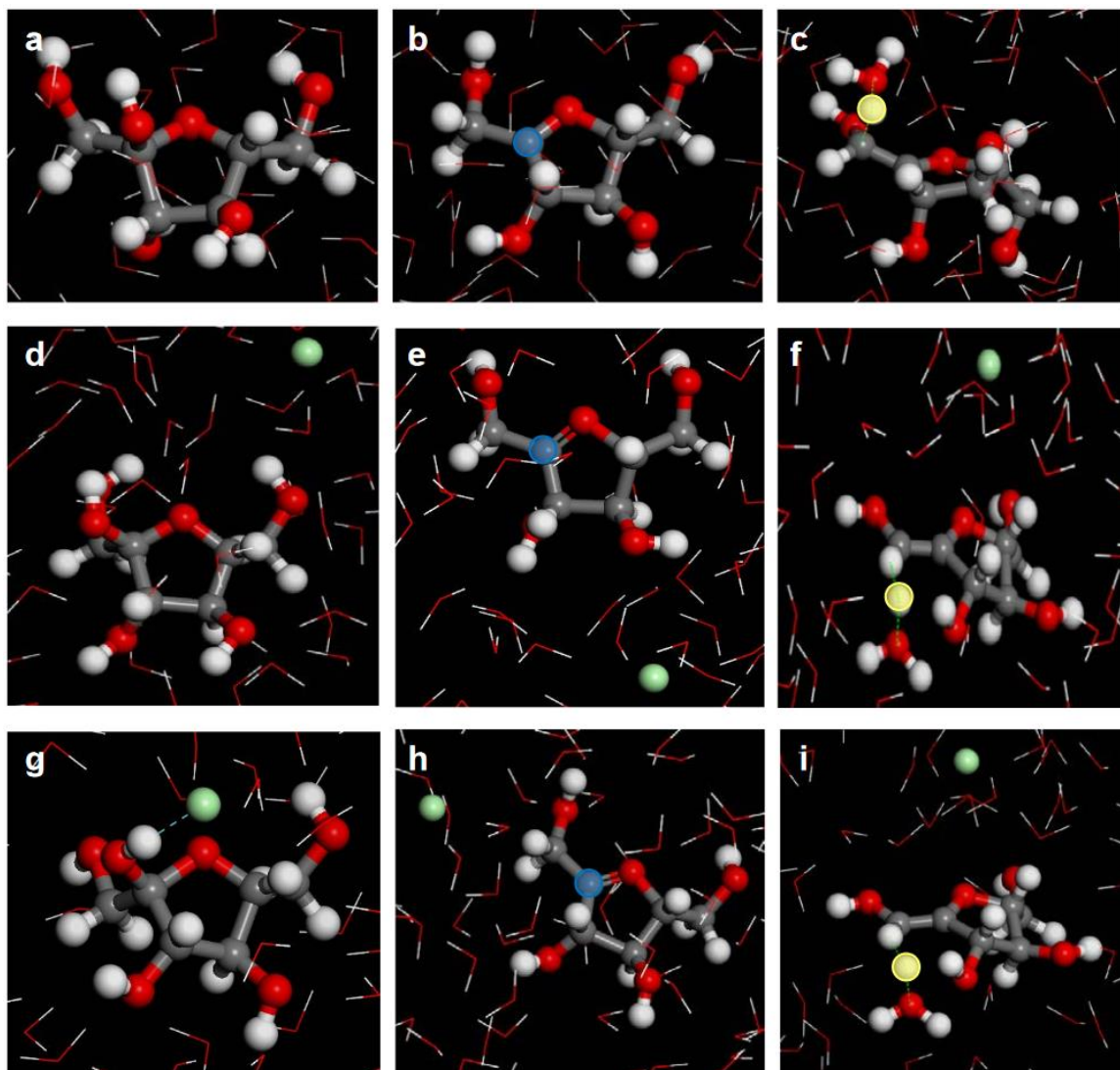
Supplementary Figure 3.6 Fructose dehydration reaction structures in water. Structures of fructose in the water system without an anion (in **a**–**c** of the first row), with a free chloride anion (in **d**–**f** of the second row), and with a bound chloride anion in the initial state (in **g**–**i** of the third row). The first, second, and third columns represent the initial, oxocarbenium ion, and transition state structures, respectively. The red, grey, green, and white spheres refer to the oxygen, carbon, chlorine, and hydrogen atoms, respectively. The yellow and blue highlighted circles refer to the reactive proton and oxocarbenium ions centers, respectively.
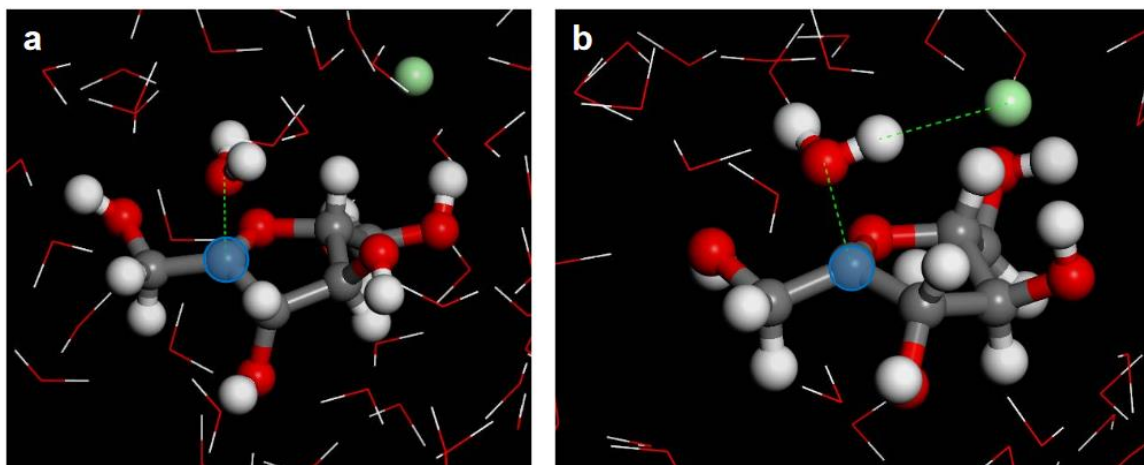
Supplementary Figure 3.7 Structures of the transition state for the oxocarbenium formation step for fructose dehydration in water. **a**, The chloride anion was solvated in bulk water in the initial state. The transition state of the oxocarbenium formation step does not involve the anion. **b**, The chloride anion was deliberately bound to the fructose hydroxyl group in the initial state. The transition state of the oxocarbenium formation step is stabilized by chloride anion. The red, grey, green, and white spheres refer to the oxygen, carbon, chlorine, and hydrogen atoms, respectively. The blue highlighted circle refers to the oxocarbenium ions center.
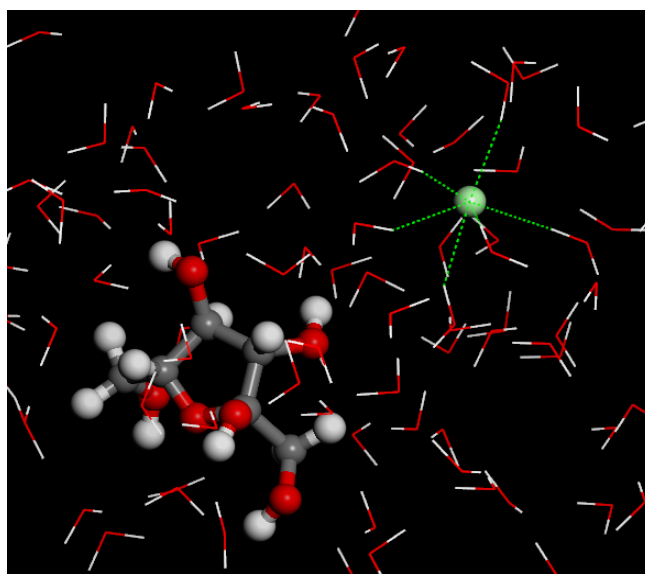
Supplementary Figure 3.8 The chloride anion in the water system shows extensive hydrogen bonding in the water solvation shell. The interaction between the chloride anion and the reactive site on fructose is inhibited as the anion is locked up in the solution phase. The red, grey, green, and white spheres refer to the oxygen, carbon, chlorine, and hydrogen atoms, respectively.

117
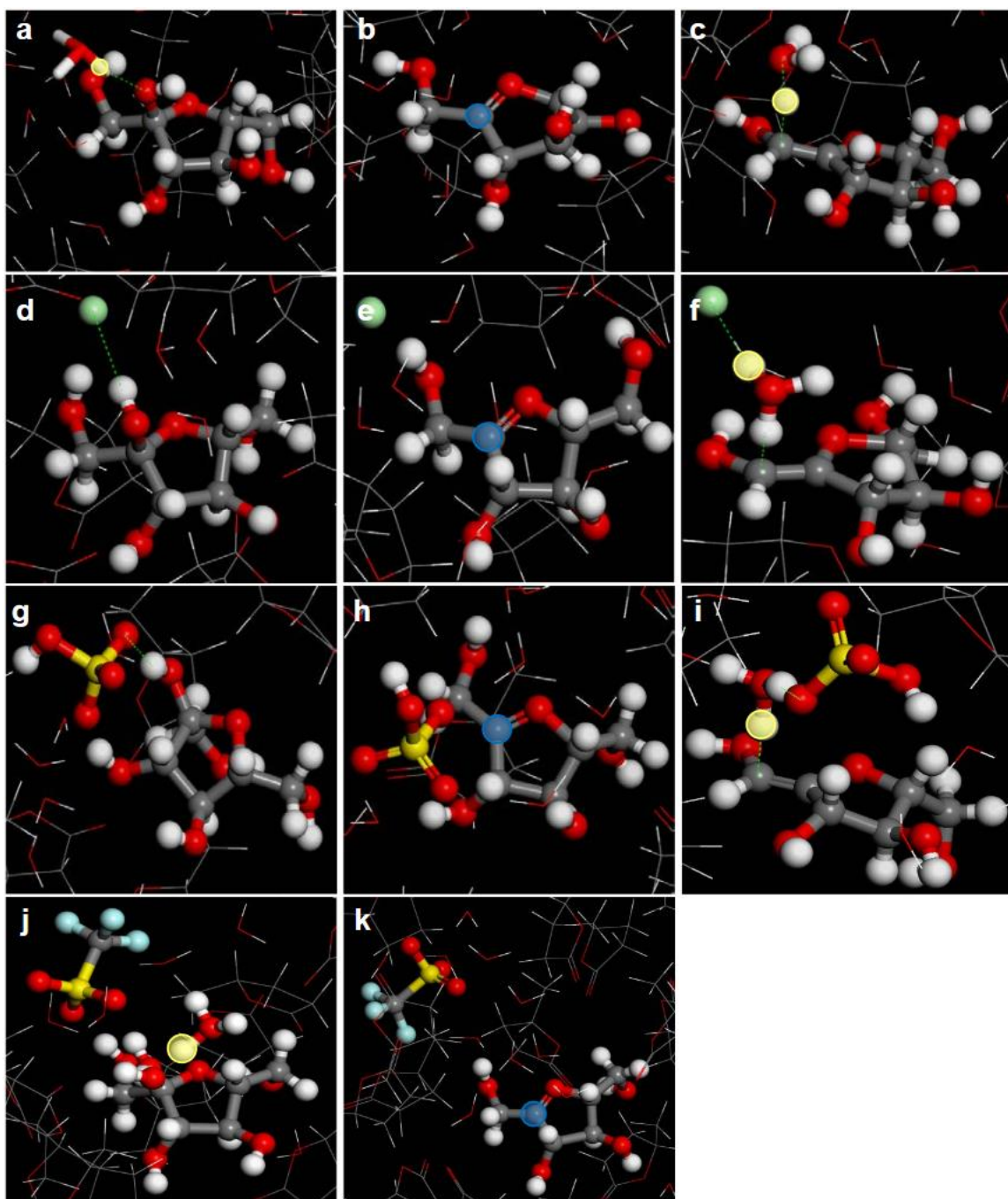
Supplementary Figure 3.9 Fructose dehydration reaction structures in GVL. Structures of fructose in the 90% GVL systems without an anion (**a**–**c**, first row), with a bound chloride anion in the initial state (**d**–**f**, second row), with a bound bisulfate anion in the initial state (**g**–**i**, third row), and with a bound triflate anion in the initial state (**j** and **k**, fourth row). The first, second, and third columns represent the initial, oxocarbenium ion, and transition state structures, respectively. The red, grey, green, white, yellow, and aqua spheres refer to the oxygen, carbon, chlorine, hydrogen, sulfur, and fluorine atoms, respectively. The yellow and blue highlighted circles refer to the reactive proton and carbenium ions centers, respectively.
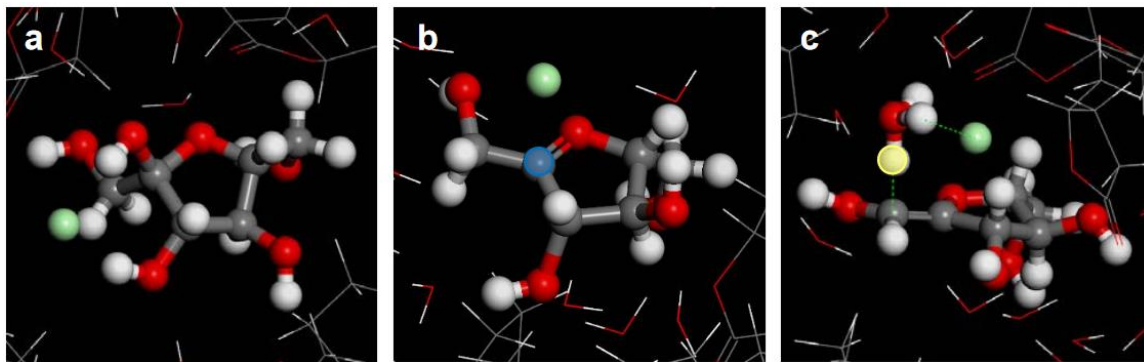
Supplementary Figure 3.10 Structures of fructose in 75% GVL with a bound chloride anion in the initial state. The first (**a**), second(**b**), and third (**c**) panel correspond to initial, oxocarbenium ion, and transition state structures, respectively. The red, grey, green, and white spheres refer to the oxygen, carbon, chlorine, and hydrogen atoms, respectively. The yellow and blue highlighted circles refer to the reactive proton and oxocarbenium ions centers, respectively.
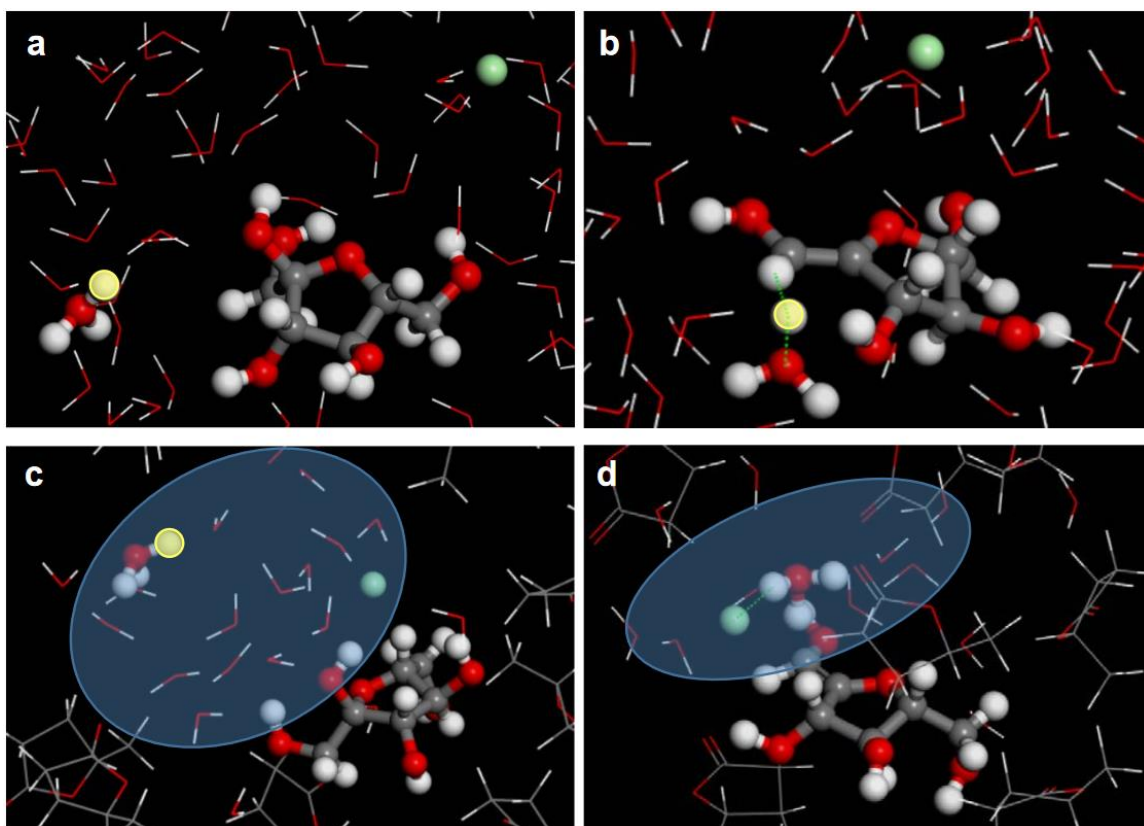
Supplementary Figure 3.11 Fructose dehydration initial and transition states in water and GVL. (**a**) The initial state and (**b**) the transition state of fructose dehydration in water with hydrochloric acid catalyst. The acid is fully dissociated into hydronium and chloride ions, where both the ions are located in the bulk solvent far from fructose. **c**, The solvation structures in 75% GVL shows a localization of water molecules in the initial state. The dissociation of acid takes place inside the hydrophilic domain, allowing for stabilization of the transition state by the chloride anion (**d**). The red, grey, green, and white spheres refer to the oxygen, carbon, chlorine, and hydrogen atoms, respectively. The yellow highlighted circle refers to the reactive proton. The blue circled regions highlight the localized hydrophilic domains.
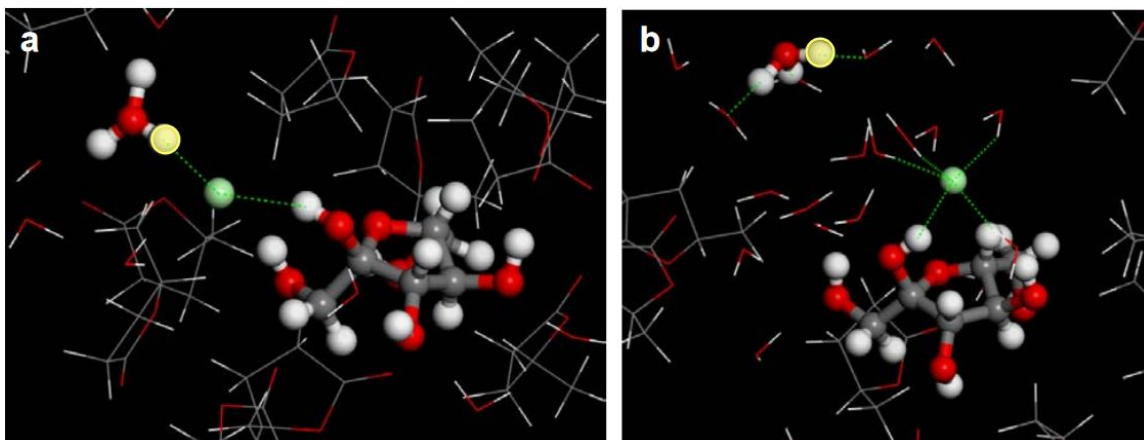
Supplementary Figure 3.12 A comparison of 0.5 M HCl acid dissociation in (a) 90% GVL, and (b) 75% GVL systems. An ion pairing is observed in the 90% GVL–water system, while the acid is fully dissociated in the 75% GVL–water system. Incomplete acid dissociation was not observed in the experimental results since the acid concentration used was much lower (~5 mM acid). The red, grey, green, and white spheres refer to the oxygen, carbon, chlorine, and hydrogen atoms, respectively. The yellow highlighted circle refers to the proton.
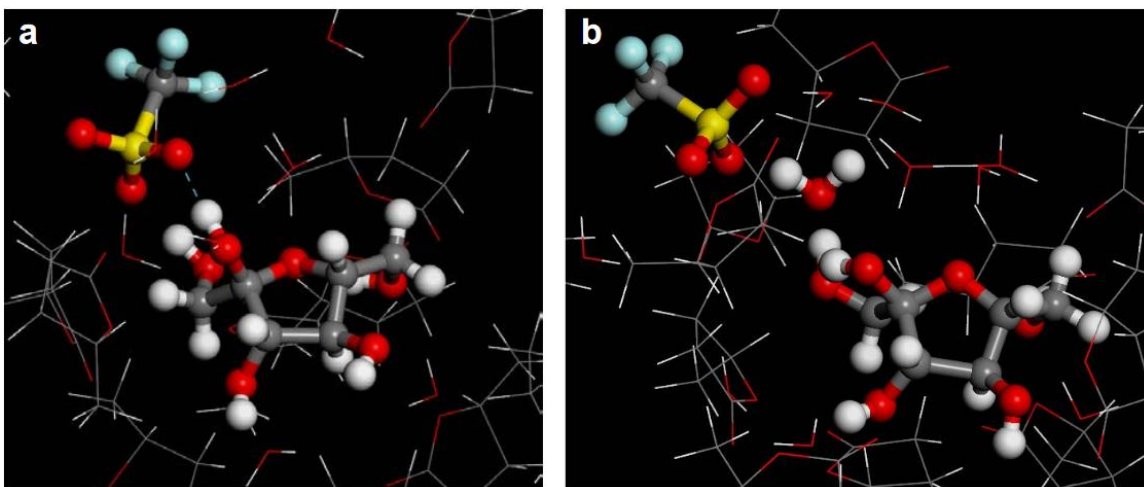
Supplementary Figure 3.13 Fructose dehydration reaction structures with triflate anion. **a**, Structures of fructose in 90% GVL with a bounded triflate anion in the initial state. **b**, The triflate ion in the previous structure migrated away from the hydrophilic domain near fructose molecule partitions with the SO_3 group of triflate in the hydrophilic domain whereas the CF_3 group is in the hydrophobic domain. The interaction between the triflate anion and reactive site near fructose is inhibited. The red, grey, green, white, yellow, and aqua spheres refer to the oxygen, carbon, chlorine, hydrogen, sulfur, and fluorine atoms, respectively.
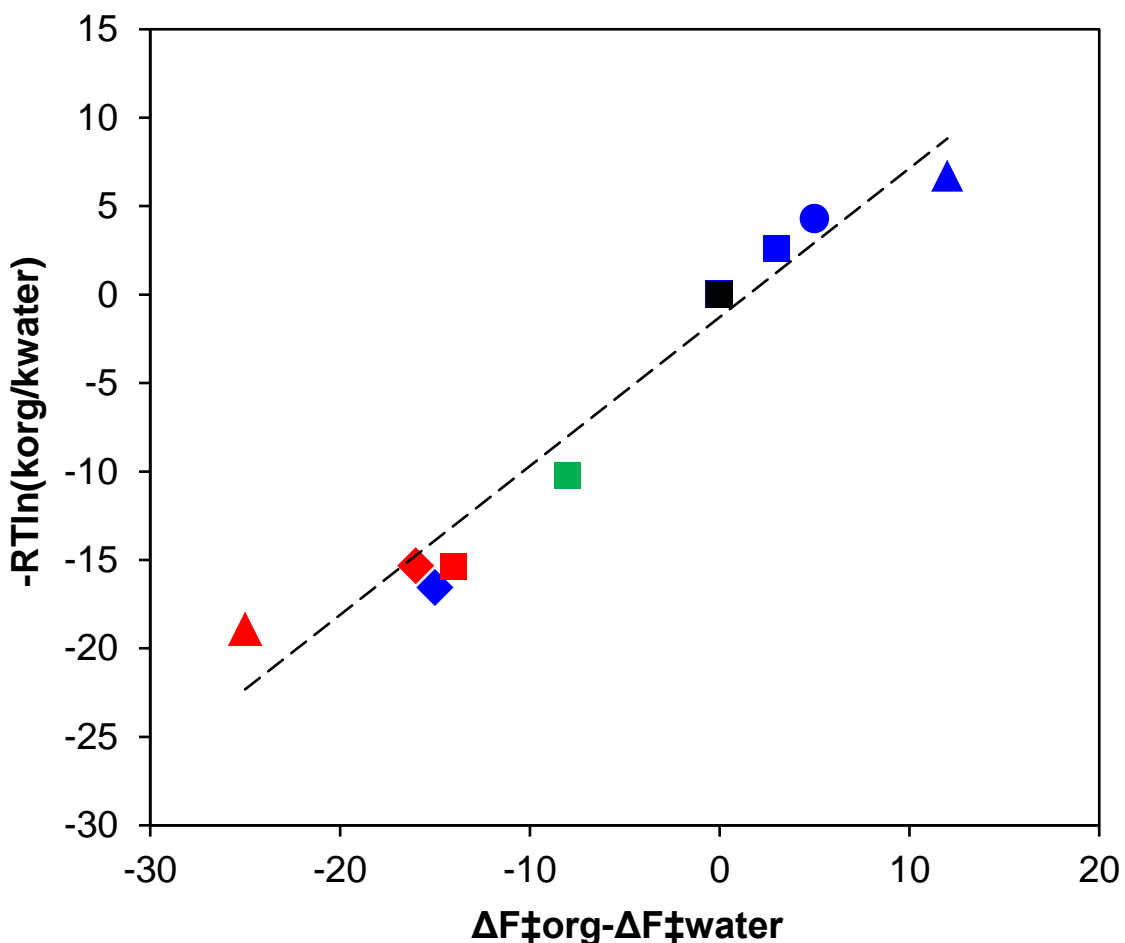
Supplementary Figure 3.14 Linear relationship between the experimentally measured and AIMD simulated activation free energies for the acid-catalyzed dehydration of different alcohols in different solvents and acids. Each data point corresponds to the following cases:

tert-butanol in H2O with H+ (black square)[24]
tert-butanol in 70% GVL/10% H2O with H+ (blue square)[24]
tert-butanol in 100% GVL with H+ (blue diamond)[24]
tert-butanol in 90% DMSO/10% H2O with H+ (blue triangle) [24]
tert-butanol in 100% DMSO with H+ (blue circle)[24]
1,2-propanediol in H2O with H+ (black square)[24]
1,2-propanediol in 90% GVL/10% H2O with H+ (green square)[24]
fructose in H2O with H+ (black square)
fructose in 90% GVL/10% H2O with H2SO4 (red square)
fructose in 90% GVL/10% H2O with triflic acid (red diamond)
fructose in 90% GVL/10% H2O with HCl (red triangle)

The black dotted line is the best fit line equation y = 0.8416x − 1.2747 with the R2 value of 0.9538, which represents a linear fit to the data. The data for H+ acid did not include an anion in computational simulations, while triflic acid was used in the experiments.
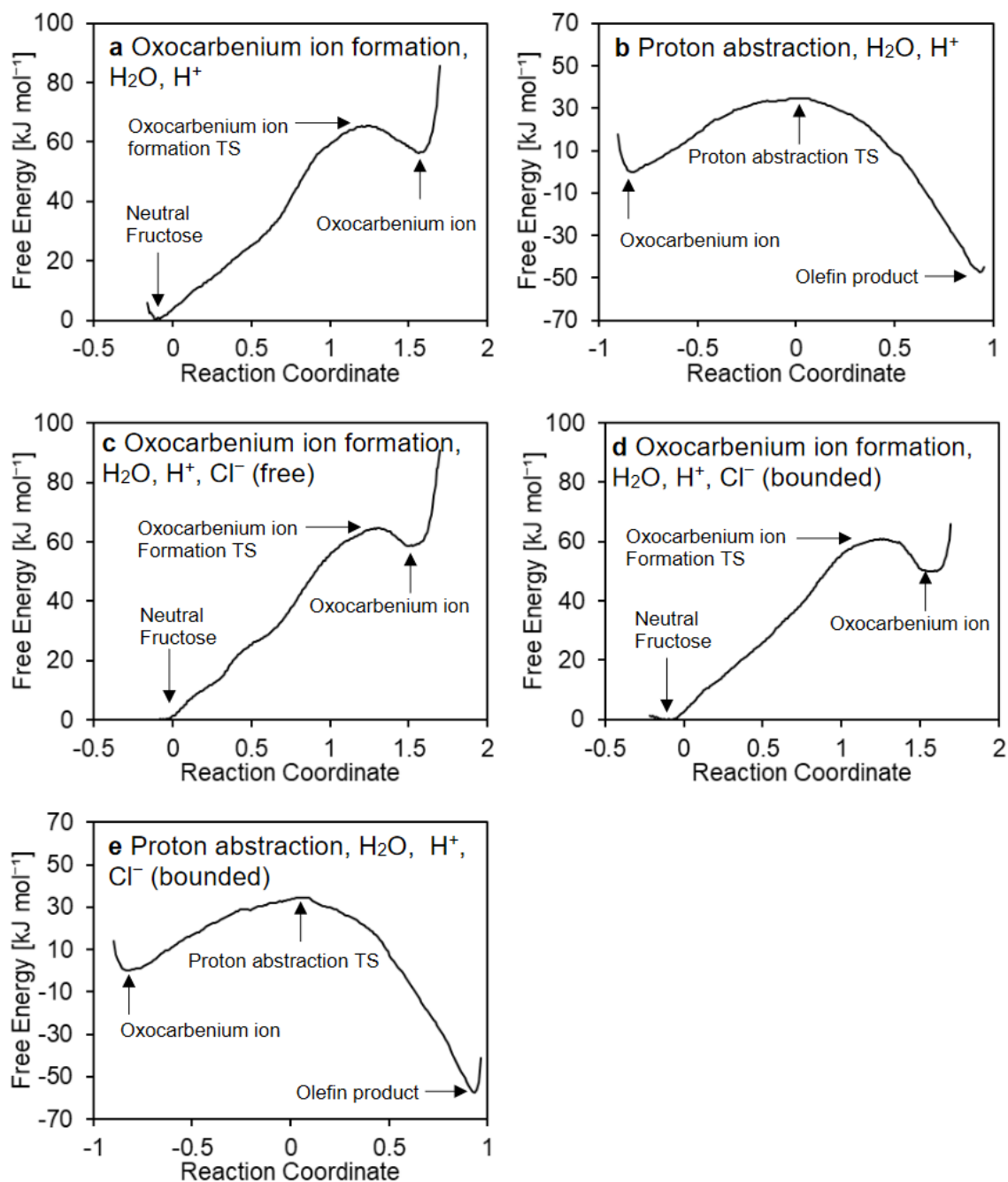
Supplementary Figure 3.15 Free energy profiles for fructose dehydration in water systems. **a**, Oxocarbenium ion formation without anion; **b**, Proton abstraction without anion; **c**, Carbenium ion formation with free chloride anion; **d**, Oxocarbenium ion formation with bounded chloride anion in the initial state; **e**, Proton abstraction proceeded from structure in (**d**). These figures (**a**–**e**) correspond to the structures shown in Supplementary Figure 3.6.
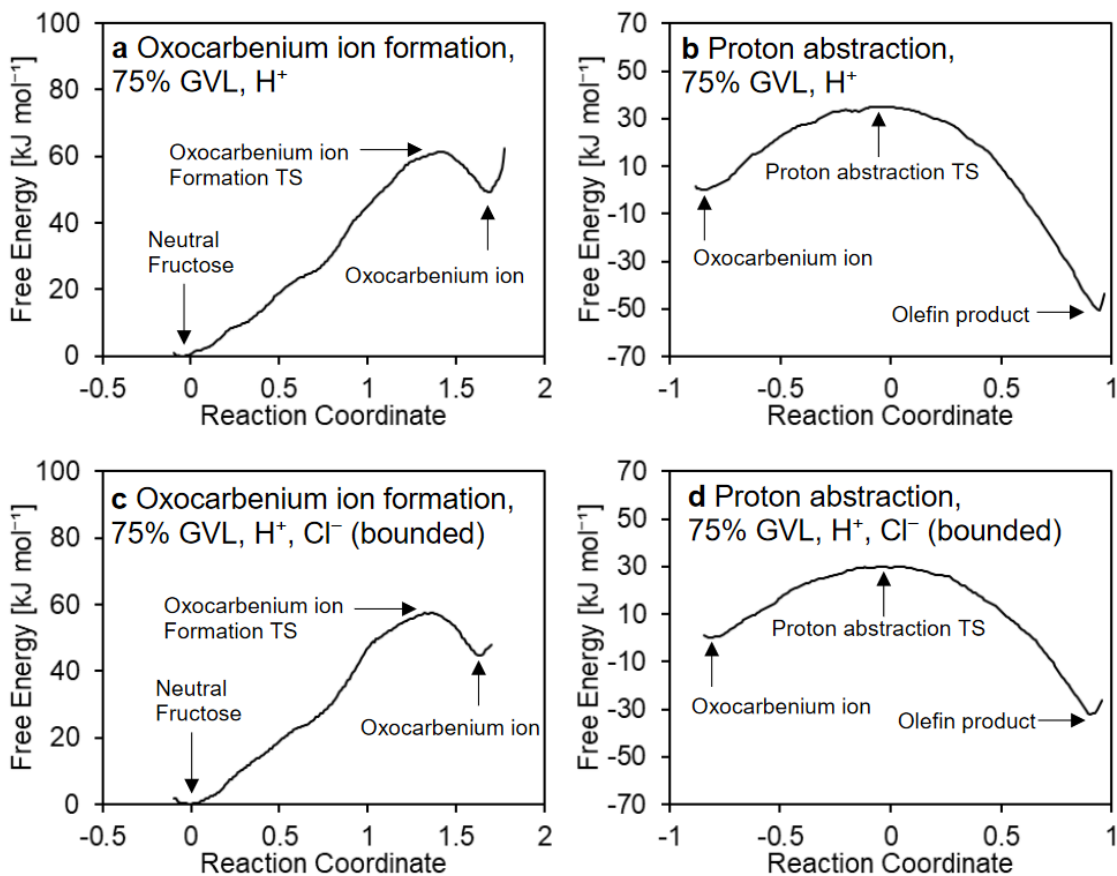
Supplementary Figure 3.16 Free energy profiles for fructose dehydration in 75% GVL systems. **a**, Oxocarbenium ion formation without anion; **b**, Proton abstraction without anion; **c**, Oxocarbenium ion formation with bounded chloride anion in the initial state; **d**, Proton abstraction proceeded from structure in (**c**).
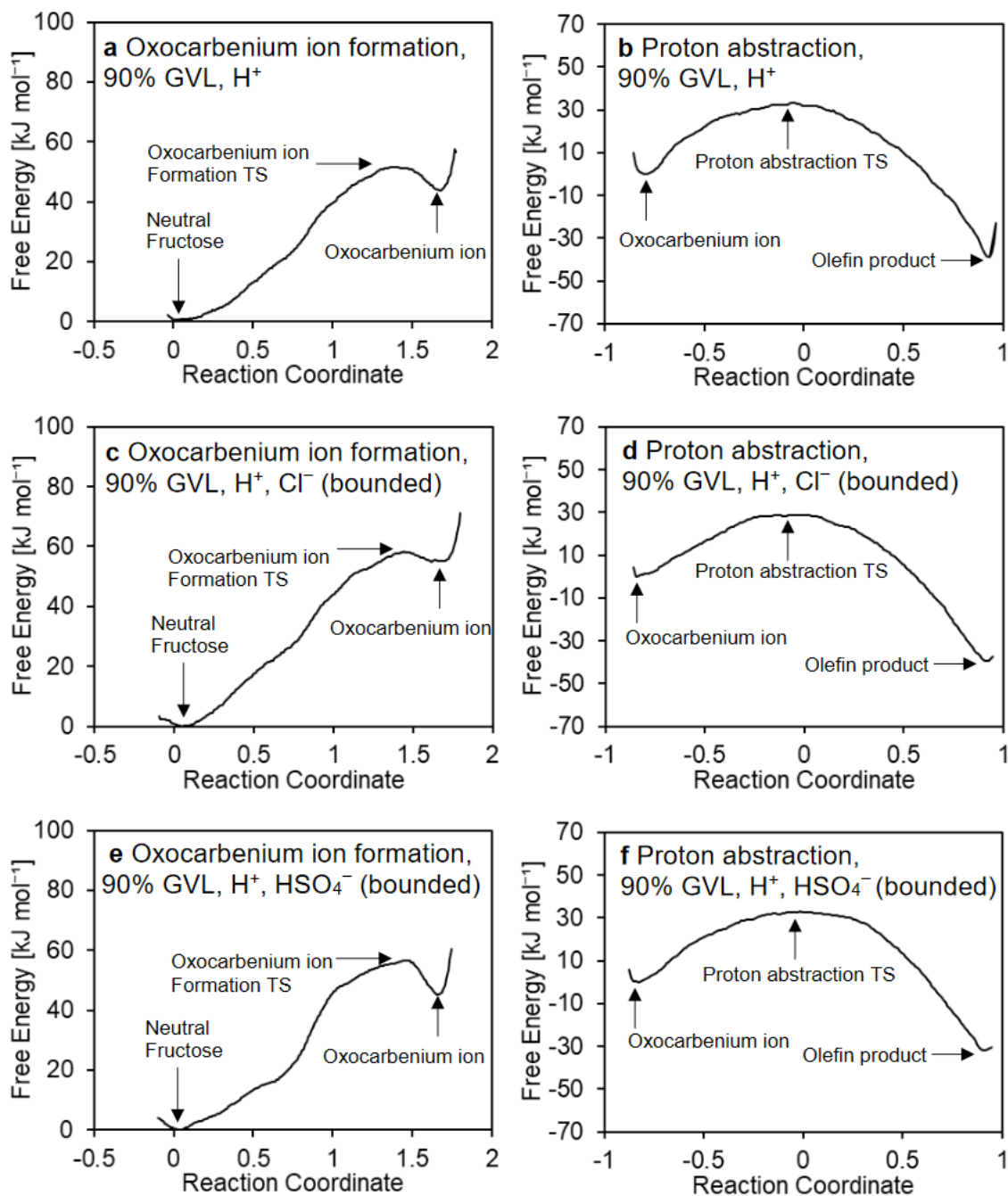
Supplementary Figure 3.17 Free energy profiles of fructose dehydration in 90% GVL systems. **a**, Oxocarbenium ion formation without anion; **b**, Proton abstraction without anion; **c**, Oxocarbenium ion formation with bounded chloride anion in the initial state; **d**, Proton abstraction proceeded from structure in (**c**); **e**, Oxocarbenium ion formation with bounded bisulfate anion in the initial state; **f**, Proton abstraction proceeded from structure in (**e**). These figures (**a**–**f**) correspond to the structures shown in Supplementary Figure 3.9.
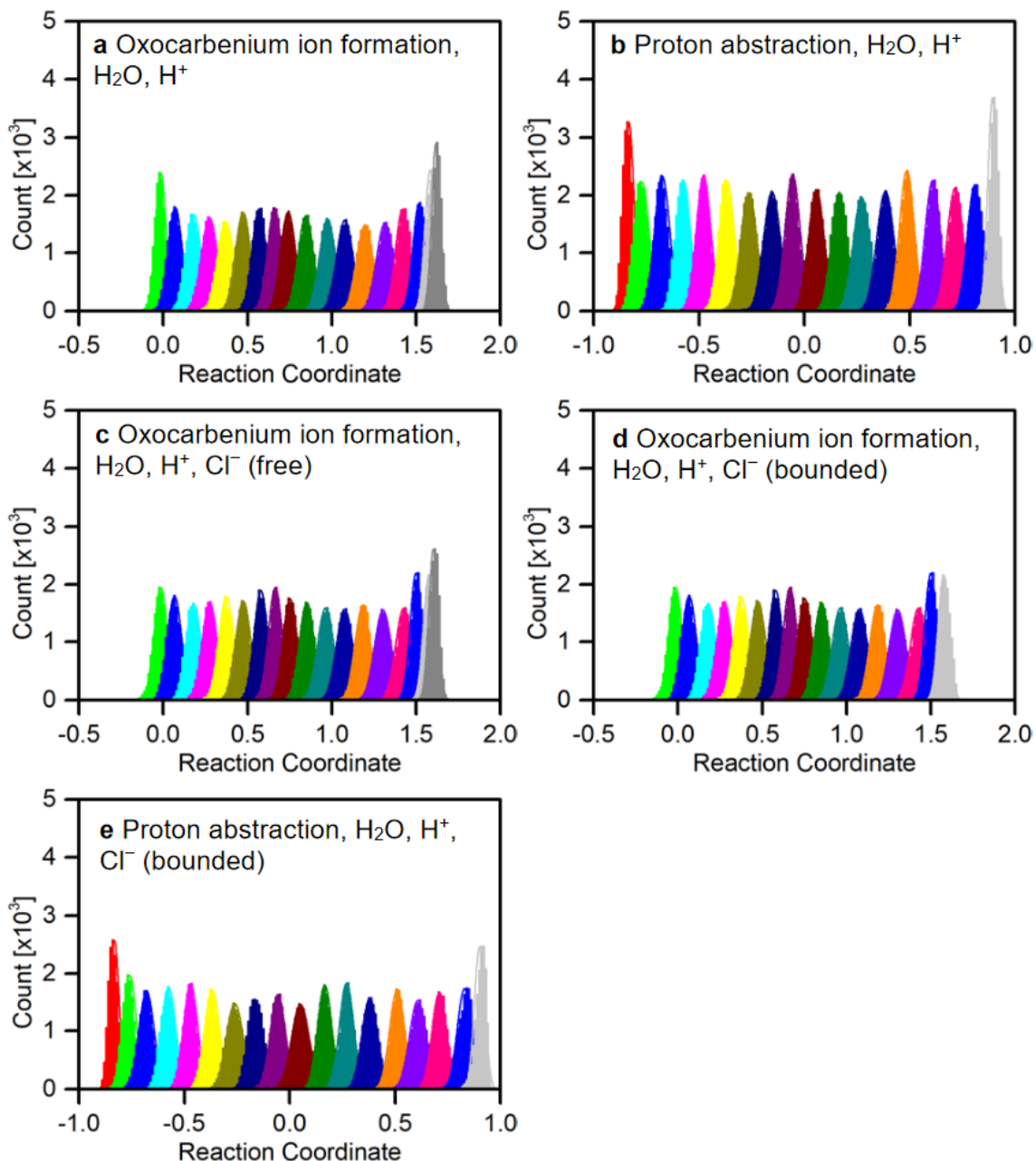
Supplementary Figure 3.18 Statistical histograms of free energy sampling for fructose dehydration in water systems. a, Oxocarbenium ion formation without anion; **b**, Proton abstraction without anion; **c**, Oxocarbenium ion formation with free chloride anion; **d**, Oxocarbenium ion formation with bounded chloride anion in the initial state; **e**, Proton abstraction proceeded from structure in (**d**). These histograms (**a**–**e**) correspond to the structures in Supplementary Figure 3.6 and free energy profiles in Supplementary Figure 3.15.
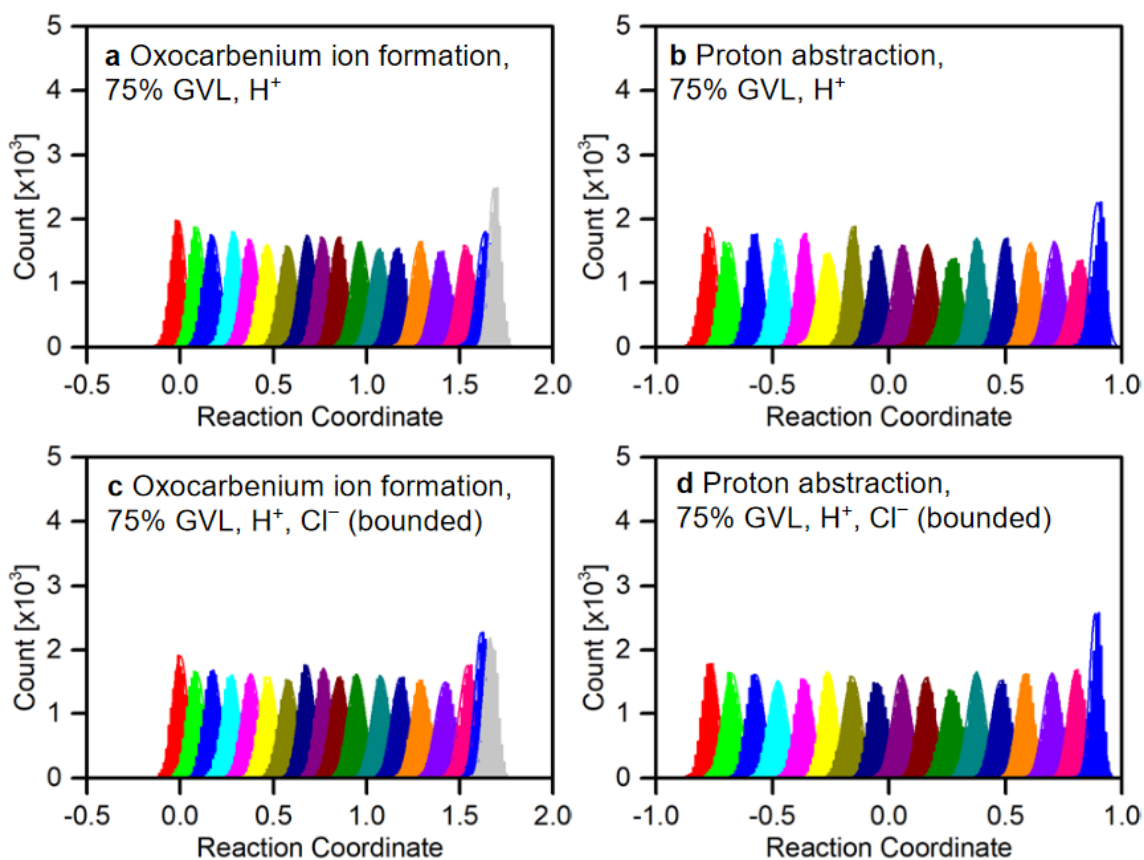
Supplementary Figure 3.19 Statistical histograms of free energy sampling for fructose dehydration in 75% GVL systems. **a**, Oxocarbenium ion formation without anion; **b**, Proton abstraction without anion; **c**, Oxocarbenium ion formation with bounded chloride anion in the initial state; **d**, Proton abstraction proceeded from structure in (**c**). These histograms(**a**–**d**) correspond to the free energy profiles in Supplementary Figure 3.16.
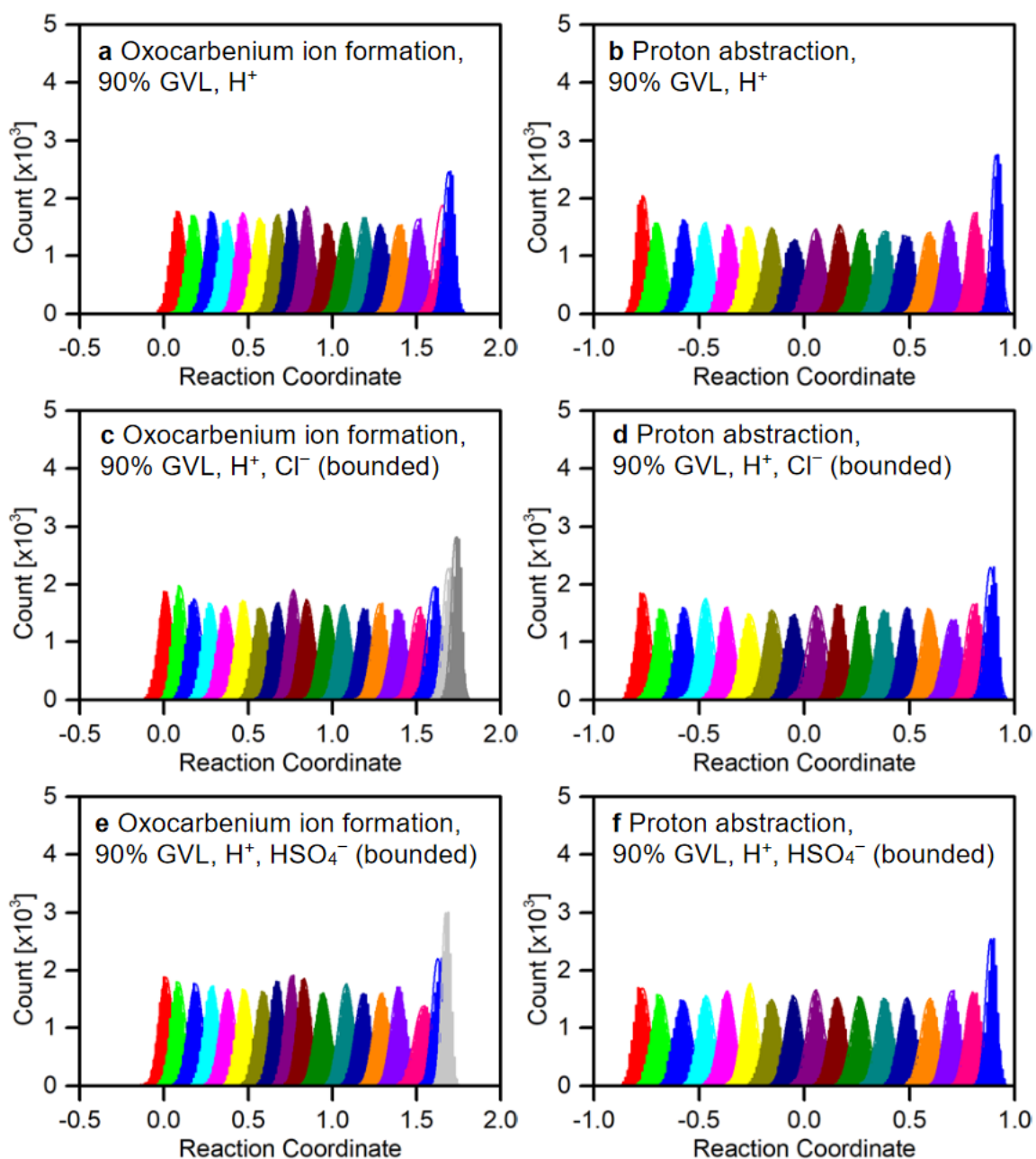
Supplementary Figure 3.20 Statistical histograms of free energy sampling for fructose dehydration in 90% GVL systems. **a**, Oxocarbenium ion formation without anion; **b**, Proton abstraction without anion; **c**, Oxocarbenium ion formation with bounded chloride anion in the initial state; **d**, Proton abstraction proceeded from structure in (**c**); **e**, Oxocarbenium ion formation with bounded bisulfate anion in the initial state; (**f**) proton abstraction proceeded from structure in (**e**); These histograms(**a**–**f**) correspond to the structures in Supplementary Figure 3.9 and free energy profiles in Supplementary Figure 3.17.

Chapter 4 – Theoretical Investigation of Solvent and Chloride Effects on the Production 5-Hydroxymethylfurfural from Glucose

Adapted from Sanpitakseree, C., Neurock, M. Theoretical Investigation of Solvent and Chloride Effects on the Production of 5-Hydroxymethylfurfural from Glucose. Manuscript under preparation.

Theoretical calculations were performed by CS under the supervision of MN.

4.1 Introduction

The liquid phase conversion of biomass often employs acid-catalyzed dehydration reactions to hydrolyze inedible cellulose and hemicellulose into sugar monomers. Further dehydration of these sugars yields carbon-neutral platform intermediates such as hydroxymethylfurfural (HMF) that can be used in the production of valuable chemicals.[4,5,11,12,17,51,91,94,141,168] Significantly higher catalytic activities for HMF production from biomass-derived sugars such as fructose can be achieved when the reactions are carried out in polar aprotic solvents, such as dimethyl sulfoxide (DMSO),[34,90,169] 1,4-dioxane,[41,42] acetone,[43–45] THF,[170–172] and γ-valerolactone (GVL).[47,50,173] The dehydration rates can be further enhanced via the addition of metal halide salts into the reaction media.[78–81] Regardless, the influence of solvents and solvent additives on the reaction paths for HMF production is largely unknown.

In an effort to understand and improve the performance of catalytic production of HMF, we carried out a computational investigation[76] and showed that the dehydration rate of fructose is enhanced in organic solvent–water mixtures as the hydrophilic periphery of

fructose provides localized hydrophilic domains that aid in catalyzing dehydration. The localization of water molecules along with an acidic proton and a chloride anion close to the reactive hydroxyl sites facilitates proton transfer from solvent to hydroxyl group and promotes dehydration. In addition, the chloride anion stabilizes the positively charged transition state that forms within the local hydrophilic cluster and further lowers the activation energy of dehydration.[77] The effects of solvent on the selectivity toward the desirable HMF and the formation of humin side product is not well understood.

Recently, Dumesic and coworkers proposed a process for the conversion of naturally abundant glucose to HMF with excellent yield and selectivity.[82] The process converts the relatively inert glucose to the more reactive fructose using Sn–β isomerization catalyst in water. The fructose can subsequently be dehydrated to HMF in acetone–water solvent systems using solution phase HCl as a catalyst, achieving 95% HMF yield at 90% fructose conversion. Herein we report on the results from *ab initio* molecular dynamics (AIMD) simulations that examine the effects of acetone–water solvent mixtures and chloride ion on the reactivity and selectivity of glucose conversion to HMF. The considered reaction paths include glucose isomerization to HMF, glucose dehydration to HMF, fructose dehydration to HMF, and HMF degradation to humins. We show that the effects of acetone–water mixtures on HMF production rate and selectivity can be explained by the change in solvation environments of the reactants and transition states.

4.2 Methods

Molecular systems for glucose isomerization were established by using the Sn–BEA lattice structure from Van der Graaff et al[174] with the Sn atom positioned at T9 site (Supplementary Figure 4.1). The $12.661 \times 12.661 \times 26.406$ Å^3 lattice includes a silanol group connected to the Sn atom which increases the flexibility of zeolite framework and facilitates the adsorption of guest molecules. The linear ring-opened glucose intermediate was subsequently coordinated on an open Sn site in bidentate binding mode (Supplementary Figure 4.2a–b). A proton from C2 hydroxyl group of glucose was transferred to a silanol group on the Sn site, resulting in a deprotonated, adsorbed glucose and a protonated silanol group (Supplementary Figure 4.2c). The adsorption isotherms of water in BEA zeolite[175] suggest approximately five water molecules in the zeolite pore at reaction condition. Subsequently, five water molecules were added into the glucose-bound Sn–BEA periodic system to represent the solvent molecules present in the zeolite pore for the glucose isomerization in water (Supplementary Figure 4.3a) whereas three acetone and two water molecules were used for a 75 wt% acetone–water system (Supplementary Figure 4.3b). The resulting periodic structures with a deprotonated, adsorbed glucose structure in BEA zeolite and solvent molecules were equilibrated prior to the free energy sampling using *ab initio* density functional theory (DFT)-based molecular dynamics (AIMD) simulations in CP2K program.[126]

Liquid-phase systems for fructose dehydration, glucose dehydration, and humins formation were prepared by placing a carbohydrate molecule, solvent molecules, a proton, and a chloride ion in a $15 \times 15 \times 15$ Å^3 periodic box using the Packmol tool.[164] The liquid water system consisted of 96 H_2O molecules, one hydronium ion, and one carbohydrate

molecule. The 75 wt% acetone–water system consisted of 18 acetone molecules, 18 H_2O molecules, one hydronium ion, and one carbohydrate molecule. For glucose and fructose systems examined in the presence of chloride ions, the anion was initially bound to C2 hydroxyl groups of glucose and fructose. Unconstrained molecular dynamics simulations were carried out to establish a radial distribution function and determine the distance between chloride ion and hydrogen on the hydroxyl groups on glucose or fructose (2.22 Å and 2.1 Å for glucose–Cl$^-$ and fructose–Cl$^-$, respectively). The prepared periodic systems were equilibrated in GROMACS software[125] for 1 ns using constant number of particles, constant volume, and constant temperature (NVT) ensembles followed by 10 ns of equilibration using constant number of particles, constant pressure, and constant temperature (NPT) ensembles. The temperature in the simulations was kept near 373 K. Molecular interactions of carbohydrates and acetone molecules were adapted from an all-atom version of Optimized Potentials for Liquid Simulations (OPLS–AA)[130,131] force field. Force fields for hydronium ion[165] and chloride anion[130] were adopted from literature. The interactions of water molecules were taken from an Extended Simple Point Charge (SPC/E) water model.[132] Particle Mesh Ewald (PME) was used to account for long-range electrostatic interactions. The final atomic coordinates and lattice sizes were taken as initial configurations for periodic *ab initio* molecular dynamics simulations (AIMD).

All systems were further equilibrated for 5 ps using AIMD without any constraints applied. The exchange and correlation energies were calculated using Perdew–Burke–Ernzerhof (PBE) functional.[134] Goedecker–Teter–Hutter pseudopotentials[136] were used to describe electronic density with a plane wave cut-off of 280 Ry. A short-ranged version of Gaussian-type double-ζ basis set[135] was used to expand molecular orbitals. DFT–D3(BJ)

dispersion corrections[137] were applied to compensate for medium and long range van der Waals interactions. A neutralizing background charge was assumed by CP2K in charged systems. Temperature of the simulations was maintained at 373 K using canonical sampling through a velocity rescaling (CSVR) thermostat.[138] A time step of 0.5 fs was used, and the mass of hydrogen atoms was replaced with the deuterium mass to attenuate fast vibration associated with light hydrogen atoms.

In addition to the *ab initio* molecular dynamics simulations in liquid phase, we also calculated radial distribution functions (RDFs) for HMF in 75 wt% acetone–water mixture and 75% GVL-water mixture. The initial molecular configurations were generated from force-field molecular dynamics simulation as described previously. The HMF, solvent molecules, and solvent additives were placed in a $30 \times 30 \times 30$ Å^3 box. The 75 wt% acetone–water system consists of 168 acetone, 180 H_2O, 10 HMF, 10 H_3O^+, and 10 Cl$^-$. The 75 wt% GVL–water system consists of 97 GVL, 180 H_2O, 10 H_3O^+, and 10 Cl$^-$.

Ab initio molecular dynamics with umbrella sampling technique was used to calculate reaction free energies and activation free energies for each elementary step (Supplementary Figures 4.4–4.10). The samplings were carried out under the same conditions as the unbiased AIMD runs. All of the calculations utilized multiple sampling windows distributed over their specific reaction coordinate, presented in Supplementary Figures 4.11–4.17. Additional windows were supplied at reaction coordinates located near transition states to ensure sufficient overlapping of sampled configurations between adjacent windows. In each sampling window, the molecular systems were further

equilibrated for 5 picoseconds followed by 15 picoseconds of data collection. Free energy

profiles were obtained using Weight Histogram Analysis Method (WHAM).[139]

All reaction coordinates used in this work were defined based on coordination

number:

$$CN_{ij} = \frac{1-(d_{ij}/c)^9}{1-(d_{ij}/c)^{14}} \tag{4.2}$$

where CN_{ij} is a coordination number of atom i with respect to atom j, d_{ij} is a distance

between atom i and j in angstroms, and c is a variable that controls the shape of equation

(4.2). The c parameter was set to 1.3 for coordination numbers involving C–H as well as

O–H bonds and 1.8 for the longer C–O and C–C bonds.

4.2.1 Reaction coordinates for glucose isomerization

Free energy calculations of glucose isomerization were performed on a

deprotonated, adsorbed glucose (Supplementary Figure 4.3). The reaction coordinate for a

hydride shift step (Supplementary Figure 4.18) was defined as:

$$\text{reaction coordinate} = CN_{C1-H} - CN_{C2-H} \tag{4.3}$$

where CN_{C1-H} and CN_{C2-H} are coordination numbers of shifting hydrogen atom with

respect to C1 and C2 carbons, respectively. A bias potential, V, was applied on each

reaction coordinate to constrain the system to target coordination numbers. The potential

function takes the harmonic form of:

134

$$V = K(CV - CV_{target})^2 \tag{4.4}$$

where K is a harmonic spring constant, CV is an instantaneous reaction coordinate described in equation (4.3), and CV_{target} is a center of the bias harmonic potential. The spring constant, K, was set to 0.7 Hartree for samplings performed using equation (4.3).

4.2.2 Reaction coordinates for fructose dehydration

Reaction coordinates for fructose dehydration were taken from our previous work[77] where the free energy samplings of fructose dehydration were performed in two stages. The first reaction coordinate corresponding to carbenium ion formation step (Supplementary Figure 4.19a) was defined as:

$$\text{reaction coordinate} = CN_{O-2H} - CN_{C-\text{all O}} \tag{4.5}$$

where CN_{O-2H} is a sum of coordination numbers of fructose hydroxyl oxygen located at C2 carbon with respect to the attached hydrogen atom and a closest water hydrogen. The $CN_{C-\text{allO}}$ term is a sum of coordination numbers for the C2 carbon of fructose with respect to the C2 oxygen of fructose, oxygen atoms in solvent, and the anion. This reaction coordinate describes a protonation of fructose C2 hydroxyl group followed by C–O bond cleavage. A bias potential with spring constant of 0.25 Hartree was used for samplings performed using equation (4.5).

The second reaction coordinate corresponding to a subsequent proton abstraction step (Supplementary Figure 4.19b) was defined as follows:

$$\text{reaction coordinate} = CN_{H-Ow} - CN_{C-H} \qquad (4.6)$$

where CN_{C-H} is a coordination number of C1 fructose carbon to a cleaving proton, and CN_{H-Ow} is a coordination number of the cleaving proton to the oxygen atom of the closest water molecule. The samplings were performed using bias potential with spring constant of 0.6 Hartree. At each time step, the water molecule associated with CN_{H-O} term is selected using the following distance equation:

$$d_{H-Ow} = \frac{\sum\limits_{i \in O_{all}} d_{H-i} \exp(200 * CN_{H-i})}{\sum\limits_{i \in O_{all}} \exp(200 * CN_{H-i})} \qquad (4.7)$$

where d_{H-Ow} is a distance from the cleaving proton to oxygen atom of the closest water molecule, and O_{all} is a set of all solvent oxygen and chloride atoms. The parameter c used in CN calculations was set to 1.8 in equation (4.2). A potential wall was also applied on the reaction coordinates for carbenium ion formation (second term of equation (4.5)) to prevent the carbenium ion from reverting to initial state. The position of potential wall was determined from the maximum observed value of the CN_{C-allO} term in the window corresponding to carbenium ion.

4.2.3 Reaction coordinates for glucose dehydration

The free energy calculations for glucose hydration were performed in three stages: glucose protonation at C2 hydroxyl group (Supplementary Figure 4.20a), C–O bond cleavage with oxygen shift (Supplementary Figure 4.20b), and oxygen shift with deprotonation at C1 hydroxyl group (Supplementary Figure 4.20c). The first reaction coordinate corresponding to glucose protonation step was defined as:

$$\text{reaction coordinate} = CN_{O-2H} \qquad (4.8)$$

where CN_{O-2H} is a sum of coordination numbers of glucose hydroxyl oxygen atom located at C2 carbon with respect to the attached hydrogen atom and the closest water hydrogen. A 0.25 Hartree spring constant was used in to constrain molecular system to target reaction coordinates.

The subsequent oxygen shift step was performed on a protonated glucose obtained from a sampling window with a target CN_{O1-2H} set to 1.85. A potential wall was applied on oxygen atom located at C2 carbon (equation (4.8)) during the free energy sampling of oxygen shift step to prevent instantaneous deprotonation of the hydroxyl group. The reaction coordinate for the oxygen shift step was defined as:

$$\text{reaction coordinate} = CN_{C2-O} - CN_{C1-O} - CN_{C-allO} \qquad (4.9)$$

where CN_{C2-O} and CN_{C1-O} are coordination numbers of ring oxygen with respect to C2 and C1 carbons, respectively. The CN_{C-allO} term is a sum of coordination numbers of glucose C2 carbon with respect to glucose O2 oxygen, oxygen atoms in solvent, and other anion. This reaction coordinate describes a C–O bond cleavage of protonated hydroxyl group at C2 carbon along with a simultaneous shifting of ring oxygen from C1 to C2 carbon. A spring constant for bias harmonic potential of 0.6 Hartree was applied. The final sampling window with a target reaction coordinate –0.8 was located near a transition state, which suggested that another reaction coordinate was needed to fully describe the dehydration reaction.

The third stage of simulation completes the oxygen shift process and simultaneously describes a deprotonation at the O1 oxygen. The simulations were performed on a final structure from sampling window using equation (4.9) with a potential wall and target reaction coordinate –0.8. The third reaction coordinate was defined as:

$$\text{reaction coordinate} = CN_{C2-O} - CN_{C1-O} - CN_{O1-H} \tag{4.10}$$

where CN_{O1-H} is a coordination number of hydroxyl oxygen located at C1 carbon with respect to the attaching hydrogen atom. A spring constant for bias harmonic potential was set to 0.35 Hartree.

4.2.4 Reaction coordinates for humins formation

Four simulation steps were used to simulate aldol addition for humins formation. These include a protonation of acetone (Supplementary Figure 4.21a), a proton abstraction of protonated acetone (Supplementary Figure 4.21b), a protonation of HMF carbonyl group (Supplementary Figure 4.21c), and an aldol addition (Supplementary Figure 4.21d). The first reaction coordinate corresponding to acetone protonation step was defined as:

$$\text{reaction coordinate} = CN_{Oace-H} - CN_{H-Ow} \tag{4.11}$$

where CN_{Oace-H} is a coordination number of acetone oxygen to a hydrogen atom of water molecules, and CN_{H-Ow} is a coordination number of the hydrogen to an oxygen atom of the closest water molecule. A 0.35 Hartree spring constant for bias harmonic potential was applied. A final structure from sampling window with a target reaction coordinate of 0.42 was used to simulate the subsequent proton abstraction of protonated acetone with a potential wall applied. The reaction coordinate of such process was defined as:

$$\text{reaction coordinate} = CN_{H-\text{Ow}} - CN_{C-H} \tag{4.12}$$

where CN_{C-H} is a coordination number of acetone carbon to a cleaving proton, and $CN_{H-\text{Ow}}$ is a coordination number of the cleaving proton to oxygen atom of the closest water molecule. The simulations were performed with bias potential with spring constant of 0.6 Hartree. The first two reaction coordinates yielded acetone in enol form, which was used as initial structure for the next simulation step.

The protonation of HMF has reaction coordinate defined as:

$$\text{reaction coordinate} = CN_{OHMF-H} - CN_{H-\text{Ow}} \tag{4.13}$$

where CN_{OHMF-H} is a coordination number of HMF carbonyl oxygen to a hydrogen atom of water molecules, and $CN_{H-\text{Ow}}$ is a coordination number of the hydrogen to an oxygen atom of the closest water molecule. A bias potential with spring constant of 0.35 Hartree was used. A final structure from sampling window with a target reaction coordinate of 0.06 was used to simulate the subsequent aldol addition step with potential wall from equation (4.13) applied to prevent instantaneous deprotonation of HMF. The reaction coordinate of the aldol addition step was defined as:

$$\text{reaction coordinate} = CN_{Cace-CHMF} \tag{4.14}$$

where $CN_{Cace-CHMF}$ is a coordination number of acetone carbon atom to HMF C1 carbon atom. The sampling on this coordinate utilized a harmonic potential with spring constant of 2.0 Hartree. A final structure from the simulations was a protonated aldol adduct which could undergo a deprotonation to yield a neutral aldol adduct.

4.3 Results and Discussions

The conversion of glucose to HMF involves multiple key intermediates shown in Figure 4.1. The HMF is produced from the dehydration of glucose using Brønsted acid. Alternatively, the glucose can be converted to fructose using Sn-BEA isomerization catalyst, which subsequently undergoes multiple Brønsted acid-catalyzed dehydrations to form HMF. We use *ab initio* molecular dynamics simulations to calculate the activation energies and reaction energies for the dehydration of glucose to HMF, glucose isomerization to fructose, and fructose dehydration to HMF in order to identify the most favorable reaction path. The calculated result for reactions leading to formation of humins is compared with the HMF production path to elucidate the effects of acetone–water solvent mixtures on reaction kinetics and selectivity toward HMF.

Recent experimental studies have shown that humins formation is largely the result of aldol addition of HMF to other carbonylic species side products.[176–178] The structures of the humins that form during glucose conversion, however, are diverse and not well-studied. In this work, we examined Brønsted-acid catalyzed aldol addition reaction between HMF and acetone as a probe of the aldol addition reactions that lead to the formation of humins. The degradation of HMF into levulinic acid and formic acid was not considered due to the large number of elementary steps involved[61] and the low yield observed experimentally. The calculated activation free energies as well as reaction free energies for the speculated elementary steps involved in the catalytic conversion of glucose to fructose, fructose to HMF, glucose to HMF, and HMF to aldol adduct are reported in Table 4.1. The reaction conditions, molecular configurations, and computational details can be found in the Methods and Supplementary Information.
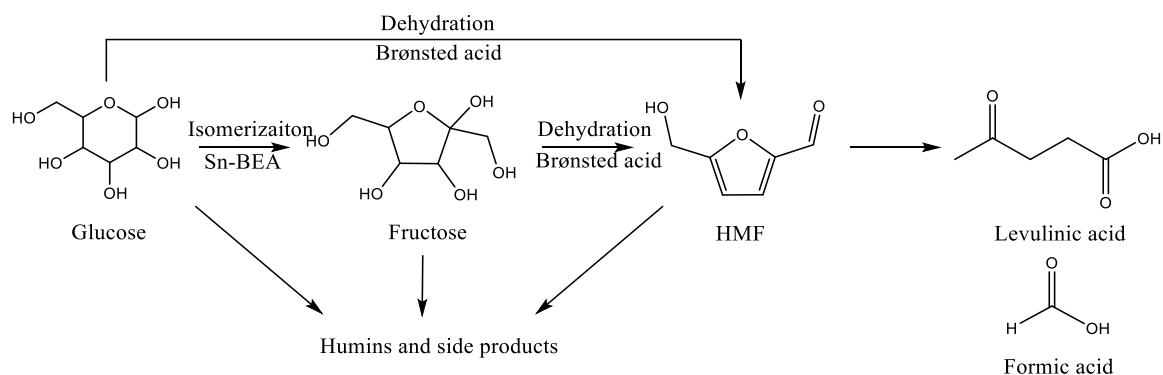
Figure 4.1 Reaction paths for the conversion of glucose to HMF.

4.3.1 Glucose isomerization

The use of fructose as a feedstock for the production of HMF is often preferred over glucose due to its high reactivity under acidic conditions. Glucose, however, can be obtained from the decomposition of lignocellulosic biomass at a much lower cost. The conversion of glucose to fructose is an effective strategy to produce carbon neutral HMF. Herein we examine the isomerization of glucose to fructose using of Sn–BEA catalyst which is known to efficiently catalyze this reaction. The reaction mechanism for glucose isomerization over Sn active site is shown in Figure 4.2.[179,180] The reaction involves a transfer of cyclic glucose from bulk solution into pores of the BEA zeolite followed by a ring opening step. The resulting linear glucose is then adsorbed onto active Sn site and subsequently deprotonates to yield a bidentate intermediate structure. The rate-determining step in the isomerization is identified to be the subsequent intramolecular hydride shift from C2 position to C1 to form a deprotonated linear fructose intermediate.[179,180]

141
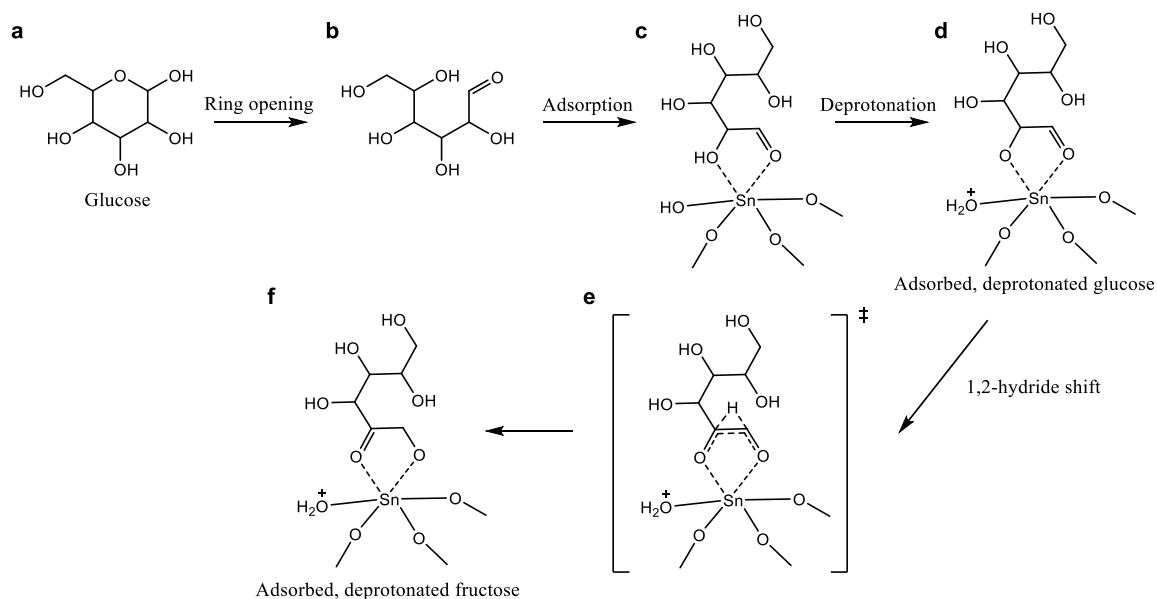
Figure 4.2 Illustration showing elementary steps for glucose isomerization to fructose catalyzed by Sn–BEA zeolite. a, 6-membered glucose; **b**, Linear glucose; **c**, Linear glucose adsorbed on the Sn active site; **d**, Deprotonated structure of linear glucose adsorbed on the Sn active site; **e**, Transition state structure of 1,2 hydride shift reaction; **f**, Structure of adsorbed, deprotonated fructose on the Sn active site.

The reaction potential energies for the glucose transfer from bulk solvent to the active site in BEA zeolite can be estimated using equation (4.1)

$$E = E(BEA \cdot Glucose) - E(BEA) - \left[E(Glucose_{gas}) + \Delta E_{solvation}(Glucose) \right] \quad (4.1)$$

where E(BEA·Glucose) is the energy of BEA structure with 6-membered ring glucose adsorbed on Sn active site in liquid phase, E(BEA) is the energy of BEA zeolite in gas phase, E(Glucose$_{gas}$) is the energy of glucose in gas phase, and $\Delta E_{solvation}$(Glucose) is the solvation free energy of glucose in solvents from gas phase. This energy for reaction in water is estimated to be –49.8 kJ mol^{-1} using zeolite cluster in gas phase with implicit solvation model.[181] The subsequent reaction potential energy of ring-opening and deprotonation steps is calculated to be 59 kJ mol^{-1}.[181] The total reaction potential energy is 9.2 kJ mol^{-1} for the glucose transfer from bulk solvent to Sn–BEA zeolite, glucose

adsorption on Sn active site, glucose ring opening, and glucose deprotonation prior to the rate-determining steps. The difference in the solvation energy of glucose in water and acetone–water mixture is typically small in comparison to the change in activation energy of chemical reactions. Therefore, we assumed 9.2 kJ mol^{-1} overall reaction energy for all the elementary steps in acetone–water mixture prior to the hydride shift step.

The intrinsic activation free energies for the isomerization of adsorbed, deprotonated glucose were calculated to be 59 kJ mol^{-1} and 62 kJ mol^{-1} in presence of water and acetone–water molecules, respectively (Supplementary Figure 4.22 a–d). These results are in good agreement with other previous computational results (~60 kJ mol^{-1}) carried out without solvent molecules.[179,182] The apparent activation free energies for the glucose isomerization based on the solvated glucose in bulk phase thus become 68.2 kJ mol^{-1} and 71.2 kJ mol^{-1} in water and acetone–water systems, respectively. The comparable activation free energies in both systems suggest that the solvent molecules in zeolite have minimal effects on the reaction rate. A close inspection of the transition state structures of hydride-shift for reactions in water and acetone–water (Figures 4.3a and 4.3b, respectively) shows the most stable structure of deprotonated glucose molecule adsorbed on the Sn active site. The shifting hydrogen atom is oriented facing the zeolite wall and thus is shielded from solvent molecules presented in the zeolite pore, prohibiting direct interaction between the hydride-shift active center and solvent molecules. As such, the isomerization of glucose to fructose should be carried out in water solvent to avoid the low glucose solubility limit in acetone–water solvents and to circumvent the cost of solvent separation.
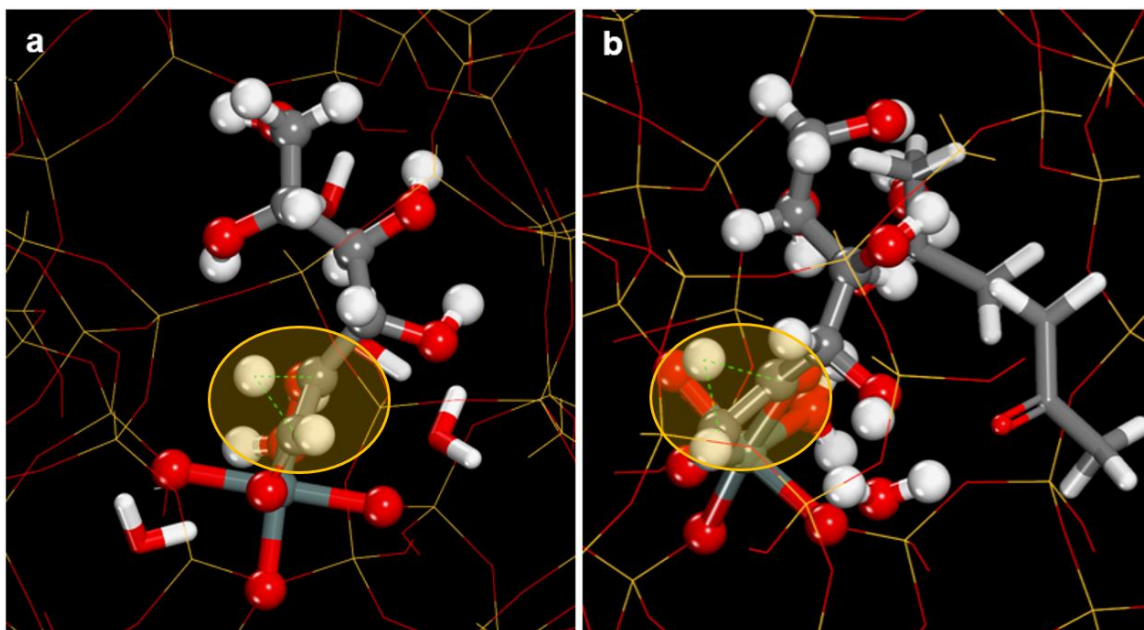
Figure 4.3 Cross sectional images of Sn–BEA zeolite showing transition states in the hydride shift step for system containing water molecules (**a**), and water and acetone molecules (**b**). The adsorbed glucose is bound to the Sn active site in bidentate mode. The shifting hydrogen atom is oriented facing in toward the hydrophobic zeolite wall, resulting in solvent shielding from the reactive center at C1–C2 carbon atoms. Oxygen atoms are shown in red, carbon atoms are shown in grey, hydrogen atoms are shown in white, and silicon atoms are shown in yellow. The glucose molecule is shown in ball-and-stick representation; zeolite framework atoms are shown in wireframe representation; solvent molecules are shown in stick representation. The active site shows a Sn atom (teal-colored) in the middle of ball-and-stick $SnO_3 \cdot H_2O$ cluster. The reactive centers (highlighted in yellow) do not interact with the solvent molecules present in the zeolite pore.

Table 4.1 Reaction free energies and intrinsic activation free energies for glucose isomerization, fructose dehydration, glucose dehydration, and humins formation. All units are reported in kJ mol^{-1}.

	Reaction Free Energy/Free Energy of Activation				Total Free Energy of Activation
Glucose isomerization					
	Isomerization‡				
Sn–BEA, H$_2$O	59				59
Sn–BEA, H$_2$O/Acetone	62				62
Fructose dehydration					
	Carbenium ion formation	Deprotonation‡			
HCl, H$_2$O	50	37			87
H^{+}, 70% Acetone	42	38			80
HCL, 70% Acetone	38	30			68
Glucose dehydration					
	Protonation	Oxygen shift‡			
HCl, H$_2$O	33	103			136
H^{+}, 70% Acetone	28	100			128
HCl, 70% Acetone	18	102			120
Humins formation					
	Acetone protonation	Acetone deprotonation	HMF protonation	Aldol addition‡	
HCl, H$_2$O	37	14	37	9	97
HCl, 70% Acetone	47	9	40	7	103

4.3.2 Fructose dehydration

The Brønsted-acid catalyzed conversion of fructose to HMF involves multiple dehydration steps, where the first dehydration is rate-determining.[96] Figure 4.4 shows elementary steps involved in the first dehydration step of fructose. The reaction proceeds with a protonation of fructose at a hydroxyl group followed by a water elimination step. The oxycarbenium intermediate that forms is highly stable due to the electron pair donation from the oxygen atom present in the ring structure. A subsequent proton abstraction step

from water molecule in the solvent results in an olefin product which undergoes instantaneous dehydrations to form HMF. The protonation of fructose is possible on all five available hydroxyl groups, but the calculations were performed only for the protonation at C2 hydroxyl group as it is the only path leading to HMF product.
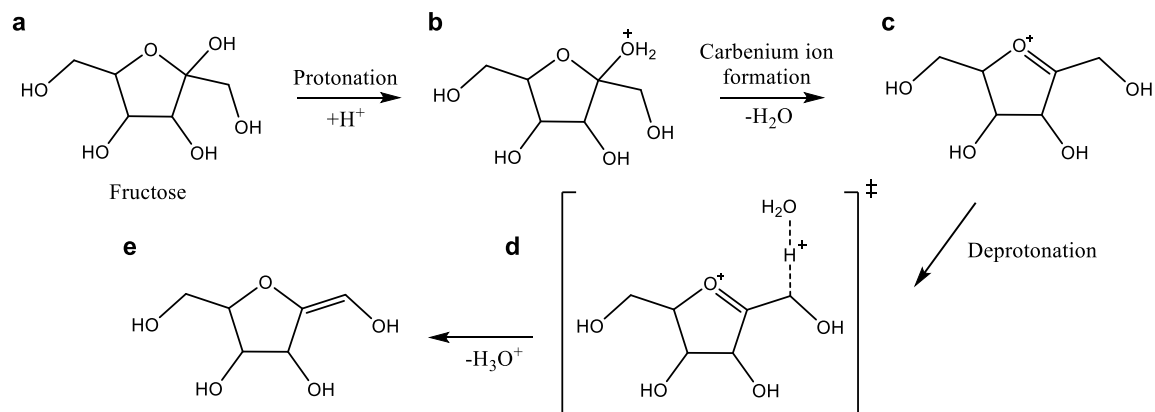
Figure 4.4 Elementary reactions for the first dehydration step of fructose to HMF using Brønsted-acid catalyst. a, 5-membered fructose; **b**, Structure of fructose protonated at C2 hydroxyl group; **c**, Oxocarbenium ion that forms after water elimination step; **d**, Transition state structure of proton abstraction step.; **e**, Olefin intermediate species.

Previous work by Mellmer at al.[76] shows that the rates and subsequent rate constants for biomass dehydration are higher in polar aprotic solvent–water mixtures than in water. The addition of metal halide anion such as chloride anion to the reaction mixtures can further improve the reaction rates and selectivities.[77] The present work investigates the influence of solvents and chloride ion on different elementary reaction paths in the conversion of glucose to HMF. *Ab initio* molecular dynamics simulations were carried out for the elementary steps shown in Figure 4.4 in liquid phase using homogeneous acid catalyst (HCl) and explicit solvent molecules. We calculated intrinsic activation energies and reaction energies as well as the overall activation free energy for the first dehydration step of fructose in pure water and in 75 wt% acetone–water mixture with HCl acid catalyst.

146

Ab initio simulations for reactions in a 75 wt% acetone–water mixture without chloride ion were also carried out to probe the effects of chloride ion on the fructose dehydration reaction.

In the acid/water system with chloride ions, the activation free energy and the reaction free energy for the protonation of fructose and the water elimination were calculated to be 65 kJ mol^{-1} and 50 kJ mol^{-1}, respectively. The resulting intermediate structure (Supplementary Figure 4.23b) for the initial dehydration is stabilized by electrons from ring oxygen atom to form oxycarbenium ion. The intrinsic activation free energy for the final proton abstraction step was calculated to be 37 kJ mol^{-1}, thus resulting in an overall apparent activation free energy of 87 kJ mol^{-1} for the first dehydration step. This number is comparable to the previously-calculated activation free energy of 93 kJ mol^{-1} for the reaction carried out at 373 K.[77] Throughout the course of the simulations, the chloride ion remains encapsulated in a solvent shell comprised of water molecules (Supplementary Figures 4.23a–c) which provides a shielding effect preventing the ion from participating in the reaction. The subsequent transformation of the olefin intermediate into hydroxymethylfurfural (HMF) is fast and therefore is not calculated.[96]

The simulations in 75 wt% acetone–water mixtures without chloride ion (Supplementary Figures 4.23d–f) resulted in a reaction free energy of 42 kJ mol^{-1} to form the carbenium ion intermediate and 38 kJ mol^{-1} intrinsic free energy of activation for the final proton abstraction step. Molecular dynamics trajectories reveal that acetone molecules in the solvent mixture promote water clustering near hydrophilic hydroxyl groups of fructose (Supplementary Figure 4.23d). The formation of hydrophilic domain allows for

proton localization near hydroxyl active site and thus facilitates the acid-catalyzed dehydration as previously observed for fructose dehydration in GVL–water mixtures. The total apparent activation free energy of 80 kJ mol^{-1} is 7 kJ mol^{-1} lower than the reaction in water and is consistent with the conclusions in our previous work.[76,77]
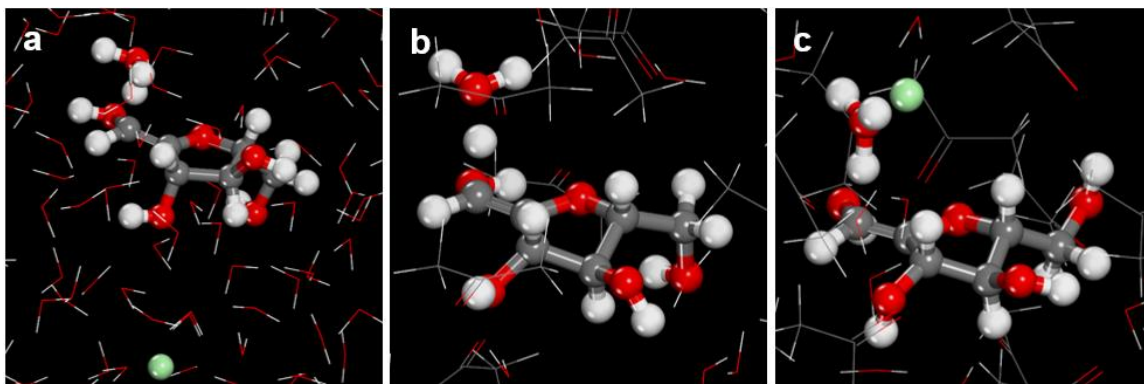
Figure 4.5 Structures of transition state of fructose dehydration reaction (**a**) in water with chloride ion, (**b**) in 75 wt% acetone without chloride ion, and (**c**) in 75 wt% acetone with chloride ion. The localization of chloride in 75 wt% acetone system near the reactive center results in stabilization of positively charged transition state by negatively charged chloride ion.

The calculations for fructose dehydration in 75 wt% acetone–water system with chloride ion were performed with the ion positioned near the C2 hydroxyl group of fructose (Supplementary Figure 4.23g). The calculated reaction free energy of carbenium ion formation and the activation free energy of subsequent proton abstraction step were found to be 38 kJ mol^{-1} and 30 kJ mol^{-1}, respectively. The overall activation free energy of 68 kJ mol^{-1} is 12 kJ mol^{-1} lower than the reaction in 75 wt% acetone–water system without chloride ion owing to the localization of chloride ion in the hydrophilic domain near reactive hydroxyl groups. Contrary to the deprotonation transition state in the pure water system (Figure 4.5a), Figure 4.5c shows the negatively charged chloride ion located on the hydrogen terminal of fructose hydroxyl group providing short-range interactions that can

stabilize the positively charged carbenium ion which further facilitates the protonation and carbenium ion formation steps. Similar stabilization of chloride ion on the transition state of fructose dehydration is also observed in other polar aprotic solvents such as γ-valerolactone (GVL)–water mixture.[77]

4.3.3 Glucose dehydration

The Brønsted-acid catalyzed conversion of glucose to HMF proceeds through three sequential water elimination steps with the first step being rate-determining.[48] Figure 4.6 illustrates reaction mechanisms for the first dehydration of 6-membered ring glucose. The protonation of glucose can proceed at all five hydroxyl groups, but only the protonation of hydroxyl group positioned at C2 carbon (Figure 4.6b) can lead to HMF formation. The subsequent elimination of water from the protonated glucose occurs simultaneously with O5–C1 bond cleavage and O5–C2 bond formation, resulting in an oxygen shift from the C1 to C2 carbon (Figure 4.6c). The positively charged 5-membered ring structure readily deprotonates at O1 position to form a ketone intermediate (Figure 4.6d), which further dehydrates to HMF. *Ab initio* molecular dynamics simulations were used to calculate the intrinsic activation free energies as well as overall activation free energies for the reaction in pure water with HCl, in 75 wt% acetone–water with HCl, and in 75 wt% acetone–water without chloride ion.
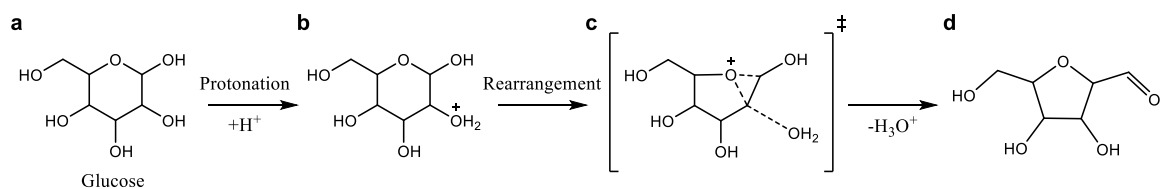
Figure 4.6 Elementary reactions for the first step in the dehydration of glucose to HMF using Brønsted-acid catalyst. **a**, 6-membered ring glucose; **b**, Structure of glucose protonated at C2 hydroxyl group; **c**, Transition state for the simultaneous water elimination and oxygen shift step; **d**, Deprotonated product

The activation free energy for the protonation of glucose in water to form the protonated intermediate (Figure 4.6b) was calculated to be 33 kJ mol^{-1}. As with the dehydration of fructose in water, the chloride ion remains fully solvated in bulk water and does not interact with the reactive species (Supplementary Figures 4.24a–c). The activation free energy for the subsequent C–O bond cleavage and oxygen shift step was calculated to be 103 kJ mol^{-1}. The overall apparent activation free energy for the first dehydration step was calculated to be 136 kJ mol^{-1} which is 49 kJ mol^{-1} higher than the apparent free energy barrier for fructose dehydration in water, likely due to the rig constraint caused by the transformation from 6-membered ring to 5-membered ring. The subsequent transformation of the ketone intermediate to HMF is lower in energy and thus not considered.[59] The relatively high activation energy of glucose dehydration and the slightly endothermic reaction energy for glucose isomerization to fructose suggest that the production of HMF from glucose via isomerization is preferred over the direct dehydration, consistent with the results and strategies proposed by Dumesic et el.[82] that isomerizes glucose to fructose in order to maximize HMF yield and conversion.
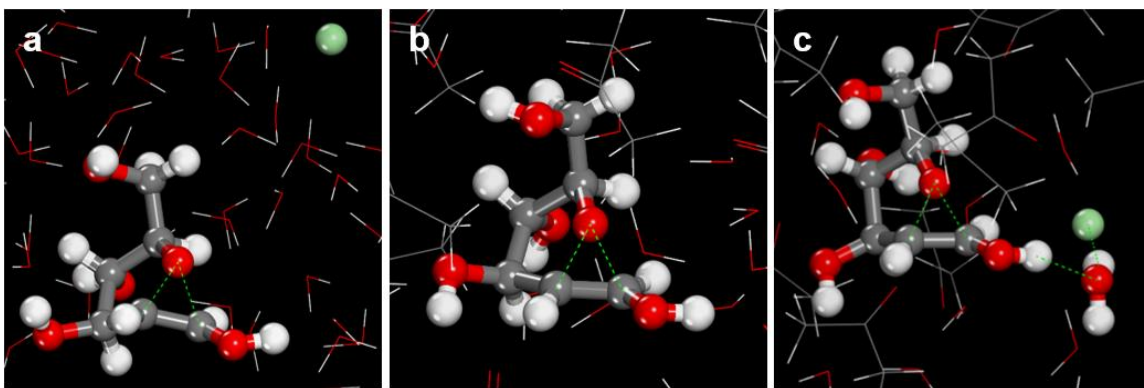
Figure 4.7 Structures of transition state of glucose dehydration reaction (**a**) in 100% water with chloride ion, (**b**) in 75 wt% acetone without chloride ion, and (**c**) in 75 wt% acetone with chloride ion. The stabilization of transition state by chloride ion is observed only in 75 wt% system.

For the reaction in 75 wt% acetone–water system without chloride ion, the activation free energy of glucose protonation step was calculated to be 28 kJ mol^{-1} (5 kJ mol^{-1} lower than the reaction carried out in pure water). This result agrees with the observation in fructose dehydration where the localization of proton near hydrophilic species facilitates the protonation (Supplementary Figure 4.24d). The activation free energy for the subsequent concerted water elimination with oxygen shift step was calculated to be 100 kJ mol^{-1}. The total apparent activation free energy of 128 kJ mol^{-1} is 8 kJ mol^{-1} lower than the reaction in water and is consistent with the solvent effects observed in fructose dehydration.

Analogous to fructose dehydration, the calculations for glucose dehydration in 75 wt% acetone–water system with chloride ion were carried out with a chloride ion positioned near the C2 hydroxyl group of glucose (Supplementary Figure 4.24g). The calculated activation free energy for glucose protonation of 18 kJ mol^{-1} is 10 kJ mol^{-1} lower than the same reaction carried out in acetone–water without the chloride ion. The activation free energy for the concerted water elimination with oxygen shift step was calculated to be

102 kJ mol^{-1} which results in an apparent free energy barrier of 120 kJ mol^{-1} for the dehydration of glucose in 75 wt% acetone–water with chloride ion. The free energy barrier is 8 kJ mol^{-1} lower than the barrier in the absence of chloride ion and thus is in good agreement with experimental observations where the dehydration of aldose sugars is enhanced upon addition of metal halides.[78–80]

The transition state complex for the dehydration of glucose reaction features the chloride ion binds to the basic water molecule located at C1 hydroxyl group (Figure 4.7c). The negative charge from chloride ion is delocalized along the hydrogen bond into the positively charged reactive center and stabilizing the transition state structure, lowering the overall activation free energy. It is worth mentioning that the transition state of glucose dehydration reaction is markedly different from that of fructose dehydration. As shown in Figure 4.7a, the transition state for the dehydration of glucose has a ring oxygen rearranging from C1 to C2 carbon, sharing the positive charge between the two carbon atoms. In contrary to the fructose dehydration, the transition state for glucose dehydration does not allow for the direct interaction between solvent molecules and the charged reactive center. Consequently, any potential interactions between ionic species such as chloride ion and the transition state of glucose dehydration will be less effective than fructose. As such, the additional 8 kJ mol^{-1} stabilization from chloride ion on the transition state of glucose dehydration in acetone–water system is lower than the 19 kJ mol^{-1} stabilization for fructose reaction.

4.3.4 Humins formation

　　　Plausible mechanisms for Brønsted acid-catalyzed aldol addition between HMF and acetone are shown in Figure 4.8. Acetone undergoes a keto-enol tautomerization (Figure 4.8a) to form an enol whereas HMF molecule can be protonated at the O1 oxygen (Figure 4.8b). The protonated HMF subsequently reacts with the enol of acetone to form an aldol adduct (Figure 4.8c). *Ab initio* molecular dynamics simulations were carried out to examine each of the elementary steps and calculate the intrinsic activation free energies, free energies of reaction, and overall apparent activation free energy in pure water and in 75 wt% acetone–water in the presence of chloride ions.
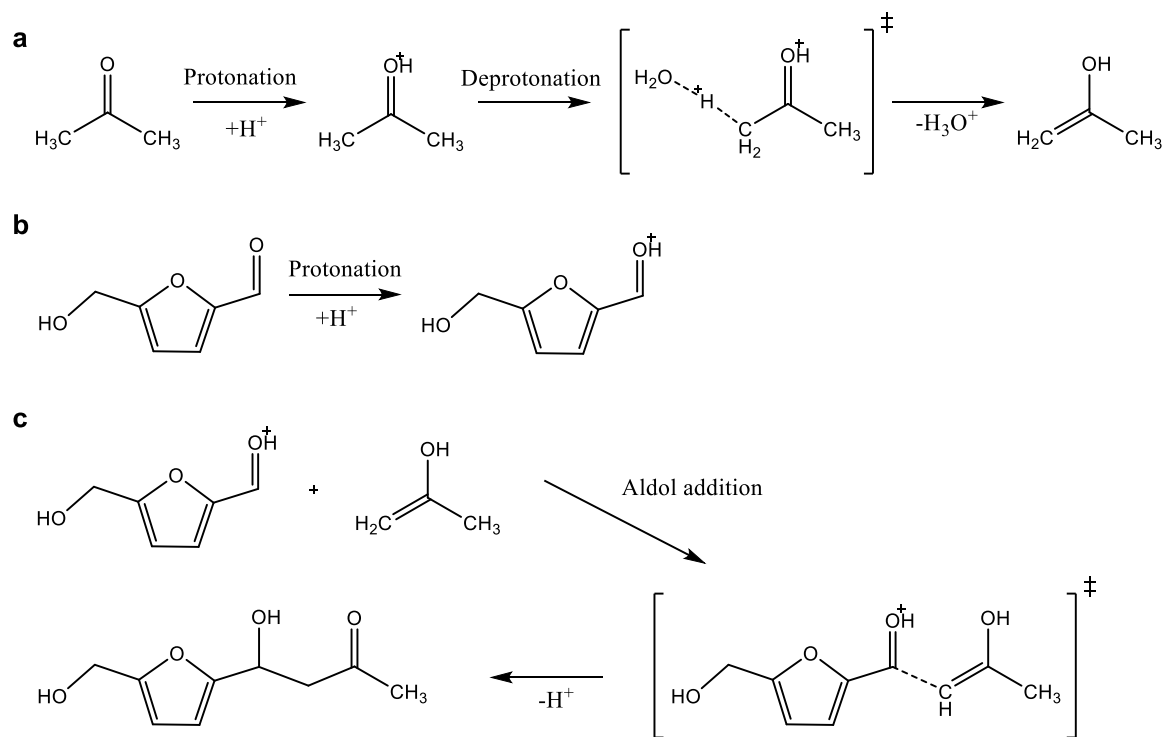
Figure 4.8 Mechanisms for Brønsted acid-catalyzed aldol addition between HMF and acetone. a, Enolization of acetone proceeds with a protonation of oxygen carbonyl, followed by a proton transfer to bulk water molecule; **b**, Protonation of HMF molecule at oxygen carbonyl; **c**, Carbon–carbon bond coupling reaction between the protonated HMF and enol acetone.

153

In the water system with chloride ions, the reaction free energies for the protonation of acetone and its subsequent deprotonation to form the enol were calculated to be 37 kJ mol^{-1} and 14 kJ mol^{-1}, respectively. The 51 kJ mol^{-1} overall reaction free energy for the keto–enol tautomerization of acetone is comparable to the 48.9 kJ mol^{-1} experimental value,[183] suggesting that acetone in enol form is less stable than the ketone form. The activation free energies for the protonation of HMF and the subsequent aldol addition were calculated to be 37 kJ mol^{-1} and 9 kJ mol^{-1}, respectively. The overall apparent activation free energy for the aldol addition of acetone and HMF in water is thus 97 kJ mol^{-1}. As with the reaction of fructose and glucose in water, the chloride ion is separated from the reactive center as shown in Figure 4.9a and, as such, does not affect the reaction energetics.
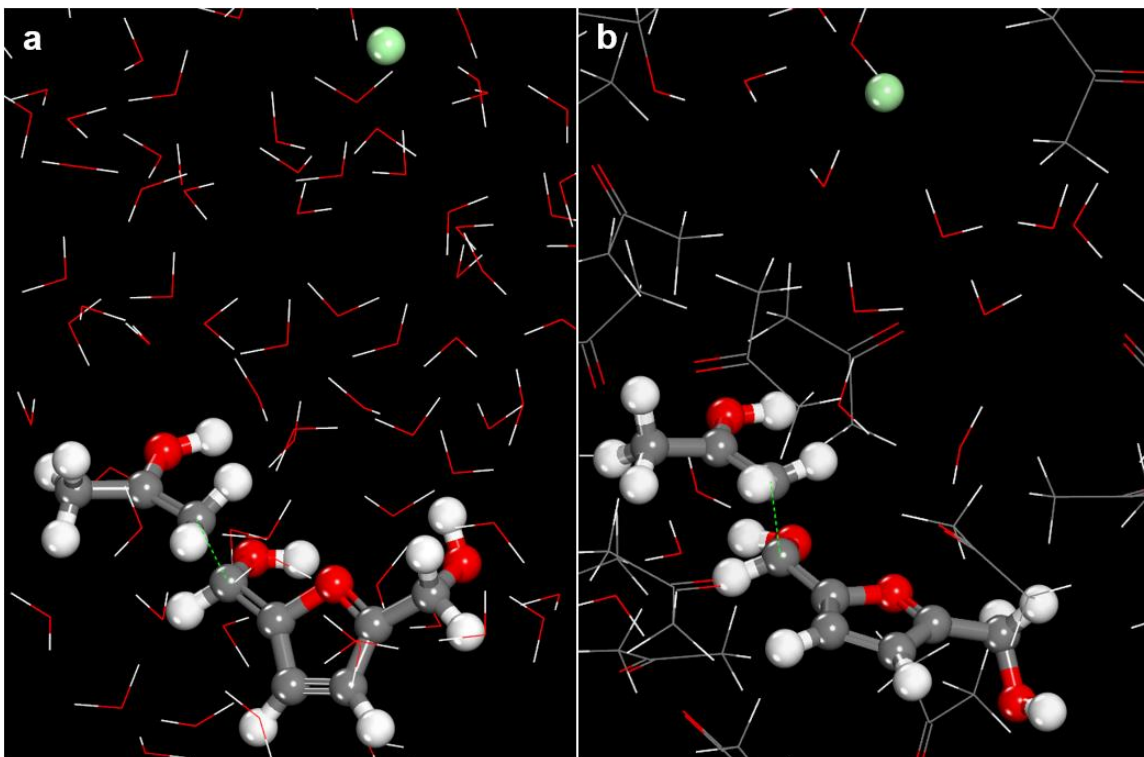
Figure 4.9 Structures of transition state for the aldol addition between acetone and HMF (**a**) in the water system with chloride ions, and (**b**) in 75 wt% acetone with chloride ions. The relatively hydrophobic acetone and HMF molecules are located in a more hydrophobic domain, while the hydrophilic chloride ion is located inside water cluster.

The calculations for aldol addition in 75 wt% acetone–water system with chloride ions resulted in a reaction free energy for acetone protonation of 47 kJ mol^{-1} and a reaction free energy for the subsequent deprotonation of 9 kJ mol^{-1} (Supplementary Figures 4.10a–b and 4.25d–e). The resulting overall reaction free energy of 56 kJ mol^{-1} for the self-tautomerization of acetone is 5 kJ mol^{-1} higher than the reaction in pure water, suggesting preferential interaction between acetone in enol form with water solvent over acetone–water mixture. The result can be explained with the fact that the hydroxyl group of enol acetone can form hydrogen bonds with water molecules and thus stabilize the solvated structure when the reaction is carried out in water. Meanwhile, the hydrogen bonding of the enol acetone with the carbonyl group of acetone solvent is much weaker and as such the acetone in enol form is less stabilized in 75 wt% acetone–water mixture.

The activation free energies for the following HMF protonation and aldol addition were calculated to be 40 kJ mol^{-1} and 7 kJ mol^{-1}, respectively. The free energy of activation for the protonation of HMF in acetone was calculated to be 3 kJ mol^{-1} higher than the reaction in water due to the fact that the carbonyl group of HMF is located in a different region from the water cluster where the proton resides (Supplementary Figure 4.25e). The protonation of HMF therefore suffers from the arose energy penalty involved with the proton transfer from the water domain to the acetone domain near HMF carbonyl group.

It should be noted that the interactions between the carbonyl group of HMF molecule and solvent molecules are markedly different from the hydroxyl group in polyols (*tert*-butanol; 1,2-propanediol; glucose; and fructose). The carbonyl group of HMF molecule is much less hydrophilic than the hydroxyl group and thus interacts weakly with

both hydrophilic and hydrophobic species. The HMF–solvent intermolecular force is therefore dictated by dipole–dipole interaction instead of the hydrogen bonding interaction. The partitioning of HMF from proton in acetone–water mixtures could be explained using the difference in dipole moments between HMF, water (1.85 D)[184], acetone (2.88 D)[184], and GVL (4.71 D).[185] The HMF molecule, bearing a carbonyl group at the reactive center, should have similar dipole moment to acetone. As such, the carbonyl group of HMF in acetone–water mixture is likely located within the more hydrophobic domain surrounded with acetones, preventing the protonation step leading to the aldol addition (Supplementary Figure 4.26). In contrast, the dipole moment of HMF will be much closer to water than GVL. Accordingly, the partitioning of GVL and water molecules in GVL–water mixture will favor the localization of HMF in the water cluster rather than the GVL domain. This explanation is consistent with experimental results where the aldol condensation in GVL–water mixtures leads to higher reaction rates than the reactions carried out in water.[186]

The effects of chloride ion on the aldol addition reaction in acetone–water is illustrated in Figure 4.9b. The chloride ion is solvated in the hydrophilic water cluster which is separated from the relatively hydrophobic reactive center in the transition state and thus has no effects on the aldol addition reaction. As a result, the 103 kJ mol^{-1} overall apparent activation free energy for the aldol addition between acetone and HMF is 6 kJ mol^{-1} higher than the same reaction in carried out water alone. The result is consistent with experimental observations that the acid-catalyzed degradation of HMF to humins is exceptionally low in acetone–water mixtures at elevated temperature.[82]

4.4 Conclusions

The effects of acetone–water mixtures along with the addition of chloride ions on the conversion of glucose to HMF and the unselective paths to form humins were investigated. *Ab initio* molecular dynamics simulations were carried out to examine the free energies associated with the elementary steps for glucose isomerization, glucose dehydration, fructose dehydration, and HMF conversion to humins. The computational results show that the solvent has little effect on the kinetics of glucose isomerization using Sn–BEA catalyst. The geometric constraints inside zeolite pores result in the shielding of the hydride shift reactive center of the transition state from solvent molecules.

The free energy barriers for the dehydration of fructose as well as the dehydration of glucose were found to be lower in pure water over the reactions carried out in acetone–water system due to the fact that the acidic proton localized in the hydrophilic domains in vicinity of reactive hydroxyl groups on fructose and glucose. Such molecular configurations can facilitate the proton transfer from bulk solvent to the hydroxyl groups and thus promote the dehydration reactions in acetone–water mixtures. The presence of chloride ions increases the rates of glucose and fructose dehydration as the chloride ion stabilize the positively charged transition states in acetone–water systems. Similar effects are not observed in the aldol addition between HMF and acetone as the HMF is located in the hydrophobic domain thus preventing its interaction with chloride ions and acidic protons that typically reside in the hydrophilic domains. Consequently, the use of acetone–water system for acid-catalyzed conversion of glucose enhances the formation rate of HMF while suppressing the humins formation, leading to HMF selectivity.

4.5 Supplementary Information
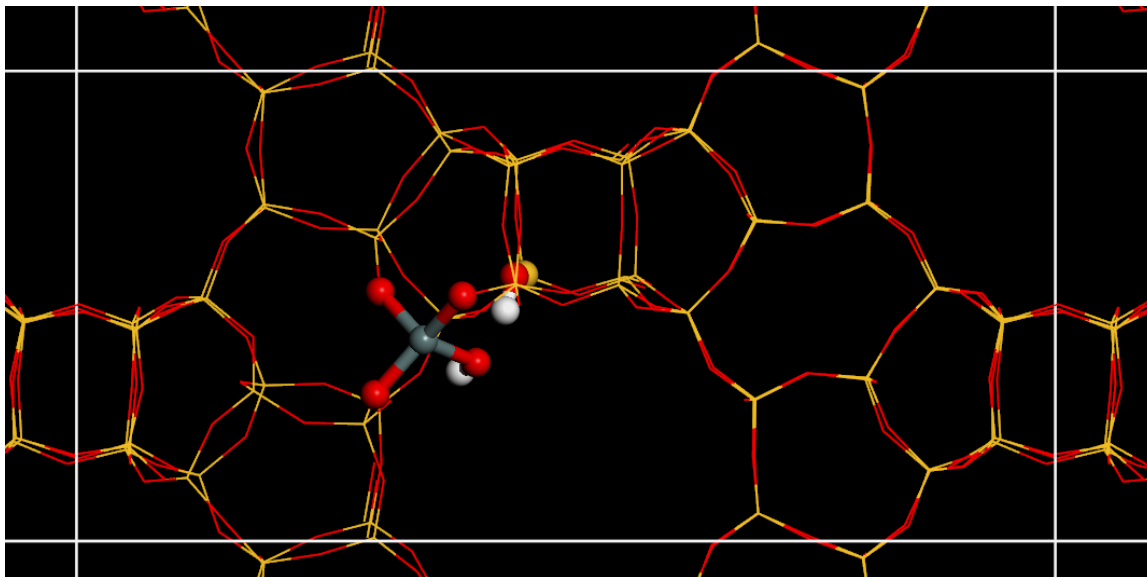
Supplementary Figure 4.1 Illustration shows a periodic structure of Sn–BEA zeolite used in the simulation of glucose isomerization with the Sn atom is located at T9 position. The $SnO_3(OH)$ active site and the adjacent silanol group are shown in ball-and-stick.
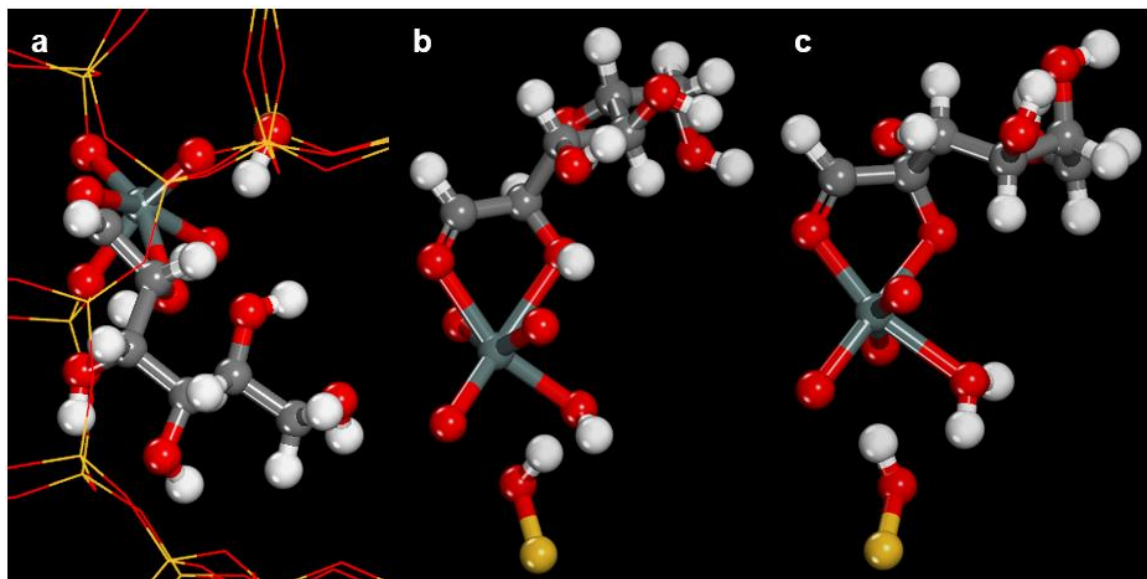
Supplementary Figure 4.2 a, Structure of linear glucose molecule adsorbed on the active site of Sn–BEA zeolite. **b,** Structure (**a**) showing only the glucose molecule, $SnO_3(OH)$ active site, and the adjacent silanol group. **c**, Structure (**b**) with the proton from C2 hydroxyl group of glucose transferred to the silanol group on the Sn site.
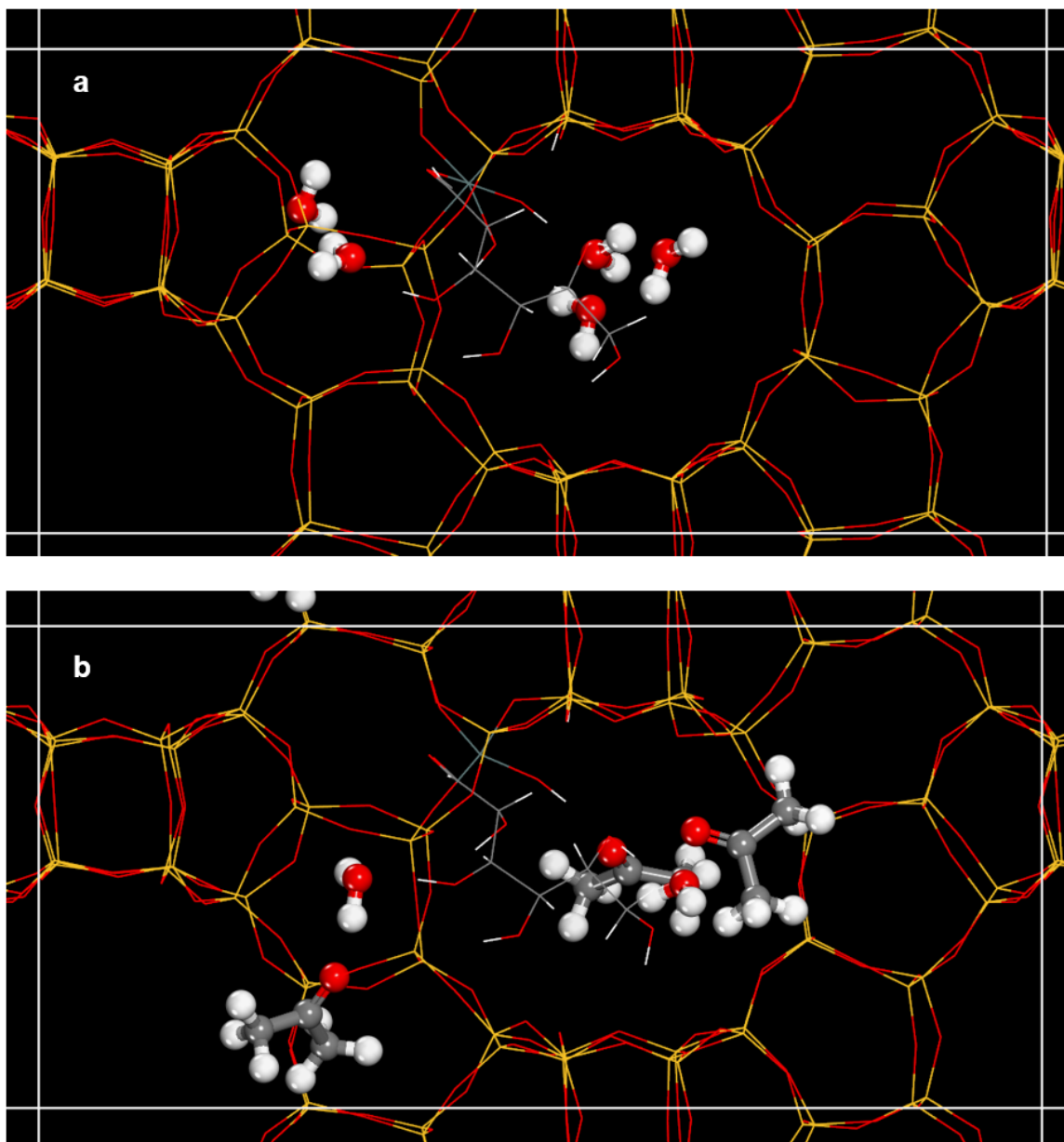
Supplementary Figure 4.3 a, A unit cell of Sn–BEA zeolite with linear glucose and five water molecules was used to simulate the isomerization reaction in water. **b,** Sn–BEA zeolite with linear glucose, two acetone, and three water molecules was used to simulate the isomerization reaction in 75 wt% acetone–water. Atoms in the zeolite framework as well as glucose are shown in lines, and solvent molecules are shown in ball-and-stick.
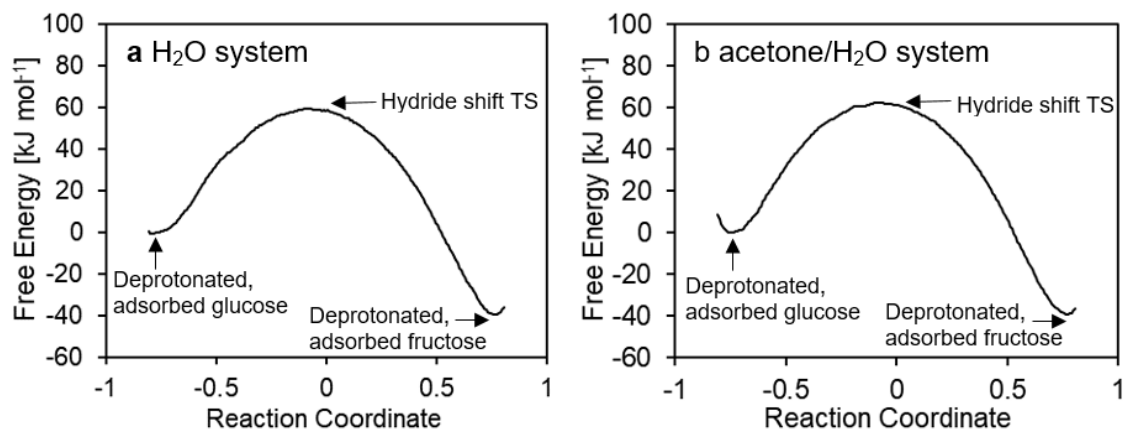
Supplementary Figure 4.4 Free energy profiles for glucose isomerization (a) in water system, (b) in acetone/ H$_2$O system.
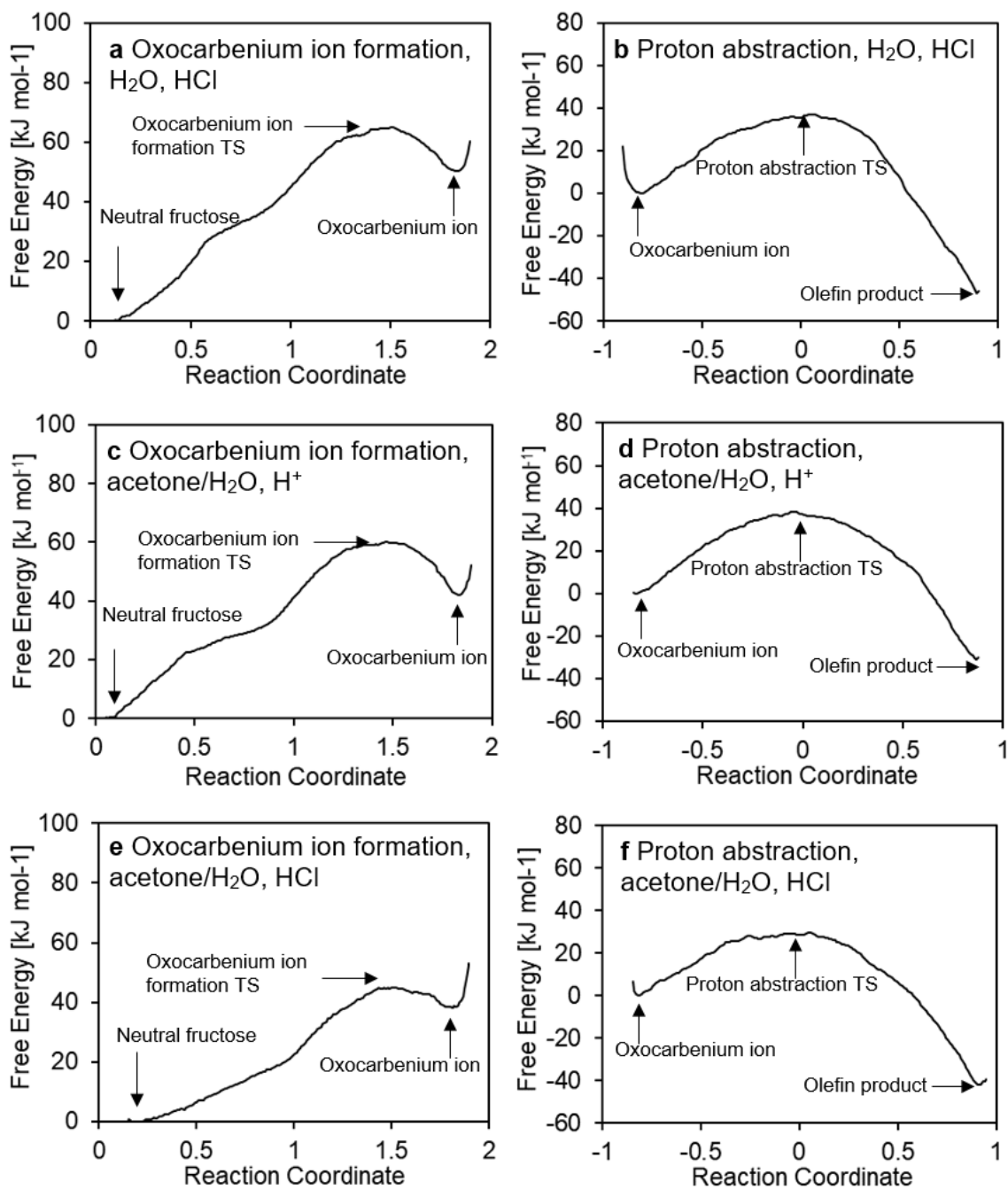
Supplementary Figure 4.5 Free energy profiles of fructose dehydration in water system with chloride ion (in **a** and **b** of the first row), in 75 wt% acetone system without chloride ion (in **c** and **d** of the second row), and in 75 wt% acetone system with chloride ion (in **e** and **f** of the third row). The first and second columns represent the oxocarbenium ion formation step and proton abstraction step, respectively.

161
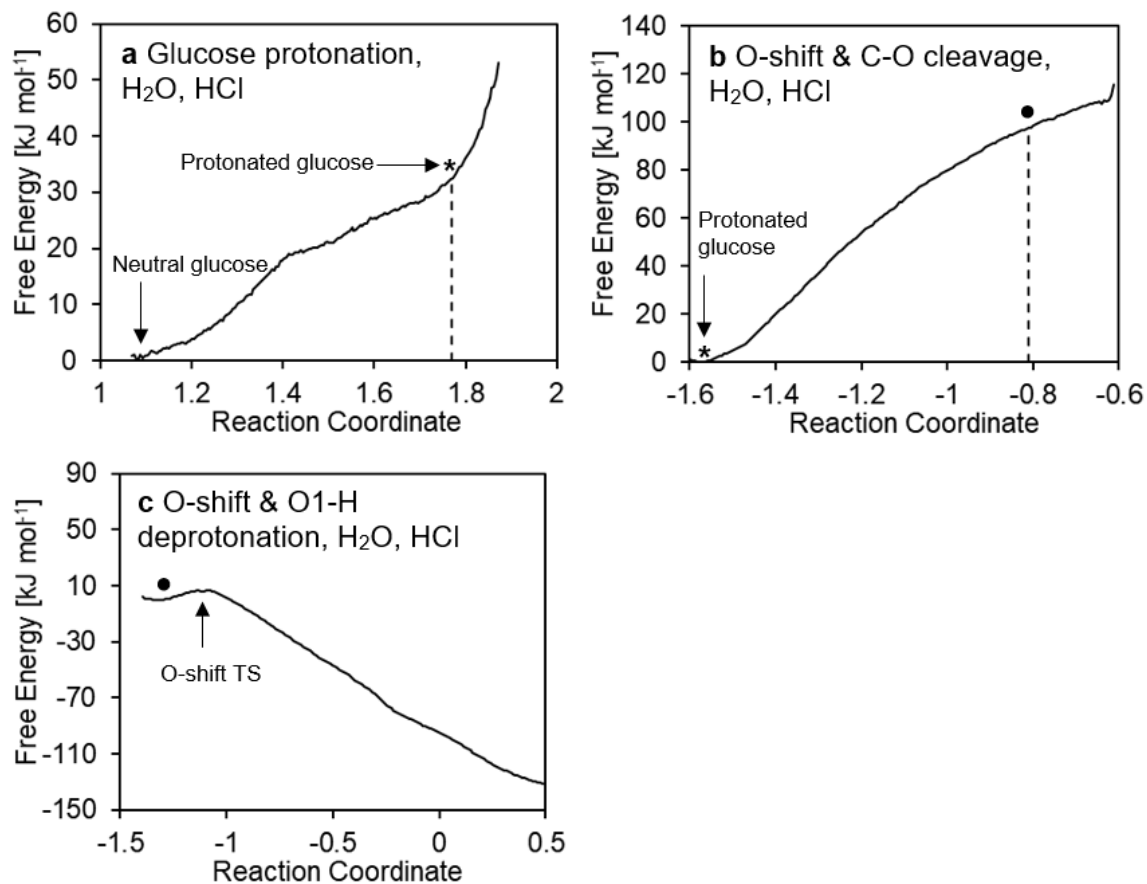
Supplementary Figure 4.6 Free energy profiles of glucose dehydration in water system with chloride ion for (**a**) glucose protonation step, (**b**) oxygen shift step with simultaneous C–O bond cleavage, and (**c**) oxygen shift step with O1–H deprotonation. The * and ● symbols denote the same energy states between plots.
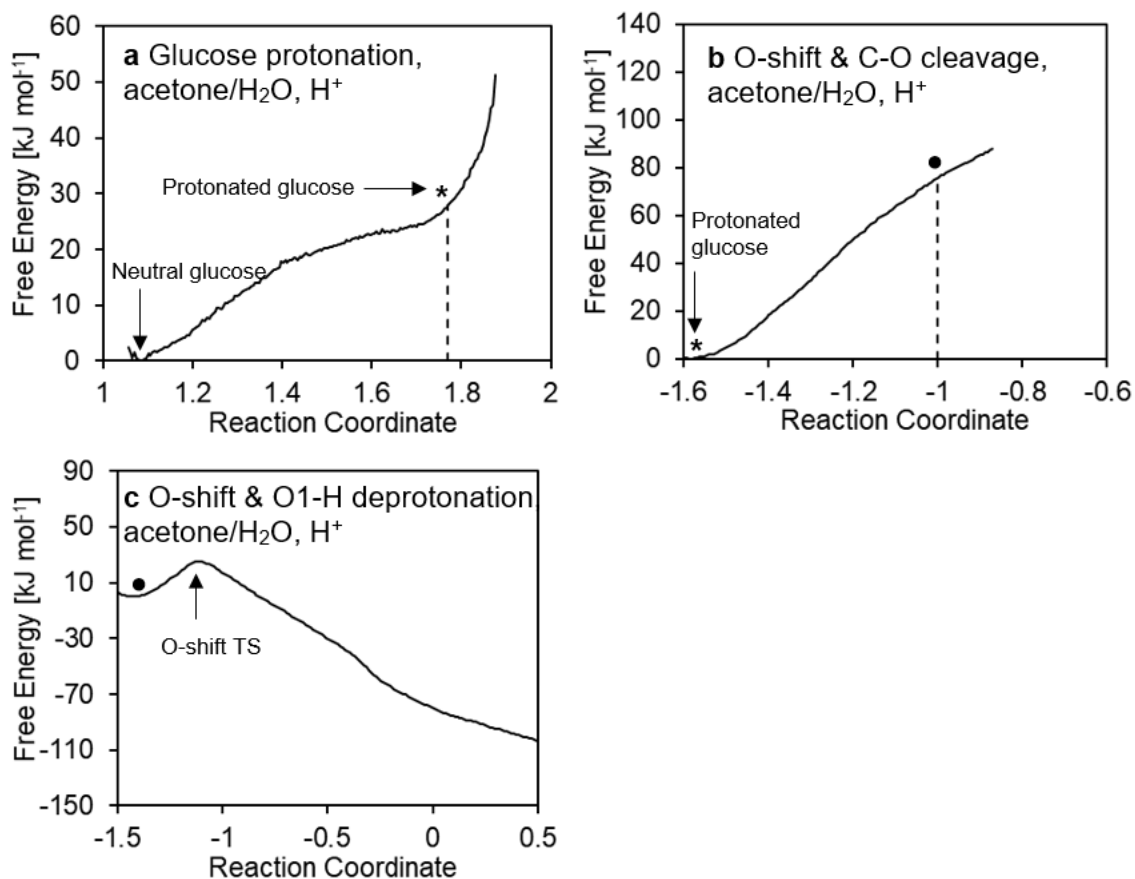
Supplementary Figure 4.7 Free energy profiles of glucose dehydration in 75 wt% acetone system without chloride ion for (**a**) glucose protonation step, (**b**) oxygen shift step with simultaneous C–O bond cleavage, and (**c**) oxygen shift step with O1–H deprotonation. The * and ● symbols denote the same energy states between plots.
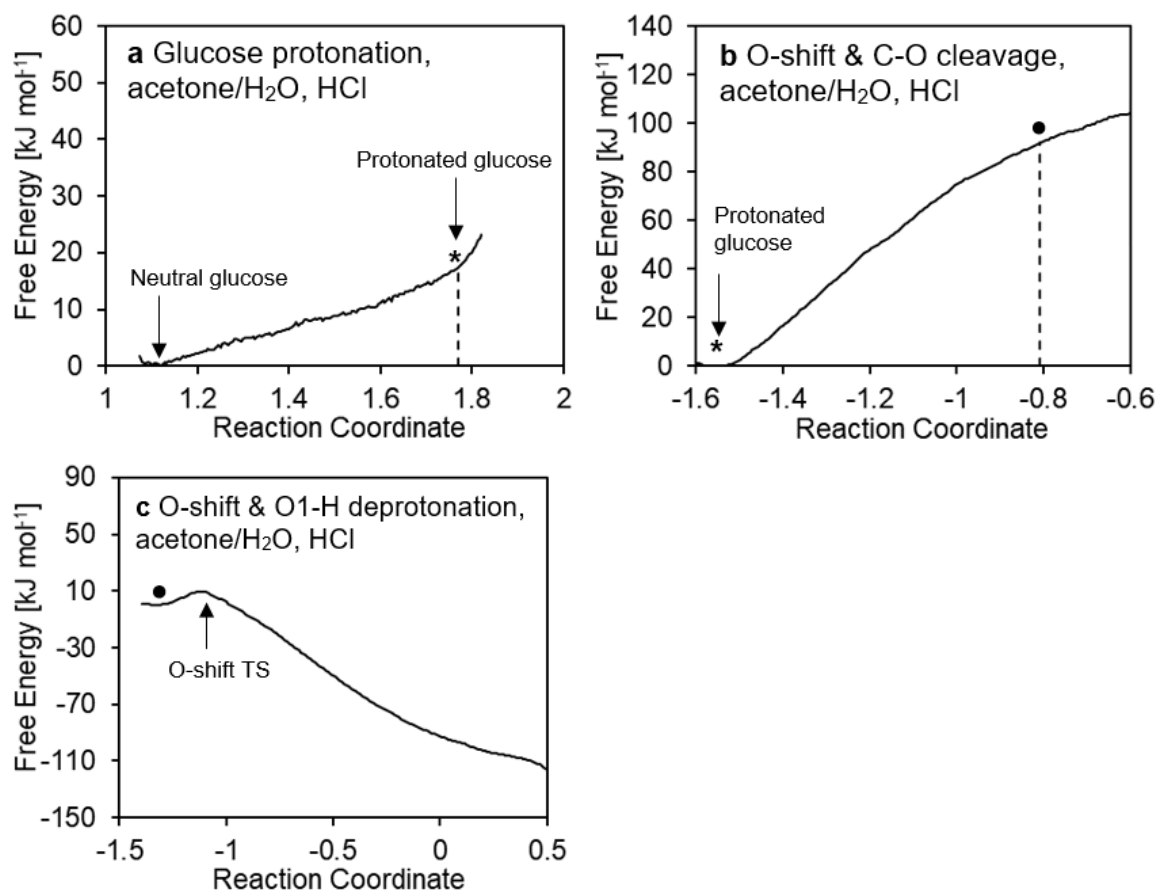
Supplementary Figure 4.8 Free energy profiles of glucose dehydration in 75 wt% acetone system with chloride ion for (**a**) glucose protonation step, (**b**) oxygen shift step with simultaneous C–O bond cleavage, and (**c**) oxygen shift step with O1–H deprotonation. The * and ● symbols denote the same energy states between plots.
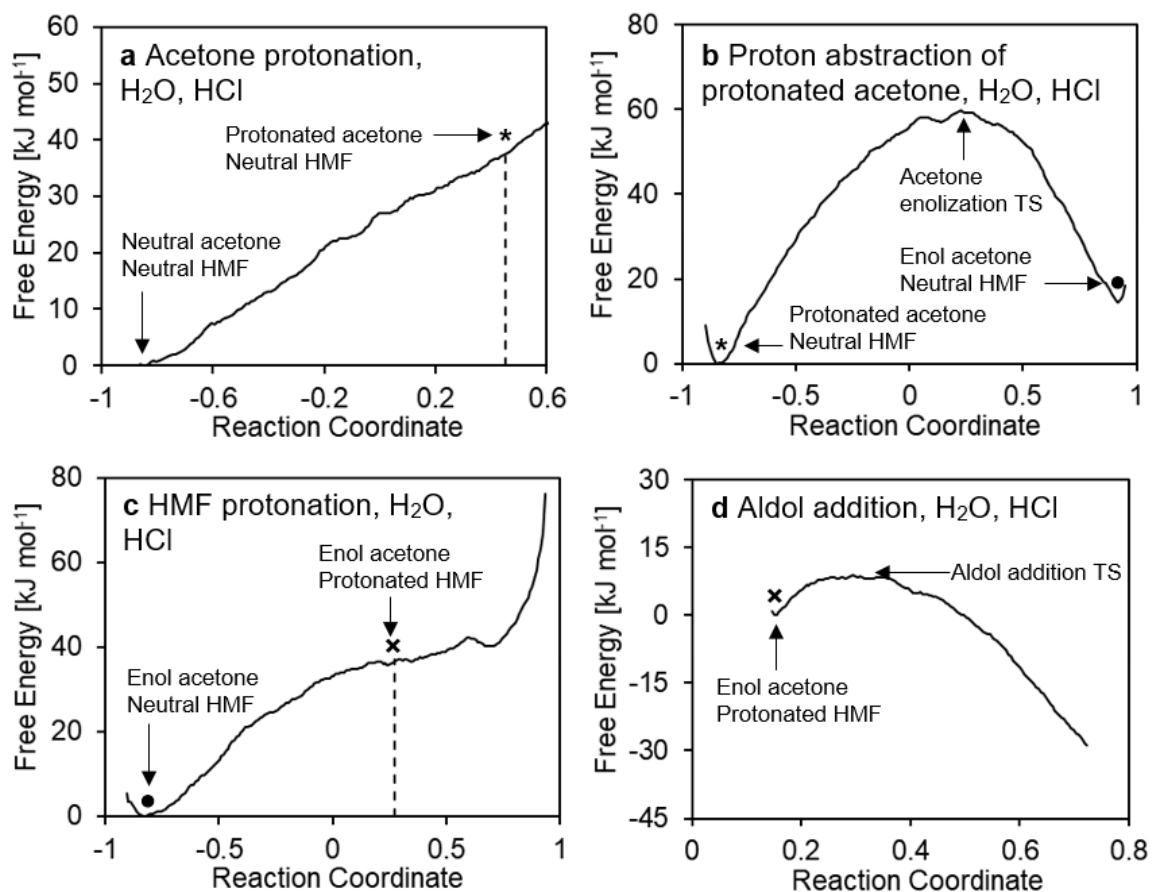
Supplementary Figure 4.9 Free energy profiles of humins formation in water system with chloride ion during (**a**) acetone protonation step, (**b**) proton abstraction step of protonated acetone, (**c**) protonation of HMF step, and (**d**) aldol addition step. The *, ●, and × symbols denote the same energy states between plots.
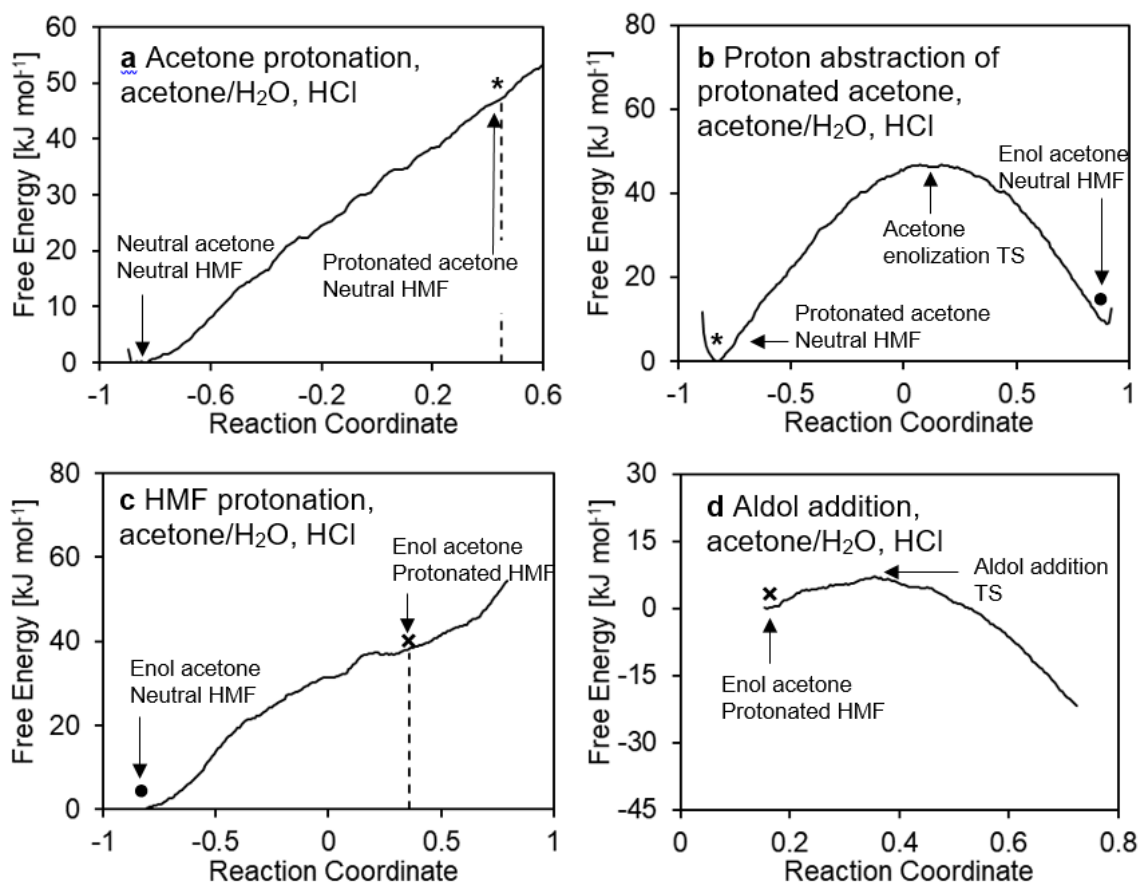
Supplementary Figure 4.10 Free energy profiles of humins formation in 75 wt% acetone system with chloride ion during (**a**) acetone protonation step, (**b**) proton abstraction step of protonated acetone, (**c**) protonation of HMF step, and (**d**) aldol addition step. The *, ●, and × symbols denote the same energy states between plots.
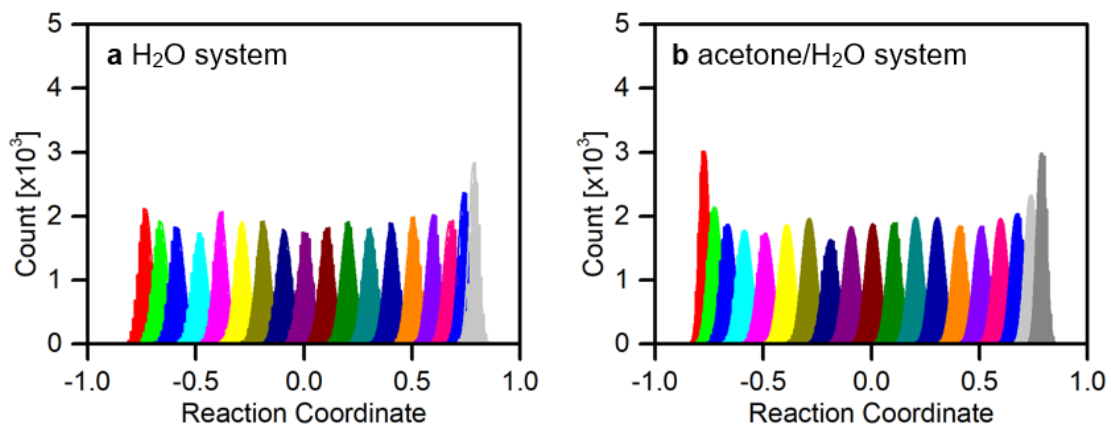
Supplementary Figure 4.11 Statistical histograms of free energy sampling for glucose isomerization (a) in water system, (b) in acetone/ H$_2$O system.
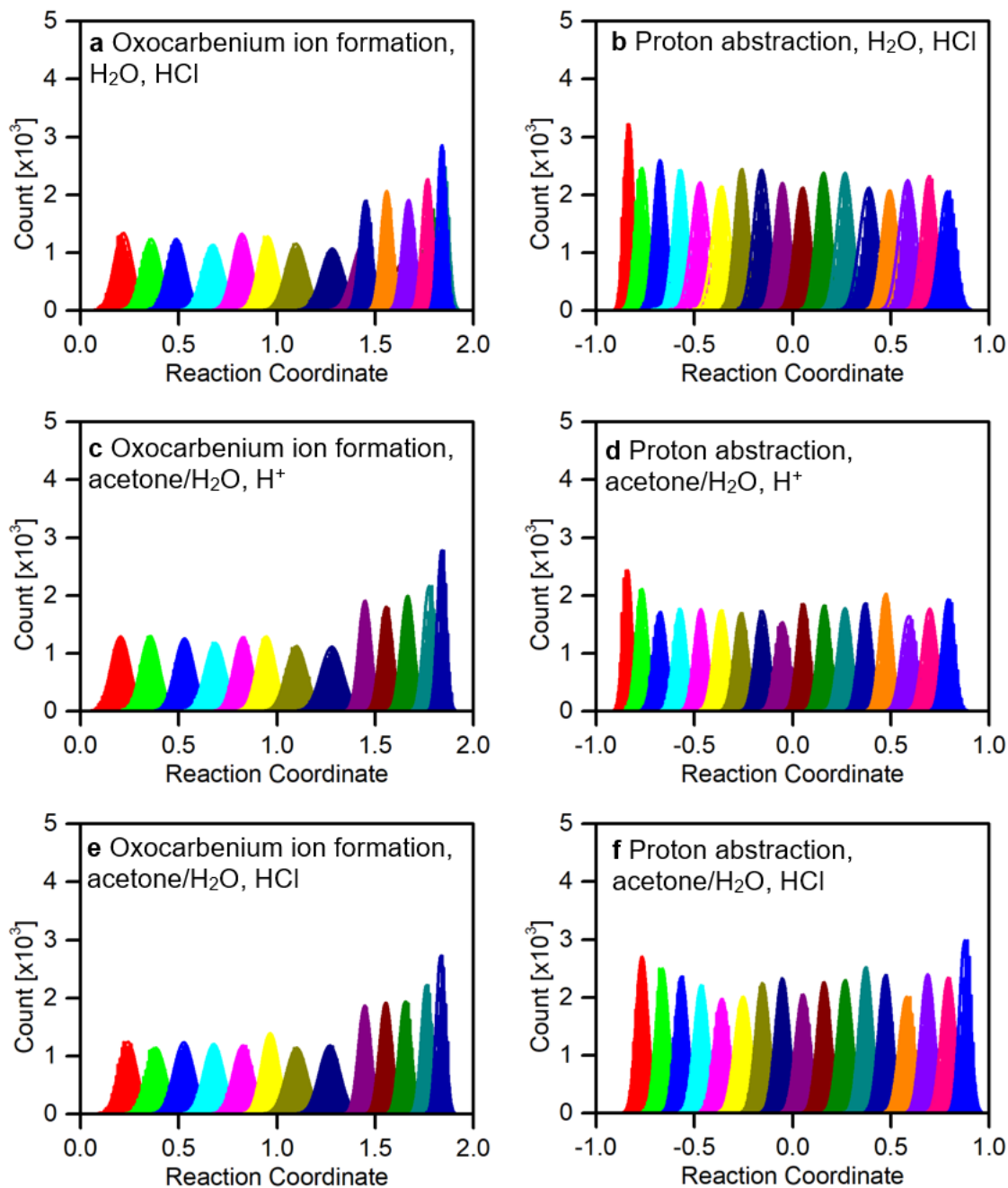
Supplementary Figure 4.12 Statistical histograms of free energy sampling for fructose dehydration in water system with chloride ion (in a and b of the first row), in 75 wt% acetone system without chloride ion (in c and d of the second row), and in 75 wt% acetone system with chloride ion (in e and f of the third row). The first and second columns represent the oxocarbenium ion formation step and proton abstraction step, respectively.
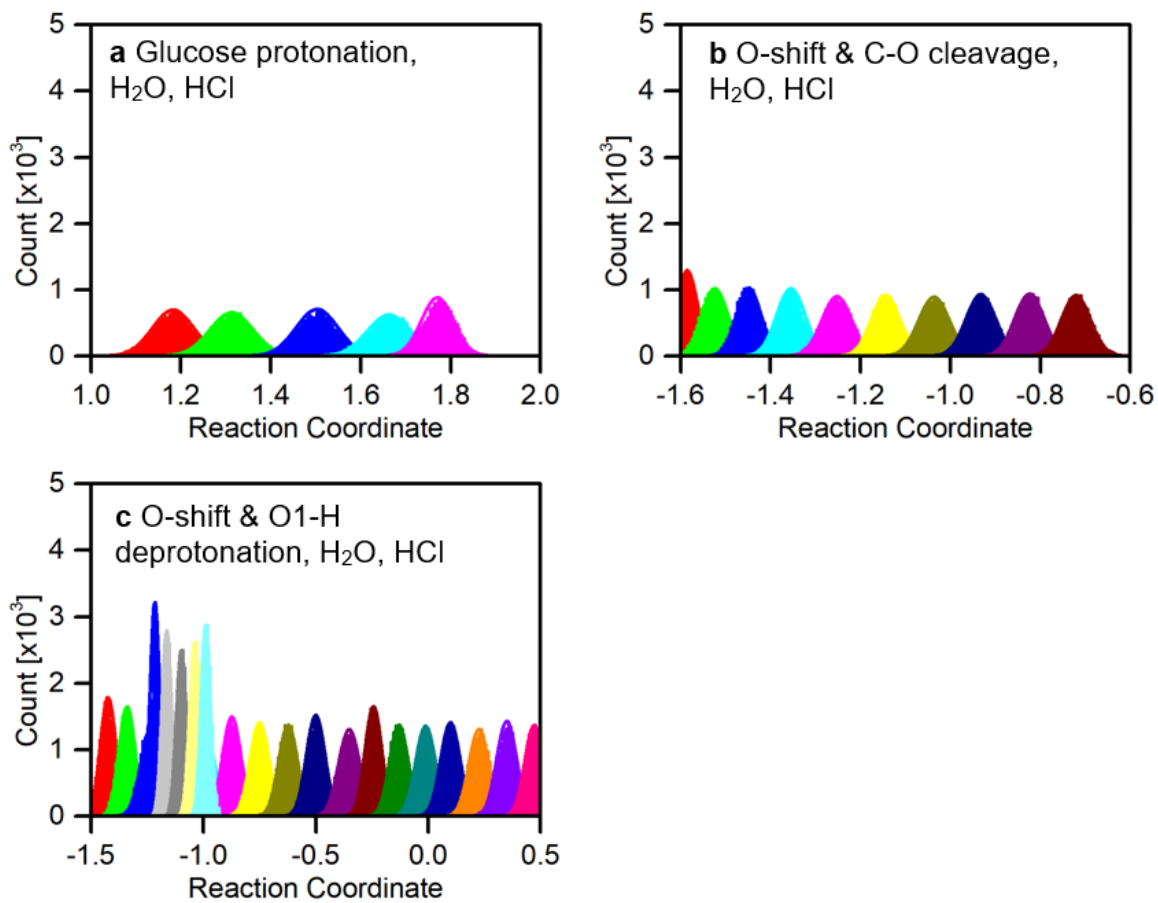
Supplementary Figure 4.13 Statistical histograms of free energy sampling for glucose dehydration in water system with chloride ion for (**a**) glucose protonation step, (**b**) oxygen shift step with simultaneous C–O bond cleavage, and (**c**) oxygen shift step with O1–H deprotonation.
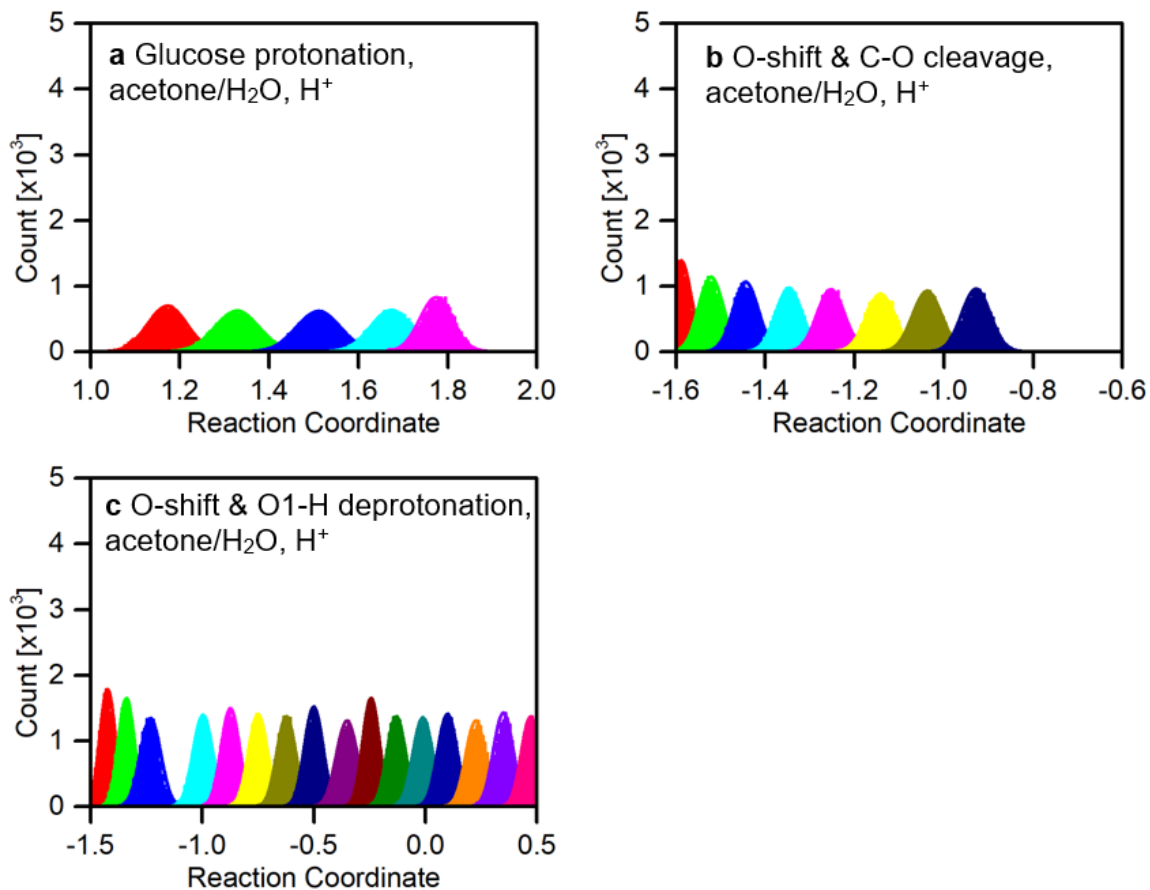
Supplementary Figure 4.14 Statistical histograms of free energy sampling for glucose dehydration in 75 wt% acetone system without chloride ion for (**a**) glucose protonation step, (**b**) oxygen shift step with simultaneous C–O bond cleavage, and (**c**) oxygen shift step with O1–H deprotonation.
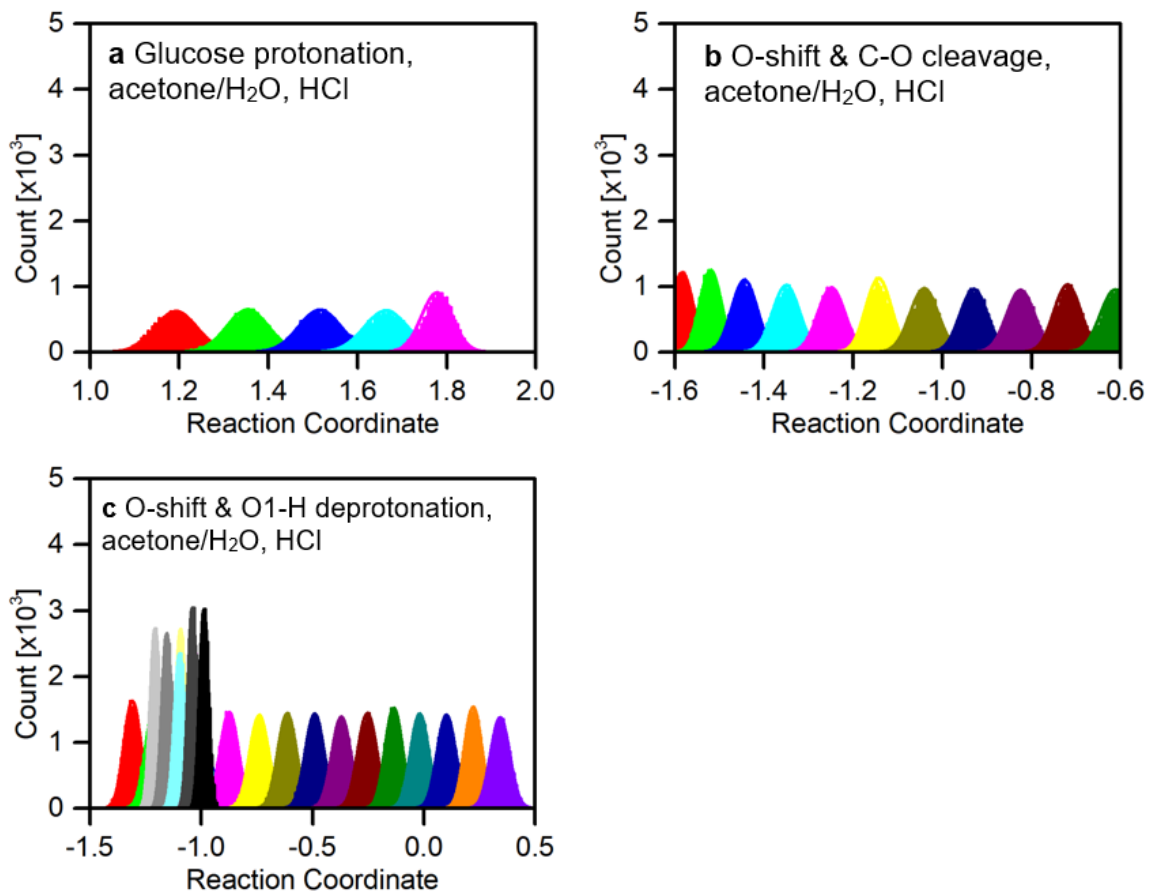
Supplementary Figure 4.15 Statistical histograms of free energy sampling for glucose dehydration in 75 wt% acetone system with chloride ion for (**a**) glucose protonation step, (**b**) oxygen shift step with simultaneous C–O bond cleavage, and (**c**) oxygen shift step with O1–H deprotonation.
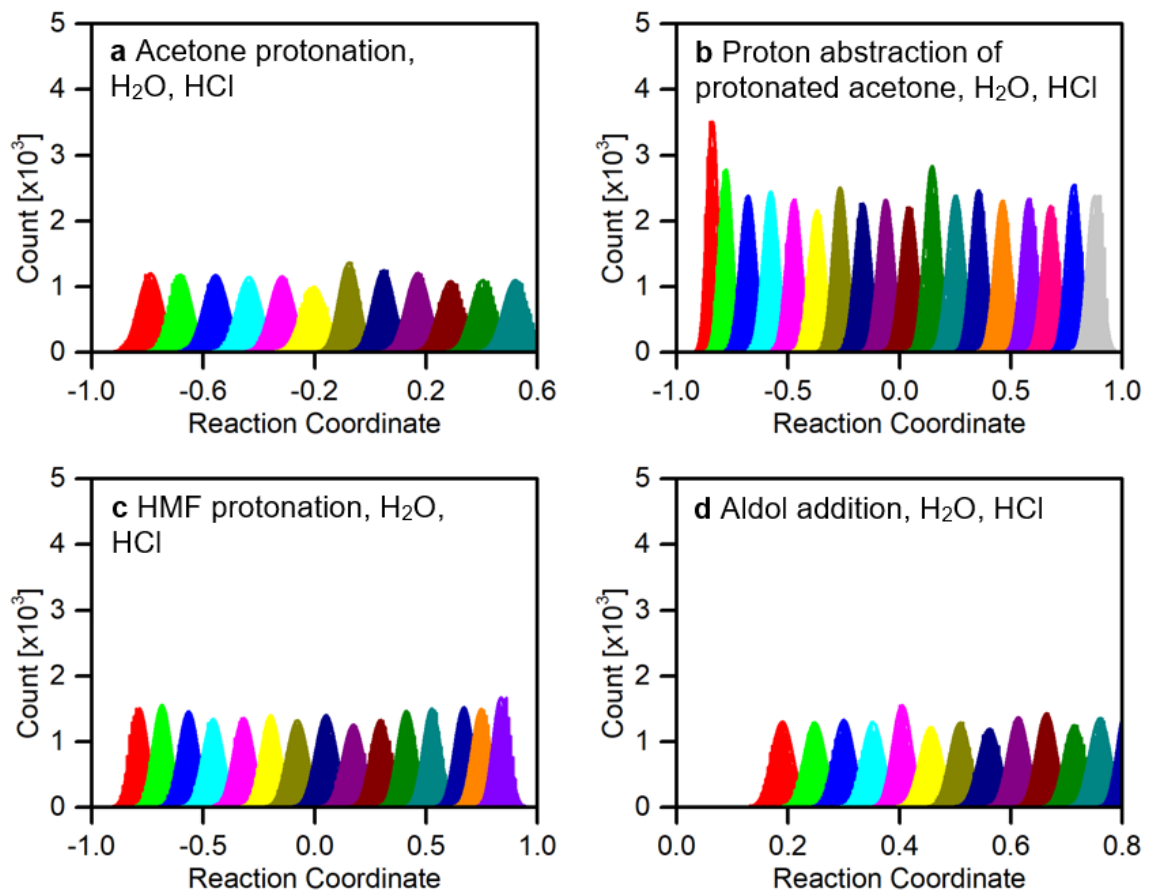
Supplementary Figure 4.16 Statistical histograms of free energy sampling for humins formation in water system with chloride ion during (**a**) acetone protonation step, (**b**) proton abstraction step of protonated acetone, (**c**) protonation of HMF step, and (**d**) aldol addition step.
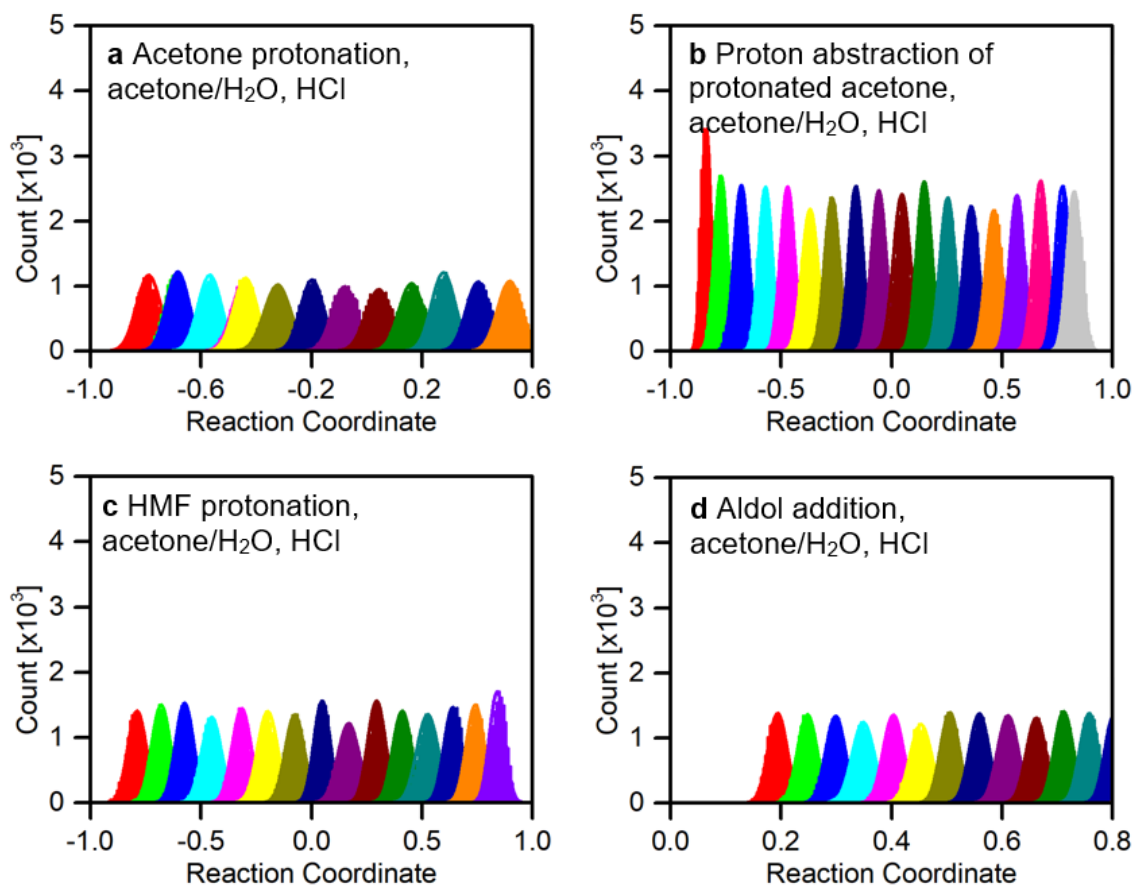
Supplementary Figure 4.17 Statistical histograms of free energy sampling for humins formation in 75 wt% acetone system with chloride ion during (**a**) acetone protonation step, (**b**) proton abstraction step of protonated acetone, (**c**) protonation of HMF step, and (**d**) aldol addition step.

$$CN_{C1-H} = CN_1$$
$$CN_{C2-H} = CN_2$$

$$\text{reaction coordinate} = CN_{C1-H} - CN_{2-H}$$
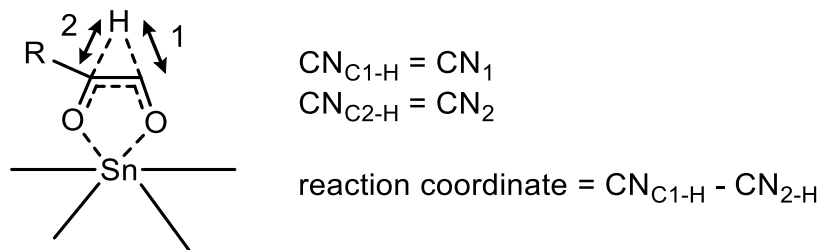
Supplementary Figure 4.18 Reaction coordinate for hydride shift step in glucose isomerization.

a

$$CN_{O-2H} = CN_1 + CN_2$$

$$CN_{C-all\,O} = CN_3 + CN_4$$

$$\text{reaction coordinate} = CN_{O-2H} - CN_{C-all\,O}$$

b

$$CN_{H-Ow} \sim CN_1$$
$$CN_{C-H} = CN_2$$

$$\text{reaction coordinate} = CN_{H-Ow} - CN_{C-H}$$
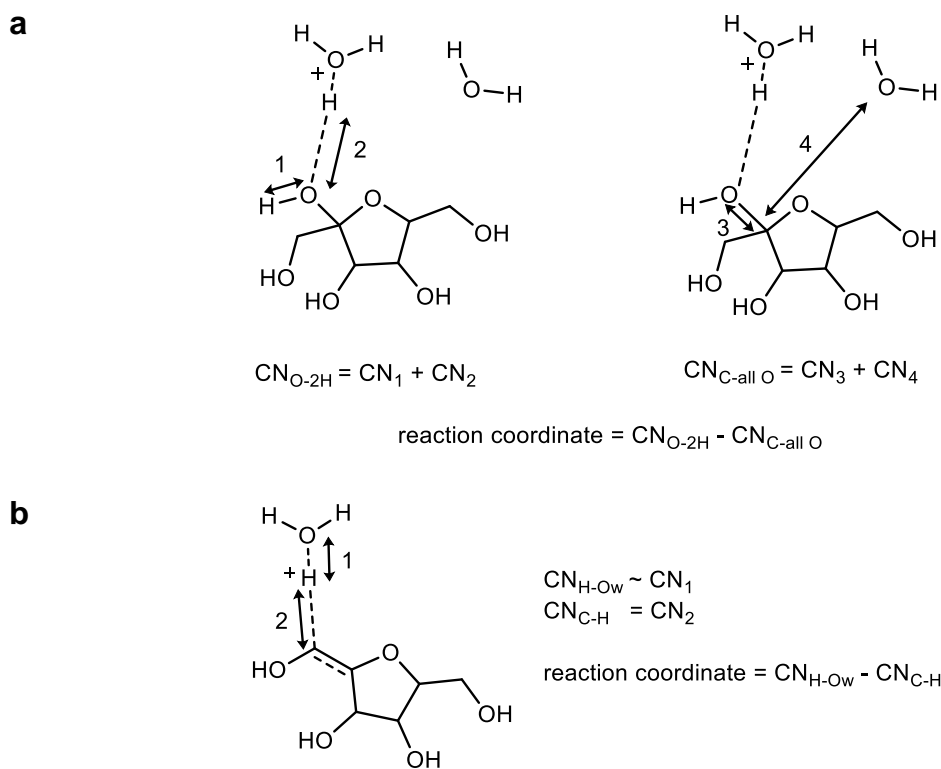
Supplementary Figure 4.19 a, Reaction coordinate for carbenium ion formation step; **b,** reaction coordinate for proton abstraction step.

a

reaction coordinate = $CN_{O-2H} = CN_1 + CN_2$

b

$CN_{C2-O} = CN_1$
$CN_{C1-O} = CN_2$
$CN_{C-allO} = CN_3 + CN_4$

reaction coordinate = $CN_{C2-O} - CN_{C1-O} - C_{C-allO}$

c

$CN_{C2-O} = CN_1$
$CN_{C1-O} = CN_2$
$CN_{O1-H} = CN_3$

reaction coordinate = $CN_{C2-O} - CN_{C1-O} - CN_{O1-H}$
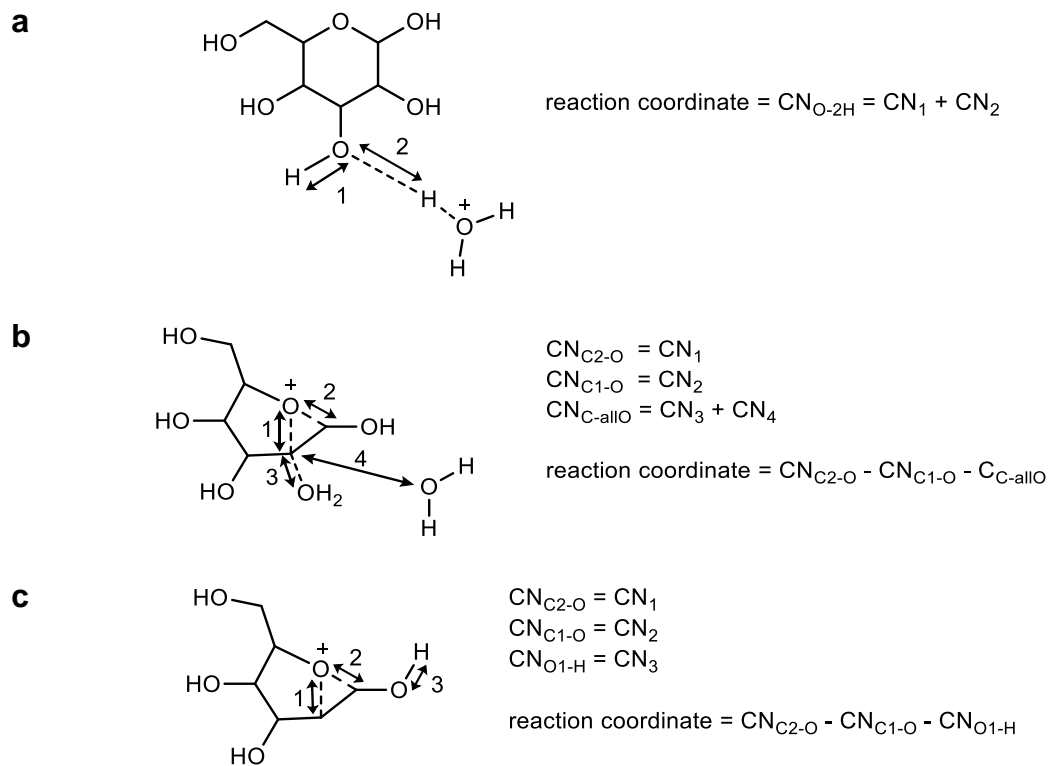
Supplementary Figure 4.20 a, Reaction coordinate for glucose protonation step; **b,** reaction coordinate for oxygen shift along with C2–O bond cleavage; **c,** reaction coordinate for oxygen shift along with deprotonation of C1 hydroxyl group.
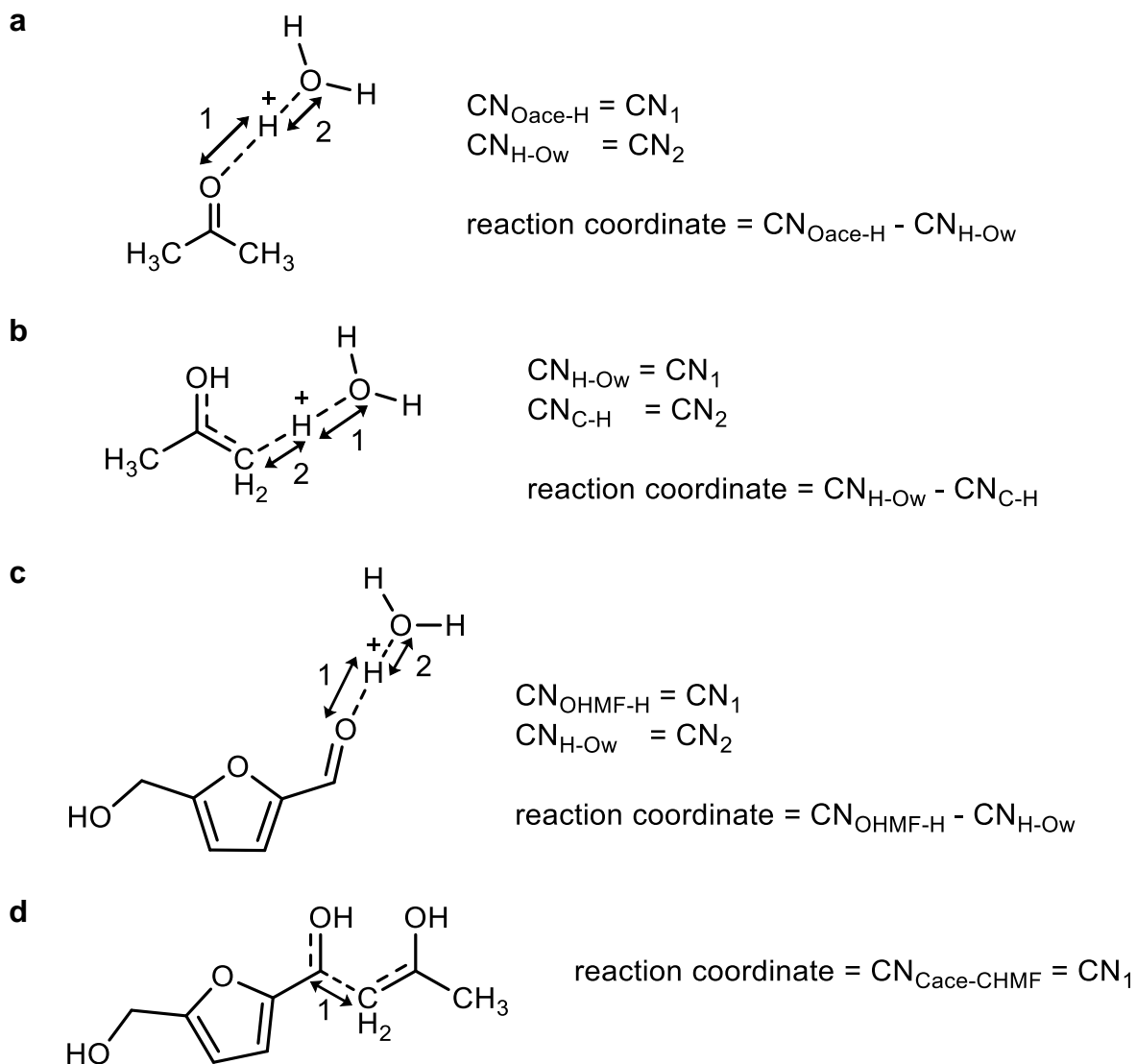
Supplementary Figure 4.21 a, Reaction coordinate for acetone protonation step; **b,** reaction coordinate for proton abstraction of protonated acetone; **c,** reaction coordinate for HMF protonation step; **d,** reaction coordinate for aldol addition step.
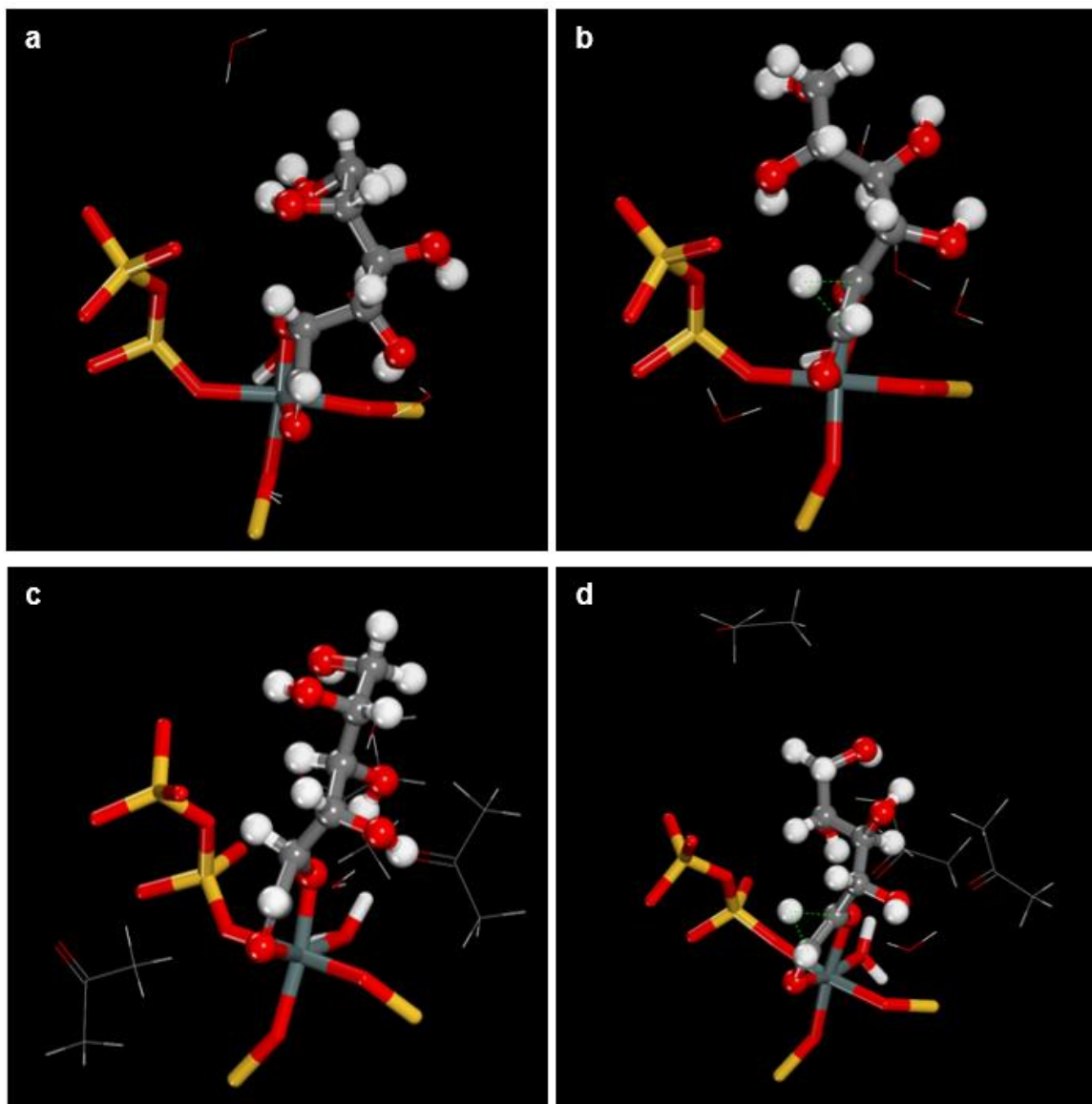
Supplementary Figure 4.22 Structures of deprotonated, adsorbed linear glucose on an open Sn site in bidentate binding mode. a, Initial state in a system with water molecules; **b**, transition state in a system with water molecules; **c**, initial state in a system with acetone/ H_2O molecules; **d**, transition state in a system with acetone/ H_2O molecules.
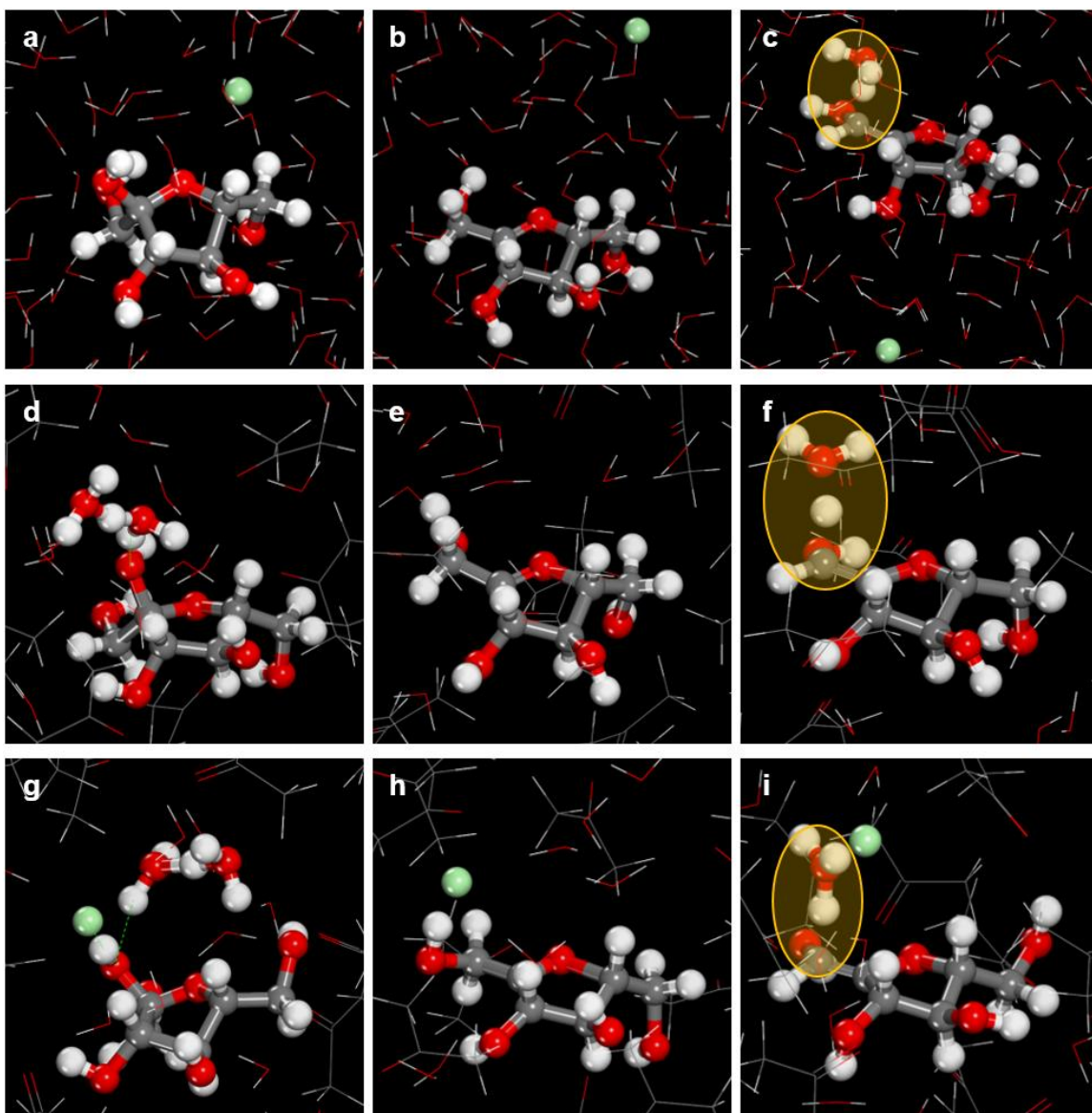
Supplementary Figure 4.23 Structures of fructose in a water system with chloride ion (in **a–c** of the first row), in 75 wt% acetone system without chloride ion (in **d–f** of the second row), and in 75 wt% acetone system with chloride ion (in **g–i** of the third row). The first, second, and third columns represent the initial, fructose carbenium ion, and transition state structures of proton abstraction step, respectively. The positive charge center is highlighted in yellow for all transition states.
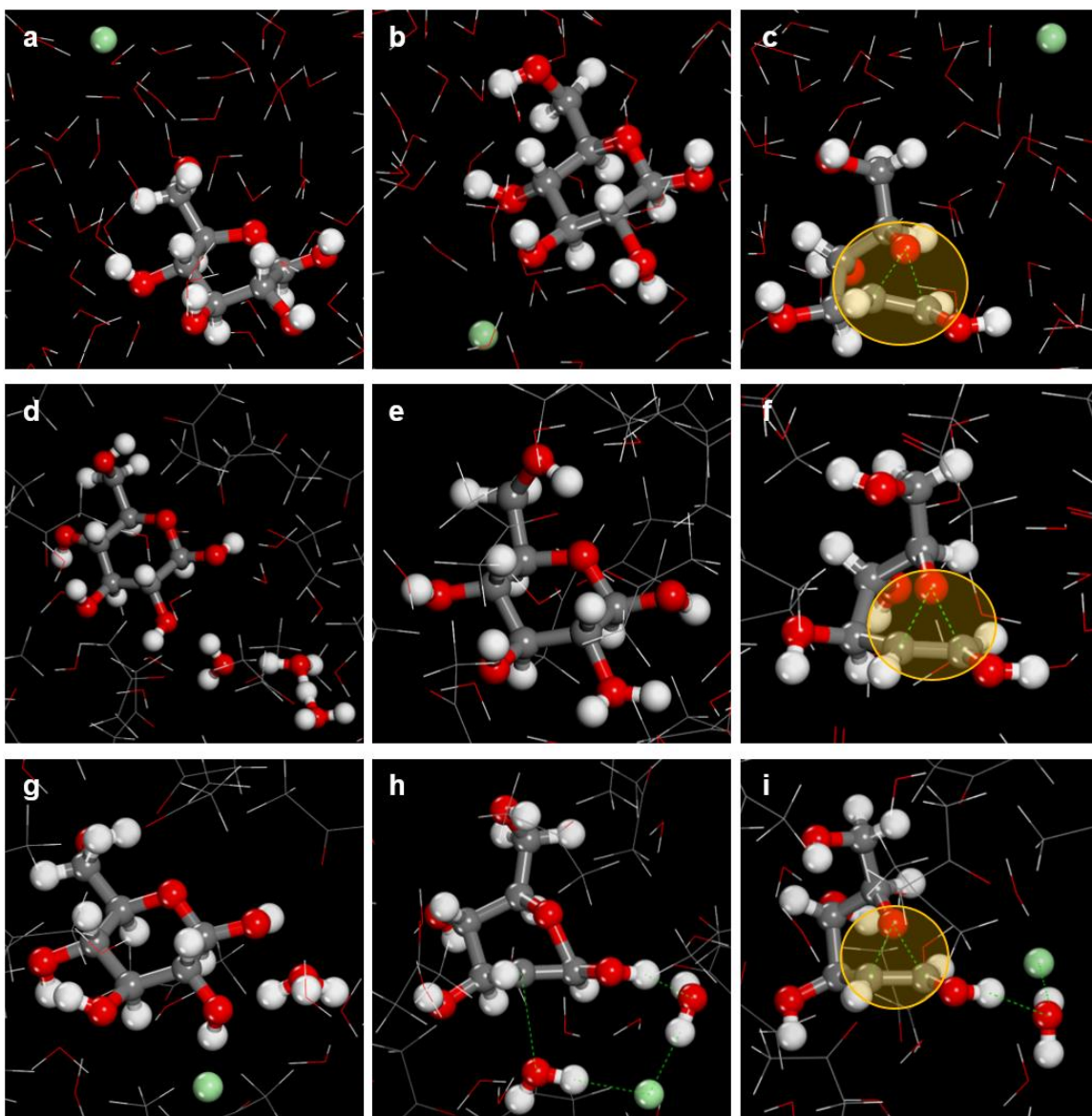
Supplementary Figure 4.24 Structures of glucose in a water system with chloride ion (in **a–c** of the first row), in 75 wt% acetone system without chloride ion (in **d–f** of the second row), and in 75 wt% acetone system with chloride ion (in **g–i** of the third row). The first, second, and third columns represent the initial state, protonated glucose, and transition state structures, respectively. The positive charge center is highlighted in yellow for all transition states.
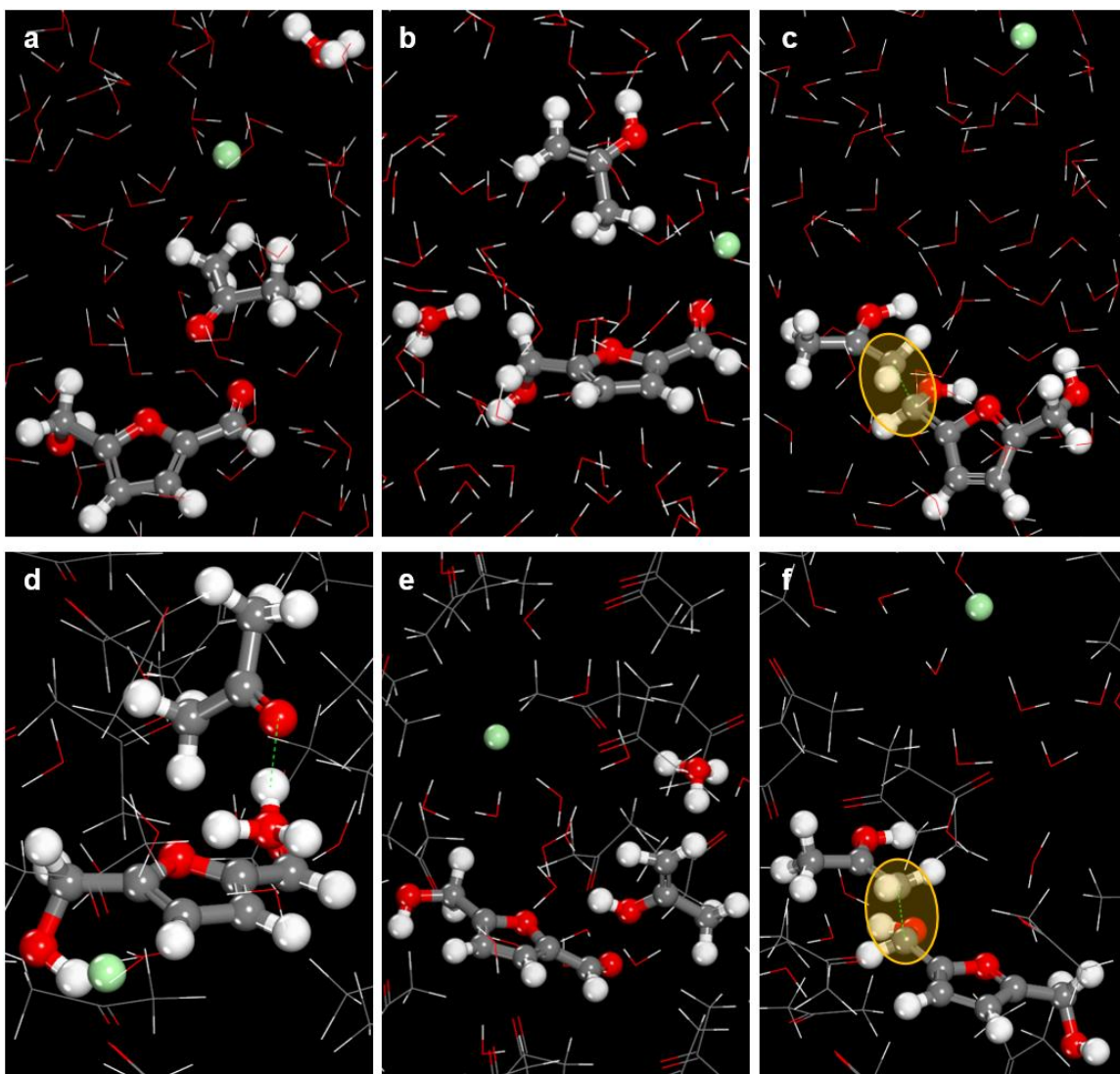
Supplementary Figure 4.25 Structures of acetone/HMF in a water system with chloride ion (in **a–c** of the first row), in 75 wt% acetone system with chloride ion (in **d–f** of the second row). The first, second, and third columns represent systems in the initial state, systems with acetone in enol form, and systems with transition state structures for aldol addition, respectively. The positive charge center is highlighted in yellow for all transition states.
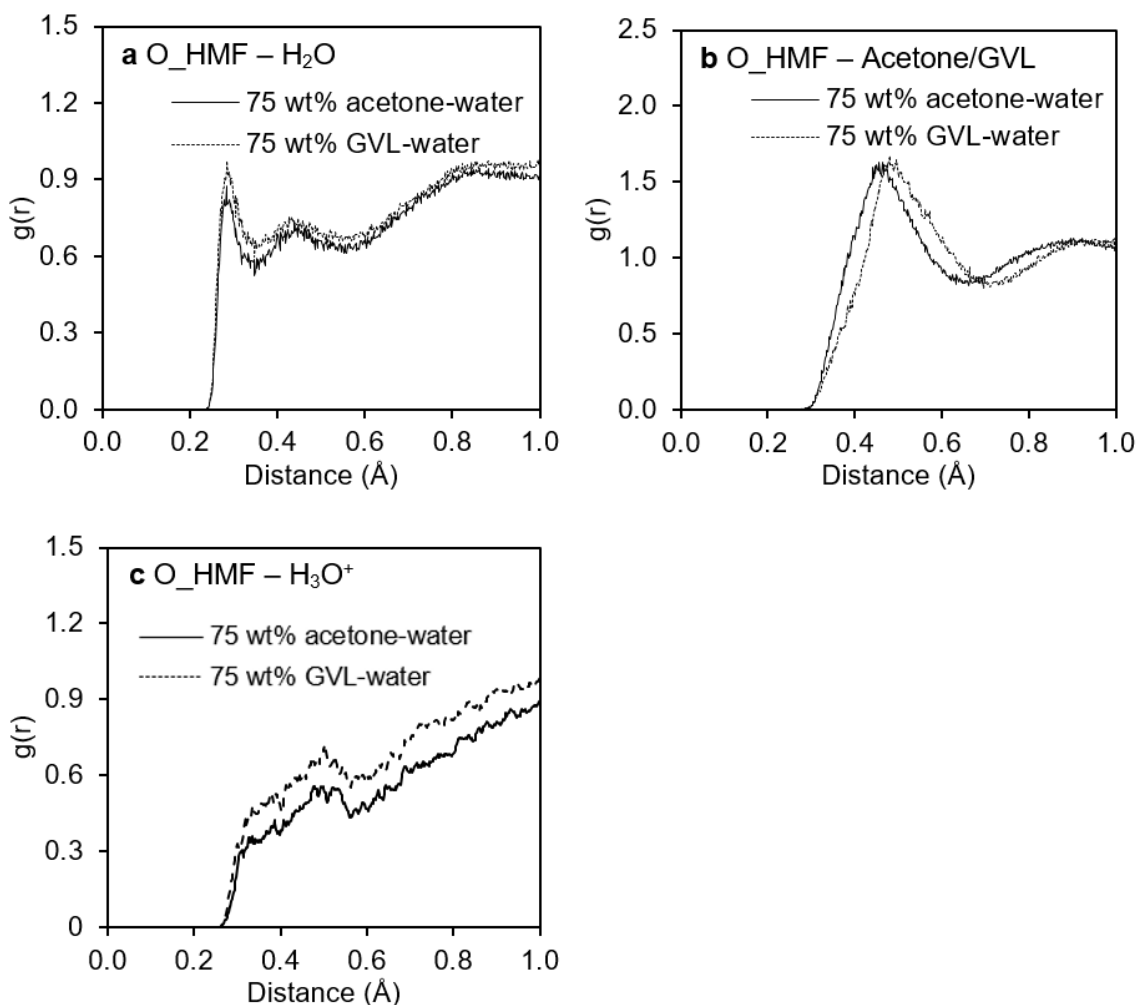
Supplementary Figure 4.26 Radial distribution functions (RDF) of the HMF oxygen carbonyl atom with respect to the center of mass of: (a) water molecules, (b) organic solvent molecules, and (c) hydronium ion. The solid lines are the RDFs in 75 wt% acetone–water mixture, and the dashed lines are the RDFs in 75 wt% GVL–water mixture. In panel **a**, the higher, broader peak of GVL–water mixture at ~0.3 Å indicates aggregation of water molecules around HMF carbonyl group to the larger extent than in acetone–water mixture. The result in consistent with RDFs in panel **b**, where the peak for acetone–water mixture at ~0.45 Å is located closer to the HMF carbonyl group than the peak for GVL–water mixture at ~0.5 Å. In addition, panel (**c**) shows the RDF of GVL–water mixture above the RDF of acetone–water mixture at all distances, clearly indicating that the HMF carbonyl group in acetone–water interacts with the hydronium ion significantly less than in GVL–water mixture.

Chapter 5 – Development of Molecular Force Field for Simulation of Cation Siting and Metal Distribution in Hydrophilic Zeolite

Adapted from Sanpitakseree, C., Neurock, M. Development of Molecular Force Field for Simulation of Cation Siting and Metal Distribution in Hydrophilic Zeolite. Manuscript under preparation.

Theoretical calculations were performed by CS under the supervision of MN.

5.1 Introduction

Zeolites are commonly used industrially as separating agents, adsorbents, and catalyts.[187–189] The use of zeolites as catalysts for reactions carried out in the liquid phase is preferred over homogeneous catalysts due to the ease of catalyst recovery. Recent studies showed multiple orders of magnitude increase in reaction rates for acid catalyzed dehydration carried out in polar aprotic media over polar protic media.[48,76] Experimental and computational studies carried out using homogeneous Brønsted acids showed that the reorganization of solvent molecules in polar aprotic–water mixtures results in the localization of acidic protons near the active sites of the substrate which facilitates protonation and promotes catalytic dehydration. For reactions carried out using heterogeneous zeolite acid catalysts, the solvation environment in vicinity of reactive site can be drastically different than in the homogeneous reaction. The preferential adsorption of different solvent and reactant molecules might play a significant role in determining the reaction kinetics. Studies of adsorption properties of zeolites will provide better insights into the interactions between the adsorbed solvent molecules, reactants, and active sites within the zeolite.

The adsorption properties of zeolites can be significantly modified by the incorporation of aluminum atoms into the zeolite framework.[190] The induced negative charge defects from aluminum atoms can be compensated by non-framework cations such as sodium, potassium, or calcium cations. The distribution of aluminum atoms among different framework T-sites can therefore influence the cation siting and adsorption properties of zeolite.[191] A substantial number of experimental, and theoretical studies have been carried out to understand and predict the cation siting and aluminum distribution in zeolitic materials.[192–201] Multiple computational approaches have been explored including energy minimization using quantum mechanical methods, classical force field molecular dynamics simulations, and classical force field Monte Carlo simulations.

The early development of force fields for cation siting in aluminosilicates simplified the complexity of zeolite by assigning identical partial charge for T-site silicon and aluminum framework atoms.[202–206] The model is considered unrealistic since aluminum atoms in the framework as well as adjacent oxygen atoms are more negatively charged than the those in siliceous zeolite. Vitale et al.[207] proposed an improved force field distinguishing different charges between silicon and aluminum atoms. However, the simulations were performed on zeolites with Si:Al = 1 which contained only one type of bridging oxygen atom. In addition, the sodium cations were also fixed onto the known cation sites thus ignoring the mobility of the cations. Jaramillo and Auerbach[208] addressed these issues by assigning different charges to silicon, aluminum, silicon–silicon bridging oxygen, and silicon–aluminum bridging oxygen atoms while allowing for the migration of sodium cations within the zeolite cavities. Nevertheless, the aluminum atoms were assigned to random framework T-sites (via Löwenstein's rule that prohibits two aluminum

framework atoms sharing the same bridging oxygen atom) and thus did not reflect the distributions in real zeolite structures.[209–211] Jeffroy et al.[212] developed a Monte Carlo method that averages the charge parameters of both types of bridging oxygen thus enabling the positional exchange between silicon and aluminum atom. While the results agree well with the experimentally observed aluminum distribution in the zeolite, the accuracy for sodium cation siting suffers.

In the present work, we develop an approach that exchanges the Si and Al clusters to more faithfully represent the local structure near the Si and Al. We report on the results from Monte Carlo simulations that utilize the approach to predict the cation siting in dehydrated sodium exchanged Faujasite (FAU) zeolite at Si:Al ratios ranging from 1 to 3. In addition, our model can replicate the aluminum distribution in both Faujasite and Mordenite (MOR) zeolites at Si: Al ratios ranging from 2.56 to 16.5 and 5 to 8.6, respectively. The model explicitly distinguishes different charge parameters for silicon, aluminum, and two types of bridging oxygen atoms. We propose a new type of Monte Carlo 'cluster swap' move that performs positional exchange between silicon and aluminum atoms along with their adjacent bridging oxygens. As such, the connectivity between T-atoms and the corresponding bridging oxygens can be preserved. This Monte Carlo move offers a much more realistic and flexible atomistic model where different charges can be assigned to each type of bridging oxygen. The force field was parameterized to fit experimentally measured cation siting in FAU and aluminum distribution in both MOR and FAU zeolites. This new Monte Carlo move can be further developed to accurately predict the thermodynamically favorable structures of zeolites under different synthesis conditions and their adsorption properties.

5.2 Methods

5.2.1 Zeolite model

The structures of FAU and MOR zeolites (Figure 5.1) were obtained from experimental neutron diffraction studies.[213,214] The FAU structure is in *Fd3m* space group with a cubic lattice parameter of 24.85 Å. The MOR structure is in *Cmcm* space group with lattice parameter 18.11 x 20.53 x 7.53 Å^3. The unit cells of FAU and MOR used in this study have Si:Al ratios that range from 1 to 16.5 and 5 to 8.6 (corresponds to number of aluminum/sodium atoms per unit cell ranging from 96 to 11 and 8 to 5), respectively. The structures for different specific Si:Al ratios were generated by replacing framework silicon with aluminum atoms at random locations according to the Löwenstein's rule. The framework atoms were kept fixed during the simulations while allowing for the exchange of cluster coordinates between SiO_4 and AlO_4 groups using our newly developed cluster swap move. Sodium cations were randomly placed into the zeolite empty space as counter charges. Periodic boundary conditions were applied to the simulation box in all directions.
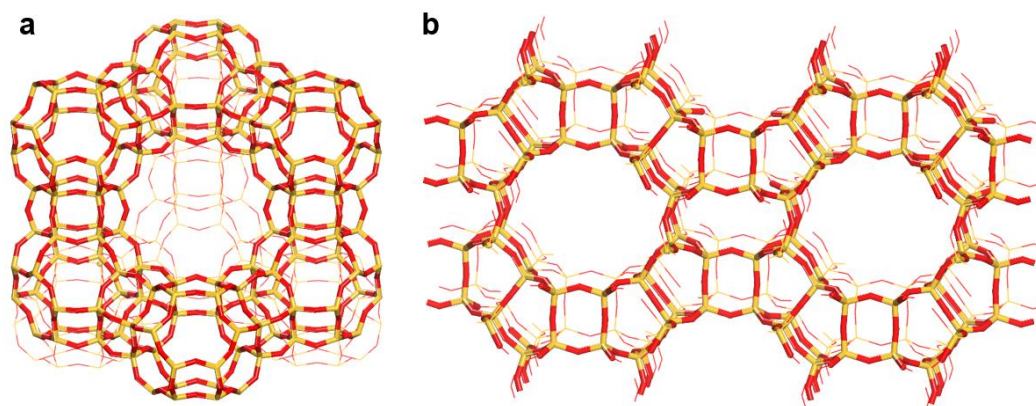
Figure 5.1 Structures of Faujasite framework (**a**), Mordenite framework (**b**). Oxygen atoms are shown in red, and silicon atoms are shown in yellow.

5.2.2 Atomic charges

The model defined the charges for framework silicon atoms (q_{Si}), aluminum atoms (q_{Al}), bridging oxygen atoms between two silicon atoms (q_{Osi}), and bridging oxygen atoms between aluminum and silicon atoms (q_{Oal}). Atomic charges were assigned by varying q_{Si} and q_{Al} parameters. The charge of sodium cation (q_{Na}) was set to +1. The parameters q_{Osi} and q_{Oal} were calculated using the relation $q_{Si} + 2\ q_{Osi} = 0$, and the q_{Oal} parameter was determined to make the net system charge equal to zero. Ewald sums were used to calculate the long-range Coulombic terms.

5.2.3 Bonded and non-bonded interactions

The potential function used in this work takes into account (1) the coulombic interaction between all atoms in the system and (2) Buckingham interactions between cations and oxygen atoms in the framework. The interactions between the cations and T-atoms were not considered because of shielding effects from framework oxygen atoms.[215] The Buckingham potential is presented in equation (5.1).

$$V_{Buckingham} = \sum_{i>j}(A_{ij}e^{-r_{ij}/B_{ij}} - C_{ij} / r_{ij}^6) \tag{5.1}$$

The initial parameters for the potential and atomic charges were obtained from a force field[208] proposed by Jaramillo and Auerbach. The parameter optimizations were carried out by first varying the Buckingham parameters to match the experimental sodium cation distribution within the FAU zeolite.[207,208,213,216–219] The charge parameters were then altered to match the experimental aluminum distribution in both FAU and MOR

zeolites.[220,221] The process was repeated until all parameters reached convergence. The optimized potential and charge parameters are reported in Table 5.1 and 5.2, respectively.

Table 5.1 Buckingham parameters for interaction between sodium cation and framework oxygen atoms

Interaction pair	$A \times 10^4$ [K]	B [Å]	$C \times 10^4$ [K·Å^6]
O – Na^a	4892.46	0.2715	122.55
O – Na^b	6115.58	0.2468	76.59

^{a} Parameters obtained in this work. ^{b} Parameters from Ref. [208]

Table 5.2 Charge parameters for all atom types in the simulation

Atom type	Partial charge^a	Partial charge^b
Si	+1.8500	+2.0500
Al	+1.8000	+1.7500
O_{Al}	−1.1625	−1.2000
O_{Si}	−0.9250	−1.0250
Na	+1.0000	+1.0000

^{a} Parameters obtained in this work. ^{b} Parameters from Ref. [208]

5.2.4 Monte Carlo simulations

The Monte Carlo simulations were carried out using the open source Towhee software.[222] For each system, three independent annealing simulations in an NVT ensemble were sequentially performed at 1500K for 20×10^6 cycles, 1000K for 20×10^6 cycles, 500K for 20×10^6 cycles, and at 298K for 100×10^6 cycles. The data acquisitions were obtained from the last 50×10^6 cycles. The sodium siting and aluminum distribution data from each replicate were then averaged and reported in Tables 5.3–5.6. Sodium cations were allowed translational moves in three dimensions and positional exchange moves with other sodium cations. Figure 5.2 illustrates the 'cluster swap move' for framework atoms where the silicon atoms and four adjacent oxygen atoms are allowed to switch coordinates with aluminum atoms and the corresponding four adjacent oxygen bridging atoms with respect

to Löwenstein's rule. This move offers advantages over traditional two atoms positional exchange between aluminum and silicon atoms such that the charge of bridging oxygen atoms is preserved, thus providing a more realistic representation of the charge distribution within the zeolites.
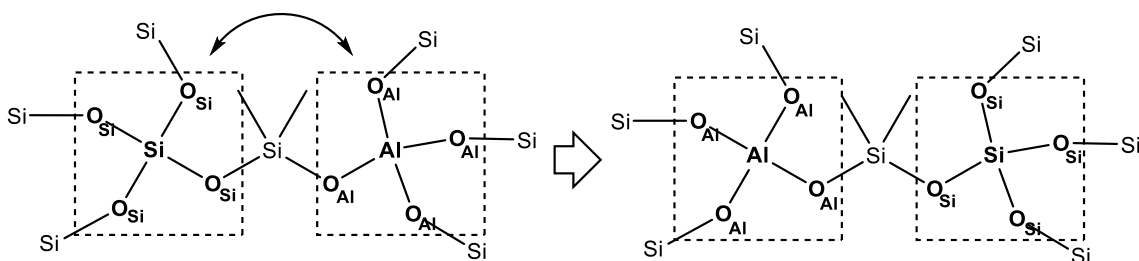
Figure 5.2 Illustration depicting a cluster swap move. A cluster of SiO_4 are allowed to switch position with another AlO_4 cluster with respect to Löwenstein's rule.

5.3 Results and Discussion

Figure 5.3 shows common cationic binding sites in FAU zeolite framework. A unit cell of FAU has 16 I sites located in the middle of hexagonal prisms connecting to sodalite cages, 32 I' sites located in the middle of 6-membered rings connecting the hexagonal prisms to sodalite cages, and 32 II sites located at the center of 6-ring windows of sodalite cages connecting to supercage. The sodium cation distribution in MOR were not calculated due to the lack of experimental data needed for meaningful comparisons.
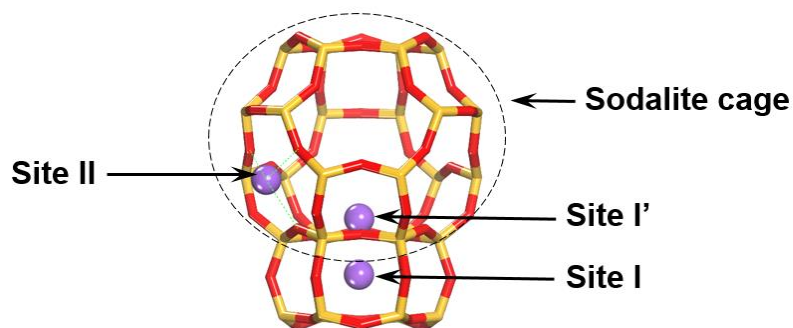
Figure 5.3 An illustration showing a sodalite cage of FAU zeolites connecting to a hexagonal prism beneath. Three cationic binding sites I, I', and II are represented by purple spheres.

The calculated results for sodium cation siting in FAU zeolite using optimized parameters are reported in Table 5.3. The II sites are largely filled at 48 sodium cation/unit cell and becomes completely filled as the number of sodium atoms exceed 53 per unit cell. The result supports the notion that cationic site II is the most favorable as the large distance between sites minimizes electrostatic repulsion between cations. The cation occupancies in site I and I' suggests favorable cation filling of site I and I' at high and low Si:Al ratios, respectively. The trend can be explained using a geometric constraint in the FAU framework which results in strong electrostatic repulsion between two cations located at site I and site I' within the same hexagonal prism. The increasing number of sodium cation therefore results in a displacement of the cations from site I to site I' in order to accommodate more cations in the system. The preferential filling at site I over the adjacent site I' at low Si:Al ratio also indicates that the stabilization of a sodium cation in site I by the 12 framework oxygen atoms in the hexagonal prism is more favorable than the short-range stabilization of a cation in site I' from 6 oxygen atoms in the 6-membered rings. Overall, the stability of sodium cation in cationic binding site follows the trend: site II > I > I' and is in good agreement with the literatures.[223]

Table 5.3 Simulation results using optimized parameters shows sodium cation siting at site I, I', and II in different systems with various number of sodium cation. The results are reported as the average number of sodium cation per type of site.

Na$^+$/u.c.	Experiment			Simulation		
	Site I	Site I'	Site II	Site I	Site I'	Site II
48[208]	2.9	11.4	27.9	0.1	15.9	30.0
53[216,217]	4.2	18.2	32.0	1.2	16.8	31.0
56[213]	7.1	18.6	32.2	2.3	16.3	31.0
57[218,219]	7.4	16.6	29.9	2.6	16.4	30.6
87[207]	0.0	32.0	32.0	0.6	28.8	32.0
96[a]	0.0	32.0	32.0	0.2	31.8	32.0

[a] Assumption based on maximum occupancy where site I' and site II are fully occupied

Contrary to the sodium cation siting, aluminum distributions cannot be directly measured experimentally. The analysis of ^{29}Si NMR data, however, provide insights into the environment of silicon atoms that can be used to construct sample zeolite structures.[224–227] Therefore, we chose to fit our parameters to readily available experimental NMR data. Silicon atoms with zero, one, two, three, and four connections to aluminum atoms are denoted as Si(0Al), Si(1Al), Si(2Al), Si(3Al), and Si(4Al), respectively (Figure 5.4). The experimental and calculated results for aluminum distribution in sodium exchanged FAU and MOR zeolites are reported in Table 5.4 and 5.5, respectively.
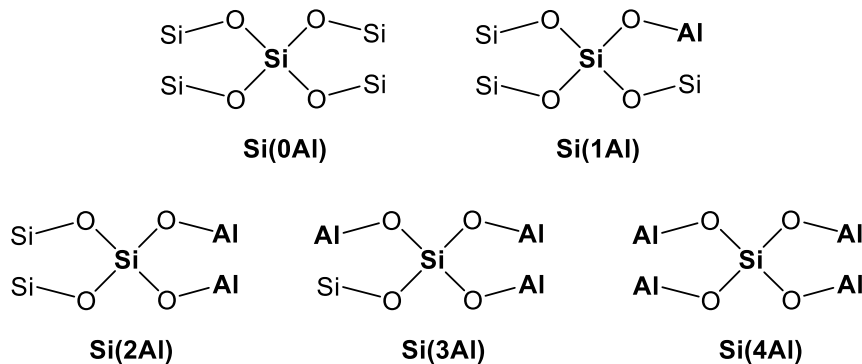
Figure 5.4 Illustration of silicon atoms with different number of connectivity to aluminum atoms. The silicon atom with all four oxygens bridging to other silicon atoms is denoted with Si(0Al). Silicon atoms with oxygen bridging to one, two, three, and four aluminum atoms are denoted with Si(1Al), Si(2Al), Si(3Al), and Si(4Al), respectively.

Table 5.4 Aluminum distribution in a unit cell of FAU zeolite categorized by the connectivity of silicon atoms to their T-atom neighbors (Figure 5.4). The reported results are the average numbers of different silicon atom types per unit cell.

Na^+ /u.c.	Experiment[220]				Simulation			
	Si(0Al)	Si(1Al)	Si(2Al)	Si(3Al)	Si(0Al)	Si(1Al)	Si(2Al)	Si(3Al)
11	136.3	44.7	0	0	142.3	33.3	5.3	0.0
18	106.8	62.6	4.4	0	113.0	50.3	10.3	0.3
31	65.2	70.8	22.4	2.4	64.7	70.7	23.7	2.0
54	12.8	57.5	50.0	14.6	12.7	59.0	45.0	18.3

The number of silicon atoms without adjacent aluminum atom, Si(0Al), is predominating in systems with 11 and 18 sodium cations. The absence of Si(2Al) and Si(3Al) in the system with 11 sodium cations suggests that the more positively charged aluminum atoms result in the repulsion between AlO_4 clusters.[228] This repulsive trend between aluminum atoms in FAU holds true at most Si:Al ratios. The number of Si(4Al) is zero in all cases and hence not reported. For system with 54 sodium cations, the high density of aluminum in the framework causes the number of isolated silicon atoms Si(0Al) to diminish. The lack of experimental data for sodium cation siting for systems with 11

sodium cations also contributes to the discrepancy between experimental and the calculated aluminum distribution, where the number of Si(1Al) from experiments and calculations are 44.7 and 33.3, respectively. The aluminum distribution follows the trend: Si(0Al) > Si(1Al) > Si(2Al) > Si(3Al) > Si(4Al) and is consistent with results reported in the literatures.[221]

Table 5.5 Aluminum distribution in MOR zeolite at various number of framework aluminum per unit cell.

Al/u.c.	Experiment[221]			Simulation		
	Si(0Al)	Si(1Al)	Si(2Al)	Si(0Al)	Si(1Al)	Si(2Al)
5	24.1	17.9	0.9	24.2	17.6	1.1
6	19.6	20.7	1.6	20.2	19.8	1.9
7	14.1	24.1	2.4	17.1	20.2	3.3
8	11.6	26.3	2.3	14.8	19.1	5.5

The aluminum distribution in MOR is similar to the trend observed in FAU. At 5 sodium cations per unit cell, the number of silicon atoms with no adjacent aluminum Si(0Al) predominates. Meanwhile, the silicon atoms Si(3Al) and Si(4Al) were not observed in all of the systems tested, emphasizing the repulsion between aluminum atoms. The limited number of silicon atoms available in a MOR unit cell results in a greater number of Si(1Al) than Si(0Al) in the systems with 6, 7, and 8 sodium cations. It is worth mentioning that the MOR unit cell can accommodate only 8 sodium cations, at which point the aluminum atoms occupy a large portion of T-sites and the cluster swap move between the SiO_4 and AlO_4 clusters are not possible without violating the Löwenstein's rule. As such, the cluster swap move in such systems is rendered ineffective, and the large deviations of calculated results from experimental data can be attributed to incomplete sampling. Further development in the swapping algorithm is required to improve the accuracy of simulation results in these cases.

Table 5.6 Aluminum occupancies in different T-sites of MOR zeolite at various number of sodium cation per unit cell.

Na$^+$/u.c.	Simulated Al occupancy			
	T1	T2	T3	T4
5	4.0	6.7	36.3	2.7
6	3.3	10.0	39.0	6.7
7	6.3	9.7	43.3	9.0
8	9.3	13.0	43.3	9.3
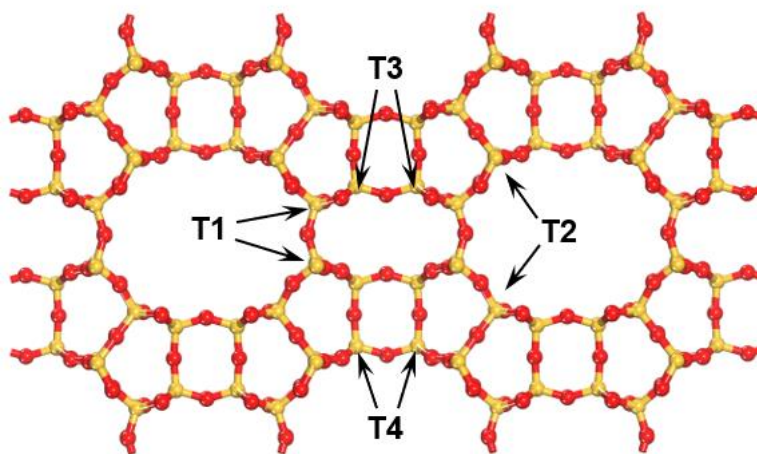
Figure 5.5 Structure of MOR zeolite showing T1, T2, T3, and T4 framework sites.

The simulated MOR structures were subsequently used to calculate the aluminum occupancies among different T-sites. It is evident from the results in Table 5.6 that the majority of aluminum atoms are located at site T3, while the rest of aluminum atoms are uniformly distributed among sites T1, T2, and T4. These results agree with other computational studies[212,229,230] that the substitution of a silicon atom for an aluminum atom at site T3 is the most favorable.

5.4 Conclusions

We developed a new Monte Carlo cluster swap move that allows the prediction of sodium cation siting simultaneously with aluminum atom distributions within FAU and

MOR zeolite frameworks. The method was parameterized using experimental data for sodium cation siting in FAU zeolite and aluminum distribution in FAU and MOR zeolites. The model successfully describes both properties with satisfying results. The accuracy of the model can be further improved with the inclusion of additional experimental data at different Si:Al ratios and adsorption data of different solvents and biomass species. The results obtained from the simulations can be used as initial structures for more complicated *ab initio* calculations.

Chapter 6 – Perspective on the First-Principles Investigations of Reaction Environment Effects in Catalyzed Reactions

Adapted from Sanpitakseree, C., Neurock, M. Perspective on the First-Principles Investigations of Reaction Environment Effects in Catalyzed Reactions. Manuscript under preparation.

6.1 Introduction

The rate of catalyzed reaction is governed by the relative stability of reactants and the transition state in the rate-determining step.[102] These relative stabilities can be controlled with the modification of molecular environments in which the reactions take place, including the modifications to catalyst composition, catalyst support, structural confinement at the active sites, or reaction media. The changes in reaction environments can also affect the activation energies in different reaction paths, leading to improvements in both reaction rates and selectivities. Understanding the role of reaction environment is therefore critical in the effective design of selective catalytic systems. We herein present the results of computational and experimental co-investigations probing the effects of reaction environments on catalyzed reactions using heteropoly acids, microporous catalysts, mineral acids, and metal composites.

The reactivity of reactions in gas phase using Brønsted solid acid catalyst is directly related to the acidic strength of the acid site,[231] which is dependent on the proton dissociation energy of its conjugate anion. However, experimental indicators such as Hammett parameters, temperature-programmed desorption of base molecules, and H–NMR spectroscopy cannot accurately measure the intrinsic strength of acid sites.[232]

Density functional theory (DFT) calculations were used to establish an acidity–reactivity relationship for gas phase dehydration of 2-butanol catalyzed by Keggin's type polyoxometalates (POM).[83,84] The consistent dehydration mechanism over different POMs enabled direct comparison between the deprotonation energy (DPE) of acid sites with the dehydration rates.[83] This concept is extended to acidic zeolites which allows for additional control over shape selectivity.[233] The dehydration reactions in zeolite catalyst are much more reactive than the POM catalyst with similar acidity.[85] The results suggest that the confinement of pore structure around the active sites can interact with the reactive species and enhance the reactivity.

In contrary to the reaction in gas phase, the reactions in liquid phase often show complex behavior in response to the change in solvation environment.[234] The highly mobile nature of liquid results in rearrangement of solvent molecules around the reactants which plays an important role in controlling the reaction kinetics.[58] A computational study of reaction in liquid phase will need to properly model these micro heterogeneities within the bulk phase. We adopted explicit solvation model in conjunction with *ab initio* molecular dynamics (AIMD) simulations in order to realistically capture the interactions between different solvent species and the solvated reactants. We used the Brønsted acid catalyzed reactions of simple alcohols in polar aprotic solvent–water mixtures as probe reactions. The reaction rates which are dictated by the extent of solvation of reactants and the transition states are largely correlated to the hydrophilicity of reactive species.[76] The rearrangement of solvent molecules to form solvation shells also allows for a co-localization of non-reactive charged species.[77] Such molecular configurations can induce

significant close-ranged interactions with the reactive species and therefore altering the reaction kinetics.

A catalytic system generally involves multiple competitive reaction paths, some of which lead to the formation of undesired side products. The reaction environment can affect not just the rates and selectivities for these competitive paths but can also alter the reaction mechanisms.[235–240] We choose a selective hydrogenation of 2-butanone over Ru(0001) metal surface[86] to show that the solvent molecules interact with transition state in alkoxy path more favorably than hydroxy path, and the change in relative activation energies in presence of solvent is sufficient to shift the dominating reaction mechanisms. In addition, the presence of solvent molecules may enable a new reaction mechanism not observed in gas phase. Such phenomenon can be observed in the electrocatalytic dissociation of gaseous water molecule over $Pt_{66}Ru_{33}(111)$ alloy which, in gas phase, undergoes a homolytic dissociation into a hydroxy and a hydrogen species adsorbed on the metal.[87] It was demonstrated that the direct participation of water solvent in the electrocatalytic dissociation of water molecule over the alloy gives rise to a much more favorable reaction path, where the water molecule dissociates into a hydroxy species on metal surface and releases hydronium ion into bulk phase.

6.2 Theoretical and Simulation Methods

The computational methods used for investigation of catalytic systems are thoroughly reviewed in the literature[241–244] along with their applications, advantages, and drawbacks. In this work, we provide concise explanations on a few methods regularly employed.

6.2.1 Molecular modelling

Molecular modelling can be categorized into molecular mechanical method and quantum mechanical method.[245] Molecular mechanical method describes complex molecular interactions using relatively simple equations with a few tunable parameters. It is prevalently used in combination with molecular dynamics to simulate chemical systems that do not require breaking and formation of covalent bonds. The low computational cost for molecular mechanics makes it a method of choice for modelling large molecular systems with several million molecules. The approach has proven very useful in the simulation of catalytic system in liquid phase where one needs to pre-equilibrate complex molecular systems prior to *ab initio* calculations.

On the other hand, quantum mechanical methods describe atomic interactions using *ab initio* methods to replicate electron density within the system. It can accurately describe rare events such as bond breaking or bond formation and thus is commonly used to simulate chemical reactions. The majority of catalytic simulations at present utilize *ab initio* density functional theory (DFT) which offers a good compromise between accuracy and computational cost.[246,247] The DFT based calculations are generally performed on chemical systems with less than a few hundred atoms with the results typically achieving an accuracy of 0.05 Å and 5–7 kcal mol^{-1} error in relative energy.[248,249] A realistic computational modeling, especially in liquid phase, will require a combination of both molecular and quantum mechanical methods to sufficiently sample molecular configurations while also calculating   the associated activation energies of the reactions.

6.2.2 Catalyst models

The accuracy of catalytic modelling also depends on the realism of the model. A simple cluster model utilizes a limited number of molecules in the system in which the reaction occurs.[249,250] In case of homogeneous reaction, this often involves the whole catalyst molecule and the reactants. For heterogeneous reactions, a portion of catalytic surface with active sites is cleaved and suspended in vacuum. The cluster model does not consider the effects of catalyst support or the geometry of catalyst cluster, resulting in cluster size artifact where the calculated properties vary with system size. In addition, the computational cost for *ab initio* calculations using cluster method rapidly increases with the number of atoms, making investigation of chemical systems involving large catalyst cluster or large reactant molecules prohibitively expensive.

An alternative approach regularly employed for heterogeneous systems is a periodic model.[251–254] A catalytic system is represented in a unit cell infinitely replicated through x, y, and z direction, creating an extended system resembling a bulk phase. Furthermore, the calculation in periodic system using plane wave method is much more efficient than the cluster method, allowing simulation of much larger chemical systems. The *ab initio* density functional theory method with periodic model are used for all computational studies presented in this work.

6.2.3 Solvation model

Implicit and explicit solvation models are available for the simulation in condensed phase.[255–257] The implicit solvation model does not include actual solvent molecules in the simulation. Rather, a continuous medium representing actual solvent molecules is applied

to the system to approximate the averaged solvent interaction with the solvated species. The continuum solvent offers much lower computational cost in comparison to explicit model. However, the method often fails to describe short-ranged interaction such as strong hydrogen bonding between solvent and solute.[257] An improvement can be made by including a small number of solvent molecules in the system near reactant vicinity while keeping the continuum solvent applied. Such method provides reasonably accurate solvent–solute interactions from explicit solvent molecules and long-range contribution from implicit solvent. Regardless, a full explicit solvation model is often required for reactions carried out in solvent mixtures especially when the behavior of reaction depends on solvent composition. In such cases, the simulations must be carried out in periodic setting with all solvent molecules present. The full explicit solvation model can capture the solvent effects caused by reconfiguration of solvent molecules as well as short-ranged interaction between solvent and the reactive center. The explicit solvation model is used in all the studies presented in this work where the solvent is involved.

6.2.4 Kinetics methods

The computational investigations utilizing density functional theory report the relative energies corresponding to the reactions carried out at low temperature while neglecting the entropic contribution that may arise at experimental condition. This is often an issue for heterogeneous reaction where the adsorption/desorption of reactive species results in large entropic change.[258] A quasi-harmonic approximation can be applied to achieve Gibbs free energies. However, the accuracy of the entropic correction method suffers greatly for simulations of reaction in liquid phase where the large number of weak binding modes between molecules contribute to the majority of the calculated entropy.

Alternatively, we used *ab initio* density functional theory simulations in conjunction with molecular dynamics and umbrella free energy sampling technique to calculate the free energy of reactions in liquid phase.[259] The approach involves simulations of multiple system replicas bridging between two different states. Statistical analysis of all the systems located at different reaction coordinates will reveal the total activation free energy and reaction free energy of chemical reactions.

6.3 Results and Discussion

6.3.1 Structure-reactivity relationship in POM clusters

A rigorous assessment of acid strength requires measurement of free energy to transfer a proton from acid to a reactant and stabilize the resulting anion and the protonated reactant that forms. Keggin-type polyoxometalates (POMs) are ideal solid acid catalyst for studying structure-acidity relationship due to their well-defined structure and tunable acidity.[260–267] The acidity of POMs can be varied by modifying the central metal atom without affecting the atomic configuration[83,260–263,267,268] which allows the comparison of acid strength between POMs with different metal center without interference from other possible factors.

The investigation of 2-butanol dehydration using POM acid catalysts was used to construct the acidity–reactivity relationship.[84] Figure 6.1 illustrates the E1 dehydration mechanisms[83,84] of 2-butanol to butene. The quasi-equilibrated adsorption of 2-butanol on a Brønsted acid site is followed by a cleavage of $C-OH_2^+$ bond, resulting in water molecule and a butoxide intermediate binding on the POM oxygen atom. The dehydration is

completed with a deprotonation of the adsorbed butoxide by the deprotonated acid site to yield a butene.
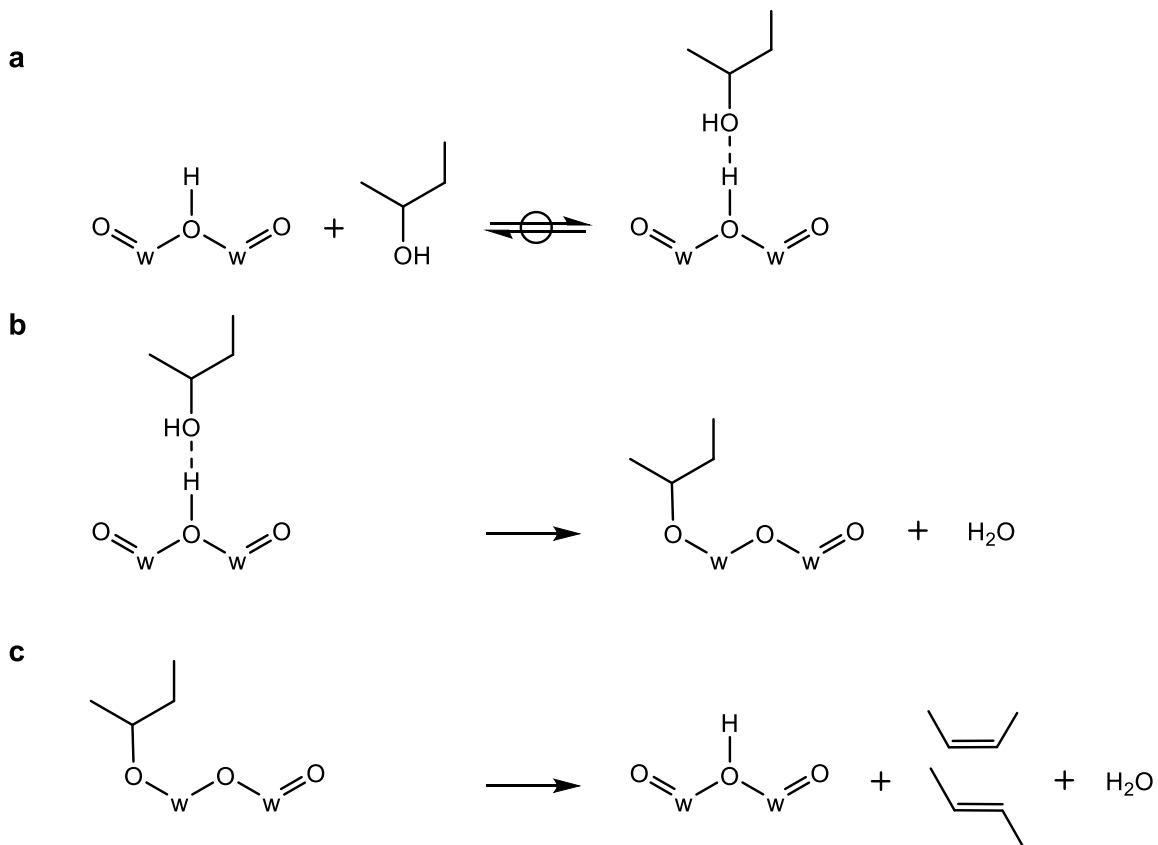
Figure 6.1 Elementary steps for 2-butanol dehydration on POM catalyst via E1 mechanism. a, Adsorption of 2-butanol on the POM Brønsted acid site. **b,** Dehydration of adsorbed 2-butanol proceeds with E1 mechanism to yield an alkoxy intermediate bound to the oxygen atom of POM catalyst. **c,** Deprotonation of alkoxy species by the deprotonated acid site to generate butane.

Born–Haber thermochemical cycle analysis[269–272] was used to show that the elimination rate constant of 2-butanol is correlated to the apparent activation energy of dehydration, which is decoupled into multiple terms shown in equation (6.1).

$$E_a = DPE + \Delta E_{rxn} + \Delta E_{int} - \Delta E_{ads} \qquad (6.1)$$

where DPE is the deprotonation energy of POM, ΔE_{rxn} is the reaction energy for dehydration in gas phase using free proton without POM anion, ΔE_{int} is the energy of carbenium ion adsorption onto the deprotonated POM, and ΔE_{ads} is the adsorption energy of 2-butanol on POM cluster. The ΔE_{rxn} term for dehydration of 2-butanol was calculated to be -713 kJ mol^{-1} and is independent of POM metal center atom. The values for E_a, DPE, and ΔE_{ads} terms are reported in Table 6.1. The calculated ΔE_{ads} term varies in a small range between -73 to -77 kJ mol^{-1}. Therefore, the change in activation energy of 2-butanol is correlated with the DPE and ΔE_{int} terms.

The POM with aluminum center ($H_5AlW_{12}O_{40}$, HAlW) has the highest charge density in the anionic shell induced by five counter charge protons. The strong ionic interaction between anion and the acidic proton results in highly stabilized protons and the highest DPE of 1121 kJ mol^{-1}, making HAlW the least acidic among all POMs tested. Meanwhile, POM with phosphorous center ($H_3PW_{12}O_{40}$, HPW) has three counter ion protons. The lower charge density on the HPW anionic shell leads to weaker ionic interaction with proton. As such, the protons on HPW are much less stabilized with the lowest DPE of 1087 kJ mol^{-1}. It follows that the highly acidic POM such as HPW can promote proton separation from the anion of POM cluster and facilitates the protonation of 2-butanol, lowering the activation energy, and driving the dehydration reaction.

Table 6.1 Deprotonation energy (DPE) of POMs with different metal center atom, 2-butanol adsorption energy, and activation energy of dehydration over POM clusters with tungsten addenda atoms. All units are reported in kJ mol^{-1}. Data is obtained from Reference [84].

Central atom	DPE	ΔE_{ads}	E_a
Al	1121	-73	146
Si	1105	-76	140
P	1087	-77	132

In addition to the acidity of the POM catalyst, the stabilization of transition state by POM anions also contributes to the change in activation energy for dehydration of 2-butanol. The deprotonation of POM and the protonation of 2-butanol results in a negatively charged POM anion cluster which interacts with the positively charged transition state carbenium ion. The POM with high electron density in the anion shell such as HAlW can stabilize the carbenium ion transition state more favorably than the POM anion with low electron density in the shell such as HPW. As such, the effect of POM metal center on the ΔE_{int} term follows the opposite trend of DPE where the highly acidic HPW is associated with poor stabilization of carbenium ion transition state. Overall, the magnitude of reactant stabilization (DPE) term dominates over the transition state stabilization from anion (ΔE_{int}) term and thus the reaction rate increases when the reaction is carried out using POMs with lower DPE.

6.3.2 Confinement effect in zeolite catalyst

The effect of reaction environment on the reaction rate is not limited only to the nature of active site. For reactions carried out in zeolite catalyst, a dispersive interaction from zeolite material can alter the relative stabilization of the reactive species and therefore affects the activation energy. We show that the dehydration of methanol to dimethyl ether (DME) can be used to measure the influence of confinement effects in various zeolite with different pore size.[85]
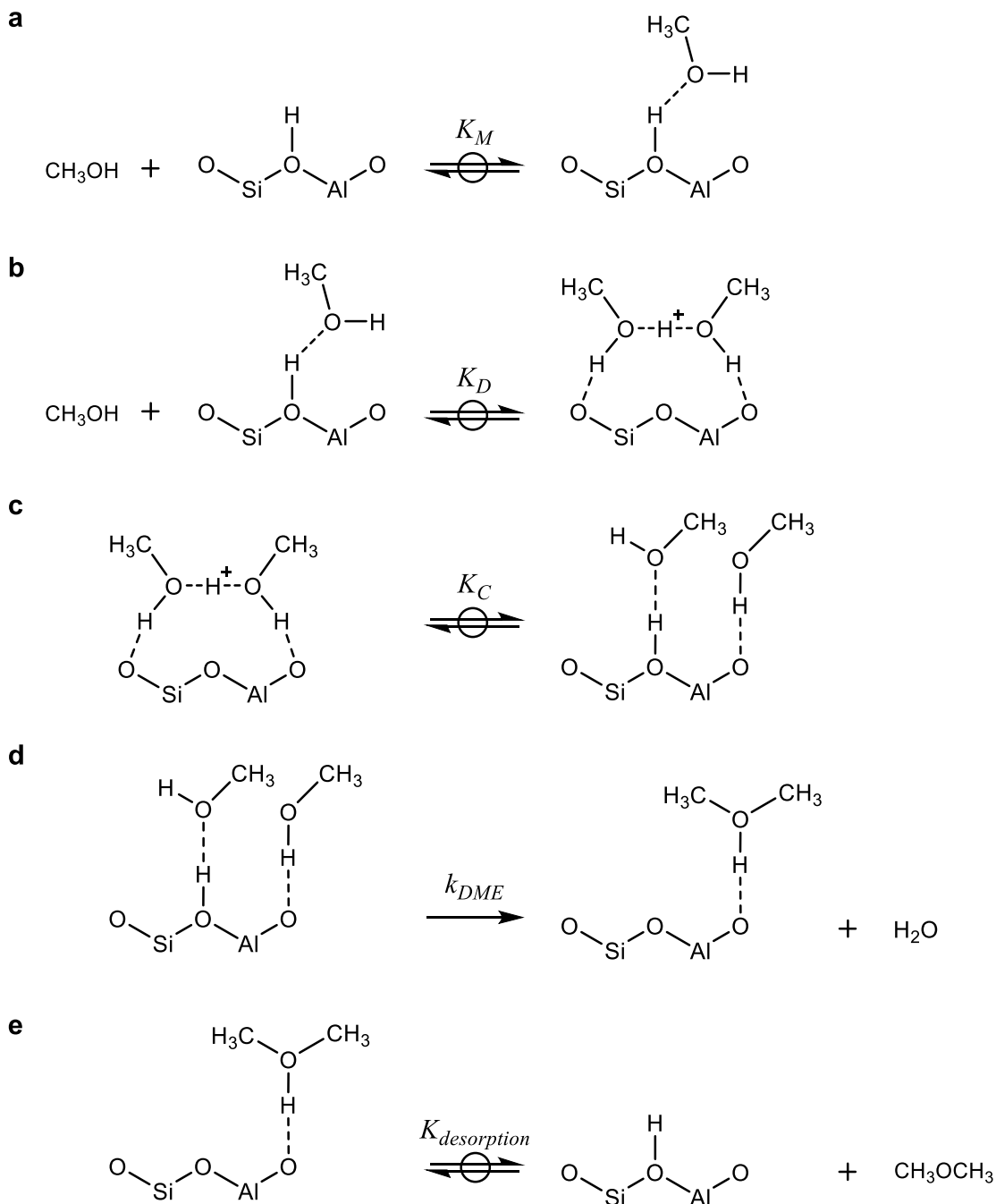
Figure 6.2 Elementary steps for the formation of dimethyl ether from methanol using zeolite acid catalyst. a, Adsorption of the first methanol on zeolite Brønsted acid site. **b**, Adsorption of second methanol to form a protonated methanol dimer. **c**, Molecular rearrangement of structure in (**b**) results in methanol co-adsorbed species. **d**, Water elimination of the co-adsorbed species yields an adsorbed dimethyl ether on the deprotonated acid site. **e**, Desorption of the dimethyl ether molecule.

The elementary steps involved in the formation of DME from methanol are illustrated in Figure 6.2. The methanol first adsorbs onto an acid site located in the zeolite pore to form a protonated methanol. Adsorption of the second methanol molecule results in the formation of a protonated dimer intermediate which undergoes a molecular reorientation to form a co-adsorbed species. The kinetically relevant water elimination of the co-adsorbed species takes place and yields a DME molecule adsorbed on the acid site. Equation (6.2)[85] shows that the normalized reaction rate is governed by equilibrium constants leading to the dimer formation, reaction rate constant in the water elimination step, and pressure of methanol gas:

$$\frac{r}{[H^+]} = \frac{k_{DME}K_C K_D P_{CH_3OH}}{1 + K_D P_{CH_3OH}} \tag{6.2}$$

where k_{DME} is the rate constant for DME formation from the co-adsorbed intermediate, K_C is the equilibrium constant for molecular rearrangement of the protonated dimer into the co-adsorbed species, K_D is the equilibrium constant for adsorption of the second methanol to form a protonated dimer, and P_{CH3OH} is the pressure of methanol feed. The dehydration of methanol was carried out using H–MFI, H–BEA, H–USY, and CD–HUSY acidic catalysts.

The assessment of confinement effect was performed by fitting experimental data to equation (6.2) and analyzing the K_D term which is correlated to the stability of protonated dimer relative to the adsorbed methanol and a methanol molecule in gas phase.[273] The transformation of methanol and adsorbed methanol into protonated dimer involves a proton transfer from acid site to the methanol molecules. Therefore, the K_D term is dependent on

both Brønsted acid site deprotonation energy (DPE) and ion pair interaction between the

positively charged protonated dimer structure and the negatively charged deprotonated acid

site. In addition, the value of K_D for the reactions carried out in zeolite also contains partly

a contribution from van der Waals dispersive interaction with the zeolite wall. The extent

of confinement interaction was measured by comparing the K_D values obtained from

reactions in zeolites against reactions using POM catalysts where the K_D values are not

affected by the dispersive interactions from catalyst structure.
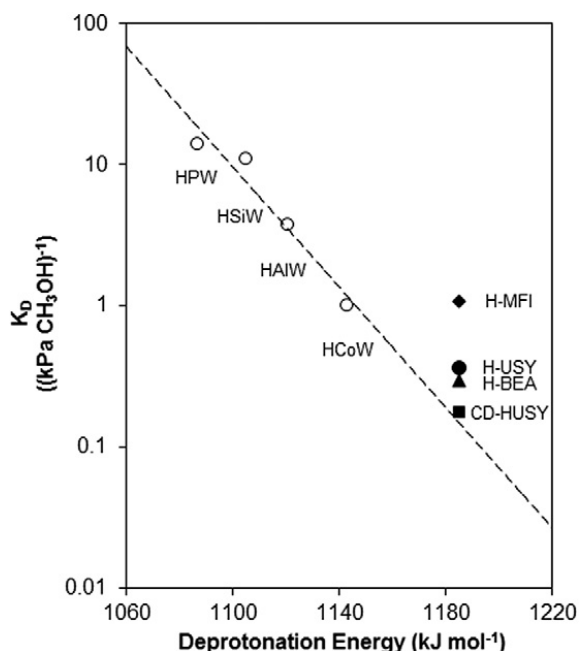
Figure 6.3 Plot shows linear relationship between equilibrium constant for second methanol adsorption (K_D) and the deprotonation energy (DPE) of acid site.[85]

The linear relationship between the deprotonation energy (DPE) of acid site and the

K_D values of methanol dehydration using POMs is shown in Figure 6.3. The value of K_D

for reactions using POMs changes from 1 to 14 as the DPE of POM cluster changes from

1145 kJ mol^{-1} to 1087 kJ mol^{-1}. The result is consistent with previous findings that a strong

acid catalyst favors the dehydration reactions. The trend line for data obtained in POMs

predicts K_D value to be 0.1 for acid sites with DPE of 1171–1200 kJ mol^{-1} (DPE of Brønsted acid sites in zeolites[274]). However, the measured K_D for the reactions in zeolites are much greater than the expected value by factor of 1.2–7.6, with the highest K_D of 1.1 in H–MFI. The deviation of K_D for reactions in zeolites from the expected value indicates a favorable equilibrium toward the protonated dimer structure resulted from factors not existing in POM clusters such as confinement effects. The stabilization of dimer by van der Waals interaction with porous zeolite channel is supported by theoretical study which shows 29 kJ mol^{-1} stabilization of CH_3OH molecules in H–MFI.[275] The value of K_D for reactions in zeolites increases as the pore diameter decreases. The result agrees with the other studies that indicate stronger dispersion interaction in zeolite with smaller pore diameter.[276,277]

6.3.3 Solvent effects in liquid-phase reactions

The reactions carried out in liquid phase are highly preferred over gas phase because of the operating cost associated with lower reaction temperature. The understanding of reaction environment in liquid phase is crucial for an effective design of selective catalytic systems. However, the environment of reactions in liquid phase is much more complex than the reactions in gas phase due to numerous possible configurations of solvent molecules interacting with reactive species. The reactants in liquid phase are encapsulated by solvent molecules which are highly mobile, complicating the interaction between solvent molecules with the solvated reactants and transition states. The changes in solvent choices, solvent composition, and temperature can significantly affect the solvation environment and the stabilization of transition state relative to reactant and result in change in reactivity.

Experimental evidences indicate that the reaction rate of acid catalyzed dehydration is enhanced when the reaction is carried out in polar aprotic–water solvent mixtures.[19,34,48,56,57,142–144,146] We investigated the effect of solvation environment using Brønsted acid catalyzed dehydration reactions of simple alcohols in polar aprotic solvent–water mixtures.[76] The choice of reactants used in our study varied in hydrophilicity, including a less hydrophilic alcohol with a single hydroxyl group (*tert*-butanol), and a more hydrophilic alcohol with two hydroxyl groups (1,2-propanediol). The solvents chosen for computational studies are dimethyl sulfoxide (DMSO) and γ-valerolactone (GVL) which have negative and positive enthalpy of mixing with water, respectively. The effects of acid catalyst in different solvent mixtures were limited with a use of triflic acid which completely dissociated in all the mixtures involved.

$$(CH_3)_3COH_{(aq)} \; + H^+_{(aq)} \qquad \rightleftharpoons \qquad (CH_3)_3COH_2^+_{(aq)} \qquad\qquad (6.3)$$

$$(CH_3)_3COH_2^+_{(aq)} \qquad\qquad \rightleftharpoons \qquad (CH_3)_3C^+_{(aq)} \qquad + H_2O_{(aq)} \qquad (6.4)$$

$$(CH_3)_3C^+_{(aq)} \qquad + H_2O_{(aq)} \qquad \rightarrow \qquad (CH_3)_2C{=}CH_{2(aq)} + H_3O^+_{(aq)} \qquad (6.5)$$

$$CH_2(OH)CH(OH)CH_{3\,(aq)} + H^+_{(aq)} \quad \rightleftharpoons \quad CH_2OHCH(OH_2^+)CH_{3\,(aq)} \qquad (6.6)$$

$$CH_2OHCH(OH_2^+)CH_{3\,(aq)} \qquad \rightleftharpoons \quad CH_2OHCHCH_3^+_{(aq)} + H_2O_{(aq)} \quad (6.7)$$

$$CH_2OHCHCH_3^+_{(aq)} + H_2O_{(aq)} \qquad \rightarrow \quad CHOCH_2CH_{3\,(aq)} \qquad + H_3O^+_{(aq)} \quad (6.8)$$
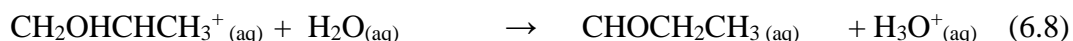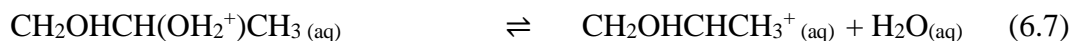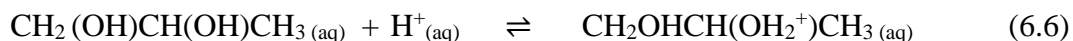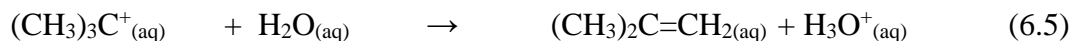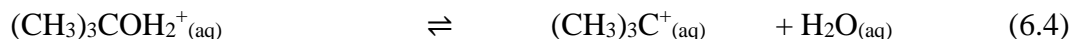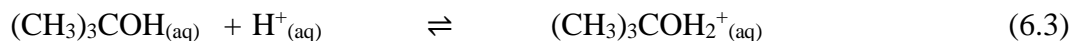
The mechanisms for the acid-catalyzed dehydrations of *tert*-butanol (equations (6.3)–(6.5)) and 1,2-propanediol (equations (6.6)–(6.8)) proceed with the protonation of the tertiary and secondary hydroxyl groups, respectively. The protonated *tert*-butanol and 1,2-propanediol undergo water elimination to form carbenium ions, which deprotonate to yield isobutene and propanal, respectively. The calculated activation energy for each

elementary step and the overall activation energy in different solvents are reported in Figure 6.4.
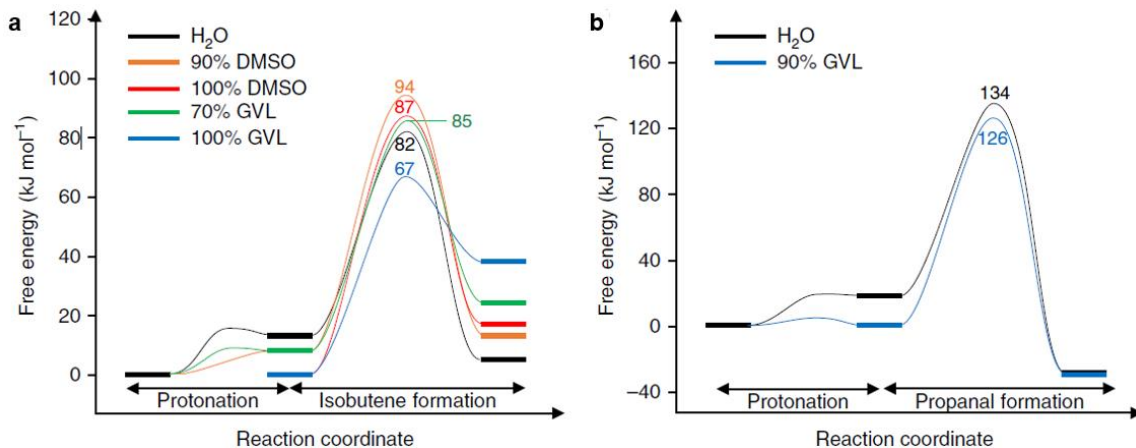
Figure 6.4 DFT simulated reaction energies and activation energies of the Brønsted acid-catalyzed dehydration of *tert*-butanol and 1,2-propanediol. a, Free energy diagram for *tert*-butanol dehydration in water (black line), 90 wt% DMSO (orange line), 100 wt% DMSO (red line), 70 wt% GVL (green line), and 100 wt% GVL (blue line). **b**, Free energy diagram for 1,2-propanediol dehydration in water (black line) and 90 wt% GVL (blue line). Figures are obtained from Reference [76].

The rate of acid-catalyzed dehydration in liquid phase is governed by the stability of transition state complex in the rate-determining step relative to the solvated proton and reactant. The difference in stability of alcohol in different solvents is generally small in comparison to the positively charged proton which interacts strongly with solvent molecules. Therefore, the major contribution to the stabilization of reactants originates from proton interaction with solvent molecules. The computational analysis of proton–solvent interaction in different solvents can reveal the source of change in activation free energy of dehydration.

210
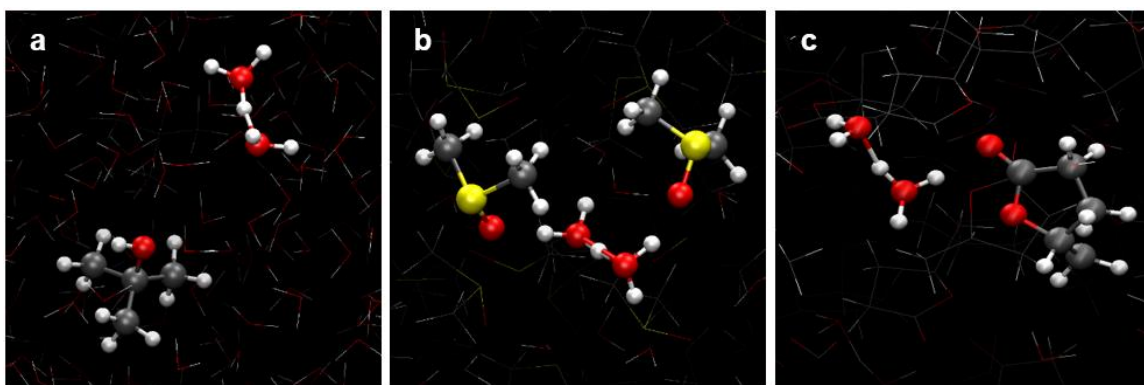
Figure 6.5 Snapshots of *ab initio* molecular dynamics simulations for a solvated proton in (a) bulk water, (b) 90 wt% DMSO, and (c) 70 wt% GVL. The strength of solvent–proton interaction increases from bulk water < GVL–H_2O clusters < DMSO–H_2O clusters. Figures are obtained from Reference [76].

In water, proton is fully solvated as hydronium ion ($H_5O_2^+$) and stabilized in solvation shells of water molecules (Figure 6.5a). The protonation of alcohol requires a relocation of solvated proton from bulk phase to water molecules localized near alcohol hydroxyl group, followed by a proton transfer from water molecule to the hydroxyl oxygen. For *tert*-butanol dehydration carried out in DMSO–water mixtures up to 90 wt% DMSO, the measured rates decrease as the DMSO composition increases (Figure 6.5b). The trajectory analysis of *ab initio* molecular dynamics simulations showed a formation of DMSO–water complex structure (Figure 6.4) in the liquid bulk phase, in agreement with previous studies of DMSO–water mixtures.[104–107] The polarity of DMSO molecule effectively stabilizes the hydrated proton structure via hydrogen bonding network. As a result, the DMSO–water–proton complex inhibits proton relocation from bulk solvent toward *tert*-butanol. The free energy sampling calculations show apparent activation free energy for dehydration increases from 82 kJ mol^{-1} in water to 94 kJ mol^{-1} in 90 wt% DMSO, consistent with the higher basicity of DMSO–water mixtures compared to pure water.[105,108] Similar solvent effect was also applicable for reactions carried out in GVLs–water

mixtures. The proton is favorably bound to GVL–water complex structure (Figure 6.5c), resulting in energy penalty to liberate the proton for the alcohol protonation step. The calculated 85 kJ mol^{-1} activation free energy for *tert*-butanol dehydration in 70 wt% GVL supports the experimental result that the dehydration rate is slower than in water.
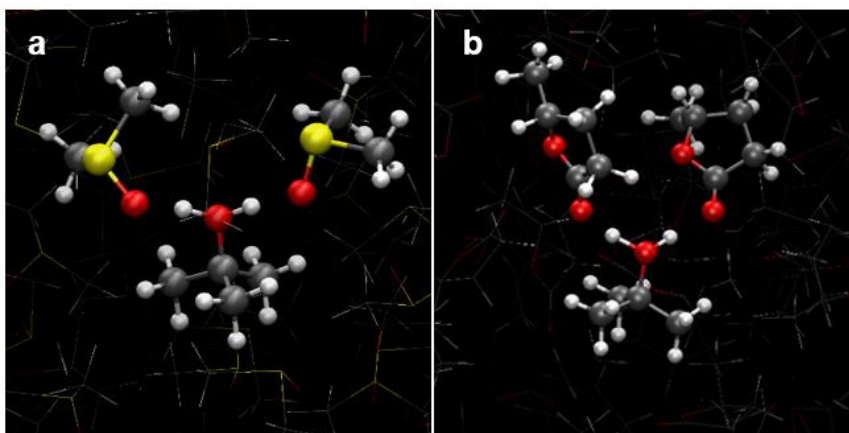
Figure 6.6 Initial state structures for *tert*-butanol dehydration in (a) 100 wt% DMSO and (b) 100 wt% GVL. The acidic proton is shown localized on the hydroxyl group of *tert*-butanol. Figures are obtained from Reference [76].

As the weight fraction of DMSO in the solution approaches 100 wt%, the proton is directly bound to DMSO molecules instead of DMSO–water cluster due to the lack of water present in the bulk. Such configuration (Figure 6.6a) results in weaker stabilization of proton than the DMSO–water cluster, but stronger than the proton stabilization in pure water as DMSO is more basic than water. The proton transfer from bulk DMSO solvent to *tert*-butanol is therefore more favorable than the reaction carried out in 90 wt% DMSO, but less favorable than the reaction in water. The calculated activation free energy for dehydration of *tert*-butanol is 87 kJ mol^{-1}, consistent with the faster dehydration rates in 100 wt% DMSO over in 90 wt% DMSO, but slower than in pure water. Such solvent configuration was also observed for *tert*-butanol in 100 wt% GVL solvent. However, the weak polarity of GVL molecule in comparison to DMSO molecule leads to a weak

interaction with other solvent molecules including water and the solvated proton. As a result, the energy penalty for liberating proton from GVL–water complex structure is not presence for dehydration reactions carried out in 100 wt% GVL solvent. Rather, the lack of proton stabilization in the initial state favors the protonation of alcohol, as reflected in the calculated activation free energy of 67 kJ mol^{-1} for *tert*-butanol dehydration in 100 wt% GVL (Figure 6.6b).
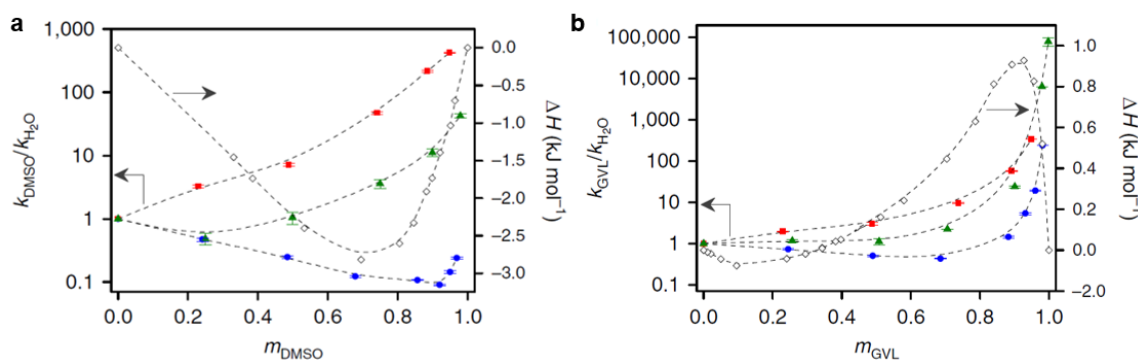
Figure 6.7 Plots showing ratios of Brønsted acid-catalyzed rate constant in organic mixtures with water ($k_{organic}$) relative to the value in water (k_{H2O}) on the left axis for *tert*-butanol (blue circles), 1,2-propanediol (green circles), and fructose (red squares). The enthalpies of mixing (ΔH) for organic solvent mixtures with water are presented in hollow diamond (right axis). The data is plotted against mass fraction (*m*) of (a) DMSO, and (b) GVL in organic solvent–water mixtures. Figures are obtained from Reference [76].

The solvation environment–reactivity relationship can be qualitatively associated to enthalpy of mixing between solvents.[100] The exothermic enthalpy of mixing (Figure 6.7) between DMSO and water suggests favorable interactions between water with DMSO molecule over interaction between water molecules, implying a formation of proton–water–DMSO complex and an additional energy cost for proton relocation from bulk solvent to localized water molecules near alcohol hydroxyl group. In contrary, the endothermic enthalpy of mixing between GVL and water near 100 wt% GVL composition indicates a stronger hydrogen bonding between water molecules over interaction between

water and GVL molecule. As such, the energy penalty for proton relocation is not present

in the dehydration reaction in concentrated GVL mixtures.
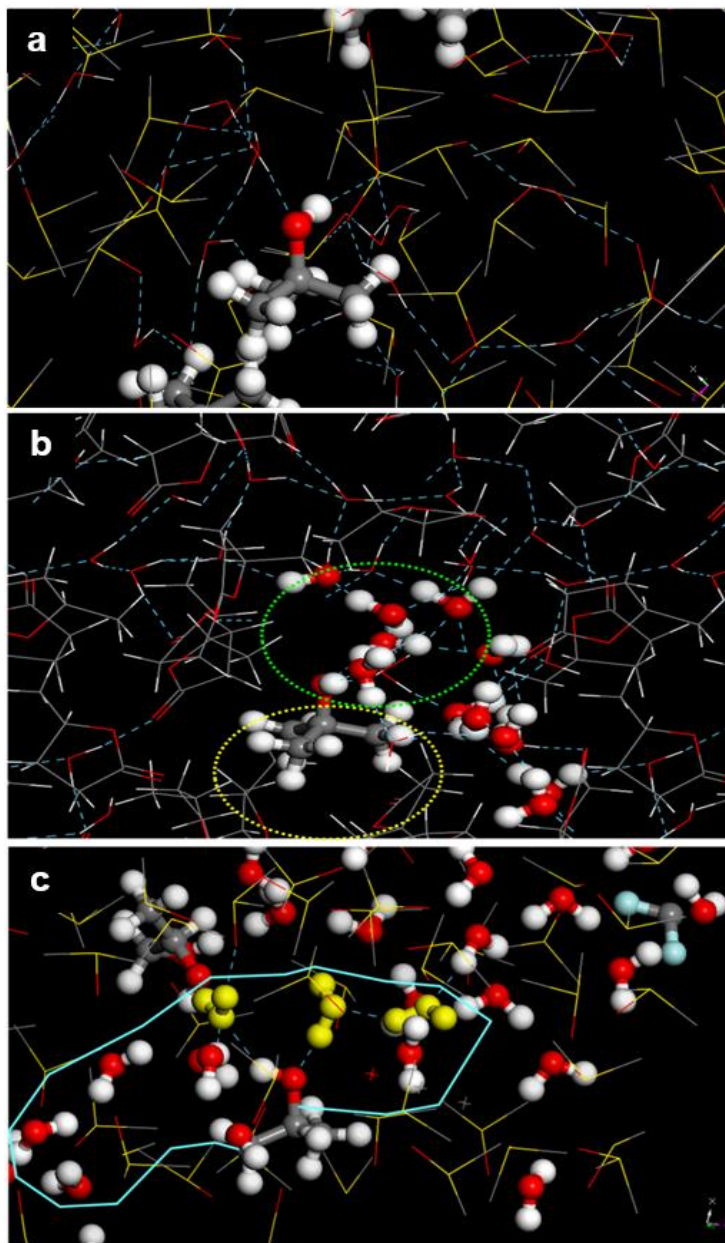
Figure 6.8 Snapshots from classical molecular dynamics simulations showing solvent reorganization on the polyol molecules. a, *tert*-butanol in 90 wt% DMSO showing water molecules dispersed between DMSO molecules due to strong DMSO interaction. **b**, *tert*-butanol in 90 wt% GVL showing hydrophilic domain (dashed green circle) near the alcohol hydroxyl group. **c**, 1,2-propanediol in 90 wt% GVL showing a water cluster of extended hydrophilic domain near the hydroxyl groups on the alcohol. Figures are obtained from Reference [76].

214

The reactivity trend for dehydration of 1,2-propanediol in GVL–water mixture is different from *tert*-butanol such that the dehydration rates are always faster in polar aprotic solvent–water mixtures. The molecular dynamics simulations reveal that 1,2-propanediol promotes a formation of hydrophilic cluster encapsulating the hydroxyl groups (Figure 6.8c). The extensive hydrogen bonding network between water molecules allows the proton to localize in the vicinity of hydroxyl groups which is more favorable than the water–cosolvent complex structure. The lack of energy penalty for proton liberation from the solvent complex facilitates the dehydration reaction, as seen from the calculated 134 kJ mol^{-1} and 126 kJ mol^{-1} activation free energy for 1,2-propanediol in water and 90 wt% GVL, respectively. Comparable trend in reactivity is also observed for dehydration of 1,2-propanediol in other polar aprotic solvent–water mixtures where the hydrophilicity of alcohol reactant results in localization of proton near reactive hydroxyl group, leading to enhanced reaction rates.

The dehydration of fructose in polar aprotic solvent–water mixtures closely follow the trend observed in 1,2-propanediol dehydration. The dehydration rate of fructose increases with the mass fraction of organic solvents, suggesting that the fructose molecule promotes the formation of hydrophilic water cluster which localize the proton and facilitates the dehydration reaction. The enhancement ratios for dehydration rate of fructose in organic solvent to rate in water are higher than the ratios for 1,2-propanediol at all solvent compositions, indicating that the higher number of hydroxyl groups in fructose molecule results in more extensive formation of water cluster which favors localization of proton more than 1,2-propanediol. Similar concept is also applicable to other reactions involving biomass molecules with various extent of hydrophilicity, including reactions

utilizing heterogeneous acid catalyst. This is evidence that the interaction pair between solvent-solvent, solvent–reactant, and reactant–reactant molecules need to be considered in order to accurately describe the solvent effects on reaction rates.

6.3.4 Effects of anion as co-catalyst
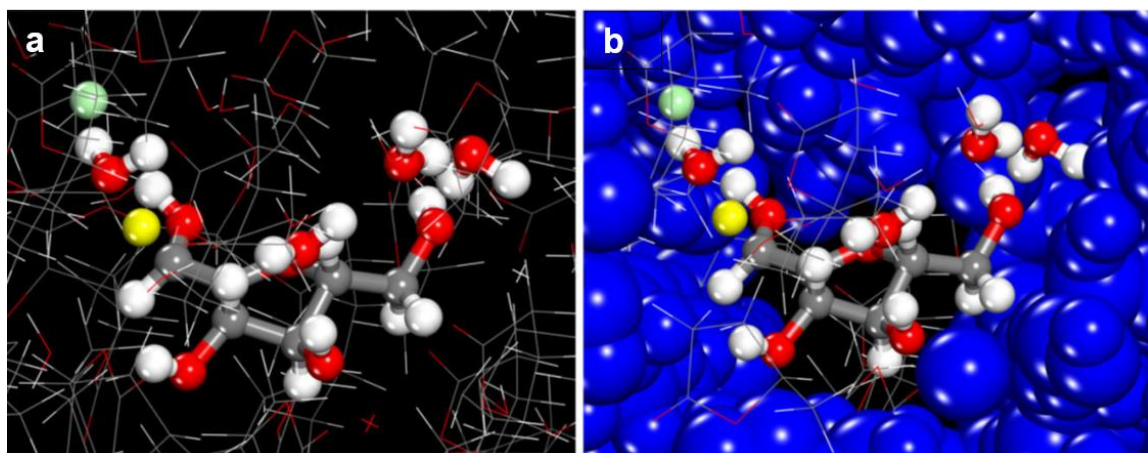
Figure 6.9 Molecular structures from *ab initio* molecular dynamics simulation showing the solvated structures of chloride anion (green atom) and the transition state in 90 wt% GVL. a, The transition state of fructose dehydration shows the proton (yellow atom) abstraction by water molecule to form enol. **b**, The molecular configuration shown in panel (**a**) with the hydrophilic shell shown in ball-and-stick structures and the outer hydrophobic shell shown in blue CPK structures. The chloride anion (green atom) is localized within the same hydrophilic shell surrounding fructose molecule and interacts directly with the positively charged reactive center. Figures are obtained from Reference [77].

In addition to the solvent–solute interactions, non-reactant solute can interact with the reactive species and affect the reaction kinetics. Experimental results show that the reactivity and selectivity of dehydration reaction are improved with addition of halide anions,[78–81] although the ions do not directly participate in the reaction mechanisms. *Ab initio* molecular dynamics simulations[77] of fructose dehydration in 90 wt% GVL with HCl as catalyst shows dissociation of acid and localization of both proton and chloride ion in the same hydrophilic water cluster near C2 hydroxyl group of fructose (Figure 6.9),

enabling the chloride ion to interact with both fructose in the initial state and dehydration transition state. The coulombic interaction between the negatively charged chloride ion and the positively charged transition state via direct hydrogen bonding results in stabilization of the transition state, lowering the activation free energy of dehydration from 84 kJ mol^{-1} to 74 kJ mol^{-1} for fructose dehydration in 90 wt% GVL with H$^+$ (no counter ion) and with HCL, respectively. In contrary, the co-catalytic effect is not observed with other conjugate anions of strong acids such as triflate anion (conjugate base of triflic acid) and bisulfate ion (conjugate base of sulfuric acid). The negative charge on the triflate and bisulfate anions are highly delocalized among oxygen atoms and therefore make them much weaker bases than the chloride ion. The interaction between weak conjugated bases and the positively charged transition state is insufficient to alter the activation free energy of fructose dehydration.

6.3.5 Solvent effects in heterogeneous reactions

The previous examples have demonstrated the role of solvent on the relative stability of reactants and transition state for reactions proceeding with a single mechanism. A catalytic system might consist of multiple reaction paths; each being affected by solvent to different extents. Therefore, the change in solvation environment could lead to a change in relative overall activation energies between competitive reactions and result in a shift in dominating reaction path.[278]

$$CH_3C(O)CH_2CH_{3\,(g)} + 2* \quad \rightleftharpoons \quad CH_3C*(O*)CH_2CH_3 \qquad (6.9)$$

$$H_{2\,(g)} \qquad\qquad\quad + 2* \quad \rightleftharpoons \quad 2H* \qquad\qquad\qquad (6.10)$$

$$CH_3C*(O*)CH_2CH_3 + H* \quad \overset{Hydroxy}{\rightleftharpoons} \quad CH_3C*(O*H)CH_2CH_3 \qquad (6.11)$$

$$CH_3C*(O*H)CH_2CH_3 + H* \quad \overset{Hydroxy}{\rightarrow} \quad CH_3CH(O*H)CH_2CH_3 \qquad (6.12)$$

$$CH_3C*(O*)CH_2CH_3 + H* \quad \overset{Alkoxy}{\rightleftharpoons} \quad CH_3CH(O*)CH_2CH_3 \qquad (6.13)$$

$$CH_3CH(O*)CH_2CH_3 + H* \quad \overset{Alkoxy}{\rightarrow} \quad CH_3CH(O*H)CH_2CH_3 \qquad (6.14)$$

Catalytic upgrading of biomass oxygenates into fine chemicals often involves a reduction of carbonyl bond into hydroxyl species such as a selective hydrogenation of aldehydes and ketones to alcohols.[9] The product distribution for the hydrogenation is controlled by surface structure and composition of the metal catalyst in addition to the reactant structures and solvents.[279] The hydrogenation of 2-butanone on Ru/SiO$_2$ catalyst[86] was chosen to probe the solvent effects on activation energies of elementary reactions that controls reaction kinetics and selectivity. The hydrogenation proceeds with an adsorption of 2-butanone onto metal surface and a dissociative adsorption of hydrogen (equations (6.9) and (6.10)). The adsorbed ketone follows a hydrogen addition as described in Horiuti–Polanyi mechanism,[280] which can occur via either hydroxy or alkoxy path.[281–286] In the hydroxy route, the surface hydrogen atom, H*, adds to the carbonyl oxygen of the adsorbed ketone to form a hydroxyalkyl intermediate (R$_1$R$_2$C*–OH, equation (6.11)), whereas the alkoxy route adds surface hydrogen to the carbonyl carbon atom to form alkoxy intermediate (R$_1$R$_2$CH–O*, (equation 6.12)). The addition of second hydrogen atom to carbonyl carbon/oxygen completes the hydrogenation for hydroxy and alkoxy route (equation (6.13) and (6.14)), respectively. Density functional theory (DFT) was used to calculate the reaction energies and activation energies for all elementary steps in both hydroxy and alkoxy paths, and the results are reported in Table 6.2.

Table 6.2 DFT calculated reaction energies and activation energies for the hydrogenation of 2-butanone to 2-butanol in gas phase, water, and 2-propanol solvent. All units are reported in kJ mol^{-1}. The functional group R$_1$ is CH$_3$CH$_2$, and the functional group R$_2$ is CH$_3$. Data is obtained from Reference [86].

Solvent	Hydroxy route			
	$R_1R_2C^* = O^* + H^* \rightarrow$ $R_1R_2C^*OH$		$R_1R_2C^*OH + H^* \rightarrow R_1R_2CHOH$	
	ΔE_{rxn}	ΔE_a	ΔE_{rxn}	ΔE_a
–	21	64	−18	72
Water	−23	20	−20	68
2-propanol	−16	32	−20	70
	Alkoxy route			
	$R_1R_2C^* = O^* + H^* \rightarrow$ $R_1R_2C^*OH$		$R_1R_2C^*OH + H^* \rightarrow R_1R_2CHOH$	
	ΔE_{rxn}	ΔE_a	ΔE_{rxn}	ΔE_a
–	−47	58	50	123
Water	−47	58	4	115
2-propanol	−42	62	6	116

The first hydrogen addition step in gas phase shows 21 kJ mol^{-1} and −47 kJ mol^{-1} for the reaction energy in hydroxy path and alkoxy path, respectively. The lower reaction energy in alkoxy path suggests that the formation of alkoxy species is more favored than hydroxy species. This result supports the notion that Ru metal has high oxophilicity[279] and that it strongly binds to oxygen as an the alkoxy intermediate. The activation energies for the second hydrogen addition step are calculated to be 72 kJ mol^{-1} and 123 kJ mol^{-1} for hydroxy path and alkoxy path, respectively. These transition states are much higher in energy than the hydroxy/alkoxy intermediates that form and thus the second hydrogen addition is considered a rate-determining step. As such, the rate of 2-butanone hydrogenation is controlled by the equilibrium adsorption of reactants, equilibrium for the first hydrogen addition, and the activation energy for the second hydrogen addition step. The overall activation energies for the hydrogenation of 2-butanone in hydroxyl and alkoxy path are 93 kJ mol^{-1} and 76 kJ mol^{-1}, respectively. The result indicates that the

hydrogenation of 2-butanone in gas phase is likely to proceed with alkoxy route over hydroxy route.
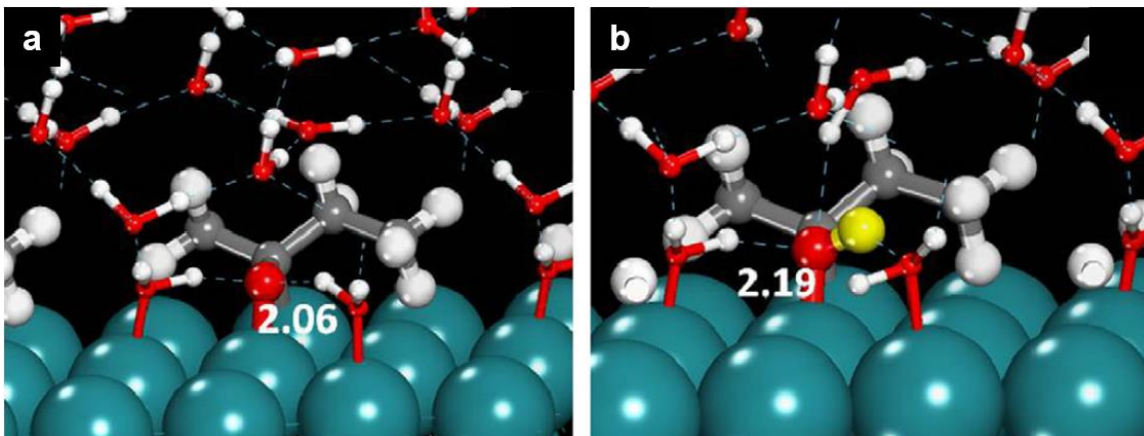
Figure 6.10 Solvated configurations in aqueous phase of (a) adsorbed 2-butanone and (b) hydroxy intermediate over Ru(0 0 0 1) surface. The hydrogen atom involved in hydrogenation is marked in yellow. Figures are obtained from Reference [86].

In the presence of water solvents, the adsorbed 2-butanone is enveloped by water molecules which form hydrogen bonds with oxygen atom in the carbonyl group and stabilize the ketone (Figure 6.10). The hydroxy and alkoxy intermediates remain in close contact with the water molecules after the first hydrogen addition step (Figure 6.10). The stabilization of intermediates that form in presence of water results in -23 kJ mol^{-1} and -47 kJ mol^{-1} reaction energy for the first hydrogen addition in hydroxy and alkoxy path, respectively. The 44 kJ mol^{-1} decrease in reaction energy for hydroxy route arises from the fact that alkoxy structure is less hydrophilic than the hydroxyl structure. Consequently, the extent of hydrogen bond stabilization from water molecules to the alkoxy intermediate is much weaker than the hydroxy intermediate. The activation energies for the rate-determining second hydrogen addition step in hydroxy and alkoxy path are lowered by approximately 4 kJ mol^{-1} and 8 kJ mol^{-1} in presence of water, respectively. The 45 kJ mol^{-}

^{1} and 68 kJ mol^{-1} overall activation energies for hydroxy and alkoxy path suggest that the hydrogenation of 2-butanone in water favor the hydroxy path.

Similar calculations were also carried out for the hydrogenation of 2-butanone in less polar solvents such as 2-propanol. The overall activation energies for both hydrogen addition steps are 54 kJ mol^{-1} and 74 kJ mol^{-1} for hydroxy and alkoxy path, respectively. For both reaction paths, the overall activation energies in 2-propanol are lower than the corresponding reactions in gas phase, but higher than the reactions in aqueous phase. The observed trend in reaction and activation energies can be correlated to solvent polarity where the less polar 2-propanol molecules form weaker hydrogen bonds with the adsorbed species and therefore provide less stabilization than water solvent but more than vacuum. This polarity–reactivity relationship is also supported by the fact that the reaction rates in non-polar solvents such as n-heptane is lower than in polar solvents.[86]

In the previous example, we showed solvent can alter the activation energies of different reaction paths by forming hydrogen bonding and providing stabilization to reactive species. The effect of solvent on chemical reactions, however, is not limited only to electronic stabilization. In many cases, solvent molecules can directly participate in the reaction and enable a new reaction mechanism.
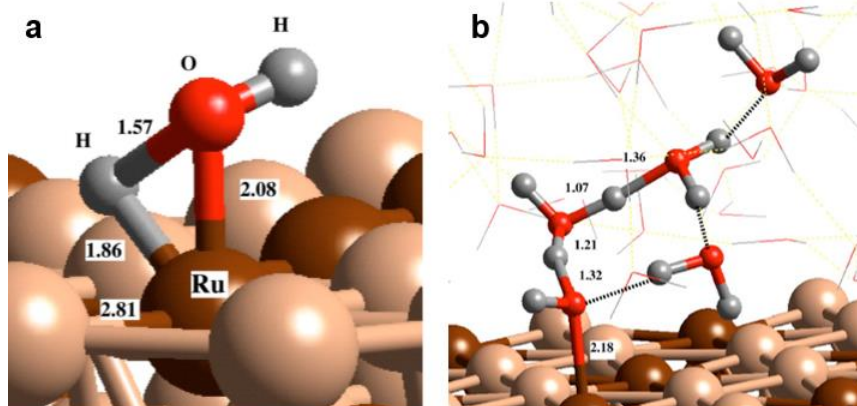
Figure 6.11 Transition state structure for the (a) homolytic dissociation of water molecule into surface-bound hydroxy and hydrogen species. (b) heterolytic dissociation of water molecule into surface-bound hydroxy and free hydronium ion. Figures are obtained from Reference [87].

Electrocatalytic dissociative reaction of water molecule over Pt–Ru alloy is one of the elementary reaction steps in the removal process of catalyst poison, carbon monoxide, from the metal surface.[287] In gas phase, a water molecule undergoes homolytic dissociation, leading to a formation of hydrogen atom and hydroxyl species bound to the metal atoms (Figure 6.11a). The presence of liquid water allows for a heterolytic dissociation mechanisms where the oxygen of water molecule is adsorbed onto metal surface, transferring a proton to another vicinal water molecule, and form a surface bound hydroxyl species along with a mobile hydronium ion in the bulk solvent (Figure 6.11b). The calculated activation energies for homolytic dissociation of water molecule over $Pt_{66}Ru_{33}(111)$ in gas phase and in liquid phase were found to be 105 kJ mol^{-1} and 80 kJ mol^{-1}, respectively. The result is consistent with the previous study[86] that highly polar solvents tend to stabilize reactive species and lower the activation free energy. The activation energy for homolytic path in liquid phase is, however, still much higher than the 27 kJ mol^{-1} activation energy for heterolytic path. Therefore, water molecules are more likely to dissociate into hydroxyl intermediate and hydronium ion, and the direct

222

participation of water solvent in the electrocatalytic dissociation of water molecule can enable a more favorable reaction mechanism not available in gas phase.

6.4 Conclusion

The modification of reaction environment in liquid phase can drastically affect the reaction rate, selectivity, and reaction mechanisms. We used computational methods to investigate effects of solvent on various reactions and showed that the reaction rate is correlated to the stability of reactants in comparison to the transition state. The interactions between solvent–solvent, solvent–solute, and solute–solute contribute to the change in reactivity observed experimentally. In gas phase, the rates for reactions carried out using Brønsted acid catalyst is directly related to acid deprotonation energy (DPE). The stronger acids with low DPE readily deprotonate and yield acidic proton which favors the acid catalyzed reaction. The confinement effects from reaction environment also need to be considered for reactions carried out in microporous acid catalyst. The interaction between silicate wall and the transition state results in a stabilization of transition state and hence lower the activation energy in comparison to reaction carried out on typical Brønsted acid catalyst. The zeolite with smaller pore size is preferred owing to the favorable close-range interaction between transition state and the pore structure, given that the pore is sufficiently large to accommodate the reactants.

The interactions between reactive species and the reaction environment in liquid phase are highly complex owing to the mobile nature of liquid phase. We used *ab initio* molecular dynamics simulation in combination with free energy sampling method to properly sample for a large number of possible solvent configurations. Molecular dynamics

trajectories in the Brønsted acid-catalyzed dehydration of simple alcohols reveal that the interactions between solvent molecules, proton, and reactants play an important role in determining the reaction rates. The acid-catalyzed reaction in highly basic solvent such as DMSO–water mixture generally leads to a stabilization of proton within proton–DMSO–water complex structure. The induced additional elementary step for proton liberation increases the total activation energy of dehydration and lowers the dehydration rate. The energy cost for additional proton transfer step can be avoided if the reactants contain multiple hydrophilic functional groups. The hydroxyl groups on alcohol promote a formation of hydrophilic domain consisting of acidic proton solvated in the hydrogen bond network between water molecules. The close distance between the proton and the reactive hydroxyl groups within the same hydrophilic domain eliminates the need for proton liberation step and allows a direct protonation of the reactant.

In contrary, solvents with relatively unfavorable interaction with water (as indicated by enthalpy of mixing) such as dioxane, tetrahydrofuran, acetonitrile, and γ-valerolactone (GVL) do not form a stabilizing complex structure with proton. Rather, they promote a formation of localized water clusters in which proton favorably resides. The dehydration reactions in such solvents are highly favored over reactions in water solvent as they allow for localization of proton near the reactive hydroxyl species regardless of reactant hydrophilicity.

Furthermore, we showed that a small negatively charged species such as chloride anion can help lowering the activation energy of dehydration reactions in polar aprotic solvent–water. The water cluster that forms around hydroxyl species promotes a

localization of the anion along with proton, allowing direct stabilization of positively charged transition state by the negatively charged chloride ion. Such effect is not observed with the use of large anions such as bisulfate or triflate ions because the negative charge on the anions are highly delocalized which results in a weak anion–transition state interaction.

For a reaction that proceeds by more than one reaction path, the change in solvation environment can alter the activation energies of competitive paths which leads to a shift in the dominating mechanism. In gas phase, the hydrogenation of 2-butanone over Ru/SiO_2 catalyst proceeds through alkoxy path over hydroxy path. The presence of water molecules stabilizes the reactive intermediates and lowers the activation energy of hydroxy path more so than the alkoxy path, resulting in a shift in mechanisms toward hydroxy intermediate formation in liquid phase. In addition, solvent molecules can directly participate in the reaction and enable a more favorable reaction path not possible in gas phase. Such reaction mechanism is demonstrated in the electrocatalytic dissociation of water molecule over Pt–Ru alloy surface which proceeds with homolytic dissociation of water molecule into adsorbed hydroxyl and hydrogen species. The introduction of water layers to the catalytic system allows the reactant water molecule to favorably dissociates heterolytically and release a proton to bulk water molecule, forming a hydronium ion.

6.5 Outlook

We have outlined the recent uses of theoretical methods to investigate the effects of reaction environment on various chemical reactions. We believe that the use of theory in combination with experiments will tremendously help with understanding the

underlying rules for the behavior of catalyzed reaction in liquid phase. In these works, we focused on the aspect of interactions between solvents and species in the kinetically relevant elementary steps while ignoring other effects such as temperature, side reactions, defect sites, catalyst support, and catalyst poisoning. We believe that a complete evaluation of catalytic system will need to take those factors into consideration.

The continuous advancement in computational power has made more accurate, lengthy calculations possible. This will allow theoretical investigations in larger, more complicated systems, especially in liquid phase where a large number of solvent molecules might be needed. The accuracy of DFT calculations could be further improved with the use of higher-level hybrid and meta-hybrid functionals at the expense of exponentially increased computational cost. In addition, most studies of surface chemistry are performed using electronic structure calculations which largely ignore the entropic effects. A free energy sampling should be implemented to properly account for the change in molecular structures and entropic contribution at elevated temperatures.

Overall, the simulations of chemical reactions will likely move toward a more realistic models with larger system size employing more accurate computational methods. The computational analysis will be performed on reaction network with multiple reaction paths rather than just a few known, dominating paths. The collaboration between experiments and simulations will be used in efficient development of selective catalytic systems.

Chapter 7 – Summary and Conclusions

First-principles quantum chemical methods were used along with a free energy sampling technique to elucidate the fundamental principles that govern the rate of Brønsted acid-catalyzed dehydration reaction of biomass derived oxygenates. We showed that the molecular interactions between solvent molecules, solvated proton, and the polyols can alter the extent of solvation of reactive species. The shift in the relative stability of these reactive species which can be tuned through the use of different solvent mixtures leading to the change in experimentally observed reactivities and selectivities.

The dehydration reactions of *tert*-butanol, 1,2-propanediol, and fructose were examined in water, DMSO–water mixtures, and γ-valerolactone (GVL)–water mixtures. The *ab initio* molecular dynamics (AIMD) trajectories show that the strong homogeneous Brønsted acids completely dissociates in water and polar aprotic solvent–water mixtures, resulting in a hydronium ion and a conjugate anion encapsulated in isolated solvation shells. The basic organic solvents such as DMSO interacts favorably with the hydronium ion and form a stable proton–DMSO–water complex. The proton stabilization in DMSO–water mixtures imposes an additional proton liberation elementary step which increases the overall activation energy of dehydration and lowers the reactivity. The formation of a stabilized proton–solvent complex, however, can be circumvented if the polyol reactant contains multiple vicinal hydroxyl groups. We showed that highly hydrophilic polyols such as 1,2-propanediol and fructose molecules promote the formation of a hydrophilic water cluster surrounding the polyol hydroxyl groups, in contrast to the more hydrophobic *tert*-butanol. Such solvent reorganization near highly hydrophilic polyols results in the localization of the acidic proton in the hydrophilic water cluster near hydroxyl groups

which in turn facilitates the dehydration reaction. As a result, the dehydration rates of 1,2-propanediol and fructose are higher in DMSO–water mixtures than in water, as opposed to the lower dehydration rates of *tert*-butanol. The formation of hydrophilic water cluster around the reactant can also be achieved with the use of less basic polar aprotic solvents that interacts weakly with water molecules such as GVL. Depending on the GVL content in the solution, the mixture can promote the formation of a hydrophilic domain localizing the reactive species regardless of reactant hydrophilicity.

Subsequently, the effects of chloride, bisulfate, and triflate conjugate anions on the Brønsted acids-catalyzed dehydration of fructose was investigated. In pure water, the dissociation of Brønsted acid yields hydronium ion and the conjugate anion solvated in separate hydration shells. The use of polar aprotic solvent–water mixtures results in the formation of a hydrophilic water cluster around the fructose molecule where both acidic proton and the anion are co-localized near the reactive hydroxyl group. The close contact between fructose hydroxyl groups and the proton facilitates the protonation step which lowers the overall activation energy of dehydration reaction. In addition, the localization of small anions such as chloride ion within the same hydrophilic domain allows for the stabilization of positively charged transition state structure and further lowers the activation energy of dehydration. In contrast, the transition state stabilization is not observed for large anions such as bisulfate and triflate anions. The negative charge on these anions is highly delocalized among their oxygen atoms which makes the interaction between the dehydration transition state and these anions much weaker than with the chloride ion.

The investigation of solvent effects was extended to the production of HMF from naturally abundant glucose. *Ab initio* molecular dynamics simulations were employed to explore the effects of acetone–water mixtures on different reaction paths including the isomerization of glucose to fructose using Sn–BEA catalyst, the dehydration of fructose to HMF, the direct dehydration of glucose to HMF, and the degradation of HMF to humins side products using homogeneous acid catalyst. The calculated overall activation energies show that the conversion of glucose to HMF occurs via the isomerization of glucose to fructose followed by the dehydration of fructose to HMF rather than the direct dehydration of glucose to HMF. The effect of organic solvent in the isomerization reaction is minimal due to the confined space within zeolite pore which prevents the interactions between the hydride shift transition state and the solvent molecules. The subsequent dehydration of fructose in acetone–water mixtures benefits from the reorganization of solvent molecules that results in the localization of proton near reactive hydroxyl group of fructose and lowers the activation energy of dehydration. In contrast, the HMF molecule is substantially less hydrophilic than fructose as it possesses three fewer hydroxyl groups. The hydrophilic domain that forms in acetone–water mixtures is therefore located far from the HMF molecule. The energy penalty for proton transfer from the hydrophilic domain to the bulk solvent near HMF molecule increases the overall activation energy for the degradation of HMF. As such, the acetone–water solvent mixtures enhance the rate of HMF production, suppress the rate of HMF degradation, and effectively improve the HMF selectivity.

The focus of this work then shifted toward the use of zeolite acid catalyst as it offers several advantages over homogeneous acids such as the shape selectivity and the ease of catalyst recovery. In order to accurately predict the number of solvent molecules available

229

in the hydrophilic acidic zeolite, we developed an atomistic model to replicate the interactions between solvent molecules and the aluminosilicate materials within Faujasite and Mordenite zeolite framework. The model features a new Monte Carlo move that allows simultaneous simulation of cation siting and aluminum distribution while preserving the connectivity of bridging oxygen framework atoms. The simulation results are able to satisfactorily reproduce the experimentally observed location of sodium cation in Faujasite as well as the aluminum distribution and occupancy in Mordenite over a broad Si/Al range. Our calculations for Faujasite have shown the greatest cationic affinity at the sites oriented toward supercage (site II) followed by the sites located in the middle of hexagonal prism (site I) and the sites positioned between sodalite cage and the hexagonal prism (site I'). The geometric constraint between site I and site I' leads to the shift of cation occupancy as the number of cations per unit cell increases. In addition, the electrostatic repulsion between aluminum atoms within the framework results in the preferential occupancy of aluminum atoms at framework site located in the side channel (site T3) of Mordenite. Our model can be further developed to include solvent and alcohol adsorption data in order to equilibrate the molecular systems in liquid phase which is necessary for *ab initio* molecular dynamics calculations.

The results from our works on solvent effects for the dehydration of biomass-derived feedstocks are compared and correlated with other studies to provide a general outlook for the effect of the reaction environment on catalyzed reactions. A structure–reactivity relationship has been established for the gas-phase dehydration reaction of 2-butanol using polyoxometalate (POM) acid catalysts, where the reaction rates have been shown to linearly increase as the deprotonation energy (DPE) of Brønsted acid site

decreases. The reaction rate is further improved with the use of a structured Brønsted acid catalyst such as zeolite. The pore structure of zeolites provides a confinement effect that stabilizes the transition state structure and lowers the activation energy in comparison to the dehydration reaction using POM catalysts with similar deprotonation energy. For reaction in liquid phase, the solute–solvent as well as solvent–solvent interactions alter the relative extent of solvation of the reactive species. The solvent reorganization can result in a localization of proton, anion, and polyol reactants depending on the solvent composition which can enhance the dehydration reactivity. The interaction of solvent molecules with different reaction paths can affect the dominating reaction mechanism as demonstrated in the hydrogenation of 2-butanone over Ru/SiO_2 catalyst, where the reaction proceeds via a hydroxy path in the presence of water as opposed to the alkoxy path in the gas phase. In addition, solvent molecules can enable new reaction paths which are not available in the gas phase. The electrocatalytic dissociation of water molecules in gas phase over a Pt–Ru metal alloy has been shown to undergo homolytic dissociation to yield hydrogen and hydroxy adsorbed species. However, the presence of water layers over metal catalyst allows for the heterolytic dissociation which releases hydronium ion to the bulk solvent. These studies have demonstrated the use of *ab initio* methods to aid in the understanding of reaction environment effects on a variety of chemical reactions.

The computational cost associated with *ab initio* calculations has become increasingly affordable with the technological advancement in the computer processors that allows for the modeling of more complicated, realistic catalytic systems such as heterogeneous reactions. Future work in this area should be performed on our zeolite force field to develop an accurate solvent adsorption model in zeolites which will be necessary

for the simulations in solvent mixtures. The studies of reaction environment in solid catalyst can be further extended to metal–organic frameworks (MOFs) as they offer a wider range of pore size selections and highly tunable active site properties.

References

1. Huber, G. W. Production of Liquid Alkanes by Aqueous-Phase Processing of Biomass-Derived Carbohydrates. *Science (80-.).* **308**, 1446–1450 (2005).

2. Chheda, J. N. & Dumesic, J. A. An overview of dehydration, aldol-condensation and hydrogenation processes for production of liquid alkanes from biomass-derived carbohydrates. *Catal. Today* **123**, 59–70 (2007).

3. Serrano-Ruiz, J. C., Braden, D. J., West, R. M. & Dumesic, J. A. Conversion of cellulose to hydrocarbon fuels by progressive removal of oxygen. *Appl. Catal. B Environ.* **100**, 184–189 (2010).

4. Serrano-Ruiz, J. C., West, R. M. & Dumesic, J. A. Catalytic Conversion of Renewable Biomass Resources to Fuels and Chemicals. *Annu. Rev. Chem. Biomol. Eng.* **1**, 79–100 (2010).

5. Serrano-Ruiz, J. C. & Dumesic, J. A. Catalytic routes for the conversion of biomass into liquid hydrocarbon transportation fuels. *Energy Environ. Sci.* **4**, 83–99 (2011).

6. Alonso, D. M., Wettstein, S. G. & Dumesic, J. A. Bimetallic catalysts for upgrading of biomass to fuels and chemicals. *Chem. Soc. Rev.* **41**, 8075 (2012).

7. Murat Sen, S., Henao, C. A., Braden, D. J., Dumesic, J. A. & Maravelias, C. T. Catalytic conversion of lignocellulosic biomass to fuels: Process development and technoeconomic evaluation. *Chem. Eng. Sci.* **67**, 57–67 (2012).

8. Wettstein, S. G., Alonso, D. M., Gürbüz, E. I. & Dumesic, J. A. A roadmap for conversion of lignocellulosic biomass to chemicals and fuels. *Curr. Opin. Chem. Eng.* **1**, 218–224 (2012).

9. Chheda, J. N., Huber, G. W. & Dumesic, J. A. Liquid-Phase Catalytic Processing of Biomass-Derived Oxygenated Hydrocarbons to Fuels and Chemicals. *Angew. Chemie Int. Ed.* **46**, 7164–7183 (2007).

10. Chheda, J. N., Román-Leshkov, Y. & Dumesic, J. A. Production of 5-hydroxymethylfurfural and furfural by dehydration of biomass-derived mono- and poly-saccharides. *Green Chem.* **9**, 342–350 (2007).

11. Román-Leshkov, Y., Barrett, C. J., Liu, Z. Y. & Dumesic, J. A. Production of dimethylfuran for liquid fuels from biomass-derived carbohydrates. *Nature* **447**, 982–985 (2007).

12. Kunkes, E. L. *et al.* Catalytic Conversion of Biomass to Monofunctional Hydrocarbons and Targeted Liquid-Fuel Classes. *Science (80-.).* **322**, 417–421 (2008).

13. West, R. M., Liu, Z. Y., Peter, M. & Dumesic, J. A. Liquid Alkanes with Targeted Molecular Weights from Biomass-Derived Carbohydrates. *ChemSusChem* **1**, 417–424 (2008).

14. West, R. M., Kunkes, E. L., Simonetti, D. A. & Dumesic, J. A. Catalytic conversion of biomass-derived carbohydrates to fuels and chemicals by formation and upgrading of mono-functional hydrocarbon intermediates. *Catal. Today* **147**, 115–125 (2009).

15. West, R. M., Tucker, M. H., Braden, D. J. & Dumesic, J. A. Production of alkanes from biomass derived carbohydrates on bi-functional catalysts employing niobium-based supports. *Catal. Commun.* **10**, 1743–1746 (2009).

16. Alonso, D. M., Bond, J. Q. & Dumesic, J. A. Catalytic conversion of biomass to biofuels. *Green Chem.* **12**, 1493 (2010).

17. Kuster, B. F. M. 5-Hydroxymethylfurfural (HMF). A Review Focussing on its Manufacture. *Starch - Stärke* **42**, 314–321 (1990).

18. Mamman, A. S. *et al.* Furfural: Hemicellulose/xylosederived biochemical. *Biofuels, Bioprod. Biorefining* **2**, 438–454 (2008).

19. Cai, C. M., Zhang, T., Kumar, R. & Wyman, C. E. THF co-solvent enhances hydrocarbon fuel precursor yields from lignocellulosic biomass. *Green Chem.* **15**, 3140 (2013).

20. Zhang, L., Yu, H., Wang, P. & Li, Y. Production of furfural from xylose, xylan and corncob in gamma-valerolactone using FeCl3·6H2O as catalyst. *Bioresour. Technol.* **151**, 355–360 (2014).

21. Mellmer, M. A., Martin Alonso, D., Luterbacher, J. S., Gallo, J. M. R. & Dumesic, J. a. Effects of γ-valerolactone in hydrolysis of lignocellulosic biomass to monosaccharides. *Green Chem.* **16**, 4659–4662 (2014).

22. Cui, J. *et al.* Direct conversion of carbohydrates to γ-valerolactone facilitated by a solvent effect. *Green Chem.* **17**, 3084–3089 (2015).

23. Rasrendra, C. B., Soetedjo, J. N. M., Makertihartha, I. G. B. N., Adisasmito, S. & Heeres, H. J. The Catalytic Conversion of d-Glucose to 5-Hydroxymethylfurfural in DMSO Using Metal Salts. *Top. Catal.* **55**, 543–549 (2012).

24. Wang, Y. *et al.* Effects of solvents and catalysts in liquefaction of pinewood sawdust for the production of bio-oils. *Biomass and Bioenergy* **59**, 158–167 (2013).

25. Salak Asghari, F. & Yoshida, H. Acid-Catalyzed Production of 5-Hydroxymethyl Furfural from <scp>d</scp> -Fructose in Subcritical Water. *Ind. Eng. Chem. Res.*

45, 2163–2173 (2006).

26.   Ishida, H. & Seri, K. Catalytic activity of lanthanoide(III) ions for dehydration of d-glucose to 5-(hydroxymethyl) furfural. *J. Mol. Catal. A Chem.* **112**, L163–L165 (1996).

27.   Carlini, C. *et al.* Selective saccharides dehydration to 5-hydroxymethyl-2-furaldehyde by heterogeneous niobium catalysts. *Appl. Catal. A Gen.* **183**, 295–302 (1999).

28.   Armaroli, T. *et al.* Acid sites characterization of niobium phosphate catalysts and their activity in fructose dehydration to 5-hydroxymethyl-2-furaldehyde. *J. Mol. Catal. A Chem.* **151**, 233–243 (2000).

29.   Seri, K., Inoue, Y. & Ishida, H. Catalytic Activity of Lanthanide(III) Ions for the Dehydration of Hexose to 5-Hydroxymethyl-2-furaldehyde in Water. *Bull. Chem. Soc. Jpn.* **74**, 1145–1150 (2001).

30.   Watanabe, M. *et al.* Glucose reactions with acid and base catalysts in hot compressed water at 473K. *Carbohydr. Res.* **340**, 1925–1930 (2005).

31.   Watanabe, M., Aizawa, Y., Iida, T., Nishimura, R. & Inomata, H. Catalytic glucose and fructose conversions with TiO2 and ZrO2 in water at 473K: Relationship between reactivity and acid–base property determined by TPD measurement. *Appl. Catal. A Gen.* **295**, 150–156 (2005).

32.   Moreau, C. *et al.* Dehydration of fructose to 5-hydroxymethylfurfural over H-mordenites. *Appl. Catal. A Gen.* **145**, 211–224 (1996).

33.   Asghari, F. S. & Yoshida, H. Kinetics of the Decomposition of Fructose Catalyzed by Hydrochloric Acid in Subcritical Water: Formation of 5-Hydroxymethylfurfural, Levulinic, and Formic Acids. *Ind. Eng. Chem. Res.* **46**, 7703–7710 (2007).

34.   Musau, R. M. & Munavu, R. M. The preparation of 5-hydroxymethyl-2-furaldehyde (HMF) from d-fructose in the presence of DMSO. *Biomass* **13**, 67–74 (1987).

35.   Nakamura, Y. & Morikawa, S. The Dehydration of D-Fructose to 5-Hydroxymethyl-2-furaldehyde. *Bull. Chem. Soc. Jpn.* **53**, 3705–3706 (1980).

36.   Seri, K., Inoue, Y. & Ishida, H. Highly Efficient Catalytic Activity of Lanthanide(III) Ions for Conversion of Saccharides to 5-Hydroxymethyl-2-furfural in Organic Solvents. *Chem. Lett.* **29**, 22–23 (2000).

37.   Kimura, H., Nakahara, M. & Matubayasi, N. Solvent Effect on Pathways and Mechanisms for <scp>d</scp> -Fructose Conversion to 5-Hydroxymethyl-2-furaldehyde: In Situ ^{13}C NMR Study. *J. Phys. Chem. A* **117**, 2102–2113 (2013).

38. Tyrlik, S. K., Szerszeń, D., Olejnik, M. & Danikiewicz, W. Selective dehydration of glucose to hydroxymethylfurfural and a one-pot synthesis of a 4-acetylbutyrolactone from glucose and trioxane in solutions of aluminium salts. *Carbohydr. Res.* **315**, 268–272 (1999).

39. Vasudevan, V. & Mushrif, S. H. Insights into the solvation of glucose in water, dimethyl sulfoxide (DMSO), tetrahydrofuran (THF) and N,N-dimethylformamide (DMF) and its possible implications on the conversion of glucose to platform chemicals. *RSC Adv.* **5**, 20756–20763 (2015).

40. Long, J. *et al.* An efficient and economical process for lignin depolymerization in biomass-derived solvent tetrahydrofuran. *Bioresour. Technol.* **154**, 10–7 (2014).

41. Jeong, J. *et al.* Commercially attractive process for production of 5-hydroxymethyl-2-furfural from high fructose corn syrup. *J. Ind. Eng. Chem.* **19**, 1106–1111 (2013).

42. Aellig, C. & Hermans, I. Continuous D-Fructose Dehydration to 5-Hydroxymethylfurfural Under Mild Conditions. *ChemSusChem* **5**, 1737–1742 (2012).

43. Bicker, M., Hirth, J. & Vogel, H. Dehydration of fructose to 5-hydroxymethylfurfural in sub- and supercritical acetone. *Green Chem.* **5**, 280–284 (2003).

44. Qi, X., Watanabe, M., Aida, T. M. & Smith, Jr., R. L. Catalytic dehydration of fructose into 5-hydroxymethylfurfural by ion-exchange resin in mixed-aqueous system by microwave heating. *Green Chem.* **10**, 799 (2008).

45. Toftgaard Pedersen, A., Ringborg, R., Grotkjær, T., Pedersen, S. & Woodley, J. M. Synthesis of 5-hydroxymethylfurfural (HMF) by acid catalyzed dehydration of glucose–fructose mixtures. *Chem. Eng. J.* **273**, 455–464 (2015).

46. Luterbacher, J. S. *et al.* Nonenzymatic sugar production from biomass using biomass-derived gamma-valerolactone. *Science (80-.).* **343**, 277–280 (2014).

47. Qi, L. *et al.* Catalytic Conversion of Fructose, Glucose, and Sucrose to 5-(Hydroxymethyl)furfural and Levulinic and Formic Acids in γ-Valerolactone As a Green Solvent. *ACS Catal.* **4**, 1470–1477 (2014).

48. Mellmer, M. A. *et al.* Solvent Effects in Acid-Catalyzed Biomass Conversion Reactions. *Angew. Chemie Int. Ed.* **53**, 11872–11875 (2014).

49. Qi, L. & Horváth, I. T. Catalytic conversion of fructose to γ-valerolactone in γ-valerolactone. *ACS Catal.* **2**, 2247–2249 (2012).

50. Gürbüz, E. I. *et al.* Conversion of Hemicellulose into Furfural Using Solid Acid

Catalysts in γ-Valerolactone. *Angew. Chemie Int. Ed.* **52**, 1270–1274 (2013).

51. Alonso, D. M. *et al.* Integrated conversion of hemicellulose and cellulose from lignocellulosic biomass. *Energy Environ. Sci.* **6**, 76–80 (2013).

52. Alonso, D. M., Gallo, J. M. R., Mellmer, M. A., Wettstein, S. G. & Dumesic, J. A. Direct conversion of cellulose to levulinic acid and gamma-valerolactone using solid acid catalysts. *Catal. Sci. Technol.* **3**, 927–931 (2013).

53. Zhao, H., Holladay, J. E., Brown, H. & Zhang, Z. C. Metal Chlorides in Ionic Liquid Solvents Convert Sugars to 5-Hydroxymethylfurfural. *Science (80-.).* **316**, 1597–1600 (2007).

54. Lansalot-Matras, C. & Moreau, C. Dehydration of fructose into 5-hydroxymethylfurfural in the presence of ionic liquids. *Catal. Commun.* **4**, 517–520 (2003).

55. Moreau, C., Finiels, A. & Vanoye, L. Dehydration of fructose and sucrose into 5-hydroxymethylfurfural in the presence of 1-H-3-methyl imidazolium chloride acting both as solvent and catalyst. *J. Mol. Catal. A Chem.* **253**, 165–169 (2006).

56. Nikolakis, V., Mushrif, S. H., Herbert, B., Booksh, K. S. & Vlachos, D. G. Fructose–Water–Dimethylsulfoxide Interactions by Vibrational Spectroscopy and Molecular Dynamics Simulations. *J. Phys. Chem. B* **116**, 11274–11283 (2012).

57. Mushrif, S. H., Caratzoulas, S. & Vlachos, D. G. Understanding solvent effects in the selective conversion of fructose to 5-hydroxymethyl-furfural: a molecular dynamics investigation. *Phys. Chem. Chem. Phys.* **14**, 2637 (2012).

58. Walker, T. W. *et al.* Universal kinetic solvent effects in acid-catalyzed reactions of biomass-derived oxygenates. *Energy Environ. Sci.* **11**, 617–628 (2018).

59. Yang, L., Tsilomelekis, G., Caratzoulas, S. & Vlachos, D. G. Mechanism of Brønsted Acid-Catalyzed Glucose Dehydration. *ChemSusChem* **8**, 1334–1341 (2015).

60. Ståhlberg, T., Rodriguez-Rodriguez, S., Fristrup, P. & Riisager, A. Metal-Free Dehydration of Glucose to 5-(Hydroxymethyl)furfural in Ionic Liquids with Boric Acid as a Promoter. *Chem. - A Eur. J.* **17**, 1456–1464 (2011).

61. Yang, G., Pidko, E. A. & Hensen, E. J. M. Mechanism of Brønsted acid-catalyzed conversion of carbohydrates. *J. Catal.* **295**, 122–132 (2012).

62. Loerbroks, C., Rinaldi, R. & Thiel, W. The Electronic Nature of the 1,4-β-Glycosidic Bond and Its Chemical Environment: DFT Insights into Cellulose Chemistry. *Chem. - A Eur. J.* **19**, 16282–16294 (2013).

63. Wang, M., Liu, C., Li, Q. & Xu, X. Theoretical insight into the conversion of xylose to furfural in the gas phase and water. *J. Mol. Model.* **21**, 296 (2015).

64. Feng, S., Bagia, C. & Mpourmpakis, G. Determination of Proton Affinities and Acidity Constants of Sugars. *J. Phys. Chem. A* **117**, 5211–5219 (2013).

65. Assary, R. S., Redfern, P. C., Greeley, J. & Curtiss, L. A. Mechanistic Insights into the Decomposition of Fructose to Hydroxy Methyl Furfural in Neutral and Acidic Environments Using High-Level Quantum Chemical Methods. *J. Phys. Chem. B* **115**, 4341–4349 (2011).

66. Assary, R. S. & Curtiss, L. A. Comparison of Sugar Molecule Decomposition through Glucose and Fructose: A High-Level Quantum Chemical Study. *Energy & Fuels* **26**, 1344–1352 (2012).

67. Assary, R. S., Kim, T., Low, J. J., Greeley, J. & Curtiss, L. A. Glucose and fructose to platform chemicals: understanding the thermodynamic landscapes of acid-catalysed reactions using high-level ab initio methods. *Phys. Chem. Chem. Phys.* **14**, 16603 (2012).

68. Lin, X. *et al.* The first dehydration and the competing reaction pathways of glucose homogeneously and heterogeneously catalyzed by acids. *Phys. Chem. Chem. Phys.* **15**, 2967 (2013).

69. Qian, X. & Liu, D. Free energy landscape for glucose condensation and dehydration reactions in dimethyl sulfoxide and the effects of solvent. *Carbohydr. Res.* **388**, 50–60 (2014).

70. Liu, D., Nimlos, M. R., Johnson, D. K., Himmel, M. E. & Qian, X. Free Energy Landscape for Glucose Condensation Reactions. *J. Phys. Chem. A* **114**, 12936–12944 (2010).

71. Qian, X., Johnson, D. K., Himmel, M. E. & Nimlos, M. R. The role of hydrogen-bonding interactions in acidic sugar reaction pathways. *Carbohydr. Res.* **345**, 1945–1951 (2010).

72. Molteni, C. & Parrinello, M. Glucose in Aqueous Solution by First Principles Molecular Dynamics. *J. Am. Chem. Soc.* **120**, 2168–2171 (1998).

73. Wang, L. *et al.* Selective Catalytic Production of 5-Hydroxymethylfurfural from Glucose by Adjusting Catalyst Wettability. *ChemSusChem* **7**, 402–406 (2014).

74. Qian, X. & Wei, X. Glucose Isomerization to Fructose from ab Initio Molecular Dynamics Simulations. *J. Phys. Chem. B* **116**, 10898–10904 (2012).

75. Mushrif, S. H., Varghese, J. J. & Vlachos, D. G. Insights into the Cr(<scp>iii</scp>

) catalyzed isomerization mechanism of glucose to fructose in the presence of water using ab initio molecular dynamics. *Phys. Chem. Chem. Phys.* **16**, 19564–19572 (2014).

76. Mellmer, M. A. *et al.* Solvent-enabled control of reactivity for liquid-phase reactions of biomass-derived compounds. *Nat. Catal.* **1**, 199–207 (2018).

77. Mellmer, M. A. *et al.* Effects of chloride ions in acid-catalyzed biomass dehydration reactions in polar aprotic solvents. *Nat. Commun.* **10**, 1132 (2019).

78. Marcotullio, G. & De Jong, W. Chloride ions enhance furfural formation from d-xylose in dilute aqueous acidic solutions. *Green Chem.* **12**, 1739 (2010).

79. Marcotullio, G. & de Jong, W. Furfural formation from d-xylose: the use of different halides in dilute aqueous acidic solutions allows for exceptionally high yields. *Carbohydr. Res.* **346**, 1291–1293 (2011).

80. Enslow, K. R. & Bell, A. T. The Role of Metal Halides in Enhancing the Dehydration of Xylose to Furfural. *ChemCatChem* **7**, 479–489 (2015).

81. Jiang, Z., Yi, J., Li, J., He, T. & Hu, C. Promoting Effect of Sodium Chloride on the Solubilization and Depolymerization of Cellulose from Raw Biomass Materials in Water. *ChemSusChem* **8**, 1901–1907 (2015).

82. Motagamwala, A. H., Huang, K., Maravelias, C. T. & Dumesic, J. A. Solvent system for effective near-term production of hydroxymethylfurfural (HMF) with potential for long-term process improvement. *Energy Environ. Sci.* **12**, 2212–2222 (2019).

83. Macht, J., Janik, M. J., Neurock, M. & Iglesia, E. Mechanistic Consequences of Composition in Acid Catalysis by Polyoxometalate Keggin Clusters. *J. Am. Chem. Soc.* **130**, 10369–10379 (2008).

84. Janik, M. J., Macht, J., Iglesia, E. & Neurock, M. Correlating Acid Properties and Catalytic Function: A First-Principles Analysis of Alcohol Dehydration Pathways on Polyoxometalates. *J. Phys. Chem. C* **113**, 1872–1885 (2009).

85. Gounder, R., Jones, A. J., Carr, R. T. & Iglesia, E. Solvation and acid strength effects on catalysis by faujasite zeolites. *J. Catal.* **286**, 214–223 (2012).

86. Akpa, B. S. *et al.* Solvent effects in the hydrogenation of 2-butanone. *J. Catal.* **289**, 30–41 (2012).

87. Desai, S. K. & Neurock, M. First-principles study of the role of solvent in the dissociation of water over a Pt-Ru alloy. *Phys. Rev. B* **68**, 75420 (2003).

88. Corma, A., Iborra, S. & Velty, A. Chemical Routes for the Transformation of

Biomass into Chemicals. *Chem. Rev.* **107**, 2411–2502 (2007).

89. Huber, G. W., Iborra, S. & Corma, A. Synthesis of Transportation Fuels from Biomass: Chemistry, Catalysts, and Engineering. *Chem. Rev.* **106**, 4044–4098 (2006).

90. Roman-Leshkov, Y., Román-Leshkov, Y., Chheda, J. N., Dumesic, J. A. & Roman-Leshkov, Y. Phase Modifiers Promote Efficient Production of Hydroxymethylfurfural from Fructose. *Science (80-.).* **312**, 1933–1937 (2006).

91. van Putten, R.-J. *et al.* Hydroxymethylfurfural, A Versatile Platform Chemical Made from Renewable Resources. *Chem. Rev.* **113**, 1499–1597 (2013).

92. Zakrzewska, M. E., Bogel-Łukasik, E. & Bogel-Łukasik, R. Ionic Liquid-Mediated Formation of 5-Hydroxymethylfurfural—A Promising Biomass-Derived Building Block. *Chem. Rev.* **111**, 397–417 (2011).

93. Binder, J. B. & Raines, R. T. Simple Chemical Transformation of Lignocellulosic Biomass into Furans for Fuels and Chemicals. *J. Am. Chem. Soc.* **131**, 1979–1985 (2009).

94. Rosatella, A. A., Simeonov, S. P., Frade, R. F. M. & Afonso, C. A. M. 5-Hydroxymethylfurfural (HMF) as a building block platform: Biological properties, synthesis and synthetic applications. *Green Chem.* **13**, 754 (2011).

95. Swift, T. D. *et al.* Kinetics of Homogeneous Brønsted Acid Catalyzed Fructose Dehydration and 5-Hydroxymethyl Furfural Rehydration: A Combined Experimental and Computational Study. *ACS Catal.* **4**, 259–267 (2014).

96. Akien, G. R. *et al.* Molecular mapping of the acid catalysed dehydration of fructose. *Chem. Commun.* **48**, 5850 (2012).

97. Carey, F. A. & Sundberg, R. J. *Advanced Organic Chemistry. Part A: Structure and Mechanisms.* (Springer, 2007).

98. Willi, A. V. Chapter 1 Homogeneous Catalysis of Organic Reactions (Mainly Acid-Base). in *Proton Transfer, Volume 8* (eds. Bamford, C. H. & Tipper, C. F.) 21–24 (Elsevier Science, 1997). doi:10.1016/S0069-8040(08)70089-X

99. Cox, B. G. *Acids and Bases: Solvent Effects on Acid-Base Strength.* (Oxford University Press, 2013).

100. Waghorne, W. E. Thermodynamics of solvation in mixed solvents. *Chem. Soc. Rev.* **22**, 285 (1993).

101. Reichardt, C. & Welton, T. *Solvents and Solvent Effects in Organic Chemistry.*

(Wiley-VCH Verlag GmbH & Co. KGaA, 2010). doi:10.1002/9783527632220

102. Madon, R. J. & Iglesia, E. Catalytic reaction rates in thermodynamically non-ideal systems. *J. Mol. Catal. A Chem.* **163**, 189–204 (2000).

103. Chia, M. *et al.* Selective Hydrogenolysis of Polyols and Cyclic Ethers over Bifunctional Surface Sites on Rhodium–Rhenium Catalysts. *J. Am. Chem. Soc.* **133**, 12675–12689 (2011).

104. Lotze, S., Groot, C. C. M., Vennehaug, C. & Bakker, H. J. Femtosecond Mid-Infrared Study of the Dynamics of Water Molecules in Water–Acetone and Water–Dimethyl Sulfoxide Mixtures. *J. Phys. Chem. B* **119**, 5228–5239 (2015).

105. Wallace, V. M., Dhumal, N. R., Zehentbauer, F. M., Kim, H. J. & Kiefer, J. Revisiting the Aqueous Solutions of Dimethyl Sulfoxide by Spectroscopy in the Mid- and Near-Infrared: Experiments and Car–Parrinello Simulations. *J. Phys. Chem. B* **119**, 14780–14789 (2015).

106. Mizuno, K., Imafuji, S., Ochi, T., Ohta, T. & Maeda, S. Hydration of the CH Groups in Dimethyl Sulfoxide Probed by NMR and IR. *J. Phys. Chem. B* **104**, 11001–11005 (2000).

107. Kirchner, B. Theory of complicated liquids Investigation of liquids, solvents and solvent effects with modern theoretical methods. *Phys. Rep.* **440**, 1–111 (2007).

108. Kalidas, C., Hefter, G. & Marcus, Y. Gibbs Energies of Transfer of Cations from Water to Mixed Aqueous Organic Solvents. *Chem. Rev.* **100**, 819–852 (2000).

109. Ripin, D. H. & Evans, D. A. Evan's pKa Table. (2005). Available at: http://evans.rc.fas.harvard.edu/pdf/evans_pKa_table.pdf.

110. Fujinaga, T. & Sakamoto, I. Electrochemical studies of sulfonates in non-aqueous solvents. *J. Electroanal. Chem. Interfacial Electrochem.* **85**, 185–201 (1977).

111. Das, K., Das, A. K. & Kundu, K. K. Ion-solvent interactions in acetonitrile + water mixtures. *Electrochim. Acta* **26**, 471–478 (1981).

112. Cox, B. G., Natarajan, R. & Waghorne, W. E. Thermodynamic properties for transfer of electrolytes from water to acetonitrile and to acetonitrile + water mixtures. *J. Chem. Soc. Faraday Trans. 1 Phys. Chem. Condens. Phases* **75**, 86 (1979).

113. Das, P. B. Thermodynamics of electrolytes in dioxane—water mixtures from conductance data. *Thermochim. Acta* **47**, 109–111 (1981).

114. Zhang, J., Das, A., Assary, R. S., Curtiss, L. A. & Weitz, E. A combined

experimental and computational study of the mechanism of fructose dehydration to 5-hydroxymethylfurfural in dimethylsulfoxide using Amberlyst 70, PO43−/niobic acid, or sulfuric acid catalysts. *Appl. Catal. B Environ.* **181**, 874–887 (2016).

115. Truhlar, D. G. Inverse solvent design. *Nat. Chem.* **5**, 902–903 (2013).

116. Struebing, H. *et al.* Computer-aided molecular design of solvents for accelerated reaction kinetics. *Nat. Chem.* **5**, 952–957 (2013).

117. Knifton, J. F., Sanderson, J. R. & Stockton, M. E. Tert-butanol dehydration to isobutylene via reactive distillation. *Catal. Lett.* **73**, (2001).

118. Mori, K., Yamada, Y. & Sato, S. Catalytic dehydration of 1,2-propanediol into propanal. *Appl. Catal. A Gen.* **366**, 304–308 (2009).

119. Courtney, T. D., Nikolakis, V., Mpourmpakis, G., Chen, J. G. & Vlachos, D. G. Liquid-phase dehydration of propylene glycol using solid-acid catalysts. *Appl. Catal. A Gen.* **449**, 59–68 (2012).

120. Clever, H. L. & Pigott, S. P. Enthalpies of mixing of dimethylsulfoxide with water and with several ketones at 298.15 K. *J. Chem. Thermodyn.* **3**, 221–225 (1971).

121. Goates, J. R. & Sullivan, R. J. Thermodynamic Properties of the System Water-p-Dioxane. *J. Phys. Chem.* **62**, 188–190 (1958).

122. Glew, D. N. & Watts, H. Aqueous Nonelectrolyte Solutions. Part XII. Enthalpies of Mixing of Water and Deuterium Oxide with Tetrahydrofuran. *Can. J. Chem.* **51**, 1933–1940 (1973).

123. Zaitseva, A., Pokki, J.-P., Le, H. Q., Alopaeus, V. & Sixta, H. Vapor–Liquid Equilibria, Excess Enthalpy, and Density of Aqueous γ-Valerolactone Solutions. *J. Chem. Eng. Data* **61**, 881–890 (2016).

124. Morcom, K. W. & Smith, R. W. Enthalpies of mixing of water+methyl cyanide. *J. Chem. Thermodyn.* **1**, 503–505 (1969).

125. Abraham, M. J. *et al.* GROMACS: High performance molecular simulations through multi-level parallelism from laptops to supercomputers. *SoftwareX* **1–2**, 19–25 (2015).

126. Hutter, J., Iannuzzi, M., Schiffmann, F. & VandeVondele, J. cp2k: atomistic simulations of condensed matter systems. *Wiley Interdiscip. Rev. Comput. Mol. Sci.* **4**, 15–25 (2014).

127. Goga, N., Rzepiela, A. J., De Vries, A. H., Marrink, S. J. & Berendsen, H. J. C. Efficient algorithms for langevin and DPD dynamics. *J. Chem. Theory Comput.* **8**,

3637–3649 (2012).

128. Parrinello, M. & Rahman, A. Polymorphic transitions in single crystals: A new molecular dynamics method. *J. Appl. Phys.* **52**, 7182–7190 (1981).

129. Nosé, S. & Klein, M. L. Constant pressure molecular dynamics for molecular systems. *Mol. Phys.* **50**, 1055–1076 (1983).

130. Jorgensen, W. L., Maxwell, D. S. & Tirado-Rives, J. Development and Testing of the OPLS All-Atom Force Field on Conformational Energetics and Properties of Organic Liquids. *J. Am. Chem. Soc.* **118**, 11225–11236 (1996).

131. Kony, D. *et al.* An improved OPLS-AA force field for carbohydrates. *J. Comput. Chem.* **23**, 1416–1429 (2002).

132. Berendsen, H. J. C., Grigera, J. R. & Straatsma, T. P. The missing term in effective pair potentials. *J. Phys. Chem.* **91**, 6269–6271 (1987).

133. Miyamoto, S. & Kollman, P. A. Settle: An analytical version of the SHAKE and RATTLE algorithm for rigid water models. *J. Comput. Chem.* **13**, 952–962 (1992).

134. Perdew, J. P., Burke, K. & Ernzerhof, M. Generalized Gradient Approximation Made Simple. *Phys. Rev. Lett.* **77**, 3865–3868 (1996).

135. VandeVondele, J. & Hutter, J. Gaussian basis sets for accurate calculations on molecular systems in gas and condensed phases. *J. Chem. Phys.* **127**, 114105 (2007).

136. Goedecker, S., Teter, M. & Hutter, J. Separable dual-space Gaussian pseudopotentials. *Phys. Rev. B* **54**, 1703–1710 (1996).

137. Grimme, S., Ehrlich, S. & Goerigk, L. Effect of the damping function in dispersion corrected density functional theory. *J. Comput. Chem.* **32**, 1456–1465 (2011).

138. Bussi, G., Donadio, D. & Parrinello, M. Canonical sampling through velocity rescaling. *J. Chem. Phys.* **126**, 014101 (2007).

139. Grossfield, A. WHAM: the weighted histogram analysis method. Available at: http://membrane.urmc.rochester.edu/content/wham.

140. Sunda, A. P. *et al.* Molecular dynamics simulations of triflic acid and triflate ion/water mixtures: A proton conducting electrolytic component in fuel cells. *J. Comput. Chem.* **32**, 3319–3328 (2011).

141. Shuai, L. & Luterbacher, J. Organic Solvent Effects in Biomass Conversion Reactions. *ChemSusChem* **9**, 133–155 (2016).

142. Alonso, D. M. *et al.* Increasing the revenue from lignocellulosic biomass: Maximizing feedstock utilization. *Sci. Adv.* **3**, e1603301 (2017).

143. Mellmer, M. A., Gallo, J. M. R., Martin Alonso, D. & Dumesic, J. A. Selective Production of Levulinic Acid from Furfuryl Alcohol in THF Solvent Systems over H-ZSM-5. *ACS Catal.* **5**, 3354–3359 (2015).

144. Ren, L.-K. *et al.* Performance of Dimethyl Sulfoxide and Brønsted Acid Catalysts in Fructose Conversion to 5-Hydroxymethylfurfural. *ACS Catal.* **7**, 2199–2212 (2017).

145. Robinson, J. M. Biomass refining by selective chemical reactions. (2012).

146. Caes, B. R. & Raines, R. T. Conversion of Fructose into 5-(Hydroxymethyl)furfural in Sulfolane. *ChemSusChem* **4**, 353–356 (2011).

147. Gallo, J. M. R., Alonso, D. M., Mellmer, M. A. & Dumesic, J. A. Production and upgrading of 5-hydroxymethylfurfural using heterogeneous catalysts and biomass-derived solvents. *Green Chem.* **15**, 85–90 (2013).

148. Luterbacher, J. S. *et al.* Lignin monomer production integrated into the γ-valerolactone sugar platform. *Energy Environ. Sci.* **8**, 2657–2663 (2015).

149. Gallo, J. M. R. *et al.* Production of Furfural from Lignocellulosic Biomass Using Beta Zeolite and Biomass-Derived Solvent. *Top. Catal.* **56**, 1775–1781 (2013).

150. Johnson, R. L. *et al.* Solvent–Solid Interface of Acid Catalysts Studied by High Resolution MAS NMR. *J. Phys. Chem. C* **121**, 17226–17234 (2017).

151. Zhu, Y. *et al.* Production of furfural from xylose and corn stover catalyzed by a novel porous carbon solid acid in γ-valerolactone. *RSC Adv.* **7**, 29916–29924 (2017).

152. He, J. *et al.* Production of levoglucosenone and 5-hydroxymethylfurfural from cellulose in polar aprotic solvent–water mixtures. *Green Chem.* **19**, 3642–3653 (2017).

153. Cao, F. *et al.* Dehydration of cellulose to levoglucosenone using polar aprotic solvents. *Energy Environ. Sci.* **8**, 1808–1815 (2015).

154. Li, M. *et al.* High conversion of glucose to 5-hydroxymethylfurfural using hydrochloric acid as a catalyst and sodium chloride as a promoter in a water/γ-valerolactone system. *RSC Adv.* **7**, 14330–14336 (2017).

155. Mascal, M. & Nikitin, E. B. Dramatic Advancements in the Saccharide to 5-(Chloromethyl)furfural Conversion Reaction. *ChemSusChem* **2**, 859–861 (2009).

156. Mascal, M. 5-(Chloromethyl)furfural is the New HMF: Functionally Equivalent But More Practical in Terms of its Production From Biomass. *ChemSusChem* **8**, 3391–3395 (2015).

157. Wong, C. Y. Y. *et al.* Stability of gamma-valerolactone under neutral, acidic, and basic conditions. *Struct. Chem.* **28**, 423–429 (2017).

158. Cai, Y., Concha, M. C., Murray, J. S. & Cole, R. B. Evaluation of the role of multiple hydrogen bonding in offering stability to negative ion adducts in electrospray mass spectrometry. *J. Am. Soc. Mass Spectrom.* **13**, 1360–1369 (2002).

159. Jiang, Y. & Cole, R. B. Oligosaccharide analysis using anion attachment in negative mode electrospray mass spectrometry. *J. Am. Soc. Mass Spectrom.* **16**, 60–70 (2005).

160. Li, H. & Smith, R. L. Solvents take control. *Nat. Catal.* **1**, 176–177 (2018).

161. Trummal, A., Lipping, L., Kaljurand, I., Koppel, I. A. & Leito, I. Acidity of Strong Acids in Water and Dimethyl Sulfoxide. *J. Phys. Chem. A* **120**, 3663–3669 (2016).

162. March, J. *Advanced Organic Chemistry: Reactions, Mechanisms and Structure.* (John Wiley & Sons, 1985).

163. Soderberg, T. *Organic Chemistry with Biological Emphasis.* (Chemistry Publications, 2016).

164. Martínez, L., Andrade, R., Birgin, E. G. & Martínez, J. M. PACKMOL: A package for building initial configurations for molecular dynamics simulations. *J. Comput. Chem.* **30**, 2157–2164 (2009).

165. Bonthuis, D. J., Mamatkulov, S. I. & Netz, R. R. Optimization of classical nonpolarizable force fields for OH − and H 3 O +. *J. Chem. Phys.* **144**, 104503 (2016).

166. Koneshan, S., Rasaiah, J. C., Lynden-Bell, R. M. & Lee, S. H. Solvent Structure, Dynamics, and Ion Mobility in Aqueous Solutions at 25 °C. *J. Phys. Chem. B* **102**, 4193–4204 (1998).

167. Canongia Lopes, J. N., Pádua, A. A. H. & Shimizu, K. Molecular Force Field for Ionic Liquids IV: Trialkylimidazolium and Alkoxycarbonyl-Imidazolium Cations; Alkylsulfonate and Alkylsulfate Anions. *J. Phys. Chem. B* **112**, 5039–5046 (2008).

168. Serrano-Ruiz, J. C., Luque, R., Sepúlveda-Escribano, A. & Sepulveda-Escribano, A. Transformations of biomass-derived platform molecules: from high added-value chemicals to fuels via aqueous-phase processing. *Chem. Soc. Rev.* **40**, 5266 (2011).

169. Wang, J., Ren, J., Liu, X., Lu, G. & Wang, Y. High yield production and purification of 5-hydroxymethylfurfural. *AIChE J.* **59**, 2558–2566 (2013).

170. Tang, J. *et al.* Insights into the Kinetics and Reaction Network of Aluminum Chloride-Catalyzed Conversion of Glucose in NaCl–H 2 O/THF Biphasic System. *ACS Catal.* **7**, 256–266 (2017).

171. Fang, X. *et al.* Efficient Conversion of Cellulose to 5-Hydroxymethylfurfural in NaHSO 4 /ZrO 2 /H 2 O-THF Biphasic System. *ChemistrySelect* **3**, 12243–12249 (2018).

172. Román-Leshkov, Y. & Dumesic, J. A. Solvent Effects on Fructose Dehydration to 5-Hydroxymethylfurfural in Biphasic Systems Saturated with Inorganic Salts. *Top. Catal.* **52**, 297–303 (2009).

173. Jiang, Z. *et al.* A one-pot microwave-assisted NaCl–H2O/GVL solvent system for cellulose conversion to 5-hydroxymethylfurfural and saccharides with in situ separation of the products. *Cellulose* **26**, 8383–8400 (2019).

174. van der Graaff, W. N. P. *et al.* Competitive Adsorption of Substrate and Solvent in Sn-Beta Zeolite During Sugar Isomerization. *ChemSusChem* **9**, 3145–3149 (2016).

175. Nguyen, V. T. M. *et al.* A comparative study of the adsorption of water and methanol in zeolite BEA: a molecular simulation study. *Mol. Simul.* **40**, 1113–1124 (2014).

176. Sumerskii, I. V., Krutov, S. M. & Zarubin, M. Y. Humin-like substances formed under the conditions of industrial hydrolysis of wood. *Russ. J. Appl. Chem.* **83**, 320–327 (2010).

177. Patil, S. K. R., Heltzel, J. & Lund, C. R. F. Comparison of Structural Features of Humins Formed Catalytically from Glucose, Fructose, and 5-Hydroxymethylfurfuraldehyde. *Energy & Fuels* **26**, 5281–5293 (2012).

178. Patil, S. K. R. & Lund, C. R. F. Formation and Growth of Humins via Aldol Addition and Condensation during Acid-Catalyzed Conversion of 5-Hydroxymethylfurfural. *Energy & Fuels* **25**, 4745–4755 (2011).

179. Christianson, J. R., Caratzoulas, S. & Vlachos, D. G. Computational Insight into the Effect of Sn-Beta Na Exchange and Solvent on Glucose Isomerization and Epimerization. *ACS Catal.* **5**, 5256–5263 (2015).

180. Román-Leshkov, Y., Moliner, M., Labinger, J. A. & Davis, M. E. Mechanism of Glucose Isomerization Using a Solid Lewis Acid Catalyst in Water. *Angew. Chemie Int. Ed.* **49**, 8954–8957 (2010).

181. Li, Y.-P., Head-Gordon, M. & Bell, A. T. Analysis of the Reaction Mechanism and

Catalytic Activity of Metal-Substituted Beta Zeolite for the Isomerization of Glucose to Fructose. *ACS Catal.* **4**, 1537–1545 (2014).

182. Li, G., Pidko, E. A. & Hensen, E. J. M. Synergy between Lewis acid sites and hydroxyl groups for the isomerization of glucose to fructose over Sn-containing zeolites: a theoretical perspective. *Catal. Sci. Technol.* **4**, 2241–2250 (2014).

183. Chiang, Y., Kresge, A. J. & Schepp, N. P. Temperature coefficients of the rates of acid-catalyzed enolization of acetone and ketonization of its enol in aqueous and acetonitrile solutions. Comparison of thermodynamic parameters for the keto-enol equilibrium in solution with those in the gas phase. *J. Am. Chem. Soc.* **111**, 3977–3980 (1989).

184. *CRC Handbook of Chemistry and Physics*. (CRC Press, 2015).

185. Alonso, J. L., Gonzalez, E., Caminati, W. & Velino, B. Reinvestigation of the microwave spectrum of γ-valerolactone. *J. Mol. Spectrosc.* **122**, 247–258 (1987).

186. Li, Q. & Simonetti, D. A. Solvation Effects on Acid-Catalyzed Reaction Paths of Propionaldehyde in the Liquid Phase. (University of California, Los Angeles, 2017).

187. *Zeolites in Industrial Separation and Catalysis*. (Wiley, 2010). doi:10.1002/9783527629565

188. Wang, S. & Peng, Y. Natural zeolites as effective adsorbents in water and wastewater treatment. *Chem. Eng. J.* **156**, 11–24 (2010).

189. Chouhan, A. P. S. & Sarma, A. K. Modern heterogeneous catalysts for biodiesel production: A comprehensive review. *Renew. Sustain. Energy Rev.* **15**, 4378–4399 (2011).

190. Chica, A., Strohmaier, K. G. & Iglesia, E. Effects of zeolite structure and aluminum content on thiophene adsorption, desorption, and surface reactions. *Appl. Catal. B Environ.* **60**, 223–232 (2005).

191. Liu, B., García-Pérez, E., Dubbeldam, D., Smit, B. & Calero, S. Understanding Aluminum Location and Non-framework Ions Effects on Alkane Adsorption in Aluminosilicates: A Molecular Simulation Study. *J. Phys. Chem. C* **111**, 10419–10426 (2007).

192. Olson, D. H. The crystal structure of dehydrated NaX. *Zeolites* **15**, 439–443 (1995).

193. Van Dun, J. J., Dhaeze, K. & Mortier, W. J. Temperature-dependent cation distribution in zeolites. 2. Dehydrated NaxHY (x = 13, 23, 42, 54), Ca15HY, and Sr27Y. *J. Phys. Chem.* **92**, 6747–6754 (1988).

194. Marra, G. L. *et al.* Cation Location in Dehydrated Na−Rb−Y Zeolite: An XRD and IR Study. *J. Phys. Chem. B* **101**, 10653–10660 (1997).

195. Sanders, M. J., Catlow, C. R. A. & Smith, J. V. Crystal energy calculations from strontium ions in zeolite A. *J. Phys. Chem.* **88**, 2796–2797 (1984).

196. Barrer, R. M. Cation partitioning among sub-lattices in zeolites. *Zeolites* **4**, 361–368 (1984).

197. Van Dun, J. J. & Mortier, W. J. Temperature-dependent cation distribution in zeolites. 1. A statistical thermodynamical model. *J. Phys. Chem.* **92**, 6740–6746 (1988).

198. Smolders, E., Van Dun, J. J. & Mortier, W. J. A statistical thermodynamical description of the cation distribution and ion exchange in zeolites. *J. Phys. Chem.* **95**, 9908–9911 (1991).

199. Gorman, A. M., Freeman, C. M., Kölmel, C. M. & Newsam, C. M. Accelerated approach to non-framework cation placement in crystalline materials. *Faraday Discuss.* **106**, 489–494 (1997).

200. Li, B., Sun, P., Jin, Q., Wang, J. & Ding, D. Simulated annealing study of cation distribution in dehydrated zeolites. *J. Mol. Struct. THEOCHEM* **391**, 259–263 (1997).

201. Herrero, C. P. & Ramirez, R. Energetics of cation ordering in the faujasite framework: Monte Carlo simulations. *J. Phys. Chem.* **96**, 2246–2253 (1992).

202. Demontis, P., Yashonath, S. & Klein, M. L. Localization and mobility of benzene in sodium-Y zeolite by molecular dynamics calculations. *J. Phys. Chem.* **93**, 5016–5019 (1989).

203. Lachet, V., Boutin, A., Tavitian, B. & Fuchs, A. H. Computational Study of p - Xylene/ m -Xylene Mixtures Adsorbed in NaY Zeolite. *J. Phys. Chem. B* **102**, 9224–9233 (1998).

204. Lee, S. H., Moon, G. K., Choi, S. G. & Kim, H. S. Molecular Dynamics Simulation Studies of Zeolite-A. 3. Structure and Dynamics of Na+ Ions and Water Molecules in a Rigid Zeolite-A. *J. Phys. Chem.* **98**, 1561–1569 (1994).

205. Smirnov, K. S., Le Maire, M., Brémard, C. & Bougeard, D. Vibrational spectra of cation-exchanged zeolite A. Experimental and molecular dynamics study. *Chem. Phys.* **179**, 445–454 (1994).

206. Schrimpf, G., Schlenkrich, M., Brickmann, J. & Bopp, P. Molecular dynamics simulation of zeolite NaY: a study of structure, dynamics, and thermalization of

sorbates. *J. Phys. Chem.* **96**, 7404–7410 (1992).

207. Vitale, G., Mellot, C. F., Bull, L. M. & Cheetham, A. K. Neutron Diffraction and Computational Study of Zeolite NaX: Influence of SIII' Cations on Its Complex with Benzene. *J. Phys. Chem. B* **101**, 4559–4564 (1997).

208. Jaramillo, E. & Auerbach, S. M. New Force Field for Na Cations in Faujasite-Type Zeolites. *J. Phys. Chem. B* **103**, 9589–9594 (1999).

209. Massiani, P., Fajula, F., Figueras, F. & Sanz, J. 29Si and 27Al MAS n.m.r. study of the distribution of Si and Al atoms in various forms of synthetic zeolite omega. *Zeolites* **8**, 332–337 (1988).

210. Newsam, J. M. Aluminium partitioning in zeolite L. *J. Chem. Soc. Chem. Commun.* 123 (1987). doi:10.1039/c39870000123

211. Han, O. H., Kim, C.-S. & Hong, S. B. Direct Evidence for the Nonrandom Nature of Al Substitution in Zeolite ZSM-5: An Investigation by 27Al MAS and MQ MAS NMR. *Angew. Chemie Int. Ed.* **41**, 469–472 (2002).

212. Jeffroy, M., Nieto-Draghi, C. & Boutin, A. New Molecular Simulation Method To Determine Both Aluminum and Cation Location in Cationic Zeolites. *Chem. Mater.* **29**, 513–523 (2017).

213. Fitch, A. N., Jobic, H. & Renouprez, A. Localization of benzene in sodium-Y-zeolite by powder neutron diffraction. *J. Phys. Chem.* **90**, 1311–1318 (1986).

214. Gramlich, V. Untersuchung und Verfeinerung pseudosymmetrischer Strukturen. (ETH, Zürich, Switzerland, 1971).

215. Auerbach, S. M., Henson, N. J., Cheetham, A. K. & Metiu, H. I. Transport Theory for Cationic Zeolites: Diffusion of Benzene in Na-Y. *J. Phys. Chem.* **99**, 10600–10608 (1995).

216. Grey, C. P. *et al.* Combined MAS NMR and X-ray Powder Diffraction Structural Characterization of Hydrofluorocarbon-134 Adsorbed on Zeolite NaY: Observation of Cation Migration and Strong Sorbate−Cation Interactions. *J. Am. Chem. Soc.* **119**, 1981–1989 (1997).

217. Jirák, Z., Vratislav, S. & Bosáček, V. A neutron diffraction study of H, Na-Y zeolites. *J. Phys. Chem. Solids* **41**, 1089–1095 (1980).

218. Mortier, W. J., Van den Bossche, E. & Uytterhoeven, J. B. Influence of the temperature and water adsorption on the cation location in Na☐Y zeolites. *Zeolites* **4**, 41–44 (1984).

219. Eulenberger, G. R., Shoemaker, D. P. & Keil, J. G. Crystal structures of hydrated and dehydrated synthetic zeolites with faujasite aluminosilicate frameworks. I. The dehydrated sodium, potassium, and silver forms. *J. Phys. Chem.* **71**, 1812–1819 (1967).

220. Korányi, T. I. Distribution of Aluminum in the Periodical Building Units of Faujasites. *J. Phys. Chem. C* **111**, 2520–2524 (2007).

221. Kato, M., Itabashi, K., Matsumoto, A. & Tsutsumi, K. Characteristics of MOR-Framework Zeolites Synthesized in Fluoride-Containing Media and Related Ordered Distribution of Al Atoms in the Framework. *J. Phys. Chem. B* **107**, 1788–1797 (2003).

222. Martin, M. G. MCCCS Towhee: a tool for Monte Carlo molecular simulation. *Mol. Simul.* **39**, 1212–1222 (2013).

223. Frising, T. & Leflaive, P. Extraframework cation distributions in X and Y faujasite zeolites: A review. *Microporous Mesoporous Mater.* **114**, 27–63 (2008).

224. Fyfe, C. A. *et al.* Detailed interpretation of the 29Si and 27Al high-field MAS n.m.r. spectra of zeolites offretite and omega. *Zeolites* **5**, 179–183 (1985).

225. Sanz, J., Herrero, C. P. & Robert, J.-L. Distribution of Si and Al in Clintonites: A Combined NMR and Monte Carlo Study. *J. Phys. Chem. B* **107**, 8337–8342 (2003).

226. Sklenak, S. *et al.* Aluminum Siting in Silicon-Rich Zeolite Frameworks: A Combined High-Resolution27Al NMR Spectroscopy and Quantum Mechanics / Molecular Mechanics Study of ZSM-5. *Angew. Chemie Int. Ed.* **46**, 7286–7289 (2007).

227. Sklenak, S. *et al.* Aluminium siting in the ZSM-5 framework by combination of high resolution 27Al NMR and DFT/MM calculations. *Phys. Chem. Chem. Phys.* **11**, 1237–1247 (2009).

228. Dempsey, E. Calculation of Madelung potentials for faujasite-type zeolites. I. *J. Phys. Chem.* **73**, 3660–3668 (1969).

229. Lu, B., Kanai, T., Oumi, Y. & Sano, T. Aluminum distribution in high-silica mordenite. *J. Porous Mater.* **14**, 89–96 (2007).

230. Shiokawa, K., Ito, M. & Itabashi, K. Crystal structure of synthetic mordenites. *Zeolites* **9**, 170–176 (1989).

231. Rigby, A. M., Kramer, G. J. & van Santen, R. A. Mechanisms of Hydrocarbon Conversion in Zeolites: A Quantum Mechanical Study. *J. Catal.* **170**, 1–10 (1997).

232. Corma, A. Inorganic Solid Acids and Their Use in Acid-Catalyzed Hydrocarbon Reactions. *Chem. Rev.* **95**, 559–614 (1995).

233. Csicsery, S. M. Shape-selective catalysis in zeolites. *Zeolites* **4**, 202–213 (1984).

234. Varghese, J. J. & Mushrif, S. H. Origins of complex solvent effects on chemical reactivity and computational tools to investigate them: a review. *React. Chem. Eng.* **4**, 165–206 (2019).

235. Carrea, G., Ottolina, G. & Riva, S. Role of solvents in the control of enzyme selectivity in organic media. *Trends Biotechnol.* **13**, 63–70 (1995).

236. MUKHERJEE, S. & VANNICE, M. Solvent effects in liquid-phase reactionsI. Activity and selectivity during citral hydrogenation on Pt/SiO2 and evaluation of mass transfer effects. *J. Catal.* **243**, 108–130 (2006).

237. Kuo, S.-J. & Parkin, K. L. Solvent polarity influences product selectivity of lipase-mediated esterification reactions in microaqueous media. *J. Am. Oil Chem. Soc.* **73**, 1427 (1996).

238. Lee, C. W. Diels-Alder reactions in chloroaluminate ionic liquids: acceleration and selectivity enhancement. *Tetrahedron Lett.* **40**, 2461–2464 (1999).

239. Aggarwal, A., Lancaster, N. L., Sethi, A. R. & Welton, T. The role of hydrogen bonding in controlling the selectivity of Diels–Alder reactions in room-temperature ionic liquids. *Green Chem.* **4**, 517–520 (2002).

240. Grieco, P. A., Garner, P. & He, Z. "Micellar" catalysis in the aqueous intermolecular diels-alder reaction: rate acceleration and enhanced selectivity. *Tetrahedron Lett.* **24**, 1897–1900 (1983).

241. Neurock, M. Perspectives on the first principles elucidation and the design of active sites. *J. Catal.* **216**, 73–88 (2003).

242. Nørskov, J. K., Bligaard, T., Rossmeisl, J. & Christensen, C. H. Towards the computational design of solid catalysts. *Nat. Chem.* **1**, 37–46 (2009).

243. Houk, K. N. & Cheong, P. H.-Y. Computational prediction of small-molecule catalysts. *Nature* **455**, 309–313 (2008).

244. Catlow, C. R. ., French, S. ., Sokol, A. . & Thomas, J. . Computational approaches to the determination of active site structures and reaction mechanisms in heterogeneous catalysts. *Philos. Trans. R. Soc. A Math. Phys. Eng. Sci.* **363**, 913–936 (2005).

245. Leach, A. R. *Molecular Modelling: Principles and Applications*. (Pearson

Education, 2001).

246. Perdew, J. P. Jacob's ladder of density functional approximations for the exchange-correlation energy. in *AIP Conference Proceedings* **577**, 1–20 (AIP, 2001).

247. Mardirossian, N. & Head-Gordon, M. Thirty years of density functional theory in computational chemistry: an overview and extensive assessment of 200 density functionals. *Mol. Phys.* **115**, 2315–2372 (2017).

248. Ziegler, T. Approximate density functional theory as a practical tool in molecular energetics and dynamics. *Chem. Rev.* **91**, 651–667 (1991).

249. VAN SANTEN, R. A. & NEUROCK, M. Concepts in Theoretical Heterogeneous Catalytic Reactivity. *Catal. Rev.* **37**, 557–698 (1995).

250. van Santen, R. . The cluster approach to molecular heterogeneous catalysis1Communication presented at the First Francqui Colloquium, Brussels, 19–20 February 1996.1. *J. Mol. Catal. A Chem.* **115**, 405–419 (1997).

251. Hafner, J. Atomic-scale computational materials science. *Acta Mater.* **48**, 71–92 (2000).

252. Hammer, B. & Nørskov, J. K. Theoretical surface science and catalysis—calculations and concepts. in 71–129 (2000). doi:10.1016/S0360-0564(02)45013-4

253. Hammer, B. & Nørskov, J. K. Theory of Adsorption and Surface Reactions. in *Chemisorption and Reactivity on Supported Clusters and Thin Films* 285–351 (Springer Netherlands, 1997). doi:10.1007/978-94-015-8911-6_11

254. Payne, M. C., Teter, M. P., Allan, D. C., Arias, T. A. & Joannopoulos, J. D. Iterative minimization techniques for ab initio total-energy calculations: molecular dynamics and conjugate gradients. *Rev. Mod. Phys.* **64**, 1045–1097 (1992).

255. Skyner, R. E., McDonagh, J. L., Groom, C. R., van Mourik, T. & Mitchell, J. B. O. A review of methods for the calculation of solution free energies and the modelling of systems in solution. *Phys. Chem. Chem. Phys.* **17**, 6174–6191 (2015).

256. Tomasi, J., Mennucci, B. & Cammi, R. Quantum Mechanical Continuum Solvation Models. *Chem. Rev.* **105**, 2999–3094 (2005).

257. Cramer, C. J. & Truhlar, D. G. Implicit Solvation Models: Equilibria, Structure, Spectra, and Dynamics. *Chem. Rev.* **99**, 2161–2200 (1999).

258. Dauenhauer, P. J. & Abdelrahman, O. A. A Universal Descriptor for the Entropy of Adsorbed Molecules in Confined Spaces. *ACS Cent. Sci.* **4**, 1235–1243 (2018).

259. Torrie, G. M. & Valleau, J. P. Nonphysical sampling distributions in Monte Carlo free-energy estimation: Umbrella sampling. *J. Comput. Phys.* **23**, 187–199 (1977).

260. Misono, M. *et al.* Catalysis by Heteropoly Compounds. III. The Structure and Properties of 12-Heteropolyacids of Molybdenum and Tungsten (H 3 PMo 12− x W x O 40) and Their Salts Pertinent to Heterogeneous Catalysis. *Bull. Chem. Soc. Jpn.* **55**, 400–406 (1982).

261. Mizuno, N., Han, W. & Kudo, T. Selective Oxidation of Ethane, Propane, and Isobutane Catalyzed by Copper-Containing Cs2.5H1.5PVMo11O40under Oxygen-Poor Conditions. *J. Catal.* **178**, 391–394 (1998).

262. Okuhara, T., Mizuno, N. & Misono, M. Catalytic Chemistry of Heteropoly Compounds. in 113–252 (1996). doi:10.1016/S0360-0564(08)60041-3

263. Kozhevnikov, I. V. Catalysis by Heteropoly Acids and Multicomponent Polyoxometalates in Liquid-Phase Reactions. *Chem. Rev.* **98**, 171–198 (1998).

264. JANIK, M., DAVIS, R. & NEUROCK, M. A density functional theory study of the alkylation of isobutane with butene over phosphotungstic acid. *J. Catal.* **244**, 65–77 (2006).

265. Janik, M. J., Campbell, K. a., Bardin, B. B., Davis, R. J. & Neurock, M. A computational and experimental study of anhydrous phosphotungstic acid and its interaction with water molecules. *Appl. Catal. A Gen.* **256**, 51–68 (2003).

266. Bardin, B. B., Bordawekar, S. V., Neurock, M. & Davis, R. J. Acidity of Keggin-Type Heteropolycompounds Evaluated by Catalytic Probe Reactions, Sorption Microcalorimetry, and Density Functional Quantum Chemical Calculations. *J. Phys. Chem. B* **102**, 10817–10825 (1998).

267. Okuhara, T., Hu, C., Hashimoto, M. & Misono, M. Acid Strength of Heteropolyacids and Its Correlation with Catalytic Activity. *Bull. Chem. Soc. Jpn.* **67**, 1186–1188 (1994).

268. Macht, J., Janik, M. J., Neurock, M. & Iglesia, E. Catalytic Consequences of Composition in Polyoxometalate Clusters with Keggin Structure. *Angew. Chemie Int. Ed.* **46**, 7864–7868 (2007).

269. Farneth, W. E. & Gorte, R. J. Methods for Characterizing Zeolite Acidity. *Chem. Rev.* **95**, 615–635 (1995).

270. Biaglow, A. I., Gorte, R. J., Kokotailo, G. T. & White, D. A Probe of Brønsted Site Acidity in Zeolites: 13C Chemical Shift of Acetone. *J. Catal.* **148**, 779–786 (1994).

271. Gorte, R. J. J. What do we know about the acidity of solid acids? *Catal. Letters* 1–

13 (1999). doi:10.1023/A:1019010013989

272. ARONSON, M. The influence of oxonium ion and carbenium ion stabilities on the Alcohol/H-ZSM-5 interaction*1. *J. Catal.* **98**, 434–443 (1986).

273. Carr, R. T., Neurock, M. & Iglesia, E. Catalytic consequences of acid strength in the conversion of methanol to dimethyl ether. *J. Catal.* **278**, 78–93 (2011).

274. Brändle, M. & Sauer, J. Acidity Differences between Inorganic Solids Induced by Their Framework Structure. A Combined Quantum Mechanics/Molecular Mechanics ab Initio Study on Zeolites. *J. Am. Chem. Soc.* **120**, 1556–1570 (1998).

275. Svelle, S., Tuma, C., Rozanska, X., Kerber, T. & Sauer, J. Quantum Chemical Modeling of Zeolite-Catalyzed Methylation Reactions: Toward Chemical Accuracy for Barriers. *J. Am. Chem. Soc.* **131**, 816–825 (2009).

276. Eder, F., Stockenhuber, M. & Lercher, J. A. Brønsted Acid Site and Pore Controlled Siting of Alkane Sorption in Acidic Molecular Sieves. *J. Phys. Chem. B* **101**, 5414–5419 (1997).

277. Eder, F. & Lercher, J. A. Alkane Sorption on Siliceous and Aluminophosphate Molecular Sieves. A Comparative Study. *J. Phys. Chem.* **100**, 16460–16462 (1996).

278. Gilbert, L. & Mercier, C. Solvent effects in heterogeneous catalysis : Application to the synthesis of fine chemicals. in 51–66 (1993). doi:10.1016/S0167-2991(08)63303-0

279. Sinha, N. K. & Neurock, M. A first principles analysis of the hydrogenation of C1C4 aldehydes and ketones over Ru(0001). *J. Catal.* **295**, 31–44 (2012).

280. Horiuti, I. & Polanyi, M. Exchange reactions of hydrogen on metallic catalysts. *Trans. Faraday Soc.* **30**, 1164 (1934).

281. Mavrikakis, M. & Barteau, M. A. Oxygenate reaction pathways on transition metal surfaces. *J. Mol. Catal. A Chem.* **131**, 135–147 (1998).

282. Okamoto, Y., Sugino, O., Mochizuki, Y., Ikeshoji, T. & Morikawa, Y. Comparative study of dehydrogenation of methanol at Pt(111)/water and Pt(111)/vacuum interfaces. *Chem. Phys. Lett.* **377**, 236–242 (2003).

283. Kua, J. & Goddard, W. A. Oxidation of Methanol on 2nd and 3rd Row Group VIII Transition Metals (Pt, Ir, Os, Pd, Rh, and Ru): Application to Direct Methanol Fuel Cells. *J. Am. Chem. Soc.* **121**, 10928–10941 (1999).

284. Ishikawa, Y., Liao, M.-S. & Cabrera, C. R. Oxidation of methanol on platinum, ruthenium and mixed Pt–M metals (M=Ru, Sn): a theoretical study. *Surf. Sci.* **463**,

66–80 (2000).

285. Desai, S. K., Neurock, M. & Kourtakis, K. A Periodic Density Functional Theory Study of the Dehydrogenation of Methanol over Pt(111). *J. Phys. Chem. B* **106**, 2559–2568 (2002).

286. Greeley, J. & Mavrikakis, M. Competitive Paths for Methanol Decomposition on Pt(111). *J. Am. Chem. Soc.* **126**, 3910–3919 (2004).

287. Watanabe, M. & Motoo, S. Electrocatalysis by ad-atoms. *J. Electroanal. Chem. Interfacial Electrochem.* **60**, 267–273 (1975).